Functional characterization of extraocular muscle in transgenic mouse models

Inauguraldissertation
zur
Erlangung der Würde eines Doktors der Philosophie
vorgelegt der
Philosophisch-Naturwissenschaftlichen Fakultät
der Universität Basel

von

Jan Eckhardt
aus Deutschland

Basel, 2020

Genehmigt von der Philosophisch-Naturwissenschaftlichen Fakultät auf Antrag von

Prof. Susan Treves

Prof. Markus Rüegg

Basel, 18 Februar 2020

Prof. Dr. Martin Spiess

Dekan

Acknowledgement

It would like to thank Prof. Susan Treves and Prof. Francesco Zorzato for the opportunity and exciting journey in the last years towards my Ph.D. Their help, constructive feedback, having patience as well as pushing me to my limits and above was invaluable. The brainstorm sessions at the end of a day with Francesco, where everything was possible, will never be forgotten. And Susan, who always gave me the freedom and support to develop, personally and intellectually.

I am also very thankful to every Perioperative Patient Safety Group members for all their support and nice memories: Moran, Sofia, Martina and Alexis and also the old but not forgotten ones (Ori, Maja, Ruben, Sven, Anne-Sylvie, Asensio and Martine). You all made the daily work a joyful experience. A special thanks goes to Chris (my coffee break buddy) for all the nice and interesting chats we had and his gentle but constant challenge of my consciousness for the environment and my meat consume.

Ein großer Dank geht auch an Konrad, meinen Mentor und Vorbild, und Klara, die mich von Anfang an herzlichst aufgenommen haben. Falls ich es irgendwann schaffe auch nur ein wenig so intelligent und bodenständig zu sein wie du, kann ich froh sein. Vielen Dank für die zahlreichen Lehrstunden und die schönen Zeiten bei euch oben auf dem Berg.

Ich möchte auch meiner Familie, meiner Mutter, Harald, meinem kleinen Bruder und Großeltern danken, die mir immer zur Seite standen und mich auf jede nur erdenkliche Weise unterstützt haben. Ich konnte immer auf euch zählen, ihr habt mich aufgebaut, wenn ich es brauchte und mich wieder auf den Boden geholt, wenn es nötig war.

All das wäre nicht machbar gewesen ohne meine große Liebe, Sarah. Du hast mir all die Jahre den Rücken gestärkt, mich motiviert und ausgehalten. Ich kann dir nicht genug danken. Christoph, mein kleiner Sonnenschein, obwohl du das noch nicht lesen oder verstehen kannst ist diese Arbeit für dich. Es gibt nichts Schöneres wie dein Lachen. Ich liebe euch!

Table of Contents

I. ABSTRACT

Extraocular muscles (EOMs) are among the fastest and most fatigue resistant skeletal muscles; they are categorized as a separate group of muscles or 'allotype' since they represent a unique group of highly specialized muscles anatomically and physiologically different from other skeletal muscles. The distinct origin and innervation of EOMs are probably responsible for their different gene and protein expression. This also applies for the excitation–contraction coupling (ECC) and the calcium handling in EOMs. The main goal of this thesis is to establish methods to study the ECC in mouse EOMs and apply these new techniques on different mouse models.

Calcium is an ubiquitous second messenger mediating numerous physiological processes, including muscle contraction and neuronal excitability. Ca^{2+} is stored in the ER/SR and is released into the cytoplasm via the opening of intracellular inositol trisphosphate receptor and ryanodine receptor calcium channels. Whereas in skeletal muscle, isoform 1 of the RYR is the main channel mediating calcium release from the SR leading to muscle contraction, the function of ubiquitously expressed ryanodine receptor 3 (RyR3) is far from clear. The previous finding of our group, that RyR3 is highly expressed in EOMs versus limb muscles (Sekulic-Jablanovic et al., 2015) is the basis of the first paper entitled "Extraocular muscle function is impaired in ryr3$^{-/-}$ mice". By using the RyR3 KO mouse we were able to show that RyR3 is an essential factor for normal vision, which is the first real functional role of this channel. In detail, the loss of RyR3 reduced the peak force and altered the twitch kinetic of isolated EOMs. Additionally, we found altered calcium transient kinetic in isolated single EOM fibers.

Mutations in the *RYR1* gene are associated with neuromuscular disorders and patients with recessive mutations are severely affected and characteristically display ptosis and/or ophthalmoplegia. Previously we constructed a compound heterozygous RyR1p.Q1970fsX16+p.A4329D (DKI) mutant mice based on a patient biopsy (Klein et al., 2012) and characterized the skeletal muscles (Elbaz et al., 2019b; a). In order to gain insight into the mechanism leading to extraocular muscle involvement, we investigated the biochemical, structural and physiological properties of EOMs from this mouse model. We also investigated the properties of EOMS of heterozygous single mutation carriers as well as mice carrying the

homozygous mutation. These studies constitute the second paper entitled ‘‘Molecular basis of impaired extraocular muscle function in a mouse model of congenital myopathy due to compound heterozygous *RYR1* mutations”. In this paper we were able to show a significant reduction in the ex vivo force of the DKI mouse, while the other lines do not show any changes. These findings were constant with a reduction in the peak calcium transients and in several ECC involved proteins. Interestingly, we also found a tremendous reduction in the specific MyHC-EO isoform. To sum it up, our results shows that the combination of a reduced content of ryanodine and dihydropyridine receptors, changes in the calcium release units and reduced MyHC-EO leads to impaired vision.

The methods and findings in this thesis will be the start of further investigation into EOM specific disorders or neuromuscular disorders which where EOMs are spared or heavy affected.

II. LIST OF ABBREVIATIONS

AD ..... Autosomal dominant
ADP ..... Adenosine diphosphate
AP ..... Action potential
AR ..... Autosomal recessive
ATP ..... Adenosine triphosphate
CaM ..... Calmodulin
CCD ..... Central core disease
CFTD ..... Congenital fiber type disproportion
CN ..... Cranial nerve
CNM ..... Centronuclear myopathy
COX ..... Cytochrome oxidase
CPEO ..... Chronic progressive external ophthalmoplegia
CPVT ..... Catecholaminergic polymorphic ventricular tachycardia
Cryo-EM ..... Cryo-electron microscopy
CSQ ..... Calsequestrin
CTD ..... C-terminal domain
DHPR ..... Dihydropyridine receptor
DKI ..... RyR1p.Q1970fsX16+p.A4329D double knock in
ECC ..... Excitation contraction coupling
EM ..... Electron microscopy
EOM ..... Extraocular muscle
FKBP ..... FK506-binding protein
KDS ..... King–Denborough syndrome
IM ..... Intermediates mesoderm
IO ..... Inferior oblique
IR ..... Inferior rectus
IV ..... In vitro contracture test
JFM ..... Junctional face membrane
KO ..... Knock-out
LPM ..... Lateral plate mesoderm
LR ..... Lateral rectus
LSR ..... Longitudinal sarcoplasmic reticulum
MH ..... Malignant hyperthermia
MHS ..... Malignant hyperthermia susceptibility
MmD ..... Multi-minicore disease
MR ..... Medial rectus
MRF ..... Myogenic regulatory factors
MSM ..... Myosin storage myopathy
MyHC ..... Myosin heavy chain
NAM ..... North american myopathy

NCX ..... Na^+/Ca^{2+} exchanger
NEM ..... Nemaline myopathy
PM ..... Paraxial mesoderm
PMCA ..... Plasma membrane Ca^{2+} ATPase
RyR ..... Ryanodine receptor
SERCA ..... Sarco/endoplasmic reticulum Ca2+-ATPase
SF ..... Selectivity filter
SO ..... Superior oblique
SR ..... Sarcoplasmic reticulum
SRM ..... Superior rectus muscle
STAC3 ..... SH3 and cysteine-rich domain-containing protein 3
TA ..... Tibialis anterior
TAM ..... Tubular aggregate myopathy
TC ..... Terminal cisternae
TK ..... Triple knock-out
VSD ..... Voltage-sensing domain
XLMTM ..... X-linked myotubular myopathy

1 INTRODUCTION

Muscles can be split into three main types: *skeletal*, *smooth* and *cardiac muscles* (Figure 1.1: Muscle types). While the skeletal muscles are mostly under voluntary control, smooth and cardiac muscles are only controlled by the autonomic nervous system or pacemaker cells. Skeletal and cardiac muscles can be grouped together based on their structural similarities, as striated muscles.

Constituting approximately 40 percent of our body mass, the skeletal muscle represents the biggest organ in our body. The main function of skeletal muscle (but not the only one) is locomotion and therefore the production of force and the ability to shortening itself. Because of the high energy uptake, it is also responsible for a significant amount of heat production and is involved in regulation of metabolism.

Smooth muscles are the contractile tissue present in many hollow organs, blood and lymphatic vessels. In comparison to skeletal muscles, they are not striated and cannot be moved voluntarily.

Cardiac muscle is classified as one muscle and not a group of muscles. Like skeletal muscle, it is striated and also shares several basic functional and structural properties. Nevertheless, it has a unique protein composition and is constructed and optimized for repeated contractions at a frequency of around 60 Hz for our entire life.

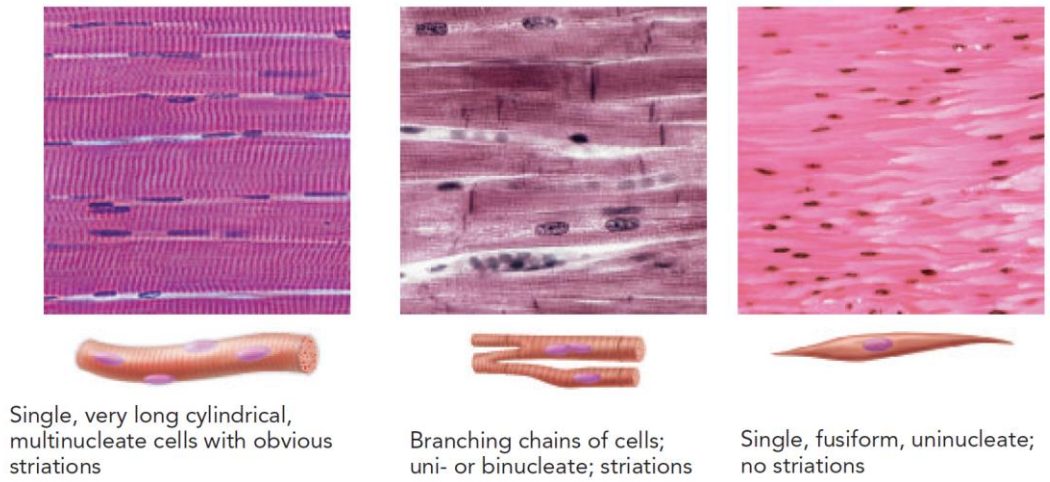

Figure 1.1: Muscle types

Histological **(top)**, cell shapes **(middle)** and description **(bottom)** of the three muscle types. From left to right: skeletal, cardiac and smooth. (Marieb et al.)

1.1 Skeletal Muscle Structure

The skeletal muscle is a highly hierarchical structure, from the top layer, the muscle itself, down to the smallest contractile elements, the myofibrils. Most skeletal muscles are attached to the bones via tendons on both sides. The muscle itself is surrounded by a connective tissue called fasciae, which separates it from other tissues or organs and helps maintain muscle integrity. Directly underneath the fasciae is a sheet of soft connective tissue, called epimysium (Figure 1.2: Structural organization of skeletal muscle). Inside the epimysium the muscles are subdivided into bundles of muscle fibers called fasciculus. These substructures are again surrounded by a layer of connective tissue called perimysium. The bundles of fibers are then subdivided into smaller compartments, the individual muscle fibers. Each muscle fiber is surrounded by the last connective tissue layer called endomysium.

The muscle fiber is a highly specialized cell type with unique features. Usually the muscle fibers span from tendon-to-tendon which depending on the muscle can be quiet long up to several centimeters in Sartorius, the longest muscle in humans. Also, the diameter varies and can be as thin as 3 μm in extraocular muscle. To reach these length muscle fiber precursor cells, called myoblasts, fuse to form myotubes. These myotubes differentiate later into muscle fibers. This differentiation path makes the muscle fibers the only type of multinucleated cell in our body. In a healthy muscle the nuclei are located at the outer membrane of the muscle fiber.

The three above mentioned connective tissue layers in muscle mainly contain collagen (reticular fibers) and elastic fibers. Each layer has a transition to the next deeper layer. Through this network, nerves and blood supply can reach the individual fibers. The individual hierarchical compartments also help for fine adjustment of contraction patterns inside each muscle. So that only parts of the muscle contract.

Each muscle fiber is enveloped by a membrane called sarcolemma. This membrane is not a connective tissue as the membranes described above but rather is surrounded by a basement membrane (extracellular matrix) which is composed of two layers. The outer one, the reticular

lamina and the inner one, the basement lamina. The inner basement lamina can be further divided into an outer lamina densa (basal membrane) and an inner lamina lucida, which is connected to the sarcolemma via glycoproteins (MacIntosh et al., 2006).

Each muscle fiber can be further subdivided into substructures, called myofibrils. These mostly tube-like structures run along the whole length of the fiber and are surrounded by membranous cisternae and a sarcoplasmic reticulum (SR) network.

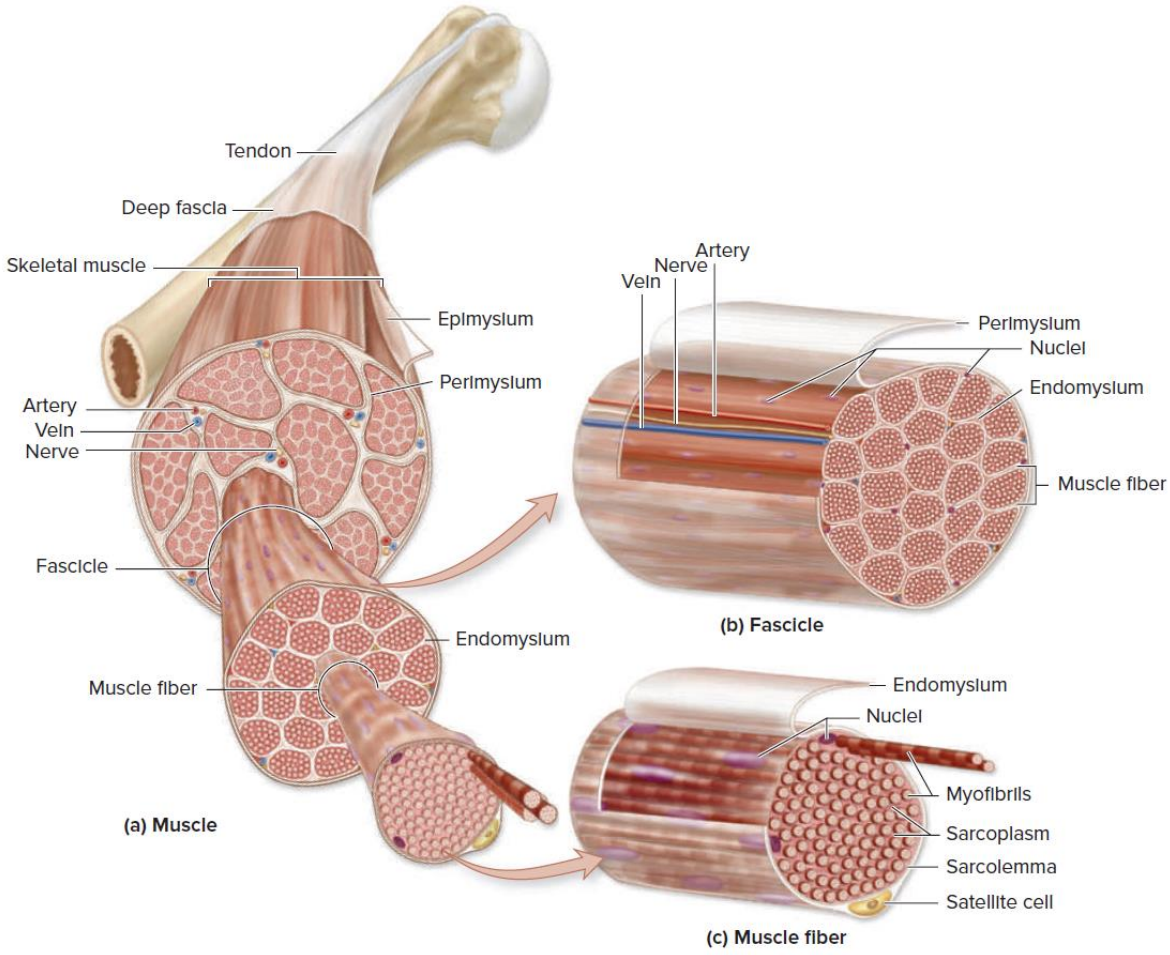

Figure 1.2: Structural organization of skeletal muscle

Hierarchical structure of the entire muscle **(a)** over the fascicle, a bundle of fibers **(b)** to individual fiber **(c)**. Each layer is separated by sheet of connective tissue from the epimysium around the muscle over the perimysium surrounding the fascicle to the endomysium and the sarcolemma around the single fiber. The smallest structure is the myofibril which separate the fiber itself (Powers and Howley, 2018).

The myofibrils are made of the smallest contractile compartments, the sarcomeres. Unlike the other substructures the sarcomeres are connected in series (chain like). This serial arrangement results in repetitive dark and pale bands, which give the skeletal muscle its name of striated muscle (Franzini-Armstrong and Peachey, 1981). The reason for the striated appearance is that the sarcomere itself is made up of two bands, the pale I-band (isotropic) and the dark A-band (anisotropic). (Figure 1.3: Organization of the sarcomere). This pattern appears inverted under polarized light.

The sarcomere has three additional, visible and distinguishable components: Z-disk, M-line and H-zone. The H-zone is a paler region inside the A-band. Its width depends on the contraction of the sarcomere. It reaches its narrowest width when the sarcomere is fully contracted. The M-line is a thin dark line inside the H-zone. All lines, bands and discs reflect the specific protein content and protein filaments composing the structures as well as the areas of overlap within the filaments.

There are two major filaments in the sarcomere: the thick myosin filaments (15-18 nm) and the thin actin filaments (5-8 nm). The myosin filaments constitute the A-band while the I -band contains the actin filaments. Myosin, the motor protein, is a dimer where each monomer has a head and a long rod region. The head region has a high affinity for actin filament and the tail builds a coil-coil structure which basically forms the filaments. The head region undergoes a conformation change when it is connected to actin, whereby the two filaments slide over each other to generate force and shortening. The energy necessary for cross-bridge-cycling is provided by the hydrolysis of adenosine triphosphate (ATP) to adenosine diphosphate (ADP) at the myosin head region. The myosin filaments are attached on either side of the M-line so that the heads can extent to both sides. The actin filaments on the other hand are attached to the Z-disk. The cross section of a sarcomere reveals a highly regular pattern of thick and thin filaments. The thick filaments form lines where each line is shifted by half the distance of two filaments. While the actin forms a hexagonal lattice around the thick filaments. Depending where the cross section is cut through the sarcomere it is possible to see both or only one of these filaments. (Figure 1.3: Organization of the sarcomere)

There are 15 classes of myosin heavy chain proteins. In skeletal muscle the most commonly found classes are class I and class II, which also define the specificity of the muscle fiber type. Fibers which contain class I (MyHC 1) are mostly slow twitch fiber and fibers which contain class II (MyHC 2) are mostly fast twitch fibers. The myosin isoform composition is just one of the structures defining the fiber type. Nevertheless, the expression of a particular myosin heavy chain isoform parallels other biochemical and cellular characteristics of the muscle fiber such as proteins composition, mitochondrial density and type of metabolism. Fast twitch fibers can be further divided into three sub types (in human into two), which are type IIA, type IIB and type IIX.

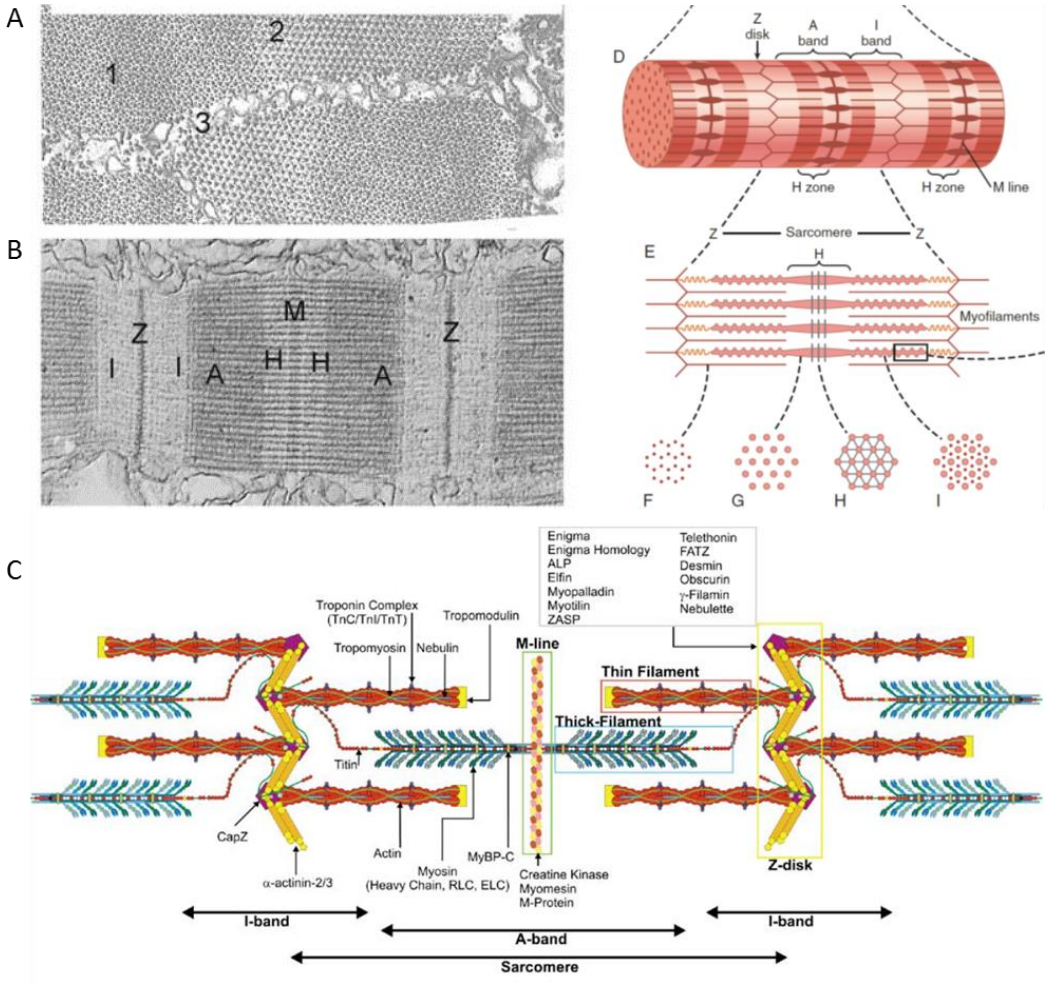

Figure 1.3: Organization of the sarcomere

(A) Electron micrograph of cross section of two sarcomeres at the level of I band (1) and H line (2) showing the real distribution of filaments in sarcomere. Individual sarcomeres are separated by the vesicles of sarcoplasmic reticulum (SR) system (3).

(B) Electron micrograph of one sarcomere sliced longitudinally. All bands and lines are marked as I, Z, A, H, and M. **(C)** Schematic representation of the sarcomere. The thick filaments, thin filaments, Z- and M-lines are indicated by blue, red, yellow and green boxes, respectively. The protein components shown to localize in the sarcomere have been directly labelled on the appropriate area of the ultrastructure. **(D & E)** Schematic representations of a myofibril and a sarcomere with bands indicated. **F - I** are cross sections at the levels indicated in D. A-B: (Zoladz, 2018) C: (Au, 2004) D-I: (Hall, 2016)

Of course, this is a simplified view of the proteins present in the sarcomere and many additional proteins are essential for a healthy working muscle. To name a few: myosins are also made up of four light chains, two essential and two regulatory; titin, which stretches from the Z-disc to the M-line where it overlaps with the titin from the other half sarcomere. It acts as a spring which holds the sarcomere together; myosin-binding proteins (MyBP), mainly MyBP-C wraps around the thick filament; troponin complex, which is located on the actin filaments. The complex binds another protein called tropomyosin and regulates the myosin binding to actin. If the Ca^{2+} concentration is low the tropomyosin blocks the myosin interaction with actin. When the Ca^{2+} concentration is high the complex can bind calcium and undergoes a conformational change with the tropomyosin and releases the myosin binding side on the actin. (Figure 1.3: Organization of the sarcomere) (Craig and Woodhead, 2006; MacIntosh et al., 2006; Hill et al., 2012; Frontera and Ochala, 2015; Craig, 2017; Zoladz, 2018)

1.2 Cranialfacial Muscles / EOMs

The craniofacial muscles are a subtype of skeletal muscles, located on the head and the neck. They are an example of skeletal muscles which are not involved in locomotion, but rather involved in vision, facial expression, breathing, mastication, swallowing, speech and other functions. Rather than grouping them on their function, craniofacial muscles can be grouped based on their developmental origin into extraocular muscles (EOM), branchiomeric muscles and hypobranchial muscles (Figure 1.4: Human craniofacial muscles) (Ziermann et al., 2018). While their clinical

relevance is growing and is based on specific diseases like strabismus, laryngeal dystonias, facial paralysis or others (McLoon and Andrade, 2012), they are even more fascinating from a research point of view because of their unique role in some neuromuscular disorders. Indeed they are selectively spared in some muscular disorders including Duchenne's muscular dystrophy (Andrade et al., 2000; Khurana et al., 1995), amyotrophic lateral sclerosis (McLoon et al., 2014) and aging (Kallestad et al., 2011). Nevertheless, extraocular muscles remain a niche research topic, on which the research publication just doubled in the last 25 years and remains stable at around 200 papers per year in the last 4 years (Web of Science: https://apps.webofknowledge.com).

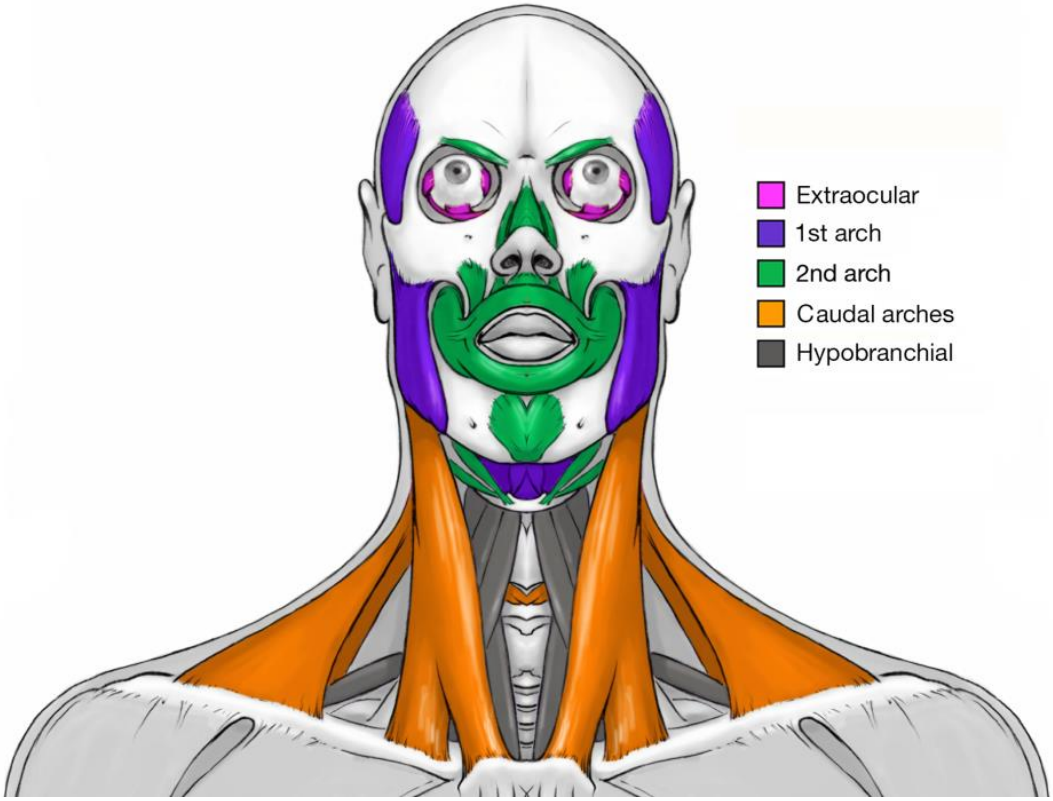

Figure 1.4: Human craniofacial muscles

Illustration of human craniofacial muscles colored according to their embryonic origin, which are either one of the branchial (pharyngeal) arches (1st arch, 2nd arch or caudal arches) or lateral mesoderm adjacent to occipital somites for the hypobranchial muscles. Extraocular muscles developed separately (Ziermann et al., 2018)

The developmental origin of most muscles in the body is the mesoderm. During embryogenesis the mesoderm splits into the lateral plate mesoderm (*LPM*), intermediate mesoderm (IM) and paraxial mesoderm (PM). In the later stages the paraxial mesoderm segments and forms the so called somites (Chang and Kioussi, 2018). These somites will subsequently develop into limb and trunk skeletal muscles, while the cardiac muscle as well as most craniofacial muscles will develop from the unsegmented PM (cranial mesoderm). After further maturation, this will be the origin of the 60 muscle groups located at the head and neck. The craniofacial muscles originating from the branchial arches can be sub grouped as follows: the muscles mainly responsible for mastication and jaw movement, derive from the 1st branchial arch and are innervated by branches of mandibular nerves (cranial nerve (CN) V), the muscles for facial expression derive from the 2nd branchial arch and are innervated by CNVII and the muscles derived from the caudal arches, also called the 3rd branchial arch, which control the larynx and the pharynx. Hypobranchial muscles including the tongue and infrahyoid strap muscles, are the only craniofacial muscle which derive from the somites and migrate to the head region during development. The last group of craniofacial muscles are the six different extraocular muscles (EOMs) (per eye), which originate from the prechordal and unsegmented paraxial mesoderm, independent from the arches (Figure 1.5: Origins of the craniofacial muscles in avian head muscle primordia) (Noden and Francis-West, 2006; McLoon and Andrade, 2012; Ziermann et al., 2018). In contrast to limb muscles, the development of craniofacial muscle seems to be more under the control of molecular markers rather than anatomical factors (Sambasivan et al., 2011).

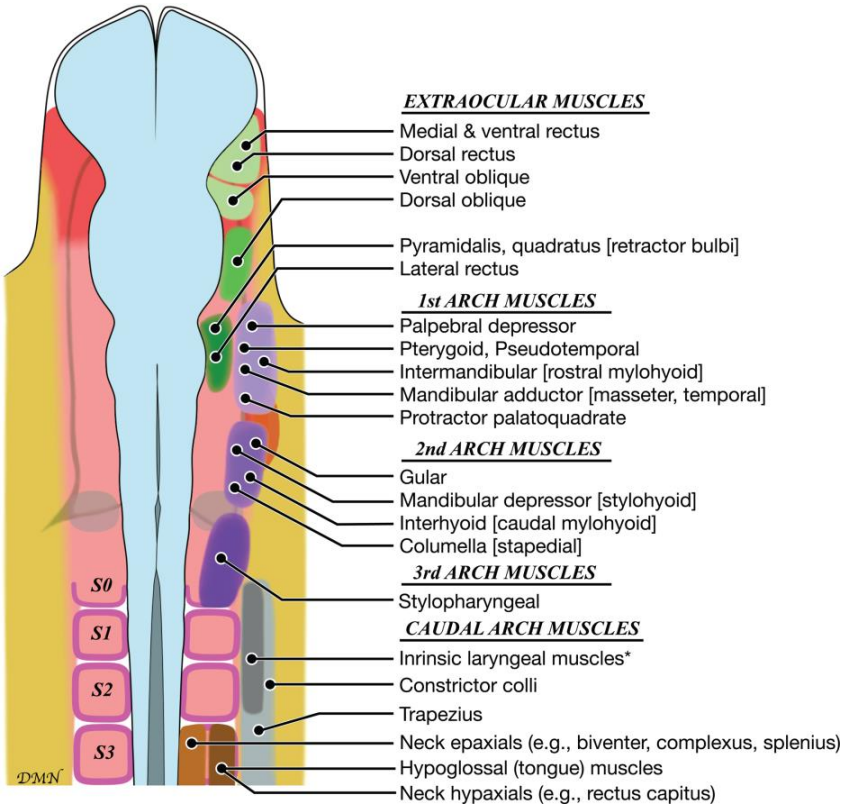

Figure 1.5: Origins of the craniofacial muscles in avian head muscle primordia

The map is based on labeling experiments by in situ injections or transplantation of already labeled precursor. These studies were done in different animals, including mice (Nathan et al., 2008; Theis et al., 2010), and developmental patterns appear to be conserved among divergent vertebrates. (Ziermann et al., 2018)

Craniofacial muscles not only have a distinct origin compared to other skeletal muscles, but their genetic program and regulatory signals make them unique. One example is that the upstream regulators of craniofacial muscle differentiation are unlike those regulating trunk and limb muscle differentiation while the myogenic regulatory factors (MRF) are the same across skeletal muscles: Tcf21, Msc, Tbx1, Pitx2 and Lhx2 are needed to activate MRF genes for head myogenesis and are not required for limb or trunk muscles, while Pax3 is not essential for head muscle development. Within the head muscle group, EOMs and muscles originating from the 1st branchial arch have a distinct genetic program, and while masticatory muscles rely on several regulators, EOMs rely heavily on Pitx2 as shown by the fact that the absence of Pitx2 expression results in the complete absence of EOMs (Tzahor, 2009; McLoon and Andrade, 2012; Michailovici et al., 2015).

1.2.1 Extraocular Muscles

As described in the previous sections, within the group of craniofacial muscles EOMs can be characterized as an individual sub-class of muscles having a distinct origin, developmental pathway and pattern of gene expression (Porter et al., 2001; Fischer et al., 2002). Furthermore, EOMs are among the fastest and most fatigue resistant skeletal muscles (Close and Luff, 1974). Seven different muscles (per eye) constitute the EOMs. They can be further divided into three subgroups according to their function. The levator palpebrae superiosis muscle which is responsible for raising the upper eyelid will not be further discussed and characteristics of the remaining 6 muscles will be presented. As shown in Figure 1.6 eye movement is controlled by: two oblique muscles (the superior oblique (SO) and the inferior oblique (IO) which can apply a torque to the globe; four rectus muscles, (superior rectus (SRM), inferior rectus (IR), medial rectus (MR) and lateral rectus (LR)). Together these 6 muscles can move the eyeball in a linear fashion in all 4 directions (up, down, left and right). Except for the inferior oblique muscle all others share the same origin at the apex of the orbit. The 4 rectus muscles arise from the common tendinous ring (also called anulus of Zinn), and the optic nerve, ophthalmic artery and some nerves also pass through this ring. Both oblique muscles are attached to the orbital walls. The superior oblique from the superonasal wall to the annulus of Zinn, while the inferior oblique is attached to the orbital floor adjacent to the lacrimal fossa, and posterior to the orbital rim (Figure 1.6 Anatomy of human extraocular muscle)(Yanoff and Duker, 2018).

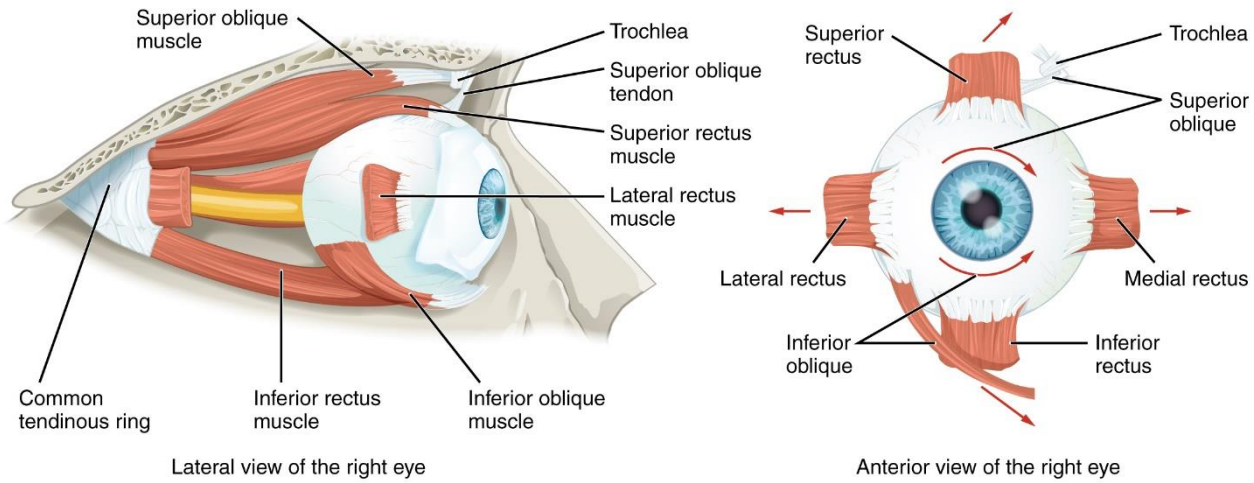

Figure 1.6 Anatomy of human extraocular muscle

Two views (sidewise/lateral: **left**; frontal/anterior: **right**) on the 6 EOM with their origin, common tendinous ring (also called annulus of Zinn), and their direction of movement (red arrows). The optic nerve is colored in orange. By OpenStax College [CC BY 3.0 (https://creativecommons.org/licenses/by/3.0)], via Wikimedia Commons

The movement of one eye is called duction. Remarkably, during duction, opposing muscles such as the medial rectus and the lateral rectus, must work together synchronously to enable purposeful eye movements. This agonist-antagonist relation is termed Sherrington's law of reciprocal innervation. The synchronized movement of both eyes in one direction is called version. For version to occur, the muscles of one eye must operate in reverse order and synchronized with the other eye, an event termed Hering's law of equal innervation (King, 2011). For example, the lateral rectus from the left globe and medial rectus from the right globe will contract simultaneously to allow both eyes to focus on the same object. These pair of agonist-antagonist muscles are called yoked muscles. There are a few exceptions violating Hering's law, for example when eyes focus on close objects and both eyes move in opposite directions. These complex interactions are the basis of our stereo vision and empower us to have a 3-dimensional stereo view of our environment, which is essential for humankind and our culture (Yanoff and Duker, 2018).

1.2.2 Microanatomy of the EOMs

Extraocular muscles also have a unique microanatomy. Every extraocular muscle consists of two different layers. In inner one, called global layer, and an outer one facing the orbital wall, called orbital layer. The most obvious difference between these two layers is that the global layer is directly connected to the sclera while the orbital layer terminates earlier and inserts directly into the connective tissue pulley. At the point where the orbital layer ends the global layer passes through the pulley. The pulley is a ring surrounding the globe and consists mainly of collagen, elastin and smooth muscle (Figure 1.7: Schematic drawing of the EOMs with their insertion into the globe and cross-section micrograph of one EOM with their two layers) (Spencer and Porter, 2005; McLoon and Andrade, 2012; Yanoff and Duker, 2018). Not long ago (Demer et al., 2000) realized for the first time that passive pulleys cannot explain the normal movements of the eye. So, they introduced the active pulley hypothesis. The current dominant theory is that the orbital layer moves the pulleys in coordination with the global layer however, this theory only applies to the rectus muscles (Ruskell et al., 2005; Miller, 2007).

But it is not only the terminal portion of the muscle which differs between the two layers. Even though both layers have a complex fiber type arrangement, the fibers present in the orbital layer have a smaller average diameter and even contain a group of fibers having a diameter of 3-4 μm (in human). Such small fibers are not present in the global layer (Figure 1.7: Schematic drawing of the EOMs with their insertion into the globe and cross-section micrograph of one EOM with their two layers). While there is a consensus in the literature that the average size of the fibers present in the orbital layer is small, the absolute size in human EOMs varies. One paper report orbital fiber diameter ranging from less than 20 μm to a maximum of 26 μm, a second paper reports average cross sections with an average diameter of around 21 μm and a third paper reports fibers of approximately 50 μm. Similar size divergences can be found for the global layer with a maximum dimeter of 40 μm in two papers, and an average of 70-80 μm in a third report. The latter also reports a group of smaller fibers in the global layer. (Stirn Kranjc et al., 2009; Kjellgren et al., 2003; Wasicky et al., 2000). Rather than saying one reference is more correct then the others this highlights the complexity of EOMs and the fact that EOMs are far from being uniform along their contraction axis. Additionally, the diameter depends on where the muscles have been sectioned.

There is also evidence showing that unlike limb muscles, EOM fibers do not span from tendon-to-tendon (Harrison et al., 2007). Finally, EOM fibers can be grouped into six fiber types characterized by the expression of specific myosin heavy chain (MyHC) isoforms, innervation and enzymatic activity (see below).

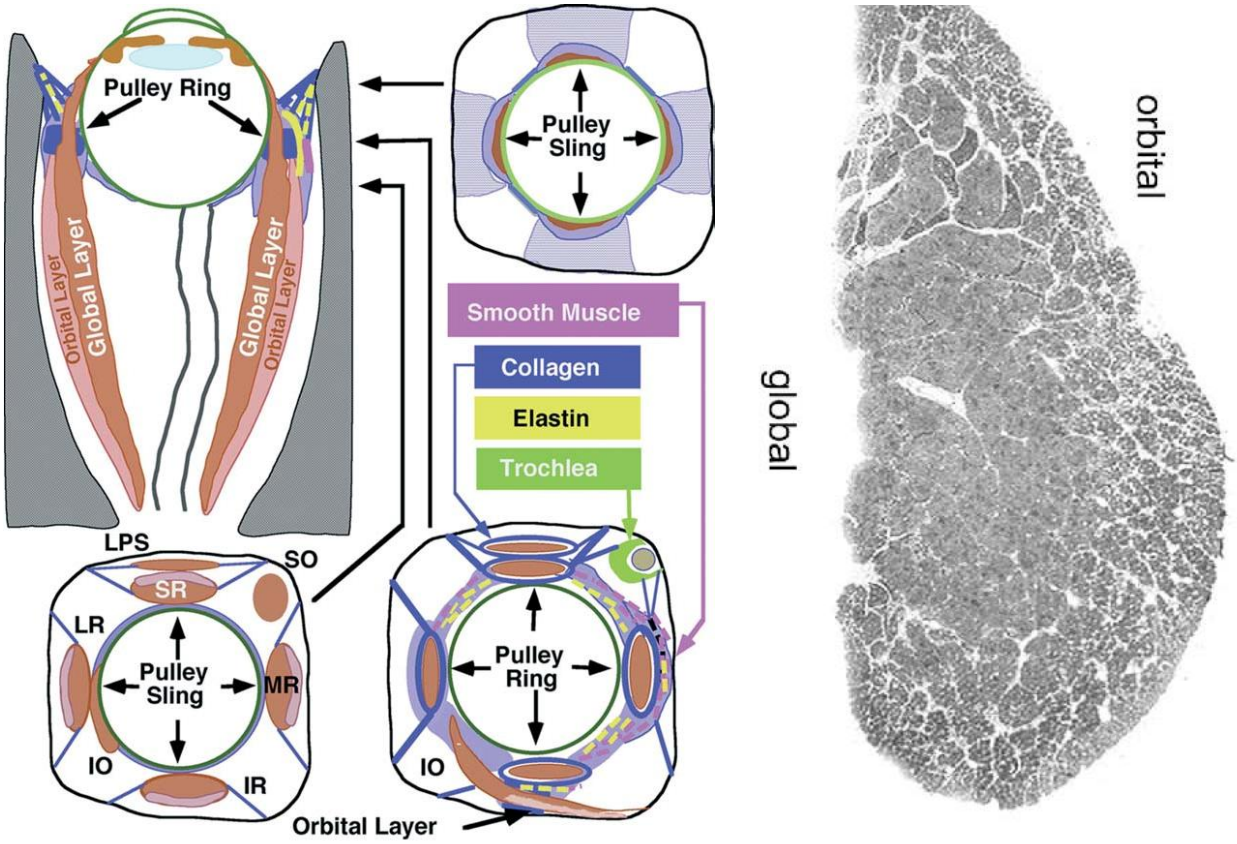

Figure 1.7: Schematic drawing of the EOMs with their insertion into the globe and cross-section micrograph of one EOM with their two layers

(Left) Anatomy of the EOM. Rectus muscles entering the globe with their global layer while the orbital layer terminates in the pulley ring. Virtual cuts through three different position perpendicular to the fiber muscle orientation. Connective tissue is marked in different colors. IO: inferior oblique; IR: inferior rectus; LPS: levator palpebral superioris; LR: lateral rectus; MR: medial rectus; SO: superior oblique; SR: superior rectus (Spencer and Porter, 2005). **(Right)** Micrograph of a monkey lateral rectus muscle showing the two layers. The c-shape orbital layer consists of fibers with a smaller diameter and surrounds the global layer(Spencer and Porter, 2005).

A third external layer in human extraocular muscles has been observed and called marginal zone. It is located outside of the orbital layer and stretches almost the full length except for the very proximal and distal regions, where the organization becomes unclear. The fibers found in the marginal zone are mainly larger than the fibers in the orbital layer or global layer, having a diameter of approximately 83 μm (Wasicky et al., 2000).

1.2.3 Innervation of EOM

EOMs are innervated by the abducens (CNVI) and the oculomotor (CNIII) except for the superior oblique which is innervated by the trochlear (CNIV).

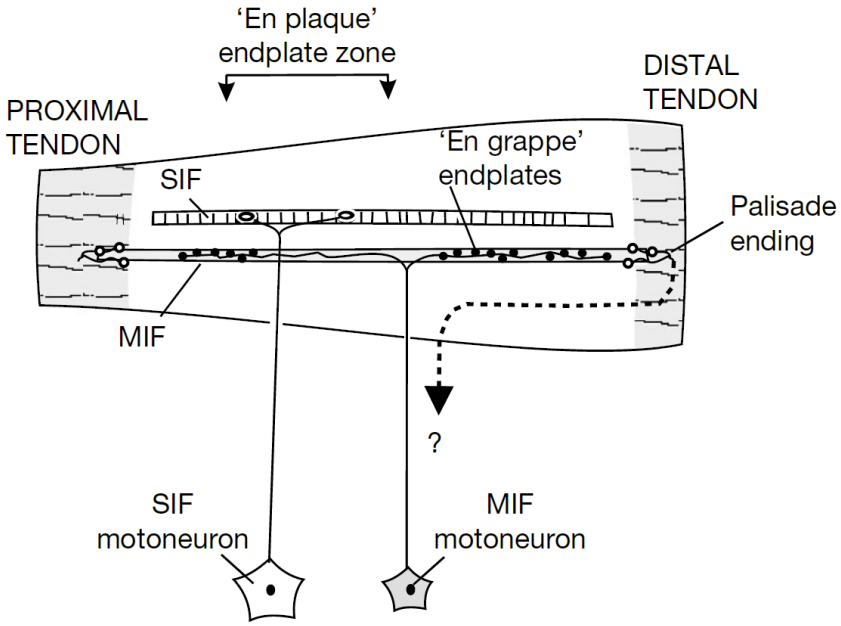

Figure 1.8: Innervation in extraocular muscle

Schematic representation of the two innervation types: singly innervated fiber (SIF) and multiply innervated fiber (MIF). The endplate zone of the SIF is called "en plaque" while the endplates of the MIF are located at the proximal (orbital and global layer MIFs) and distal end (only global layer) and are called "en grappe" because they look like a bunch of grapes. Palisade endings are only found in the global layer at the distal ends (Büttner-Ennever, 2007).

In EOM two types of innervations can be found, singly innervated fibers (SIF) and multiply innervated fibers (MIF) (Figure 1.8: Innervation in extraocular muscle) (Pachter et al., 1976). In contrast skeletal muscles contain almost exclusively SIFs and MIFs are only rarely found (Morgan and Proske, 1984). Even though the neuromuscular junctions of EOMs are very similar to those of limb skeletal muscles from a biochemical point of view (Khanna et al., 2003), the proportion of nerve fibers to muscle fibers is more than 10 times higher (1:3 to 1:5 or 1:12) in extraocular muscles compared to (1:50 to 1:125) in skeletal muscles (Tibrewal and Kekunnaya, 2018; Pineles et al., 2018; Mühlendyck, 1978; Von Noorden and Campos, 2002). While the SIFs follow the all-or-none contraction as occurs in limb skeletal muscles, the MIFs only generate a local contraction at the endplates and the force does not propagate along the muscle fiber (Büttner-Ennever, 2007).

1.2.4 Myosin Heavy Chain and Fiber Type Composition of Extraocular Muscles

Initially EOM fibers were characterized almost exclusively by their innervation and mitochondrial density (Mayr, 1971). Subsequently, reports showed that EOMs have a complex myosin heavy chain (MyHC) isoform composition and this MyHC composition was overlaid on the already existing fiber types. It should be mentioned that limb skeletal muscles can be divided into four different groups depending on the MyHC isoform they express. MyHC type 1 (slow, β -cardiac, MYH7), MyHC type 2A (fast MYH2), MyHC type 2X (2D, fast MYH1) and MyHC 2B (fast MYH4). The presence of a specific MyHC isoform also parallels the oxidative metabolic activity of the particular muscle type: slow oxidative, slow twitch, and fatigue resistant fibers contain mainly MyHC type 1; fast-twitch, oxidative, glycolytic and mostly fatigue resistant fibers contain MyHC 2A; fast-twitch, glycolytic and fast fatigable fibers mainly contain MyHC 2B (this isoform is not present in human muscles), and fast-twitch, intermediate fatigue resistant fibers mainly contain MyHC 2X humans (Schiaffino and Reggiani, 2011; Talbot and Maves, 2016). Aside these four isoforms, mature EOMs also contain MyHC isoforms which are present during development and not in adult skeletal muscles including: embryonic MyHC (MyHCemb, MYH3) and neonatal/perinatal MyHC (MyHCneo, MYH8) as well as specialized isoforms: alpha-cardiac MyHC (MyHC α -card, MYH6) and the EOM specific MyHC MyHCeom, MYH13). Nevertheless, the presence of all MyHC isoforms was not always confirmed by different investigators studying

EOMs. Sometimes they weren't able to identify some isoforms and they termed them as unidentified isoforms (Stirn Kranjc et al., 2009; Kranjc et al., 2000; Rushbrook et al., 1994; Rubinstein and Hoh, 2000; Bicer and Reiser, 2009; McLoon and Andrade, 2012). Furthermore, there are also reports showing that the orbital layer and globular layer expressing different MyHC isoforms. The global layer expresses more isoforms then the global one. Additional the MyHC isoform composition changing along the muscle axis (Figure 1.9:Longitudinal and cross-section staining for different myosins in adult rectus muscle) (Bicer and Reiser, 2009; Zhou et al., 2010; Park et al., 2012) and even within a single fiber (Bicer and Reiser, 2009; Zhou et al., 2010; McLoon et al., 2011). These "hybrid" fibers also occur in limb skeletal muscles but only under stress or injury (Caiozzo et al., 2000). Recently, two reports identified two ancient MyHC isoforms (MYH14/7b and MYH15) in mammalian EOMs (Rossi et al., 2010; Lee et al., 2019) as well as the non-muscle isoform myosin IIB (nmMyHCIIB, MYH10)(Figure 1.10: Myosin heavy chain genes and their phylogenic tree) (Moncman and Andrade, 2010).

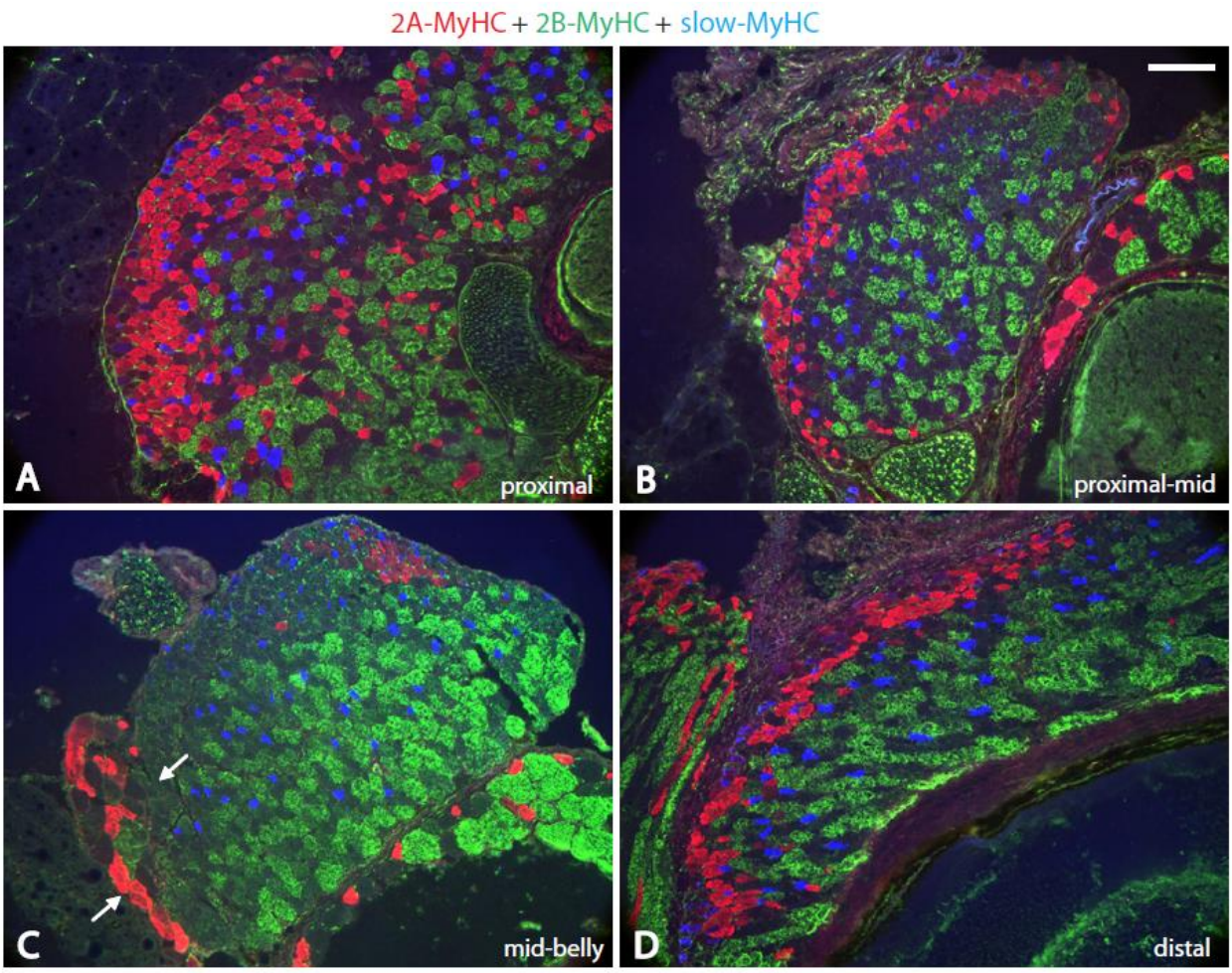

Figure 1.9:Longitudinal and cross-section staining for different myosins in adult rectus muscle

Cross-section antibody staining for MyHC 2A (red), MyHC 2B (green), and slow-MyHC/ MyHC type 1 (blue) at different positions along a mouse EOM from proximal **(A)**, proximal-mid **(B)**, mid-belly **(C)**, and distal **(D)**. The orbital and global layer can also be distinguished by their different MyHC composition: MyHC 2A is mainly in the orbital layer as well as at the proximal and distal ends and not present in the belly regions. MyHC 2B is only expressed in the global layer throughout the whole muscle length. MyHC type 1 can be found scattered across both layers. No co-expression in the same fiber of these three isoforms can be found. Arrows in C indicates adjacent muscles. Scale bar: 100 μm (Zhou et al., 2010)

If this complex MyHC isoform expression pattern is combined with the type of innervation and other factors it is possible to classify different fiber types within the EOMs. Initially EOMs were grouped by into two groups (Siebeck and Kruger, 1955), later into three groups based on their mitochondria density and distribution into coarse, fine and granular EOM muscle fibers (Durston, 1974). But even before their classification (Mayr, 1971) suggested a classification into six groups, two groups in the orbital layer and four in the global layer, which is usually today the accepted standard. The six groups are, from orbital to the global layer and from most abundant to the least abundant: singly innervated, fast and high fatigue resistant in the orbital layer (1); , multiply innervated, fast and slow, and variable fatigue resistant in the orbital layer (2); in the global layer: "red", singly innervated, fast and high fatigue resistant (3); "white", singly innervated, fast and low fatigue resistant (4); "intermediate", singly innervated, fast and intermediate fatigue resistant (5); multiply innervated, slow and high fatigue resistant (6) (Table 1: Extraocular muscle fiber types) (Kranjc et al., 2000; Skalicky, 2015).

	Orbital layer		Global layer			
Fiber type	Singly innervated	Multiply innervated	Red singly innervated	White singly innervated	Intermediate singly innervated	Multiply innervated
% Fibers within the layer	80	20	33	32	25	10
Contraction mode	Twitch	Mixed	Twitch	Twitch	Twitch	Non-twitch
Contraction speed	Fast	Fast and slow	Fast	Fast	Fast	Slow
Fatigue resistance	High	Variable	High	Low	Intermediate	High

Table 1: Extraocular muscle fiber types

The six major fiber types are sorted by their appearance in the muscle layer. Two fiber types are present in the orbital layer and four in the global layer. Type of innervation is indicated in the fiber type name. Additionally, contraction mode, speed and fatigue resistance are shown. Fiber types are divided according to fatigue resistance and innervation (Skalicky, 2015).

But the literature is not homogeneous when it comes to EOM classification and other classifications can be found in the literature. There are studies which classify only five types, four in the global and three in the orbital layer with two types found in both layers (Rashed et al., 2010); in a more recent study ,the same investigators found six different types, four in each layer with two types found in both layers (Rashed and El-Alfy, 2012). Others studies also classified six different types but three different ones in each layer (Spencer and Porter, 2005). Human EOMS are even more complex; They have not two but three layers in the EOMs. It has been reported that they have two fiber types in the orbital layer and three in the global layer. Additionally three fiber types were characterized in the third layer, the marginal zone: one singly innervated and two multiply innervated types, a high and low oxidative (Wasicky et al., 2000).

A different hypothesis is that EOMS are a continuum rather than distinct types and that continuum is what allows these complex muscles to function in such a precise way (McLoon et al., 2011). The basis of this hypothesis is that the continuum would also take into account innervation, metabolism as well as force, shortening velocity as well as MyHC pattern into consideration (McLoon et al., 2011). And even the first paper describing EOM fiber types described the mitochondria density as a ‘‘spectrum’’ (Mayr, 1971). Beside that this hypothesis might be correct the distinct fiber types nevertheless helps tremendously to communicate and avoid misunderstanding between investigators.

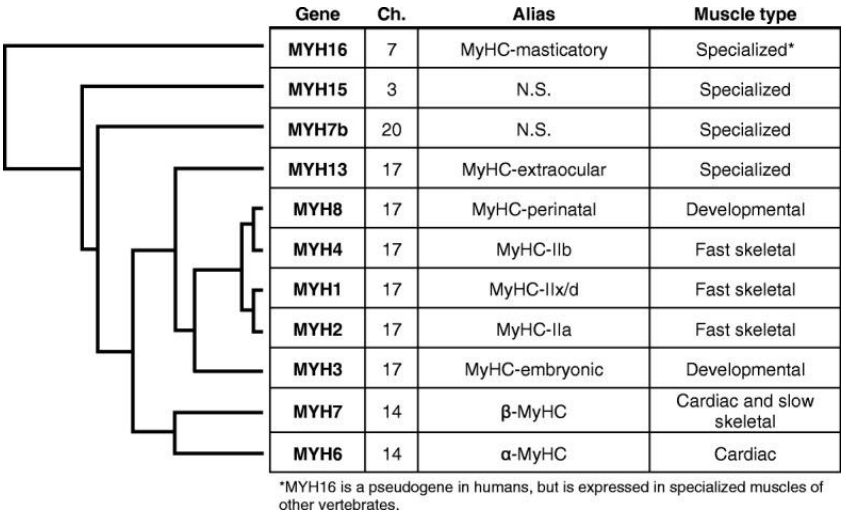

Gene	Ch.	Alias	Muscle type
MYH16	7	MyHC-masticatory	Specialized*
MYH15	3	N.S.	Specialized
MYH7b	20	N.S.	Specialized
MYH13	17	MyHC-extraocular	Specialized
MYH8	17	MyHC-perinatal	Developmental
MYH4	17	MyHC-IIb	Fast skeletal
MYH1	17	MyHC-IIx/d	Fast skeletal
MYH2	17	MyHC-IIa	Fast skeletal
MYH3	17	MyHC-embryonic	Developmental
MYH7	14	β-MyHC	Cardiac and slow skeletal
MYH6	14	α-MyHC	Cardiac

*MYH16 is a pseudogene in humans, but is expressed in specialized muscles of other vertebrates.

Figure 1.10: Myosin heavy chain genes and their phylogenic tree

Table of human myosin heavy chain genes with their chromosome location (Ch.), protein alias (N.S. refers to no specification), and primary muscle tissue of expression. The phylogeny on the left indicates the evolutionary relationship between the human sarcomeric myosin heavy chain genes (this cladogram does not reflect accurate scale) (Lee et al., 2019)

1.2.5 Diseases Affecting the Extraocular Muscles

One of the most common human diseases in the field of ophthalmology is strabismus, with a prevalence of 2% - 5% (Dorr et al., 2019). It is characterized by a misalignment of the eyes, so that they point in different directions. This results in one eye being fixed on what the patient intends to look at (the fixing eye) and the other eye looking at something else (the deviated eye). There are subtypes of strabismus depending on the position towards which the deviated eye is pointing to: the eyes can deviate inwards (esotropia or crosseyed), outwards (exotropia or wall eye), vertically upwards (hypertropia) or vertically downwards (hypotropia). The brain of the handles the double image by blurring the one from the deviated eye. In long-standing strabismus, this blurred image is completely suppressed by the brain and the patient only sees a single image. A more rarely found strabismus form is when the brain merges the two images so that two objects appear at the same place. But in all cases the patient suffers from a reduced depth perception. A very early onset of strabismus can also lead to amblyopia or lazy eye. It is a permanent reduced vision of the deviated eye and is caused by a reduced visual cortex development.

The first step of strabismus therapy is to rule out a retinoblastoma. After this is ruled out the treatment and management of strabismus can take place. In some case of esotropia due to far-sighting strabismus can be treated with correction glasses. Prism glasses can be used for any strabismus type for the temporary comfort. But the most common treatment is strabismus surgery. The surgery can be done on one or both eyes and the surgeons usually has two options to correct the eye position. They can shorten the EOM by cutting parts away or they can alter their position where they attach onto the sclera. If the patient also suffers from amblyopia and is young enough the fixing eye can be patched so that the visual cortex can develop properly, and

the strabismus surgery follows later. Usually if the eye alignment is attained and maintained to the mid-teens it tends to remain stable.

(Helveston, 2010)

Another EOM disease condition is ophthalmoplegia. Ophthalmoplegia is the paralyses or weakness of eye muscles. Two types of ophthalmoplegia exist, chronic progressive external (CPEO) and internuclear ophthalmoplegia. Internuclear ophthalmoplegia is caused by nerve damage on fibers controlling the lateral eye movement which leads to double vision. CPEO is characterized by slowly progressive weakness and inability to move the EOM and eyelid muscle, levator palpebrae superioris. The drop of the eyelid, called Ptosis, may be a first incident for CPEO. The spectrum of disease which causes CPEO is wide but typically a mitochondrial disorder is the underlying cause. Indeed, the range of mutations causing CPEO is wide: from large-scale mtDNA rearrangements, to point mutations in transfer RNA genes to alterations of genes maintaining mtDNA encoded by the nuclear genome. CPEO may be a sufficient phenotype to diagnose a mitochondrial disease, nevertheless patients often present other symptoms as well. Nevertheless, a differential diagnosis is essential to exclude disease such as Grave's disease, myasthenia gravis or glioma which can also cause CPEO. There is no current treatment known for CPEO. (Al Kahtani et al., 2016; McLoon and Andrade, 2012)

These are by far not the only disease affecting EOMs. The one described in the previous paragraph are the more EOM exclusive disorders while section 1.3.5 Congenital Myopathies describes some disease which affect EOM as well. Other disease with EOM involvement are for example myasthenia gravis, Graves' disease, Miller Fisher syndrome, amyotrophic lateral sclerosis. (McLoon and Andrade, 2012)

1.3 Excitation Contraction Coupling (ECC)

Beside the sarcomere, the contractile part of the muscle, (Paragraph 1.1: Skeletal Muscle Structure) there is also a fine network of SR surrounding the sarcomeres and network of tube-like structures or invaginations of the sarcolemma perpendicular to the muscle fiber. This so-called T-tubule (transverse tubule) system together with parts of the SR forms the triads (skeletal muscle) or dyads (cardiac muscle). The T-tubules penetrate deep into the muscle fibers and

cardiomyocytes. There are also longitudinal tubules connecting the T-tubules. This tube system is the basis for rapid contraction propagation in either direction longitudinal along the fiber and dominantly transversal into the fiber. (Figure 1.11: T-tubule system and triads)

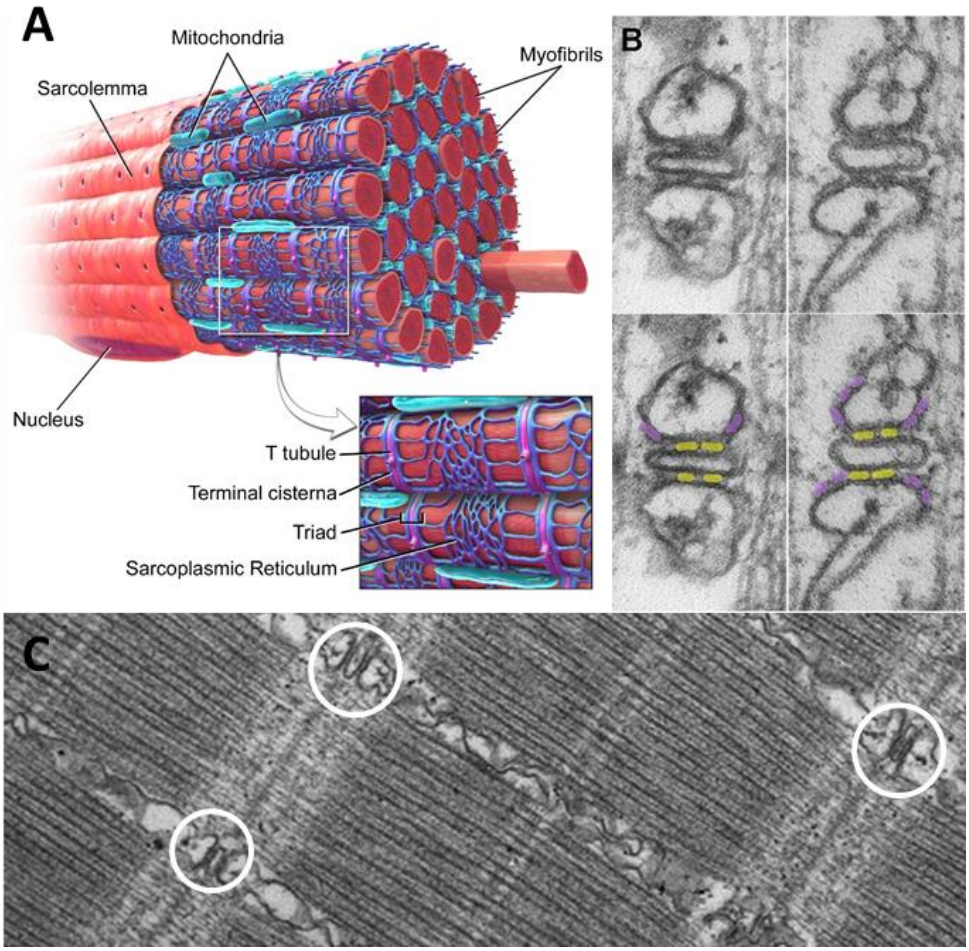

Figure 1.11: T-tubule system and triads

(A) Schematic representation of a muscle fiber showing T-tubules and SR network. Note that t-tubules go deep into the muscle fibers and are surrounded by SR and mitochondria. **(B)** EM photomicrograph of individual triads. RyRs are marked according to their location in yellow (junctional) or purple (prejunctional). **(C)** EM photomicrograph of a muscle fiber cross section from zebrafish, showing multiple sarcomeres. Triads are indicated with white circles. A: (Blausen.com staff, 2014); B-C: modified from (Perni et al., 2015)

Excitation contraction coupling (ECC) describes the mechanism linking activation of contraction initiated by the action potential (AP), to muscle contraction. From a general point of view ECC in skeletal and cardiac muscle are similar, but there are distinct differences which gives them their unique properties. These differences will be discussed in sections 1.3.1 and 1.3.2 below. In all striated muscles, the starting point of ECC is depolarization of the sarcolemma. The action potential propagates along the sarcolemma to reach all sides of the fiber. When the AP reaches the T-tubules it propagates along the T-tubules deep inside the muscle fiber. When it reaches the triads (or dyad), the signal is transmitted inside the muscle fiber leading to the release of Ca^{2+} from the SR into the myoplasm. As detailed in a previous chapter 1.1 Skeletal Muscle Structure the Ca^{2+} ions will then trigger the uncovering of the myosin binding side on the actin molecule leading to sarcomere contraction. T-tubules are surrounded by the terminal cisternae of the SR giving rise to triads if they are surrounded by two cisternae or dyads if they are surrounded by one cisterna.

Many proteins are involved in ECC and these will be discussed in detail in section 1.3.4 but the two key players involved in electrical signal from the AP into a chemical gradient, a rise in myoplasmic [Ca^{2+}] are the dihydropyridine receptor (DHPR; also called L-type Ca^{2+} channel) and the ryanodine receptor (RyR). DHPRs are located within the T-tubules and are integral components of the sarcolemma, while the RyRs sit in the terminal cisternae membrane of the SR. The Ca^{2+} released from the SR to the myoplasm leading to contraction is first buffered quickly by parvalbumin before it is subsequently pumped back into the SR by the sarco/endoplasmic reticulum Ca^{2+} transport ATPase (SERCA) or transported out of the fibers via Na^{+}/Ca^{2+} exchanger (NCX) and plasma membrane Ca^{2+} ATPase (PMCA).

Most of these proteins involved in ECC exist as multiple isoforms composed of more than 1 subunit depending on the muscle type and these will be discussed in the next two sections.

1.3.1 ECC in Skeletal Muscle

A healthy skeletal muscle mainly expresses triads containing skeletal muscle specific macromolecular complexes of RyR and DHPR isoforms, i.e. the RyR1 and the DHPR complex

containing the $Ca_v1.1$ skeletal muscle specific α1S subunit. A specific feature of these two complexes is that they are mechanically coupled. When the AP moves along the T-tubule and reaches the DHPR, it causes the latter to undergo a conformational change which allows it to come into contact with the and open the RyR1 present in the junctional region of the SR. The open RyR1 allow the Ca^{2+} to flow into the myoplasm and then bind to troponin-C activating the cross-bridge cycle and thus muscle contraction (Figure 1.12: Skeletal ECC and see section 1.1 Skeletal Muscle Structure). This mechanical coupling between $Ca_v1.1$ and RyR1 is exclusive for the RyR1 isoform and its absence cannot be compensated by other isoforms such as RyR2 or RyR3. The same applies for the α1S isoform subunit of the DHPR.

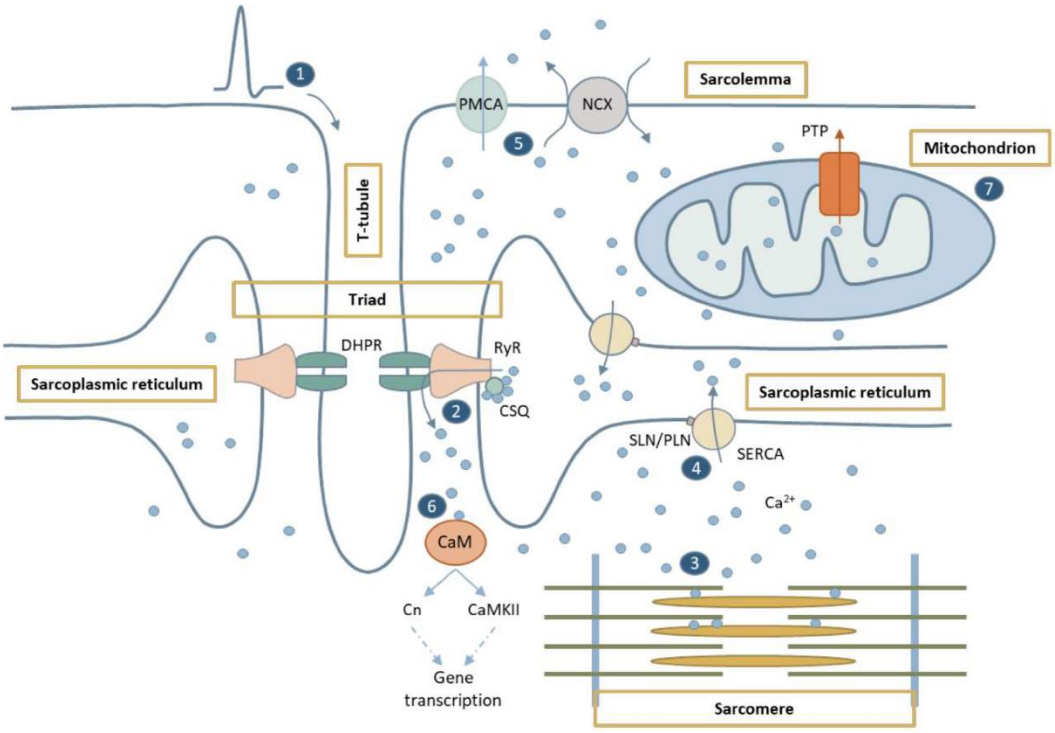

Figure 1.12: Skeletal ECC

Representation of skeletal ECC. When the depolarization of sarcolemma reaches the T-tubules (1), the voltage sensing DHPRs undergo a conformational change and activate RyR1 channels resulting in Ca^{2+} release from the SR (2). Ca^{2+} diffuses to the sarcomere where it binds to the contractile proteins and initiates muscle contraction (3). Muscle relaxation takes place when Ca^{2+} is pumped back into the SR by SERCAs (4) or pumped out of the muscle fiber by membrane ion exchangers or pumps (NCX,

PMCA) (5). Myoplasmic Ca^{2+} can also bind to other high affinity calcium binding proteins such as NFAT, S100, CaM etc thereby activating intracellular Ca^{2+}-dependent signaling pathways resulting in muscle gene regulation (6). High levels of myoplasmic Ca^{2+} can also be sensed by mitochondria (7), where they stimulate the ATP synthesis required for muscle contraction and relaxation. (Lasa-Elgarresta et al., 2019)

Electron microscopy revealed that the RyR1 are organized in regular checkerboard arrays of two rows at the terminal cisternae of the junctional SR, called couplons (Figure 1.13: Couplons and DHPR-RyR arrangement). The square profile of the RyR1 (see section 1.3.4 ECC Proteins) is tilted by 22° relative to the axis of the tubule. Each RyR1 can bind up to four DHPRs so that it looks like the DHPRs sits on the corner of a square forming the so-called tetrads. The coupled RyR1-DHPRs complex are called calcium release unit (CRU). It is postulated that tetrads occur in an alternating way forming a checkerboard array of coupled and uncoupled RyR1s.

This leads to the existence of a second calcium release mechanism, namely the calcium induced calcium release (CICR). While the DHPR is the physiological activator of the RyR1, RyR1 can also be activated by Ca^{2+} itself. The importance of this mechanism lies in the fact that only half of the RyR1 are coupled while the other half are not coupled to a DHPR (Figure 1.13: Couplons and DHPR-RyR arrangement). So that Ca^{2+} from coupled RyR1s can activate uncoupled RyR1 in close proximity. The CICR mechanism was largely accepted by the scientific community for decades until recently some doubts arose and there are now hypothesis that the uncoupled RyR1 if present in mature mammalian fibers, work as spacers between coupled RyR1, necessary to maintain the structural integrity of the couplons. Simulation studies as well as biochemical evidence also suggest that additional uncoupled RyR1 serve as a channel reserve for the coupled RyR1 to prolong the natural cycle of the RyR1 array.

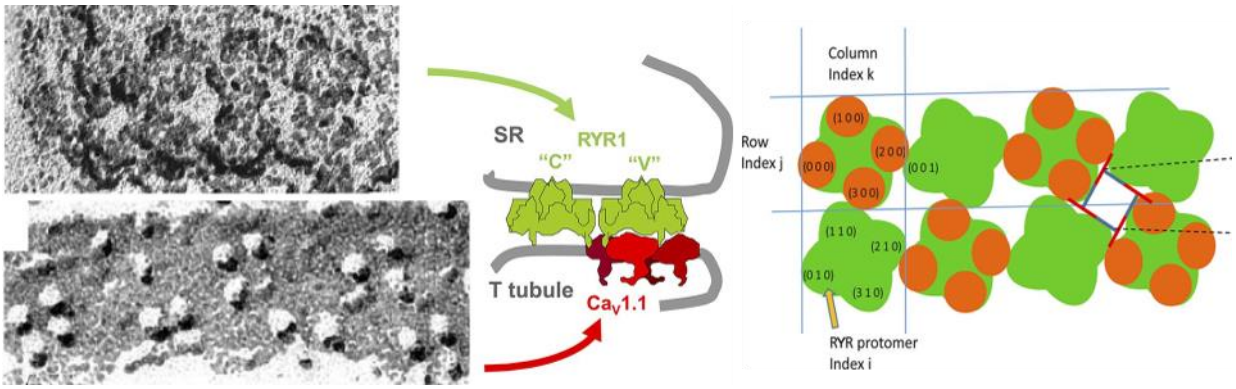

Figure 1.13: Couplons and DHPR-RyR arrangement

(A) Freeze-dried rotary shadowed junctional SR membrane from guinea pig. **(B)** Tetrads of particles ($Ca_V1.1$) in a freeze-fractured T tubule membrane from toadfish muscle, presented with the same orientation and magnification. **(C)** Canonical couplon, with array notation (side view inside diagram). RYR tetramers (or channels, or feet; green) are identified by a row index j (which in T tubule couplons range between 0 and 1) and a column index k (0–3 in the case illustrated). In this canonical configuration, even channels are fully occupied by Ca_Vs (orange elements). Individual protomers are identified by index i (0–3), increasing clockwise within the RYR tetramer. The horizontal distance between centers of adjacent RYRs is ~30 nm. (Ríos et al., 2019)

The skeletal DHPR (an L-type Ca2+ channel) is capable of transporting a calcium current but the amount of transported calcium is very small and not essential for skeletal muscle ECC as recently reported in a study with a non-conducting DHPR from zebrafish.

Subsequent to its release from troponin-C in fast twitch muscles Ca^{2+} is buffered by parvalbumin before being pumped back into the SR by SERCA. Two main SERCA isoforms are present in mature mammalian muscle fibers and their distribution mainly depends on the fiber type. The slow type I fibers usually express SERCA 2 while the fast type II fiber mainly express SERCA 1. Co-expression of both isoforms in some human muscles has been reported.

(Rebbeck et al., 2014; Calderón et al., 2014; Drum et al., 2016; Hernández-Ochoa and Schneider, 2018; Franzini-Armstrong, 2018; Ríos, 2018; Díaz-Vegas et al., 2019; Ríos et al., 2019)

1.3.2 ECC in Cardiac Muscle

Cardiomyocytes, the cardiac counterpart of skeletal muscle fibers, are single nucleated cells and are much smaller than skeletal muscle fibers but contain a fully developed T-tubule system which helps propagate the AP along and through the whole cell. In comparison of skeletal muscles cardiac muscles express RyR2 and the α1C subunit of the DHPR. These cardiac isoforms are not mechanically coupled (as are the skeletal isoforms) but the α1C subunit of the DHPR acts as a voltage sensor and calcium channel so that heart ECC relies on influx from the extracellular environment and ECC occurs through a process of CICR. In other words, the Ca^{2+} transported by the DHPR triggers a large release of Ca^{2+} from the SR via RyR2 and this leads to cardiac contraction.

To maintain a stable CICR the cardiac DHPR must be activated by a longer pulse explaining why the AP in the heart is longer, lasting around 200 ms (Figure 1.14: ECC in the heart).

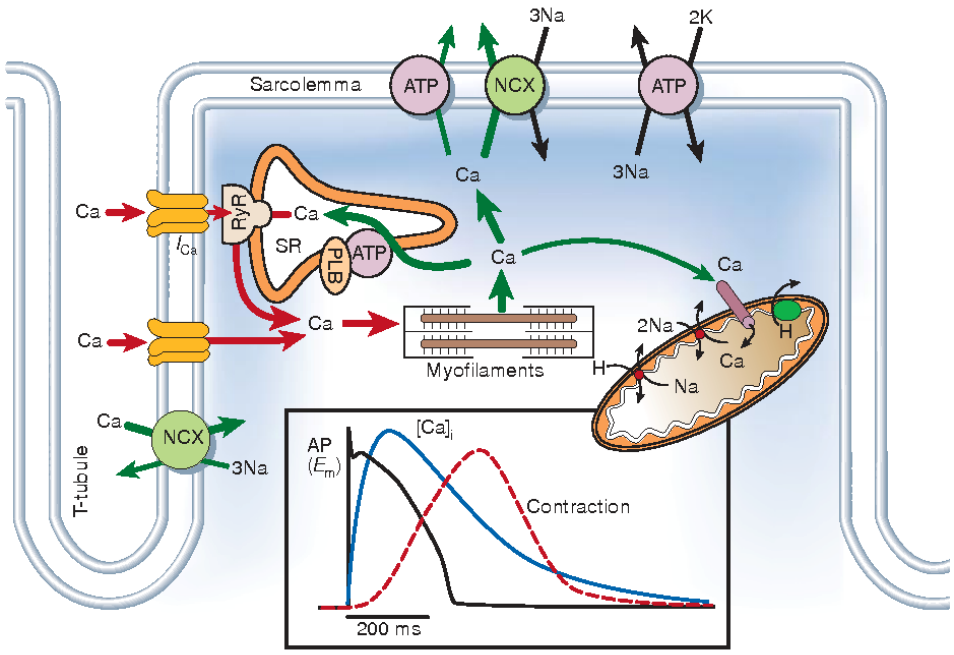

Figure 1.14: ECC in the heart

Schematic representation of ECC in the heart. Note the CICR through the DHPR which are not in close proximity to the RyR2. The black box shows the chronology of the ECC from the AP to Ca^{2+} release to cardiac muscle contraction. (Bers, 2002)

Because in cardiac cells RyRs and DHPRs are not mechanically coupled, the structure of CRUs (calcium release units) and T-tubule pattern look different than those in skeletal muscle. Instead of one terminal cisternae being located on each side of the T-tubule, only one terminal cisternae is present and the structure is called a dyad. Additionally, structured couplons and tetrades are missing from cardiomyocytes. Super-resolution microscopy experiments have recently shown that in cardiac cells there are clusters of ~14 RyR2 in peripheral coupling and up to ~100 in the intracellular site. It is estimated that for each DHPR opening at a dyad, 4-6 RyR will release Ca^{2+} from the SR.

(Bers, 2002; Lanner et al., 2010; Greenstein and Winslow, 2011; Gambardella et al., 2017; Eisner et al., 2017; Ríos, 2018; Zipes et al., 2018; Hamilton and Terentyev, 2019)

1.3.3 ECC in EOM

Only little is known about the ECC in EOMs. One study investigated the Ca^{2+} homeostasis in EOM derived myotubes compare to skeletal ones (from tibialis anterior, TA) in rats. Myotubes from EOMs showed an elevated calcium release when stimulated by ionomycin or high K^+ levels. This can be interpreted as a higher Ca^{2+} content of EOMs compared to limb muscles. Furthermore, transcript levels in myotubes and mature muscles were compared between EOMs and TA. A tremendous upregulation of several mRNAs from proteins involved in Ca^{2+} handling including, SERCA2, Na^+/Ca^{2+}-exchanger, phopholamban, calsequestrin 2, S100A1 and calmodulin to name a few, was found. This up-regulations was more pronounced in mature muscles compared to myotubes. The most interesting finding is the mRNA expression of the slow/cardiac isoform of calsequestrin (calsequestrin 2) and SERCA (SERCA 2). The presence of calsequestrin 2 was confirmed by western blot. The authors concluded their findings in schematic representing the difference EOM ECC compare to TA. (Figure 1.15: Model of EOM vs TA muscle Ca^{2+} homeostasis) (Zeiger et al., 2010)

An older study did not really contribute to the understanding of EOM ECC but showed their distinct gene expression compared to leg muscles. They showed that 4.5 % (13 genes) of the overall changes (>= 2-fold change) are in genes involved in the ECC. (Porter et al., 2001)

Two more recent studies from our lab investigated the ECC in human EOMs in more detail (Sekulic-Jablanovic et al., 2015, 2016a). They confirmed the upregulation of the genes of calsquestrin 2 (*CASQ2*) and EOM specific MyHC 13 (*MYH13*) at the mRNA level as well as found new upregulations like *RYR3*, *TRDN*, *ASPH1*, *SRL* and *PVALB* and downregulation like *MYH1*, *CACNA1S*, *RYR1*, *SERCA1*, *CASQ1*, *JPH1*. They confirmed the RyR1, $Ca_v1.1$, calsquestrin, sarcalumenin, junctophilin-1 and SERCA1 protein content by western blot. Interestingly they found $Ca_v1.2$ in the EOM biopsies, which is absent from limb muscles. They confirmed these findings through immunohistochemistry and showed the $Ca_v1.2$ is located on the sarcolemma of myotubes. Additionally, they confirmed the above mentioned higher Ca^{2+} release triggered by KCl and showed that EOM myotubes have higher levels of Ca^{2+} in their SR but a lower resting Ca^{2+} concentration.

To summarize, the ECC in EOM is not well understood but multiple evidence shows that there are significant differences compared to the limb muscles and that EOMs also show characteristics of cardiac ECC. Additionally, EOMs have unique features including the expression of RyR3.

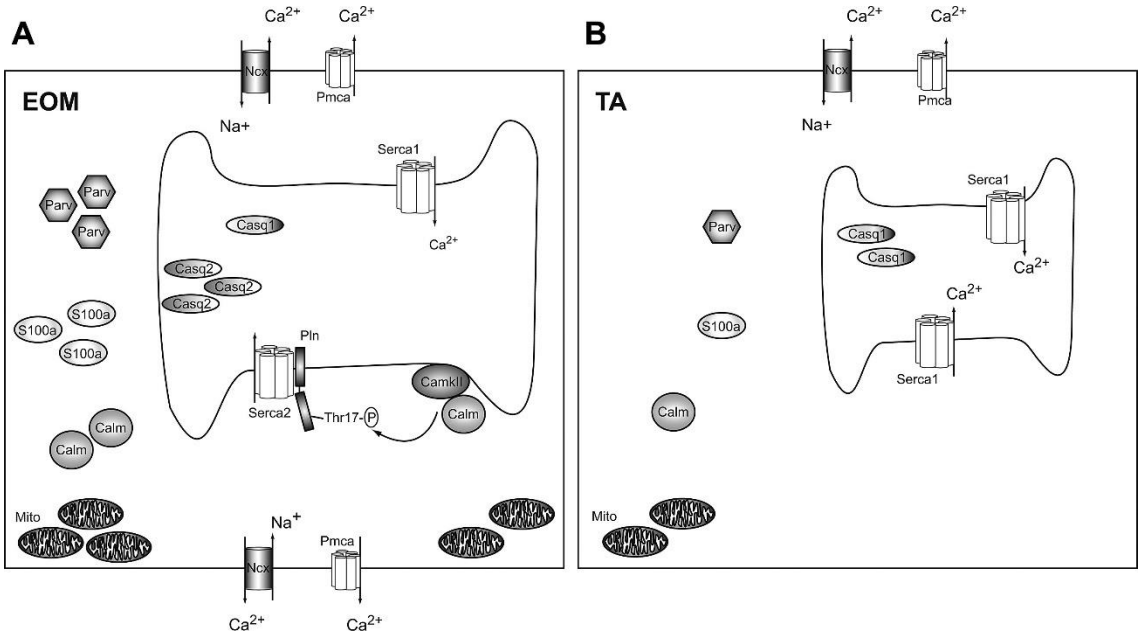

Figure 1.15: Model of EOM vs TA muscle Ca^{2+} homeostasis

(A) shows an EOM muscle cell with a larger SR, numerous pumps (Pmca: plasma membrane Ca2+-ATPase, Ncx: Na^+/Ca^{2+}-exchanger) and transporters in both the sarcolemma and the sarcoplasmic membrane and many Ca2+ binding proteins in the

cytosol (S100a, parvalbumin: Parv and Calm: calmodulin) and SR (Casq1 and Casq2), as well as numerous mitochondria (Mito). CamkII (Ca2+/calmodulin dependent kinase II) phosphorylates Pln (phospholamban) at Thr17 (phosphorylated threonine 17 residue), which regulates Serca2. Schematic **(B)** represents a TA muscle cell containing a smaller SR, fewer pumps and transporters and less Ca2+ binding proteins in the cytosol and SR compared with EOM. (Zeiger et al., 2010)

1.3.4 ECC Proteins

1.3.4.1 Ryanodine receptors (RyRs)

As mentioned above, ryanodine receptors (RyRs) are Ca^{2+} release channels located in the SR in muscle cells or endoplasmic reticulum in non-muscle cells. Their name derives from the fact that they bind with high affinity to the plant alkaloid ryanodine. Ryanodine locks the Ca^{2+}channels in an open sub conductance state at nanomolar concentrations, while at high concentrations (>100 μM) it acts as an inhibitor (Fleischer et al., 1985; Meissner, 1986; Lattanzio et al., 1987). Each functional RyR Ca^{2+} channel is a homotetramer, each subunit is >500kDa (~5000 amino acids) giving a total of ~2.2 MDa for one complete channel. In mammals three RyR isoform are known to be expressed, namely RyR1, RyR2 and RyR3 and these are encoded by three different genes on three different chromosomes. The RyR1 is the main isoform expressed in skeletal muscle (Takeshima et al., 1989; Zorzato et al., 1990a). RyR2s are primarily found in cardiac muscle (Otsu et al., 1990; Nakai et al., 1990a) and RyR3 which was originally referred to as brain isoform (Hakamata et al., 1992) was later found to be ubiquitously expressed, especially during development (Ogawa et al., 2000; Lanner et al., 2010).

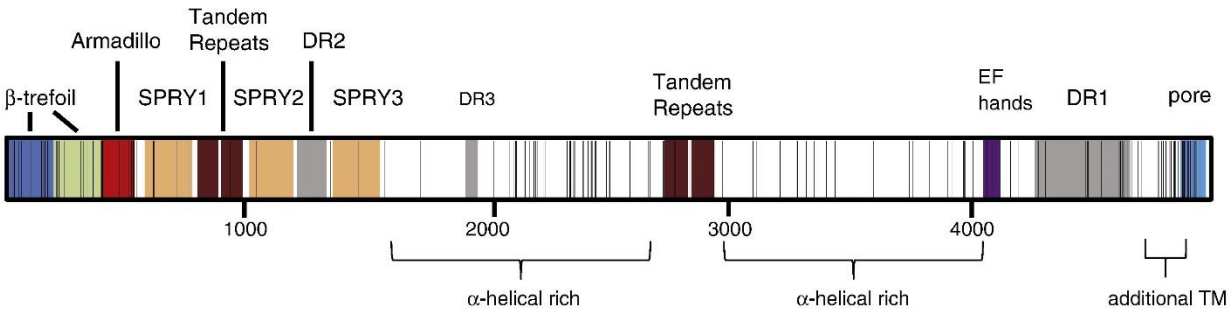

Figure 1.16: RyR domain architecture

Linear view of the RyR1 protein sequence. Domains are colored individually and labeled with the type of predicted or known fold. Divergent regions (DR1-DR3) are colored in gray. TM, transmembrane. Black vertical lines indicate positions of suspected disease-causing mutations in RyR1.(Van Petegem, 2015)

The amino acid sequence similarity of the three isoforms is ~65 % (Hakamata et al., 1992) and ~11% of the sequence is encompassed by three regions, DR1-DR3 (also called D1-D3 (Lanner et al., 2010; Hwang et al., 2012)) with the largest divergence of these regions being found between RyR1-RyR3 (Van Petegem, 2015). The first region in the sequence, DR2, is critical for the mechanical interaction between RyR1 and $Ca_v1.1$ while the other regions appear to be regulatory domains (Ca^{2+} and caffeine (only DR1)) (Figure 1.16: RyR domain architecture & Figure 1.20: Protein and ion binding domains of RyR1) (Lanner et al., 2010; Hwang et al., 2012).

RyR1

The largest ryanodine receptor isoform is RyR1 with one subunit having a molecular mass of ~565kDa; the gene encoding RyR1 is located at chromosome 19q13.2, spans 106 exons and encodes for alternatively spliced isoforms of 5038 and 5033 amino acids. The highest levels of expression of RyR1 are found in the junctional region of the terminal cisternae of the SR of skeletal muscle (Franzini-Armstrong and Nunzi, 1983; Hakamata et al., 1992; Zorzato et al., 1990b). However, low levels of RyR1 can be found in several other tissues such as vascular smooth muscle cells (Neylon et al., 1995; Lopez et al., 2016), stomach, cerebellum, Purkinje cells, adrenal glands, antigen presenting cells and B-lymphocytes (Marks et al., 1989; Takeshima et al., 1989; Furuichi et al., 1994; Giannini et al., 1995; OTTINI et al., 1996; Vukcevic et al., 2008, 2010)

Because of their large size and distribution within intracellular membranes, the crystal structure of RyR1 was not obtained, but cryo-electron microscopy (cryo-EM) studies have been invaluable and have elucidated the RyR1 structure at near atomic resolution. While numerous papers agree on the overall mushroom shape of the RyR1 (Samsó et al., 2005; Kimlicka and Van Petegem, 2011), only recent progress in single-particle cryo-EM, enabling resolutions up to atomic levels from membrane proteins (Liao et al., 2013), resulted in structures of the closed state RyR1 with resolution from 3.8 Å to 6.1 Å. These results allowed the construction of atomic-level RyR1 models and poly-alanine-level RyR1 models from rabbits RyR1 (Zalk et al., 2015; Yan et al., 2015;

Efremov et al., 2015). Each monomer of the channel can be split into four main domains, the shell, core solenoid, pore domains and C-terminal domain (CTD). While the largest part of the RyR1, the cap, is located in the cytosol the rest is mainly distributed across six transmembrane helices (S1-S6) from the pore domain. But only S5 and S6 form the actual pore (Figure 1.17: Architecture of the ryanodine receptor). The cap is ~ 270 Å × 270 Å × 100 Å and contains ~80% of the RyR1 mass while the trans-membrane domain is ~ 120×120×60Å. The structural models have been the bases for further crystal structure studies of smaller recombinant RyR1 domains to understand the function of RyR1 and allosteric coupling between shell and pore (Hwang et al., 2012; des Georges et al., 2016; Clarke and Hendrickson, 2016; Santulli et al., 2018).

The ATP binding site shown in Figure 1.17 plays a key role in gating. The positively charged residues of the TaF domain of the core solenoid can bind to the triphosphate tail of ATP, which acts as link between the CTD and the TaF domain and can trigger the conformational change of these two domains, which is essential for the gating. This conformational change sequential to Ca^{2+} and AP/caffeine binding makes the monomer more rigid and activates the RyR1 leading to big lateral shift of the monomer resulting in the opening of the RyR1. The exact mechanism of opening still remains unknown but there are two possible hypotheses: 1: The more rigid monomer allows the shell to bend the S6 helix in the pore region by thermal movement. 2: An unknown locking mechanism is released by the conformational change, which leads to bending of the monomer and opening of the pore (Santulli et al., 2018).

Mutations in *RYR1* are linked to various disorders ranging from the pharmacogenetic disease malignant hyperthermia, to different forms of congenital myopathies including dominant and recessive myopathies (Hwang et al., 2012). These will be described in more detail in section 1.3.5 Congenital Myopathies.

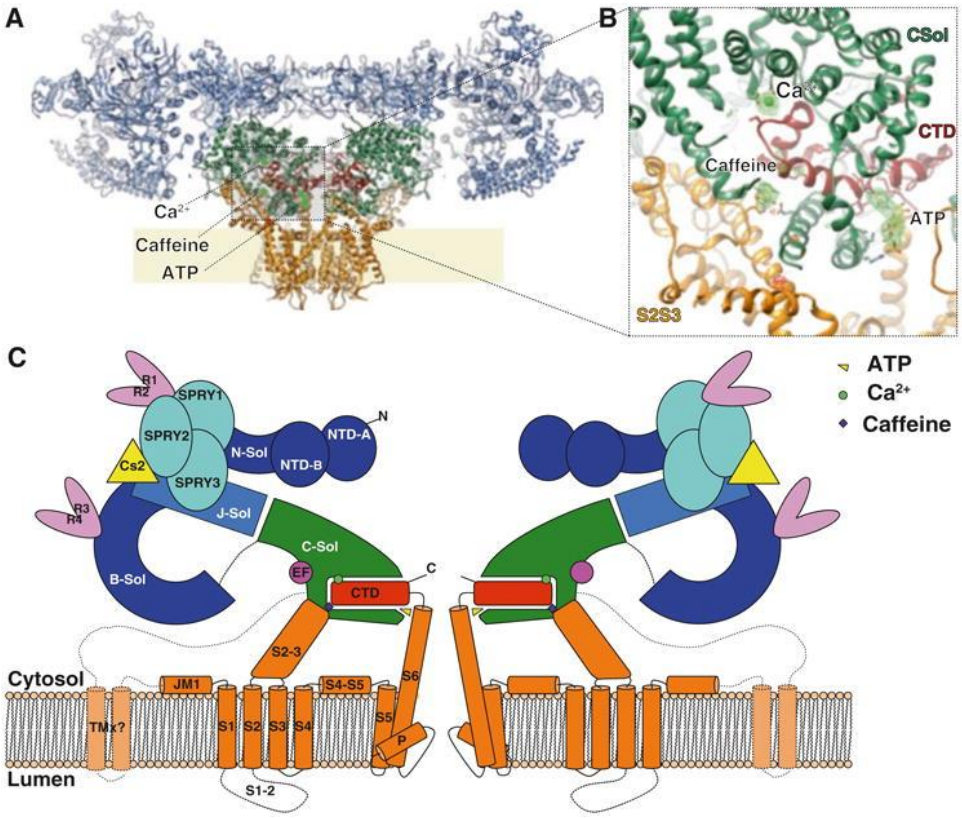

Figure 1.17: Architecture of the ryanodine receptor

(A) Ribbon representation, with the shell (residues 1–3666; light blue), core solenoid (residues 3667–4253; green), pore domain (residues 4540–4956; orange), and CTD (residues 4957–5037; dark red). **(B)** Zoom onto the CTD area showing ligands and locally aligned difference density map calculated between the EGTA-only map and Ca2+, ATP, and caffeine map (green/red mesh), contoured at 5s. **(C)** Schematic representation of RyR1. J-sol, junctional solenoid; B-sol, bridge solenoid; C-sol, core solenoid; N-sol, N-terminus solenoid. TMx, putative additional transmembrane helices (Van Petegem, 2015; Santulli et al., 2018)

RyR2

The second largest ryanodine receptor is RyR2 with one subunit having a molecular mass of ~564kDa; the gene encoding this isoform is location on chromosome 1q43, spans 102 exons and encodes for a protomer of 4967 amino acids. RyR2 was first found in and is the major isoform in cardiac tissue (Nakai et al., 1990b; Otsu et al., 1990). But subsequently high levels of expression were found in Purkinje cells of the cerebellum and cerebral cortex (Lai et al., 1992), where it is

involved in cognitive functions (Liu et al., 2012). It is also highly expressed in vascular smooth muscle (Berridge, 2008), as well as in insulin secreting pancreatic beta cells (Santulli et al., 2015). and in low levels in adrenal glands, kidney, lungs, ovaries, stomach and thymus (Kuwajima et al., 1992; Giannini et al., 1995).

The RyR2 is also composed of four identical subunits and its near-atomic 4.4 and 4.2 Å resolutions has given important information regarding its closed and open states (Peng et al., 2016). This study superimposed the open and closed states and found almost no change in the conformation of the selectivity filter (SF), the pore helices, and the supporting helices on S5 and S6 (residues 4790 to 4840). Rather a deviation around residue Phe4854 after helix S6 was found, leading to an outward tilt of all four S6 and an opening of the gate by ~8 Å (Figure 1.18: Structure of the open and closed RyR2) (Peng et al., 2016).

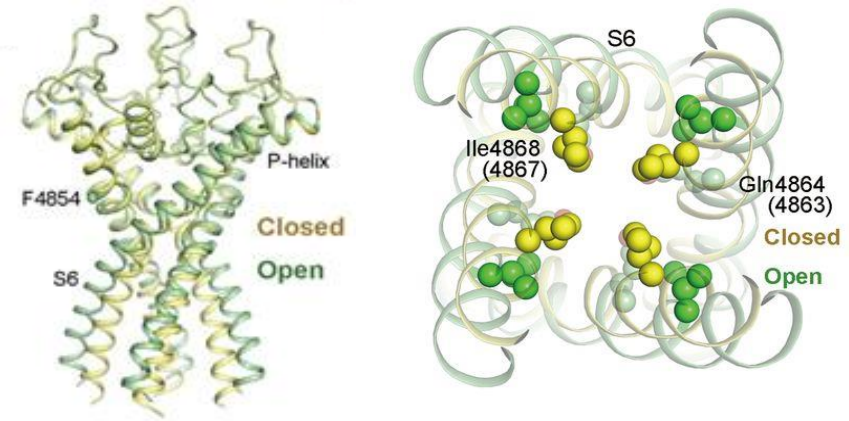

Figure 1.18: Structure of the open and closed RyR2

(Left) Conformational changes of the S6 helices of the pore domain in the open and closed RyR2 structures. They are superimposed relative to the selectivity filter and supporting turrets (residues 4790 to 4840). The SR luminal side is placed on top. **(Right)** Cytoplasmic view of the dilation of the intracellular gate in the open RyR2. The constriction residues in the closed and open states, Ile4868 and Gln4864, respectively, are shown as spheres and colored yellow in the closed and green in the open structures (Peng et al., 2016)

RyR2 mutations are mainly linked to cardiac diseases such as catecholaminergic polymorphic ventricular tachycardia (CPVT) (Priori et al., 2001; Laitinen et al., 2001, 2003; Xiong et al., 2018) and arrhythmogenic right ventricular cardiomyopathy type 2 (ARVD2) (Tiso et al., 2001)

RyR3

The smallest isoform of ryanodine receptors is RyR3 with one subunit having a molecular mass of ~552kDa; it is encoded by a gene located on chromosome 15q13.3-q14, spans 107 exons and encodes for a protein of 4870 amino acids. It has one more splicing variant: isoform 2: ~551kDa and 4865 amino acids. RyR3 was first identified in the brain (Hakamata et al., 1992; Nakashima et al., 1997) explaining why it sometimes called the brain isoform. But this terminology is misleading since RyR3 is widely expressed in many tissues (Lanner et al., 2010; Zhang et al., 2011) including hippocampal neurons, thalamus, Purkinje cells, corpus striatum (Hakamata et al., 1992; Lai et al., 1992; Furuichi et al., 1994); skeletal muscles with the highest expression in the diaphragm (Marks et al., 1989; Neylon et al., 1995); smooth muscle cells of the coronary vasculature, lung, kidney, ileum, jejunum, spleen, stomach of mouse and aorta, uterus, ureter, urinary bladder, and esophagus of rabbit (Giannini et al., 1992; Hakamata et al., 1992; Giannini et al., 1995; OTTINI et al., 1996).

RyR3 is the least studied RyR isoform but a recent study suggests that it plays a role in Alzheimer's disease, specifically RyR3s in cortical neurons are neuroprotective in TgCRND8 mouse model of Alzheimer's disease (Supnet et al., 2010). Though its detailed structure has not been investigated its overall structure is similar to that of RyR1 & RyR2 (Sharma et al., 2000; Liu et al., 2001).

RyR1 and RyR2 knock-out (KO) mouse models are lethal and pups die at birth or during embryonic development (Takeshima et al., 1995, 1998), whereas RyR3 KO mice show no obvious impairments and have a normal lifespan and no reproductive problems (Takeshima et al., 1996; Clancy et al., 1999). Nevertheless RyR3 may play a role in the development of skeletal muscle and it was shown that in mice the diaphragm expresses RyR3 from the 18th day of the embryonic stage up to 15 days postnatally and subsequently decreases until it is almost undetectable (Tarroni et al., 1997). In line, isolated neonatal skeletal muscles fibers from RyR3 KO mice show a decrease of force development elicited by either caffeine or electrical stimulation even though ECC seemed to be normal (Takeshima et al., 1996; Barone et al., 1998)

Interestingly, transfection experiments of adult mouse muscle fibers have shown that RyR3 is essential for calcium sparks and CICR amplification. These findings are consistent with the fact that mammalian muscles lose the ability to produce sparks postnatally, and in conjunction the expression of RyR3 is down-regulated (Pouvreau et al., 2007). In their study Pouvreau et al. show that RyR3s are localized on the parajunctional membranes (Figure 1.19: Localization of RyR3), immediately adjacent to the junctional region and must be activated by a CICR mechanism since they don't interact structurally (Protasi et al., 2000) or functionally (Fessenden et al., 2000) with DHPRs. (Pouvreau et al., 2007). These results are consistent with EM studies made on toadfish and frog skeletal muscles (Felder and Franzini-Armstrong, 2002). The amplification of spontaneous Ca^{2+} releases by single couplons of RyR3 was also confirmed in zebrafish (Perni et al., 2015).

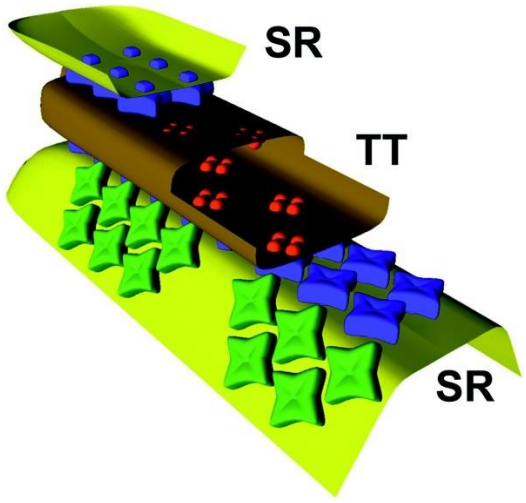

Figure 1.19: Localization of RyR3

Model of a triad with two different RyR isofroms (RyR1 and RyR3). RyR1 (blue) are placed as parallel double row in the junctional feet while the RyR3 (green) in a zigzag double row pattern at the parajunctional feet. T tubule (TT), SR sacs (SR) (Felder and Franzini-Armstrong, 2002).

Regulators

The large cap/shell of RyRs with ~500 000 Å^2 gives them plenty of space for tens of signaling molecules for positive and negative regulation. Even though they share an overall sequence homology of ~65% and their similar structure, different RyR isoforms can show different effects by the same regulators.

The most obvious regulator is Ca^{2+}. Cytosolic Ca^{2+} acts as activator at low concentrations (~ 1 μM) and as an inhibitor at high concentrations (~ 1 mM). This is accomplished by two different Ca^{2+} binding sites, of high and a low affinity (Meissner et al., 1986, 1997). But the Ca^{2+} -dependent activation varies between the three RyR isoforms. RyR2 and RyR3 are activated by Ca^{2+} to a greater extent than RyR1 and require higher Ca^{2+} concentrations for inactivation (Ogawa et al., 2000; Lanner et al., 2010). In contrast, at high cytosolic Ca^{2+} concentrations, Mg^{2+} is a potent inhibitor of RyR1 (Lamb, 2000; Meissner, 2002) but a weak inhibitor of RyR2 and RyR3. Additionally, luminal Ca^{2+} (in the SR) can stimulate the Ca^{2+} release by RyR1 & RyR2 (Lanner et al., 2010; Chen et al., 2014).

Aside Ca^{2+} and Mg^{2+} there are many other regulators of RyRs. Some of them contain an EF-hand such as calmodulin (CaM) or S100. CaM is a ~ 17-kDa protein containing four EF hands in two domains, the N-lobe and C-lobe, that can bind directly to RyRs. CaM can also bind Ca^{2+} so has two states, the Ca^{2+}free state, called ApoCaM, and the Ca^{2+}bound state, Ca^{2+}/CaM. The effect of CaM varies on the state and the RyR isoform it binds to (Menegazzi et al., 1994; Guerrini et al., 1995; Van Petegem, 2015). Cryo-EM studies have revealed that the two states have different bindings sites on the RyR1 (Samsó and Wagenknecht, 2002; Huang et al., 2012). In contrast to this ApoCaM binds in the RyR2 roughly the same location as Ca^{2+}/CaM in RyR1 which is coherent with their function on the RyRs: At high Ca^{2+} levels it inhibits both RyR1 and RyR2, at low Ca^{2+} levels, so as ApoCaM, it activates RyR1 but inhibits RyR2 (Ikemoto et al., 1995; Tripathy et al., 1995; Buratti et al., 1995; Fuentes et al., 1994). Similarly, the small calcium binding protein S100 was found to bind to and regulate the activity of RyR1 (Susan Treves et al., 1997).

FK506-binding proteins (FKBPs) 12 and 12.6, also called calstabin1 and calstabin2, are two small proteins, of 12 and 12.6 kDa, that act as regulators of RyR channel activity. Co-purification studies showed that one FKBP binds to one RyR subunit, that is 4 molecules of FKBP per functional

channel tetramer (Jayaraman et al., 1992; Kushnir and Marks, 2010). While FKBP12 preferably binds to RyR1, FKBP12.6 prefers RyR2. FKBPs have a low affinity for RyR in the open state but a high affinity for RyRs in the closed state, even though the exact affinity of the two proteins has not been precisely determined (Wagenknecht et al., 1996; Van Petegem, 2015). They play a critical role for preventing RyRs from leaking Ca^{2+} and for coupled gating between RyRs. The effect of FKBP12 on RyR1 is that it can make it harder for the RyR1 to open by decreasing the appearance of sub conductance states (Brillantes et al., 1994; Venturi et al., 2014; Van Petegem, 2015). While it has the opposite effect on the RyR2 and act as an antagonist of FKBP12.6 (Galfré et al., 2012).

There are more regulatory proteins which act directly or indirectly on RyRs (Figure 1.20: Protein and ion binding domains of RyR1 & Figure 1.21: Regulators of RyRs), including: calsequestrin, histidine-rich Ca2+ binding protein, homer, junction, S100A1, sorcin, triadin (Hwang et al., 2012). But RyR is also regulated by post-translational modifications, including phosphorylation, oxidation and nitrosylation (Bellinger et al., 2008). These modification occur mainly on the cytosolic shell and alter the shell's dynamics (Santulli et al., 2017b, 2018).

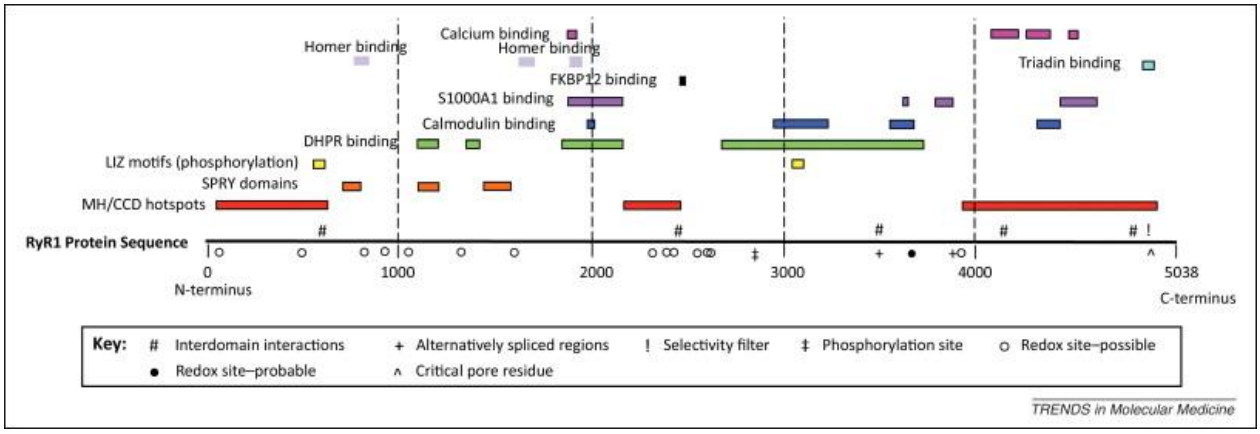

Figure 1.20: Protein and ion binding domains of RyR1

Protein and ion binding domains across the RyR1 protein sequence colored individually. (Hwang et al., 2012)

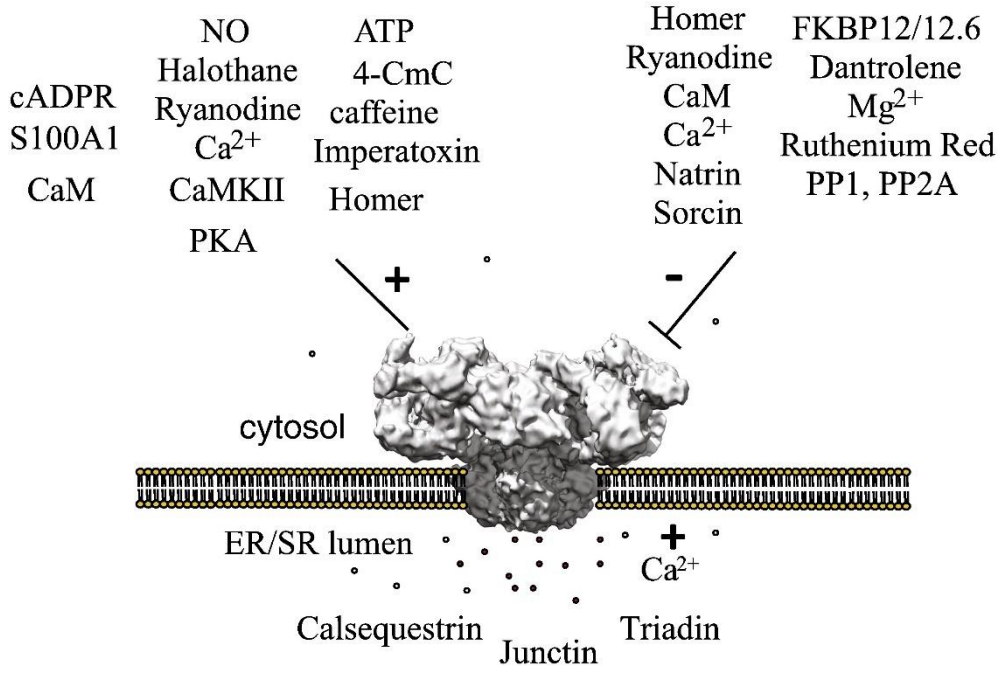

Figure 1.21: Regulators of RyRs

An overview of some proteins and molecules regulating RyRs. They can either be stimulators (+) or inhibitors (-) of RyR Ca^{2+} release. Some can even have both effect depending on their concentration (Van Petegem, 2015)

1.3.4.2 Voltage-gated Calcium Channels / $Ca_v1.1$ & $Ca_v1.2$

The voltage-gated calcium channels present in skeletal and cardiac muscles ($Ca_v1.1$ and $Ca_v1.2$) belong to a superfamily of transmembrane ion channels, including voltage gated sodium and potassium channels (Catterall, 1995). Within the voltage-gated calcium channel family there are many sub-families. The group consist of ten channels grouped into five sub-types: L-type ($Ca_v1.1$-$Ca_v1.4$), P/Q-type ($Ca_v2.1$), N-type ($Ca_v2.2$), R-type ($Ca_v2.3$) and T-type ($Ca_v3.1$- $Ca_v3.3$). L-type calcium channels (L for long lasting) are also known as dihydropiridine receptors (DHPR) because of the blocking effect of 1,4-dihydropyridines. Phenylalkylamines and benzothiazepines also block the activities of these channels. DHPRs are large macromolecular structures composed of several subunits including $\alpha1$, $\alpha2\delta$, $\beta1$, and γ. The largest subunit is the pore- forming $\alpha1$ subunit which also serveS as voltage sensor. The core subunit is the specific protein underlying the different characteristics of the ten voltage-gated calcium channels, whereby each channel has a different $\alpha1$ subunit, $Ca_v1.1$ the $\alpha1S$ and $Ca_v1.2$ the $\alpha1C$. These two $\alpha1$ subunits are encoded by distinct

genes, namely *CACNA1S* and *CACNA1C.* The other 8 α1 subunits and the genes encoding them have similar names differentiated by a different last letter (*A-I*). Each α1 subunit within the same sub-group shares more than 70% identical amino acid sequence while across the different sub-groups (ex. Ca_v2, Ca_v3 etc.) the sequence similarity falls below 40%.

α1 subunits contain ~2000 amino acids and have a molecular mass of 190-250 KDa. They contain four highly homologous but non-identical intramembrane domains (I–IV). Every domain consists out of six transmembrane alpha helical segments (S1-S6) while the amino- and caboxy- terminal ends are located in the cytosolic space. The S1-S4 alpha helical segments of each domain is responsible for the voltage sensing feature of the α1 subunit and is called voltage-sensing domain (VSD). The voltage-sensing ability is thought to be given by the presence of alternating positively charged arginine or lysine residues at every third or fourth position in S4 separated by two hydrophobic residues. Studies have shown that during depolarization the S4 moves outwards, across the plane of the T-Tubule membrane thereby establishing the determinants for voltage sensitivity. S5 and S6 on the other hand, form the pore domain while the pore loop between S5 and S6 is responsible for the ion selectivity of the channel. Only three mutations in the poor loop of domain I, III and IV can change the ion selectivity from Ca^{2+} to Na^{+}. (Figure 1.22: Structure and membrane topology of of $Ca_v1.1$ the α1S) (Catterall et al., 2003; Hernández-Ochoa and Schneider, 2018; Zipes et al., 2018)

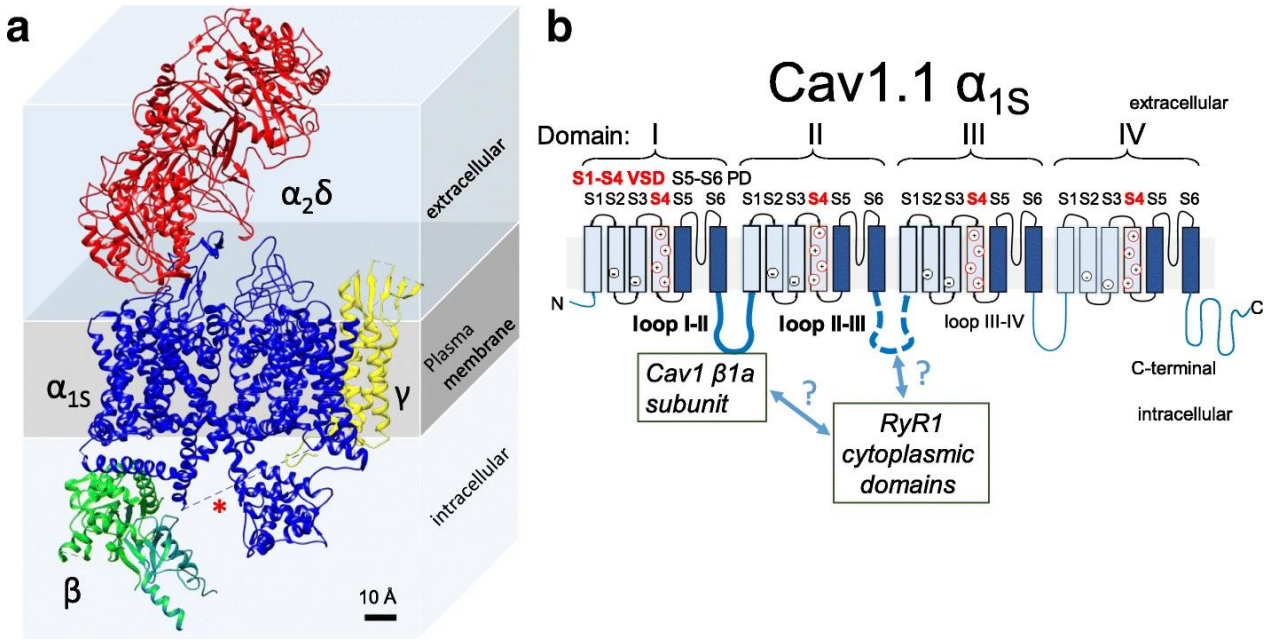

Figure 1.22: Structure and membrane topology of of $Ca_v1.1$ the α1S of the DHPR

(a) Cryo-EM reconstruction of the DHPR showing the different subunits that compose it. Side view at 3,6 Å. The α1 subunit is highlighted in blue. Auxiliary β-, α2δ-, and γ-subunits are colored in green, red, and yellow, respectively. The asterisk represents the missing II-III loop in the cryo-EM structure. **(b)** $Ca_v1.1$ membrane topology with its four domains (I-IV), transmembrane domains (S1-S6) and its intracellular loops which interact with other proteins involved in ECC. (Hernández-Ochoa and Schneider, 2018)

One main difference between $Ca_v1.1$ and $Ca_v1.2$ is the loop between domain II and III. In skeletal muscles, the $Ca_v1.1$ is mechanically coupled to the RyR1 through the II-III loop. While also other regions, for example the I- II loop, may interact with the RyR1, the loop II-III is essential for this interaction. $Ca_v1.2$ on the other hand, does not interact directly with the RyR2 and activates the RyR2 through a mechanism of CICR. The result of this is that $Ca_v1.1$ forms tetrads with up to four $Ca_v1.1$ connected to one RyR1 tetramer (Figure 1.23: Structure of the $Ca_v1.1$ (α1S subunit of the DHPR) and its interactions with RyR1).

The auxiliary β-, α2δ-, and γ-subunits contribute to trafficking, anchorage, and regulatory functions. The intracellular β-subunits have a molecular mass of 55 kDa and can be expressed as

four isoforms encoded by four different genes (*CACNB1-4*). The 4-TM γ-subunits consist of eight isoforms encoded by eight different genes (*CACNG1-8*). The extracellular α2δ-subunits are actually two subunits from one gene, the α2 and the δ, linked via a disulfide bond and have a combined size of 170 kDa. The δ- subunit has one TM region while the α2 is completely extracellular. There are four different isoforms encoded by four different genes (*CACNA2D1-4*). (Zipes et al., 2018)

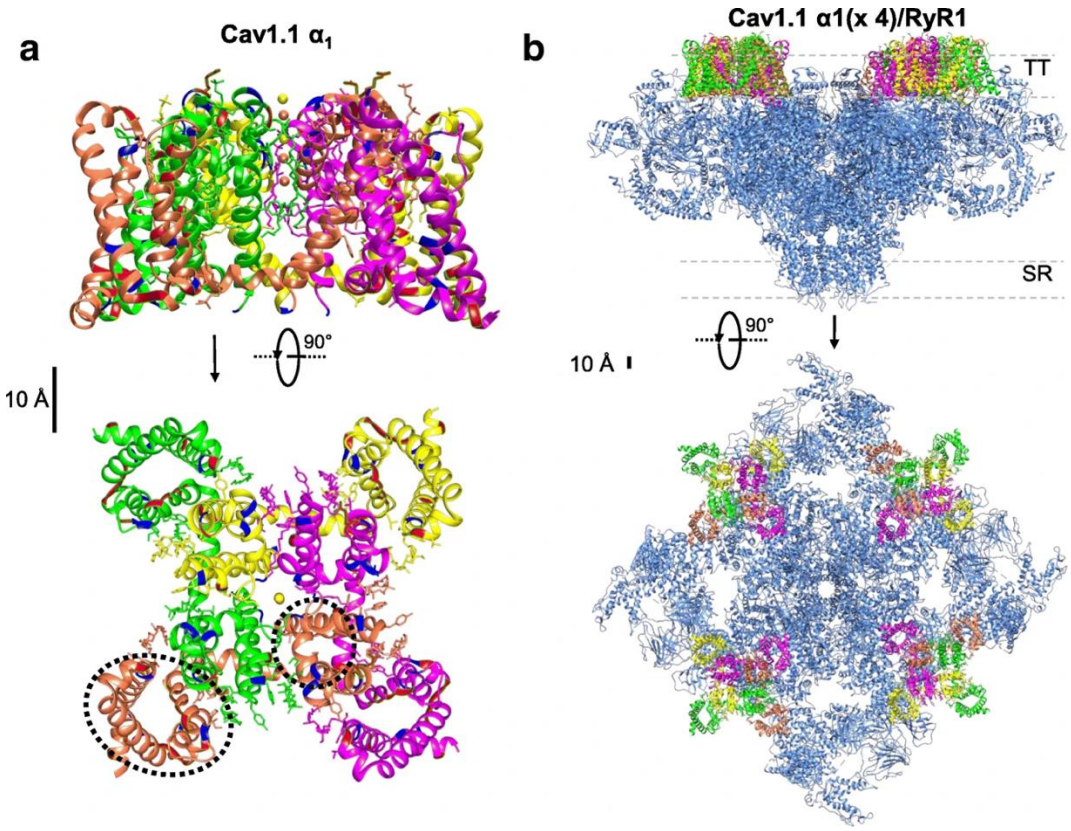

Figure 1.23: Structure of the $Ca_v1.1$ (α1S subunit of the DHPR) and its interactions with RyR1

(a) cryo-EM reconstruction of the $Ca_v1.1$ subunit from two views: top=side view, bottom=upper view. The auxiliary subunits, the cytoplasmic tails, and loops are not shown. Its four domains are colored differently. Positively charged residues are indicated in red, negatively charged residues are shown in blue. The voltage sensing domains (S1-S4) is not in close proximity to the pore forming domain (S5-S6) as

indicated by the dashed ellipse for S1-S4 and the dashed circle for S5-S6. **(b)** Side (top) and upper (bottom) views of cryo-EM reconstruction of the RyR1 and four $Ca_V1.1$ forming a tetrad. (Hernández-Ochoa and Schneider, 2018)

1.3.4.3 Sarco/endoplasmic Reticulum Ca2+-ATPase

The sarco/endoplasmic reticulum Ca2+-ATPase (SERCA) is a 110 kDa, type P pump, with one cytosolic "headpiece" region and one transmembrane region, located in ER and SR. The cytosolic region can be split into three domains named according to their function: the nucleotide binding domain (N) which binds ATP, the phosphorylation domain (P) that drives ATP hydrolysis leading to the phosphorylation of the catalytic Asp residue, and the actuator domain (A) that catalyzes dephosphorylation of the P-domain and is involved in the transmission of the conformational change. The transmembrane domain consists of ten hydrophobic membrane spanning helices with two binding sites for Ca^{2+}. SERCA is the most abundant protein in the terminal cisternae and the longitudinal SR, where it can make up to 80-85 % of the total protein content (Meissner, 1975; Costello et al., 1986; Zorzato et al., 1986). SERCAs transport two Ca^{2+} into the SR/ER per ATP hydrolysed (MOLLER et al., 2005; Toyoshima, 2009; Brini and Carafoli, 2009; Zipes et al., 2018) .

There are three main isoforms, SERCA1-3, encoded by three different genes, *ATP2A1-3*. Additional alternative splicing variants of the main SERCAs extend the number of isoforms to twelve: SERCA1a-b, SERCA2a–d, SERCA3a–f. SERCA1 is exclusively expressed in adult (SERCA1a) and fetal (SERCA1b) fast-twitch skeletal muscles. SERCA2a is expressed in slower muscles, in particular in slow-twitch skeletal muscles and cardiac muscles. SERCA2c and SERCA2d can be also found in low amounts in the heart, while SERCA2b can be found in all tissues. The SERCA3 isoforms are usually found in non-muscle tissues (Periasamy and Kalyanasundaram, 2007).

SERCAs can be inhibited by orthovanadate as well as with specific inhibitors such as thapsigargin, cyclopiazonicacid, and 2.5-di(t-butyl) hydroquinone. SERCAs are physiologically regulated by phospholamban, sarcolipin and myoregulin. Depending on its degree of phosphorylation, phospholamban can acts as an inhibitor for SERCA2a in the heart and slow twitch muscles, (MacLennan and Kranias, 2003); sarcolipin regulates SERCA1 activity in a Ca^{2+} concentration-dependent way in fast-twitch skeletal muscles (Odermatt et al., 1998); myoregulin is a

micropeptide encoded within a long non-coding RNA sharing similarities with phospholamban and sarcolipin which is present in all skeletal muscles (Anderson et al., 2015).

1.3.4.4 Calsequestrin

Calsequestrin (CSQ) is an abundant low affinity high capacity Ca^{2+} binding protein localized in the SR. It is mainly present in the lumen of the terminal cisternae (Saito et al., 1984; Costello et al., 1986; Franzini-Armstrong, 1987; Wagenknecht et al., 2002). It exists as two isoforms, CSQ1 (apparent molecular mass of 63 KDa) and CSQ2 (apparent molecular mass of 55 KDa), encoded by two genes, *CASQ1* and *CASQ2*. CSQ1 is the only isoform expressed in fast-twitch skeletal muscle while slow-twitch muscle express CSQ1 and CSQ2, even though CSQ1 remains the dominant isoform. In the heart only CSQ2 can be found. Both isoforms can be present as monomers or polymers; calsequestrin polymerizes when the Ca^{2+} concentration in the lumen of the SR is high (~1mM). One mole of CSQ1 can bind up to 50 moles of Ca^{2+}. Beside buffering and storing Ca^{2+}, CSQ1 is thought to regulate the activity of RyRs indirectly, mainly by binding to junctin and triadin. It is postulated that RyR1, CSQ1, traidin and junctin from a large protein complex (Yáñez et al., 2012; Barone et al., 2015; Elíes et al., 2020).

1.3.4.5 Parvalbumin

Parvalbumin is also a Ca^{2+} binding protein but unlike CSQ, it is present predominantly in fast twitch muscles and is a cytosolic protein. It has two Ca^{2+} binding sites. During contraction Ca^{2+} binds with high affinity to troponin-C before getting buffered by parvalbumin and subsequently being pumped back into the SR via SERCA. Under resting conditions, parvalbumin binds Mg^{2+} which is later replaced by Ca^{2+}. It has been suggested that this buffering helps speed up muscle relaxation explaining why parvalbumin is only expressed in fast-twitch muscles but almost absent in slow-twitch muscles. (Baylor and Hollingworth, 2003; Yáñez et al., 2012)

1.3.4.6 JP-45

As the name suggests JP-45 has a molecular mass of 45 kDa and is located on the junctional face membrane of the SR. It has one transmembrane domain with the C-terminus in the lumen of the SR and the N-terminus in the cytosol. It binds to the I-II loop of the skeletal α1S subunit of the DHPR and interacts with calsequestrin (1 and 2) via its luminal carboxy-terminal domain. Through

this interaction, the JP-45/CSQ complex is a negative regulator of Ca^{2+} entry through the DHPR during EC-coupling. (Zorzato et al., 2000; Anderson et al., 2003; Mosca et al., 2013)

1.3.4.7 STAC3

SH3 and cysteine-rich domain-containing protein 3 (STAC3), the third isoform of the adaptor STAC protein family, is a relatively newly discovered protein involved in ECC. The gene encoding STAC3 is mutated in patients with the congenital myopathy, Native American myopathy (Horstick et al., 2013) (Horstick et al., 2013; Zaharieva et al., 2018). Recently it was shown that STAC3 binds to both $Ca_v1.1$ and RyR1, that it is essential for the transport of $Ca_v1.1$ to the plasma membrane and may be the missing link mediating the mechanical coupling between $Ca_v1.1$ and RyR1. STAC3 can also bind to $Ca_v1.2$, but this has a different effect as it greatly slows the rate of current inactivation (Polster et al., 2015). STAC3 was also shown to be essential for voltage dependent Ca^{2+} release (Nelson et al., 2013).

1.3.4.8 Others

Beside the proteins described many additional ones are present in the SR and triads and are involved in ECC (Figure 1.24:Protein components of the skeletal SR involved in the ECC). To name some: junctate, junctin, junctophilin, triadin, SRP-35, sarcalumenin and mitsugumin-23. (Treves et al., 2009)

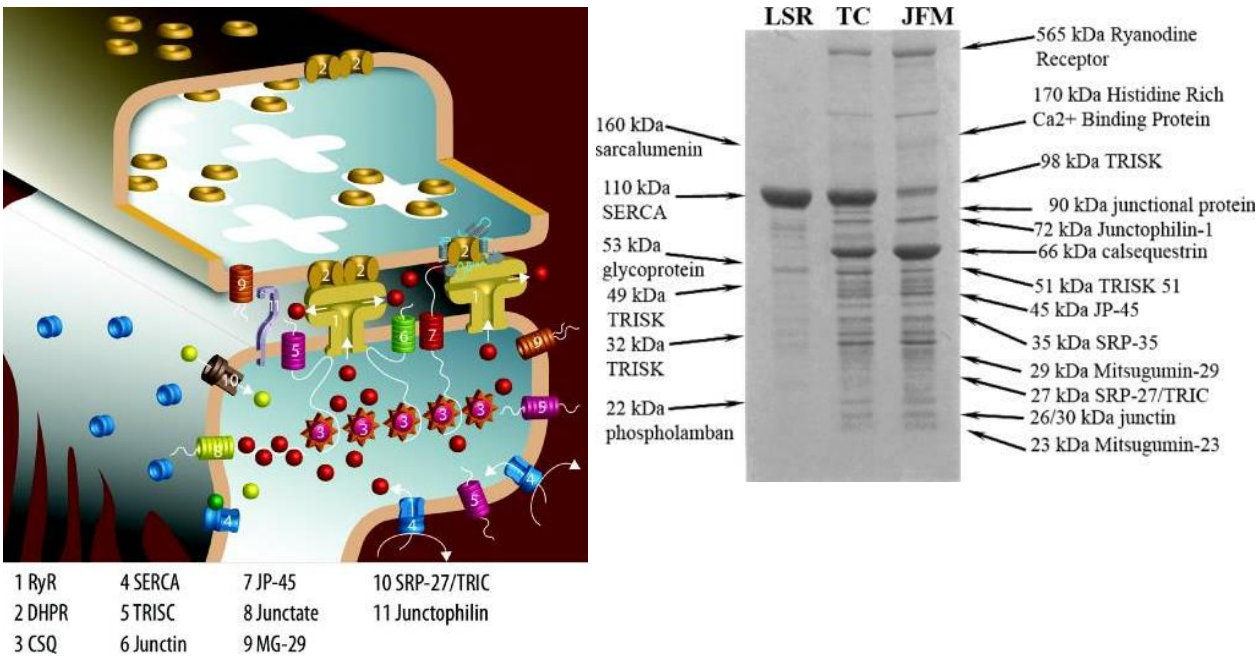

Figure 1.24:Protein components of the skeletal SR involved in the ECC

(Left) Schematic representation of proteins involved in ECC showing their location in the SR and TT-system. **(Right)** Coomassie Brilliant Blue stained gradient (5–15%) SDS-PAGE of proteins involved in the ECC from the longitudinal sarcoplasmic reticulum (LSR), the terminal cisternae (TC) and the junctional face membrane (JFM) obtained from rabbit SR. (Treves et al., 2009)

1.3.5 Congenital Myopathies

Congenital myopathies are a group of non-dystrophic neuromuscular diseases caused by mutations in over 20 genes. Their clinical and histopathological features are heterogenous but usually they have an early onset, are diagnosed by neurologists based on the characteristics of the muscle biopsy. Disease progression can be variable, ranging from sever prenatal forms to a slowly progressing form of the disease. Typical weakness in axial and proximal muscles can be found in patients with diverse subsets of congenital myopathies while extraocular, cardiac or respiratory muscle involvement are specific for diseases caused by mutations in specific genes and constitute a smaller subgroup. The most commonly mutated gene in human congenital myopathies is *RYR1*, the gene encoding the skeletal isoform RyR1, but mutations in other genes such as myotubularin 1 (*MTM1*), selenoprotein N (*SEPN1*), $Ca_v1.1$ (*CACNA1S*), *STAC3*, *BIN1* and

DNM2 are also frequently (Table 2: Genes implicated in congenital myopathies and related conditions) (Jungbluth et al., 2018).

Gene symbol	Chromosomal location	Protein	Condition	Inheritance
Sarcoplasmic reticulum Ca^{2+} release, excitation–contraction coupling and/or triadic assembly				
RYR1[a]	19q13.1	Ryanodine receptor 1 (skeletal)	CCD[a]	AD, AR
			MmD[a]	AD, AR
			CNM	AR
			CFTD	AR
			KDS	AR, AD
STAC3	12q13.3	SH3 and cysteine-rich domain-containing protein 3	NAM	AR
ORAI1	12q24.31	Ca^{2+}-release-activated Ca^{2+} channel protein 1	TAM	AD
STIM1	11p15.4	Stromal interaction molecule 1	TAM	AD
			Stormorken syndrome	AD
MTM1[a]	Xq28	Myotubularin	XLMTM	X-linked
BIN1[a]	2q14	Amphiphysin II	CNM[a]	AR, AD
DNM2[a]	19p13.2	Dynamin 2	CNM	AD
SPEG	2q35	Striated muscle preferentially expressed protein kinase	Congenital myopathy with central nuclei and cardiomyopathy	AR
CCDC78	16p13.3	Coiled-coil domain-containing protein 78	Congenital myopathy with cores and central nuclei	AD
CACNA1S	1q32	Voltage-dependent L-type Ca^{2+} channel subunit-α1S	Congenital myopathy with EOM	AD, AR
SEPN1[a]	1p36.13	Selenoprotein N	MmD[a]	AR
			CFTD	AR

Table 2: Genes implicated in congenital myopathies and related conditions

AD, autosomal dominant; AR, autosomal recessive; CCD, central core disease; CFTD, congenital fiber type disproportion; CNM, centronuclear myopathy; EOM, extraocular muscle involvement; KDS, King–Denborough syndrome; MmD, multi-minicore disease; MSM, myosin storage myopathy; NAM, North American myopathy; TAM, tubular aggregate myopathy; XLMTM, X-linked myotubular myopathy. a=Genes most commonly implicated in the classic structural congenital myopathies, and the corresponding conditions.(Jungbluth et al., 2018)

Over 300 mutations in *RYR1* have been identified in patients affected by different diseases plus 200 additional mutation which does not modify the channel function and so does not result in a disease. There are three hotspots where most of the disease causing mutations are located: N-

terminal (∼1–600), the central (∼2000–2600) and the C-terminal (∼4000–5000) region (Santulli et al., 2017a). Another hotspot is the phosphorylation domain (Yuchi et al., 2012).

1.3.5.1 Central Core Disease

Central core disease (CCD) was first described 1956 (Shy and Magee, 1956), occurs in 1:100 000 live births and comprises 16-30% of all congenital myopathies, thus it is the most common congenital myopathy (Santulli et al., 2017a; Jungbluth et al., 2018). Patients present clinically with hypotonia, delayed motor milestones, predominantly proximal weakness and skeletal abnormalities such as scoliosis. Also, a positive in vitro contracture test (IVCT) for malignant hyperthermia susceptibility (MHS) is a frequent symptom. Histologically CCD is characterized by the presence of centrally located cores with reduced oxidative activity, mainly in type 1 fibers; the cores run along the fiber axis for a substantial distance on longitudinal sections (Figure 1.25: Histopathology of central cores in CCDs). The histopathological findings gave the disease its name and serve as a diagnostic criterium together with the clinical symptoms. Another typical finding is the reduction or absence of mitochondria, myofibrillar disorganization and accumulation of abnormal Z band material, as seen in EM pictures (Jungbluth, 2007b).

CCD is mostly caused by dominant *RYR1* mutations, often missense, and are located at disease causing hotspots (Figure 1.26: Distribution of CCD and MmD causing mutations across *the* RYR1 gene). Disease progression is mostly slow or even static and most patients have mild to moderate symptoms (Jungbluth et al., 2018). Aside the most severe cases, almost all patients achieve the ability to walk. Often patients classified as having a recessive form of CCD are more severely affected and have a prenatal onset. Some also exhibit respiratory impairment which may affect their life span (Jungbluth, 2007b). All patients diagnosed as having CCD share the common phenotype that their extraocular muscles are spared and that they do not have an associated cardiomyopathy (Jungbluth et al., 2011).

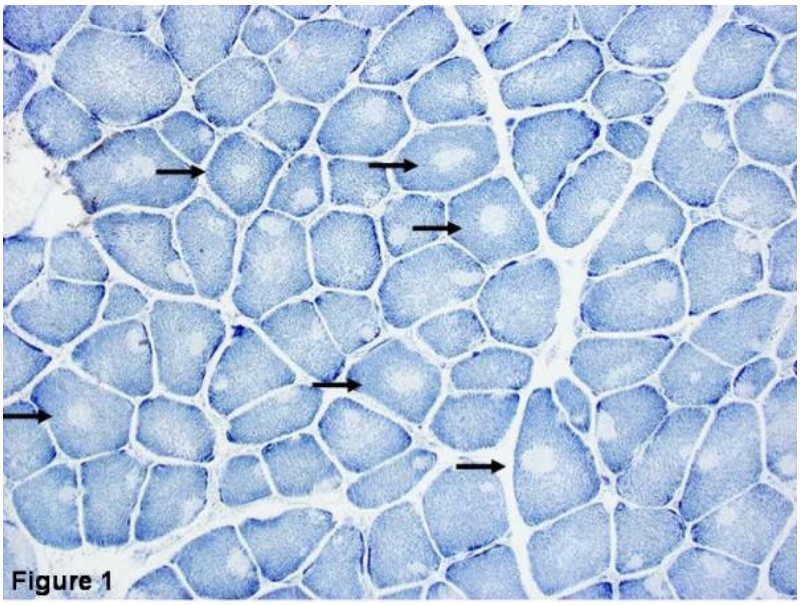

Figure 1.25: Histopathology of central cores in CCDs

Transverse section from the rectus femoris stained with NADH-TR. Dark staining indicates high oxidative type 1 fibers with cores in almost all fibers. Arrows show the typical cores located in the center of the muscle fiber but occasionally multiple cores and eccentrically located cores can appear. (Jungbluth, 2007b)

1.3.5.2 Multi-Minicore Disease

Another type of core myopathy is multi-minicore disease (MmD). The distinct separation of CCD, MmD and malignant hyperthermia is sometimes not possible due to their pathological and genetic overlap and are often discussed together by reviews. Unlike CCD, MmD is mostly caused by recessive *RYR1* mutations or also by mutations in *SEPN1* (*SELENON*) and in some cases in *MYH7* as well as a few other genes (Jungbluth et al., 2018). It has an estimated prevalence of 3.5 – 5.0:100 000 (Jungbluth, 2007a) and unlike CCD, MmD is predominantly caused by recessive *RYR1* mutations which are evenly distributed across the *RYR1* gene and do not cluster within particular hotspots (Figure 1.26: Distribution of CCD and MmD causing mutations across the *RYR1* gene) (Treves et al., 2008b; Hwang et al., 2012; Santulli et al., 2017a).

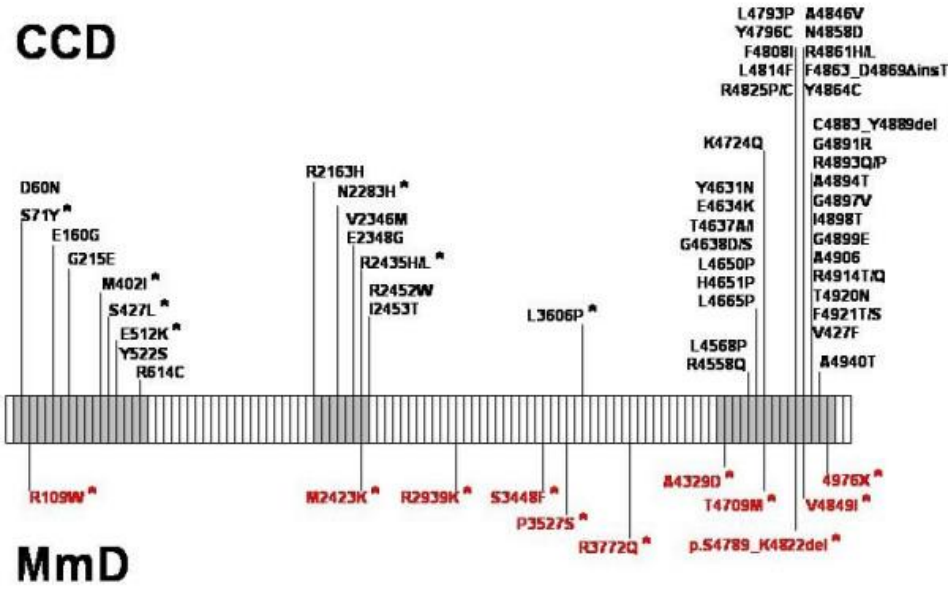

Figure 1.26: Distribution of CCD and MmD causing mutations across the *RYR1* gene.

Schematic representation of the *RYR1* gene with the distribution of dominant and recessive (*) mutations associated with central core disease (CCD, in black) and multi-minicore disease (MmD, in red). Notable the "hotspots" CCD causing mutations, highlighted in grey. (Figure courtesy of Dr Haiyan Zhou) (Jungbluth, 2007a)

The clinical symptoms of MmD can vary highly depending on the genetic background. In general, MmD usually has an early childhood or infancy onset with hypotonia and proximal weakness up to reduced prenatal fetal movements and polyhydramnios. Rare cases with an adult onset are reported which results occasionally in respiratory or cardiac failure. The classical clinical feature of MmD are spinal rigidity, scoliosis and respiratory impairment. Also, axial muscle weakness and muscle wasting is prominent and the proximal muscle groups are generally more affected then distal muscles, particular those of the shoulder girdle. Aside the classic MmD, MmD can be further divided into three additional groups based on the clinical symptoms: a severe prenatal form with arthrogryposis multiplex congenita; a moderate form with hand involvement and an MmD form with eye muscle involvement, specifically with ophthalmoplegia. The classic MmD is mostly due

to recessive mutations in the *SEPN1* gene while the MmD with ophthalmoplegia is caused by recessive *RYR1* mutations and not a feature of *SEPN1* mutations. Also, respiratory impairment is usually milder than in the classic form. Another unique feature of MmD caused by *RYR1* mutations is the potential risk of MHS (see next paragraph) which is not the case for *SEPN1* mutations. (Jungbluth, 2007a; Jungbluth et al., 2011, 2018).

The histopathology of MmD can be as heterogenous as the clinical symptoms and reflects the heterogenous gene involvement. In general, MmD muscle biopsies show multifocal, well-circumscribed areas with reduction of oxidative staining and low myofibrillar ATPase. In comparison to CCD, the cores only extend a short distance along the fiber axis, can affect type 1 and type 2 fibers and are typically unstructured. *SEPN1* related MmD shows numerous small lesions (“minicores”), sometimes less defined so that they appear as uneven stains. *RYR1* related MmD on the other hand typically shows multiple larger lesions (“multicores”). (Figure 1.27: Histopathology of multi-minicore disease) (Jungbluth, 2007a; Jungbluth et al., 2011)

Currently there is no curative treatment available for core myopathies, CCD and MmD and patient management is mainly supportive (Jungbluth et al., 2011).

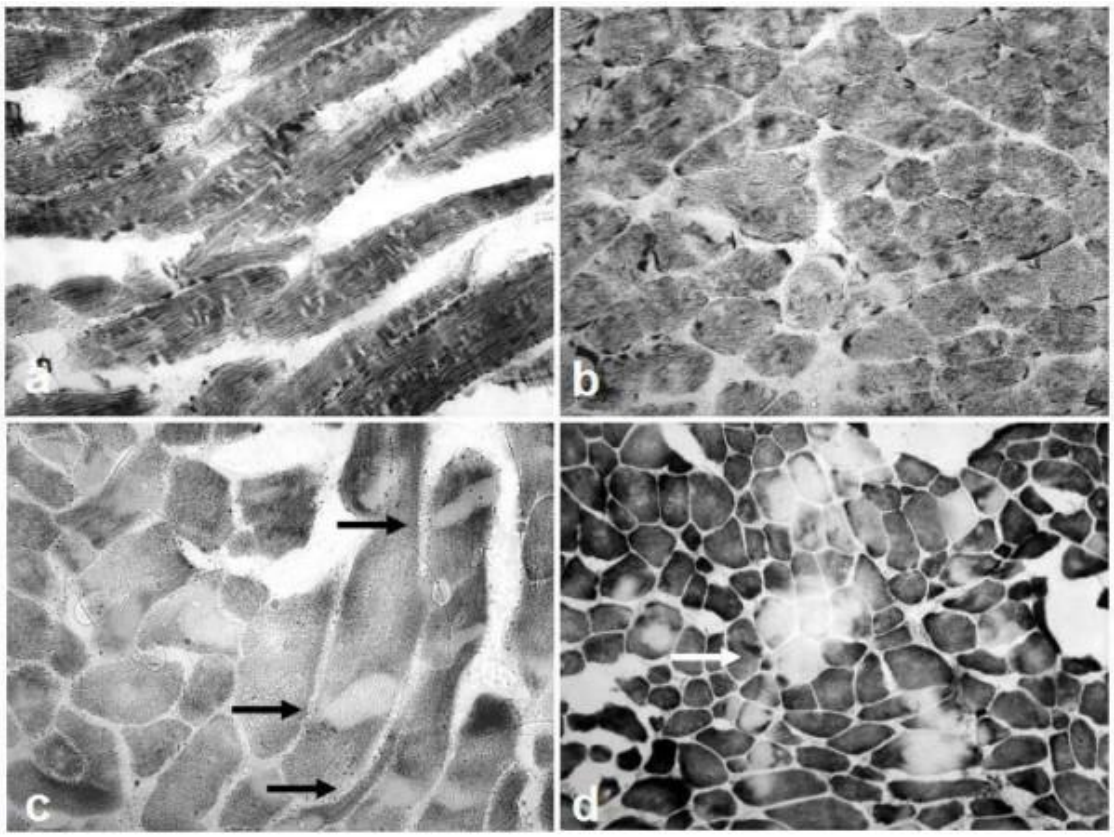

Figure 1.27: Histopathology of multi-minicore disease

NADH-TR **(a–c)** and cytochrome oxidase (COX) **(d)** stains, horizontal **(a,c)** and transverse **(b,d)** sections of muscles from a 3-year-old **(a–b)** and a 9-year-old girl **(c–d)** from different families. Numerous small lesions ("minicores") of limited extent can be seen in a and b. Larger lesions ("multicores") throughout the entire fiber diameter are found in c (arrows) and d, which can occasionally affect the same area in adjacent fibers (arrows in d). (Jungbluth, 2007a)

1.3.5.3 Malignant Hyperthermia

Unlike the above-mentioned diseases, malignant hyperthermia susceptibility (MHS) is a pharmacogenetic disorder inherited in an autosomal dominant way. It is triggered by volatile halogenated anesthetic (e.g., halothane) and muscle relaxants (e.g., succinylcholine). The so caused episodes of MHS are typically rapid and life-threatening if left untreated. An MH crisis is characterized by a rapid increase in body temperature, muscle contractures, leading to organ failure and death. The physiological reason is a Ca^{2+} leak from the SR through the mutated RyR1

causing the muscles to contract resulting in a hypermetabolic state and leading to metabolic acidosis. An acute episode can be stopped and treated by dantrolene which inhibits the Ca^{2+} leak from the RyR1. More than 150 *RYR1* point mutations have been identified in humans. An MH reaction occurs 1:50 000–100 000 anesthetized adults and 1:15 000 anesthetized children. MH susceptibility (MHS) was originally tested using the in-vitro contraction test (IVCT) (Lanner et al., 2010; Rosenberg et al., 2015; Santulli et al., 2017a, 2018) but now this is often replaced by genetic testing.

1.3.5.4 Centronuclear Myopathy

Centronuclear myopathy (CNM), as the name suggest, is characterized histologically by numerous centrally and multiple located nuclei. Genetically it is more diverse then the other congenital myopathies. The most severe form of CNM is the X-linked recessive form with patients carrying mutations in the myotubularin gene *MTM1* (X-linked myotubular myopathy, XLMTM). Other more mild forms of CNM are associated with autosomal dominant mutations in dynamin 2 (*DNM2*) and amphiphysin II (*BIN1*), and autosomal recessive mutations in *RYR1*, *BIN1* and *TTN* (Jungbluth et al., 2018).

While the central and multiple nuclei are predominant histopathological characteristics, other changes can appear over time (Figure 1.28: Histopathology of CNM). These include central zones with either accumulation or absence of oxidative enzyme activity (visualized by NADH staining), radial strands surrounding the central zone in many fibers, and type 1 fiber predominance and hypotrophy (Treves et al., 2008a). Histopathological differences can be found depending on the mutated gene (Jungbluth et al., 2018).

The clinical symptoms of CNM can be as diverse as their mutations but one clinical feature that almost all CNM patients have in common (except patients with *TTN* mutations) is that they show extraocular muscles involvement.

XLMTM, the most severe form, manifests at birth and typically affect males, due to the fact that it is X- linked. Affected children are severely hypotonic, show weak and contractured muscles. Respiratory involvement is prominent, and patients often require supportive ventilation.

CNM caused by dominant mutations in *DNM2* or *BIN1* are usually milder. Recessive *RYR1* CNM has a substantial clinical overlap with MmD (Jungbluth et al., 2018).

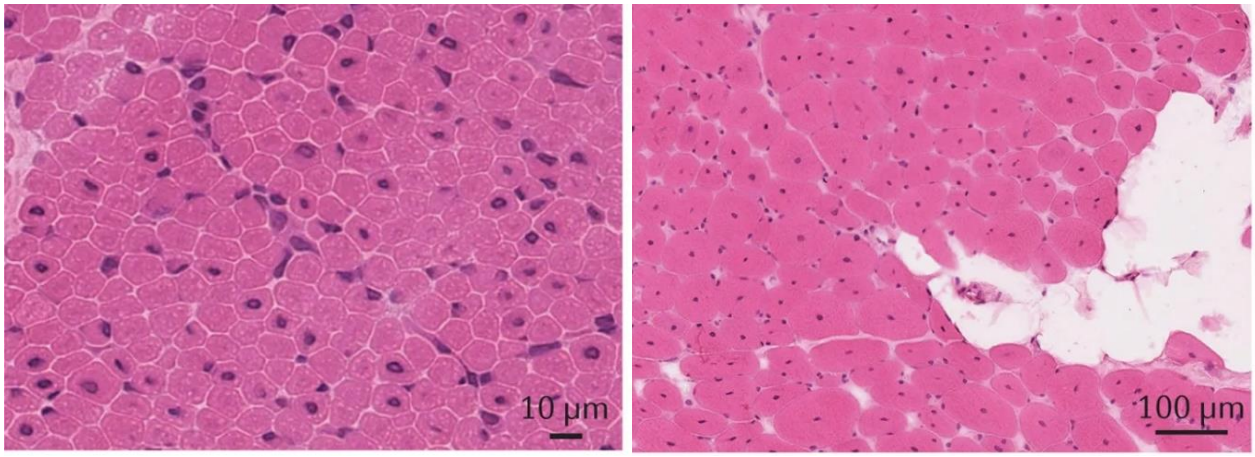

Figure 1.28: Histopathology of CNM

Hematoxylin and eosin staining of muscle biopsies from a male neonate with X-linked recessive myotubular myopathy **(Left)** and an adult with DNM2-related CNM **(Right)**. The CNM typical centrally placed nuclei can be seen in both biopsies. The DNM2-related CNM shows additional perimysial fatty infiltration. (Jungbluth et al., 2018)

1.3.5.5 Other Congenital Myopathies

There are many more congenital myopathies besides those described in this section. Thus, the purpose of this sub-section is to mention additional congenital myopathies without going into details.

Nemaline myopathy (NEM) is named because of the characteristic inclusion bodies, nemaline bodies (greek nema is thread) in the muscles. NEM patients suffer from muscle weakness and hypotonia from the neonatal period on but also late onset cases have been reported. While more than ten genes are mutated in patients with NEM, the most common mutations are dominant mutations in *ACTN1*.

Congenital fiber type disproportion (CFTD) is a more rare disease. Patients also show muscle weakness and hypotonia and the histopathological characteristic is that type 1 fibers are substantially smaller than type 2. Genes which are associated with CFTD are *TPM3*, *RYR1*, *ACTA1*, *SEPN1* and *MYH7*. (Jungbluth et al., 2018)

2 RESULTS

2.1 Introduction

Extraocular muscles are a highly specialized muscle group and their clinical relevance becomes apparent in the context of diseases like strabismus, laryngeal dystonias and facial paralysis where they play a key role. But maybe even more interesting is that EOMs are spared in some neuromuscular disease and congenital myopathies while heavily affected in others (Jungbluth et al., 2011). Even though most papers in the literature focus on EOM corrective surgery or of EOM histopathology, little is known about function at the molecular level. Recently our group investigated Ca^{2+} homeostasis at different points of maturation of human extraocular muscles (Sekulic-Jablanovic et al., 2015, 2016b). While these studies brought light to the expression of transcripts and proteins involved in muscle ECC, they only investigated the regulation of Ca^{2+} homeostasis at the level of myotubes, precursor cells of muscle fibers and biochemical studies were limited to small human muscle biopsies.

This novel study was therefore undertaken to overcome these limitations and study Ca^{2+} homeostasis of EOMs in isolated single muscle fibers from mice. Even though human samples are scarce but more interesting than samples from mice, when it comes to EOM this is not the full truth. In fact, since human samples come from corrective surgery most of the fibers are cut and/or broken due to the surgical procedure and to the priority given to the patient ‘s well- being rather than the condition of the biopsy for research. Therefore, such biopsies cannot be used for functional force measurements or single fiber studies. The same holds true for muscle biopsy from an organ donor. But muscle biopsies are a good source of satellite cells which can be differentiated in vitro into myotubes and thus they were used in the first studies of our research group to start characterizing the biochemical and physiological characteristics of human EOMs.

On the other hand, EOMs from mice are more easily available then human samples and it is possible to use the available or new disease models to study the impact of specific mutations or gene ablation on EOM function.

One should keep in mind however, that EOMs from mice are quite small, ca. 4-5 mm in length and a fraction of a millimeter thick (from my own observation), compared to human samples or even to the commonly studied mouse muscles EDL and soleus. Murine EOMs are located in and surrounded by the orbit, a bone cavity in the skull (Figure 1.6 Anatomy of human extraocular muscle). This makes it difficult to isolate intact EOMs from mice. If someone wants to measure force on EOMs, they are facing another problem, they do not have a classical tendon. On one side the six EOMs merge into a tendinous ring, annulus of Zinn, and on the other side they enter more less directly the sclera. This makes classical ligation on the tendon as with EDL or soleus not possible.

Beside the general challenges encountered when assessing EOM force, I also faced great difficulties when isolating single fibers from the EOMs, a step which is necessary in order to carry out calcium measurements. Regular collagenase digestion mixes like the ones used for FDB or EDL fiber isolation do not work for EOMs. Compared to FDBs, EDLs or soleus muscles EOMs have a higher relative amount of connective tissue which has a different biological composition. For example: the pulley ring contains high levels of elastase as well as smooth muscle cells. So the digestion mix und isolation method needed to be adjusted accordingly.

Therefore, in the beginning my effort focused on overcoming the above-mentioned challenges and develop and optimize methods to measure force on EOMs and isolate single EOM fibers to study Ca^{2+} kinetic in individual fibers as well as to perform immunohistochemistry. The goal was to use these techniques to investigate the physiological properties of EOMs and understand how and why they are affected in some diseases.

In the first paper we used the new established methods to tie in with our paper "Characterization of excitation–contraction coupling components in human extraocular muscles" (Sekulic-Jablanovic et al., 2015). In fact, in the paper by Sekulic-Jablanovic et al we showed that RyR3 transcripts are highly upregulated in human EOMs compared to leg muscles. We confirmed this interesting upregulation in mouse EOMs and this constituted the starting point of our study of the physiological role of RyR3 in EOM. To conduct this, we used the RyR3 KO mouse that was created by Prof. Hiroshi Takeshima's group. Their studies had shown that RyR3 KO mice show no alteration in muscle development and no muscle impairment. Except for some cognitive

impairment and decreased social contact these mice have normal growth and reproductive capacities (Takeshima et al., 1996; Matsuo et al., 2009). This mirrors the idea that RyR3 is not directly involved in the EC coupling process. Since no one had ever investigated RyR3 in the context of EOMs the RyR3 KO mouse was a useful model and constitutes the basis of our paper "Extraocular muscle is impaired in ryr3$^{-/-}$ mice" (Eckhardt et al., 2019) . In this paper we were able to show an EOM impairment in the RyR3 KO mouse; this is the only muscle which shows a functional impairment in the absence RyR3.

In our second manuscript, which is currently under review, we moved from the more basic research of EOMs to disease models. It is well known that EOM involvement in congenital myopathies is predominantly associated with recessive *RYR1* mutations. We recently created the RyR1p.Q1970fsX16+p.A4329D double knock in (referable as DKI mice) based on the genotype of a severely affected child (Klein et al., 2012) . We were able to show that the general phenotype of the DKI mouse recapitulates the clinical picture of the patient: showing muscle cores, reduced force in EDL and soleus muscles, reduced RyR1 protein content, decreased electrically evoked Ca^{2+} transients (Elbaz et al., 2019a). Therefore, in this second paper we used this mouse model to study the effect of recessive *RYR1* mutations on the function of EOMs. We were able to show that muscles from this DKI mouse exhibit a tremendous force reduction and reduced electrically evoked Ca^{2+} transients. Another unique finding in the DKI mouse is the reduction, or better the almost absence, of MyH13, the EOM specific myosin heavy chain. Remarkably, these changes are specific to the DKI and not present in single heterogeneous *RYR1* mutant carriers nor in the mouse carrying the RYR1A4329D mutation at the homozygous state. In conclusion we unraveled the molecular basis of the functional defect of EOM in congenital myopathies carrying recessive *RYR1* mutations.

2.2 Paper 1

Extraocular muscle function is impaired in ryr3$^{-/-}$ mice.

***One sentence summary*:** RyR3s play an important role in extraocular muscles

Jan Eckhardt[1], Christoph Bachmann[1], Marijana Sekulic-Jablanovic[2], Volker Enzmann[3, 4], Ki Ho Park[5], Jianje Ma[5], Hiroshi Takeshima[6], Francesco Zorzato[1, 7]* & Susan Treves[1,7] *#

[1]Departments of Anesthesia and [2]Biomedicine, Basel University Hospital, Hebelstrasse 20, 4031 Basel, Switzerland; [3]Department of Ophthalmology, Bern University Hospital and Inselspital; [4]Department of Biomedical Research, University of Bern, Freiburgstrasse 14, 3010 Bern, Switzerland; [5]Department of Surgery, Davis Heart & Lung Research Institute, The Ohio State University Medical Center, Columbus, OH 43210, U.S.A.; [6]Graduate School of Pharmaceutical Sciences, Kyoto University, Kyoto 606-8501, Japan; [7]Department of Life Sciences, Microbiology and Applied Pathology section, University of Ferrara, Via Borsari 46, 44100 Ferrara, Italy.

*Contributed equally to this paper

[#] Correspondence and requests for materials should be addressed to S.T. (susan.treves@unibas.ch).

Published Online: 13 May, 2019 | Supp Info: http://doi.org/10.1085/jgp.201912333

JGP Journal of General Physiology

RESEARCH ARTICLE

Extraocular muscle function is impaired in *ryr3*$^{-/-}$ mice

Jan Eckhardt[1,2], Christoph Bachmann[1,2], Marijana Sekulic-Jablanovic[2], Volker Enzmann[3,4], Ki Ho Park[5], Jianjie Ma[5], Hiroshi Takeshima[6], Francesco Zorzato[1,2,7]*, and Susan Treves[1,2,7]*

Calcium is an ubiquitous second messenger mediating numerous physiological processes, including muscle contraction and neuronal excitability. Ca^{2+} is stored in the ER/SR and is released into the cytoplasm via the opening of intracellular inositol trisphosphate receptor and ryanodine receptor calcium channels. Whereas in skeletal muscle, isoform 1 of the RYR is the main channel mediating calcium release from the SR leading to muscle contraction, the function of ubiquitously expressed ryanodine receptor 3 (RYR3) is far from clear; it is not known whether RYR3 plays a role in excitation–contraction coupling. We recently reported that human extraocular muscles express high levels of RYR3, suggesting that such muscles may be useful to study the function of this isoform of the Ca^{2+} channel. In the present investigation, we characterize the visual function of *ryr3*$^{-/-}$ mice. We observe that ablation of RYR3 affects both mechanical properties and calcium homeostasis in extraocular muscles. These changes significantly impact vision. Our results reveal for the first time an important role for RYR3 in extraocular muscle function.

Introduction

RYRs are intracellular calcium channels mediating calcium release from ER/SR intracellular calcium stores (Takeshima et al., 1989; Zorzato et al., 1990). Three main isoforms of RYRs encoded by different genes sharing an overall amino acid identity of ∼65% have been identified in vertebrates (Ogawa et al., 2000; Meissner, 2017). In skeletal muscle, RYR1 is mostly located on the terminal cisternae junctional face membrane, where it is involved in excitation–contraction coupling (ECC), the process whereby a change in membrane potential is converted into calcium release, leading to muscle contraction (Endo, 1977; Takeshima et al., 1989; Zorzato et al., 1990; Ríos and Pizarro, 1991). RYR2 is predominantly expressed in the cardiac muscle SR, where it is activated by a process called CICR, leading to repetitive contractions of the heart (Bers, 2002). RYR3 is ubiquitously expressed on ER/SR membranes, with high levels of expression in the central nervous system, smooth muscle cells, and developing muscles (Giannini et al., 1992, 1995; Clark et al., 2010; Vaithianathan et al., 2010).

In skeletal and cardiac muscles, RYR1 and RYR2 are either directly coupled to or in close proximity to the dihydropyridine receptor (DHPR; Ríos and Pizarro, 1991; Franzini-Armstrong and Jorgensen, 1994; Protasi et al., 2000; Bers, 2002). A coupling partner has not been identified for RYR3, though it has been suggested that RYR3 may act as an amplifier and release Ca^{2+} by a CICR mechanism (Protasi et al., 2000; Yang et al., 2001). Lower vertebrates such as fish, frogs, and birds express both RYR1 (referred to as αRYR) and RYR3 (referred to as βRYR) in their skeletal muscles (Airey et al., 1990; Percival et al., 1994). In contrast to αRYRs, which are located on the junctional face membrane, βRYRs are expressed parajunctionally, where they cannot support ECC but are involved in the generation of Ca^{2+} sparks (Perni et al., 2015).

From a functional point of view, the three RYR isoforms share several biophysical properties, including activation by submicromolar [Ca^{2+}], calmodulin, ATP, and caffeine, as well as inhibition by micromolar [Mg^{2+}], low and high calmodulin, ruthenium red, and procaine. They also share similar units of conductance (Ogawa et al., 2000). Nevertheless, there are important differences, such as RYR3's increased resistance to inactivation by high concentrations of Ca^{2+} (Ogawa et al., 2000). From a physiological point of view, RYR3s are not essential, as reflected by the fact that *ryr3*$^{-/-}$ mice grow and reproduce

[1]Department of Anesthesia, Basel University Hospital, Basel, Switzerland; [2]Department of Biomedicine, Basel University Hospital, Basel, Switzerland; [3]Department of Ophthalmology, University Hospital of Bern, Bern, Switzerland; [4]Department of Biomedical Research, University of Bern, Bern, Switzerland; [5]Department of Surgery, Davis Heart & Lung Research Institute, The Ohio State University Medical Center, Columbus, OH; [6]Graduate School of Pharmaceutical Sciences, Kyoto University, Kyoto, Japan; [7]Department of Life Sciences, Microbiology and Applied Pathology section, University of Ferrara, Ferrara, Italy.

*F. Zorzato and S. Treves contributed equally to this paper; Correspondence to Susan Treves: susan.treves@unibas.ch.

normally and do not exhibit gross abnormalities in smooth muscle cell function (Takeshima et al., 1996). However, developing skeletal muscles from *ryr3*$^{-/-}$ mice exhibit reduced twitch amplitudes in response to electrical stimulation and caffeine addition, but the lack of RYR3 does not apparently impact the function of adult muscles (Bertocchini et al., 1997). Interestingly, *ryr3*$^{-/-}$ mice exhibit behavioral abnormalities, including increased locomotor activity, impaired performance in the water maze, and a mild tendency to circular running (Balschun et al., 1999).

Extraocular muscles (EOMs) are classified as a distinct muscle allotype when compared with limb and dorsal muscles. They are either selectively spared in certain congenital muscle diseases such as Duchenne muscular dystrophy or preferentially affected in conditions such as myasthenia gravis and mitochondrial myopathies, indicating that they are biochemically different from their limb muscle counterpart. EOMs have a unique embryonic origin, can be singly or multiply innervated, contain a large number of mitochondria, are highly vascularized, do not store glycogen, are fatigue resistant, and express distinct myosin heavy chain (MyHC) isoforms (Spencer and Porter, 1988; Hoh et al., 1989; Kaminski and Ruff, 1997; Porter et al., 2001; Ketterer et al., 2010; Zhou et al., 2010). Furthermore, they contain a population of preactivated satellite cells that continuously fuse into existing myofibers under "uninjured" conditions (McLoon and Wirtschafter, 2002a,b; Stuelsatz et al., 2015).

While investigating the biochemical and physiological characteristics of human EOMs, we reported that such muscles contain a distinct toolkit component of the proteins involved in ECC, as they express both $Ca_v1.1$ and $Ca_v1.2$ (the skeletal and cardiac isoform of the α 1 subunit of the DHPR, respectively), calsequestrin 1 and 2, RYR1, and RYR3, resulting in distinct intracellular calcium homeostasis properties (Sekulic-Jablanovic et al., 2015). In the present study, we used the *ryr3*$^{-/-}$ mouse model to investigate the function of RYR3 in EOMs. Our data show that constitutive ablation of RYR3 significantly affects both the mechanical properties of mature EOMs and calcium homeostasis, and we propose that these changes are responsible for the impaired visual functions of *ryr3*$^{-/-}$ mice.

Materials and methods

Animal model and ethical permits

The *ryr3*$^{-/-}$ mouse model was generated by Takeshima et al. (1996). Experiments were performed on 8–12-wk-old mice. All experimental procedures were approved by the Cantonal Veterinary Authorities (BS Kantonales Veterinäramt permit numbers 1728 and 2115 and BE Kantonales Veterinäramt BE32/15). All experiments were performed in accordance with relevant guidelines and regulations.

Assessment of visual acuity by the Morris water maze task

Visual acuity was tested using the cued Morris water maze (Enzmann et al., 2006; Zulliger et al., 2011). A round gray tank of 1.7-m diameter filled to a height of 30 cm with water at room temperature (23 ± 1°C) was used. The water was made opaque by the addition of nontoxic white paint. A video camera fastened above the center of the pool recorded the swimming pattern of the mice using a video tracking system (Ethovision XT11; Noldus Information Technology). The water surface was virtually divided into four quadrants, and there were four entry zones to the pool. A white, round platform with a diameter of 20 cm was placed in one quadrant at a distance of 50 cm from the border and 1.5 cm above the water surface. Four entry zones were marked outside the pool. The room was illuminated at an intensity of <150 Lux. Animals were transferred to the experimental room 72 h before the experiments in order to acclimatize them. The light in the room was switched on at 6 a.m., and the mice were exposed to 12-h light/dark cycles. Mice were provided with water and food ad libitum. On day 0, mice performed a habituation run, swimming for 60 s in the water maze. On day 1, mice performed four trials with the platform at a fixed position and varying each of the four entry zones; the test duration was 60 s per run. If the mice did not find the platform after 60 s, then they were guided to it by hand and allowed to stay on it for 10 s. On day 2, the tests were repeated similarly to day 1, except that the platform was moved in the opposite quadrant. The following parameters were evaluated: swimming velocity, total distance moved, and time to reach the platform. The results are presented as average per experimental group, per day. Heat maps showing the relative combined traces of the mice for each group were generated using Ethovision.

Optokinetic reflex (OKR)

The OptoMotry System from CerebralMechanics was used to measure the OKR as previously described (Prusky et al., 2004; Thomas et al., 2004). Briefly, a virtual cylinder comprising a vertical sine wave grating was projected in 3-D coordinate space on computer monitors (17" LCD computer monitors, model 1703FP; Dell) arranged in a square around and projecting to the testing area, consisting of a platform positioned 13 cm above a mirrored floor under a likewise mirrored lid. To record the behavior of the mice, a video camera (DCR-HC26; Sony) was positioned directly above the platform and connected to a computer, allowing live video feedback. The computer was also used to project the virtual cylinder on the monitors in a 3-D coordinated space, controlling the speed of rotation and geometry of the cylinder and spatial frequency of the stimuli. The image on the monitors was expanded by the mirrors on the floor and the ceiling, thereby creating a virtual 3-D world. To measure under scotopic conditions, light levels were attenuated with cylindrical neutral density filters (R211 0.9ND; LEE Filters) inside the tracking area, thereby reducing the ambient light in the testing area to a luminance level of −4.5 log cd m^{-2}.

During testing, the mice stood unrestrained on the platform tracking the 3-D pattern with a reflexive head movement. The movements of the mice on the platform were followed by the experimenter with a crosshair superimposed on the video image to center the rotation of the virtual cylinder with the x–y positional coordinates of the crosshair at the mouse's viewing position, maintaining the pattern at a constant distance from the animal. Mice normally stopped moving when a grating perceptible to them was projected onto the cylinder wall and the

cylinder was rotated and began tracking the pattern with reflexive head movements in concert with the rotation. The decision of whether the mouse tracked the pattern or not was made by the experimenter based on evident head movement against the stationary arm of the crosshair. Animals that slipped or jumped off the platform during the test trial were returned to the platform, and testing was continued. The measurements were always made in the morning, and all animals were acclimated to the testing by placing them on the platform for a few minutes without testing. Two independent experimenters were blinded both to the genotype and to previous records.

Electroretinography

Mice were dark-adapted overnight. The animals were then anesthetized using 80 mg/kg ketamine (Ketalar 50 mg/ml; Pfizer AG) and 1 mg/kg medetomidine (Domitor; Orion Pharma). Pupils were dilated at the time of anesthesia by topical instillation of 2.5% phenylephrine + 0.5% tropocamide (MIX-Augentropfen; ISPI), and oxybuprocaine (Oxybuprocaine 0.4% SDU Faure; Thea Pharma) was used for additional local anesthesia. The anesthetized mice were positioned in the recording apparatus (Ganzfeld stimulator Q400; Roland Consult). The scotopic electroretinogram was elicited at different light intensities (−25, −20, −10, 0, +10, and +15 dB). Eight flashes (256-ms duration) were presented at 0.1 Hz with a 20-ms interval, and the responses were averaged. A- and B-wave amplitudes were quantified using the RETI-port/scan 21 analysis tool (Roland Consult). The anesthesia was revoked by injection of 2.5 mg/kg atipamezole (Antisedan; Orion Pharma), but never before 30 min after initiation of the anesthesia.

Isometric force measurements

Isolated EOMs were mounted intact on a MyoStation (Myotronic). The force transducer was equipped with small hooks. One of the rectus muscles, mainly medial, was tied with a prolene suture (EP8703H; Ethicon) by stitching through the eyeball close to the entry point of the muscle. The other side was ligated on the left over the orbital socket bone with a surgical suture (SP102; Look). After ligation, the remaining EOMs, the optic nerve, and the retractor bulbi muscle were surgically removed. For the force measurements, EOMs were stimulated with a single pulse of 0.5 ms and of 24.6 V. Experiments were performed at 30°C. Muscle force was digitized at 4 kHz using an ADInstruments. Results were analyzed using the principal-component analyses (Hwang et al., 2013) included in the OriginPro 2017 (OriginLab Corp) software package.

Quantitative real-time PCR

Total RNA was extracted from the EOMs using Trizol (15596–018; Invitrogen) following the manufacturer's protocol. After treatment of the RNA with deoxyribonuclease I (18068–015; Invitrogen), 1,000 ng was reverse transcribed using the high-capacity complementary DNA (cDNA) Reverse Transcription kit (4368814; Applied Biosystems). cDNA was amplified by quantitative real-time PCR using Power Sybr Green Master Mix (4367659; Applied Biosystems) as previously described (Sekulic-Jablanovic et al., 2015, 2016). The sequence of the primers used for quantitative PCR (qPCR) is given in Table S1. qPCR was performed on a 7500 Fast Real-Time PCR machine from Applied Biosystems using 7500 software v2.3. Gene expression was normalized to expression *ACTN2*, which is present in all muscle fiber types. Results are expressed as fold change of gene expression in *ryr3*$^{-/-}$ mice compared with its expression in WT mice, except for when the vales of RYR1 and RYR3 were compared in EOMs from WT mice, in which case the value of RYR3 was set to 1.

Electrophoresis and immunoblotting

Total muscle homogenates were prepared form flash-frozen EOM samples in 10 mM HEPES, pH 7.0, 150 mM NaCl, 1 mM EDTA, and anti-protease (11873580001; Roche) as previously described (Sekulic-Jablanovic et al., 2015, 2016). Protein concentration was determined using a Protein Assay Kit II (5000002; Bio-Rad Laboratories), and BSA was used as a standard. SDS-PAGE, protein transfer on to nitrocellulose membranes, and immunostaining were performed as previously described (Sekulic-Jablanovic et al., 2015), except for parvalbumin. In the latter case proteins were separated on a 10% Tris-Tricine gel (Schägger and von Jagow, 1987) and subsequently transferred onto nitrocellulose. The following primary antibodies were used for Western blotting: rabbit anti-RYR1 (8153S; Cell Signaling), goat anti-$Ca_v1.1$ (sc-8160; Santa Cruz), rabbit anti-$Ca_v1.2$ (sc-25686; Santa Cruz) rabbit anti-calsequestrin-1 (C-0743; Sigma) and calsequestrin-2 (ab-3516; Abcam), goat anti-SERCA1 (sc-8093; Santa Cruz), goat anti-SERCA2 (sc-8095; Santa Cruz), mouse anti-MyHC (05–716; Millipore), mouse anti-MyHC13 (4A6; DSHB Iowa), rabbit anti-Desmin (sc-14026; Santa Cruz) and rabbit anti-parvalbumin (PV25; Swant), and rabbit anti-JP-45 (Zorzato et al., 2000). Secondary peroxidase conjugates were Protein G-peroxidase (P8170; Life Technologies) and peroxidase-conjugated goat anti-mouse IgG (A2304; Sigma). The immunopositive bands were visualized by chemiluminescence using the WesternBright ECL-HRP Substrate (K-12045-D50; Advansta) or the Chemiluminescence kit from Roche (11500694001; Roche) on a Vilber Fusion Solo S system. Statistical analysis of the intensity of the immunopositive bands was determined using ImageJ/FIJI (Schindelin et al., 2012). The intensity values were normalized to the intensity of the indicated skeletal muscle-specific protein.

Single-fiber isolation

Mice were sacrificed with a Pentobarbital overdose, their hearts were cannulated, and the circulatory system was washed with mammalian Ringer buffer (137 mM NaCl, 5.4 mM KCl, 1 mM $MgCl_2$, 0.1% glucose, and 11.8 mM HEPES, pH 7.4). Subsequently, 17 ml of a collagenase cocktail prepared in modified mammalian Ringer buffer (137 mM NaCl, 5.4 mM KCl, 0.5 mM $MgCl_2$, 1.8 mM $CaCl_2$, 0.1% glucose, and 11.8 mM HEPES, pH 7.4) containing 20 mg collagenase type I (*Clostridium histolyticum* type I, C0130; Sigma), 6 mg collagenase type 2 (LS004176; Worthington Biochemical Corporation), and 2.5 mg Elastase (LS002294; Worthington Biochemical Corporation) was injected into the circulatory system. EOMs were removed under a dissecting microscope and further digested in a small Erlenmeyer flask

containing 0.2% collagenase type 2 and 0.1% Elastase, in mammalian Ringer for 70 min at 37°C, 5% CO_2. At the end of the digestion, fibers were gently separated from the tendons by passing them through progressively narrower pipette tips.

Immunofluorescence

Isolated EOM fibers were pipetted onto laminin and collagen-coated Ibidi µ-Slide 4 well or µ-Slide 8 well chambers (#80426 and #80826). The fixation and permeabilization steps depended on the antibody being used. For $Ca_v1.1$ and $Ca_v1.2$, 4% paraformaldehyde (made in PBS) was used as a fixative and 1% Triton in PBS for permeabilization and processed as previously described (Treves et al., 2011). For RYR1 and $Ca_v1.1$ staining, fibers were fixed in ice-cold (−20°C) methanol for 15–30 min and permeabilized in 2% Triton in PBS for 20–30 min. After staining with the appropriate secondary antibodies, the fibers were incubated with 4′,6-diamidino-2-phenylindole (DAPI) to visualize the nuclei. The following primary and secondary antibodies were used: rabbit monoclonal anti-RYR1 (D4E1, #8153; Cell Signaling), mouse monoclonal anti-$Ca_v1.1$ (IIC12D4 and IIID5E1; Iowa Hybridoma bank), rabbit anti-$Ca_v1.2$ (sc-25686; Santa Cruz), Alexa Fluor 568 donkey anti-mouse IgG (A10037; Invitrogen), and Alexa Fluor 488 chicken anti-rabbit IgG (A21441; Invitrogen). A Nikon A1R confocal microscope with a 60× oil-immersion Plan Apo VC Nikon objective (numerical aperture, 1.4) was used to make the images (Lopez et al., 2016).

Single-fiber calcium measurements

All measurements were performed at room temperature. The resting Ca^{2+} fluorescence in single fibers was measured on glass-bottom culture dishes (P35G-0-14-C; MatTek) using the ratiometric calcium indicator fura-2 AM (F1201; Invitrogen; Treves et al., 2011; Sekulic-Jablanovic et al., 2015, 2016). For electrically evoked Ca^{2+} transients, isolated EOM fibers were allowed to settle on laminin (L2020; Sigma) and collagen-coated µ-Slide 4 well from Ibidi. Fibers were incubated for 20 min at 20°C in Ringer's solution containing 10 µM of the low-affinity calcium indicator Mag-Fluo-4 AM (M14206; Invitrogen; Hollingworth et al., 2009). Custom-designed 3-D-printed electrodes were used to stimulate the fibers with a 0.5-ms bipolar pulse using a computer-controlled stimulator (MyoDat+ Stimulator Amplifier; Myotronic). A Nikon A1R laser-scanning confocal microscope (Nikon Instruments) with a 60× oil-immersion Plan Apo VC Nikon objective (numerical aperture, 1.4) in resonant mode at super-high temporal resolution (7,918 lps) was used to record the linescans. For spark measurements, fibers were loaded with 5 µM Fluo-4 (F14217; Invitrogen), and experiments were performed as previously described (Lopez et al., 2016).

Myotube isolation and calcium measurements

Isolated EOMs were minced into small fragments. Satellite cells contained within the fragments were allowed to grow on laminin-coated glass bottom culture dishes (P35G-0-14-C; MatTek Corporation) in growth medium (DMEM plus 4.5 mg/ml glucose, 10% horse serum, 5 ng/ml insulin, 200 mM glutamine, 600 ng/ml penicillin G and streptomycin, and 7 mM HEPES, pH 7.4), and once a sufficient number of myoblasts had grown, the culture medium was switched to differentiation medium (DMEM plus 4.5 mg/ml glucose, 0.5% BSA, 10 ng/ml epidermal growth factor, 0.15 mg/ml creatine, 5 ng/ml insulin, 200 mM glutamine, 600 ng/ml penicillin G and streptomycin, and 7 mM HEPES, pH 7.4) to obtain myotubes, as previously described (Sekulic-Jablanovic et al., 2015). The resting calcium concentration and the total amount of rapidly releasable Ca^{2+} stores were measured using the ratiometric calcium indicator fura-2 AM as previously described (Sekulic-Jablanovic et al., 2015, 2016). For measurements of myotube calcium oscillations and sparks, cells were loaded with 5 µM Fluo-4 as previously described (Sekulic-Jablanovic et al., 2015, 2016) and experiments were performed at room temperature.

Analysis of calcium transients

Linescans were saved as stacked images using the microscope software (NIS-Elements, version 4.60). A plug-in for Icy (de Chaumont et al., 2012) was written to concatenate the linescans and calculate their profiles in one step. The plugin has the possibility of adding regions of interest and performing calculations on the regions of interest. For analysis of the peak Ca^{2+} and Ca^{2+} kinetics in fibers and myotubes a Ca^{2+} analysis program in Microsoft's .net Framework (https://visualstudio.microsoft.com) was designed. The analysis of the Ca^{2+} peaks for fibers and myotubes is similar but not identical; the fiber profile files contain only one transient, and the program requires information only on the number of header columns contained within the file. The myotube profiles are larger since they contain multiple transients. Therefore, the program requires an additional file (Peak-Summary) to analyze their profiles, containing, among other information, data relative to the beginning, the end, and the location of the maximum value of each peak within the profile. The Peak-Summary files were created in OriginPro 2018 by a batch peak search of the raw data.

For analysis of the Ca^{2+} transient, the baseline was calculated as the average of the first 5 ms of the profile. Once the maximum height of the transient was reached, the ΔF/F was calculated. The beginning of the peak was defined as the time where the transient increased by 5% of the maximum height, with respect to the baseline, for the first time. Time to peak (TTP) is the time from the beginning of the peak to the maximum height. Time to half peak (TTHP) is the time from the beginning of the peak to the time where the transient increases by 50% of the maximum height with respect to the baseline for the first time. Half relaxation time (HRT) is the time from the maximum height until the time where the transient is higher than 50% of the maximum height, for the last time. These parameters were calculated by the Ca^{2+} analysis program. For an automated kinetic analysis of the fiber transient, a Savitzky–Golay smoothing with polynomial order of 2 and window size of 12 was applied, while the ΔF/F calculations were done on the raw data. Savitzky–Golay smoothing is known for preserving the area, position, and width of peaks better than a moving average filter (Guiñón et al., 2007; Ostertagova and Ostertag, 2016).

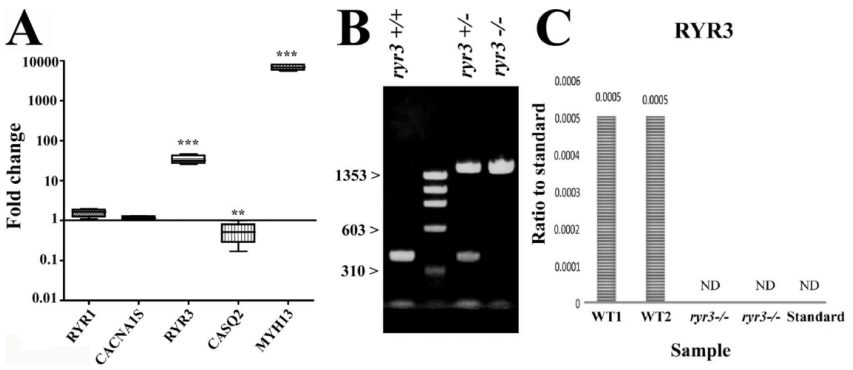

Figure 1. ***RYR3* is expressed in murine EOM. (A)** Expression of ECC transcripts in mouse EOM muscles. Transcript levels were quantified by qPCR in muscles from three WT mice (performed twice in triplicate). Values are plotted as mean (SEM) change in EOM vs. hindlimb muscles, which was set as 1. **, P < 0.01; ***, P < 0.001, Student's *t* test. Primers used are detailed in Table S1. **(B)** Genotyping WT and *ryr3*$^{-/-}$ mice using the primers detailed in Table S1; PCR amplification of genomic DNA from the *ryr3*$^{-/-}$ mouse yields a DNA fragment that is >1,000 bp larger than that of WT mice, compatible with the insertion of a >1,000-bp cassette in exon 1. Amplification of genomic DNA from heterozygous mice shows the presence of the smaller WT allele and the larger allele containing the inserted cassette. **(C)** Mass spectrometry analysis of EOMs from two WT and two *ryr3*$^{-/-}$ mice shows the absence of RYR3. ND, not detectable.

Statistical analysis and graphical software

Statistical analysis was performed using the unpaired two-tailed *t* test for equal variance and the unpaired two-tailed Welch's *t* test for unequal variance and unequal sample size. Means were considered statistically significant when the P value was <0.05. Data were processed, analyzed and plotted using the software OriginPro 2018 (OriginLab Corporation). Images were assembled using Adobe Photoshop CS (version 8.0).

Online supplemental material

Fig. S1 shows that retinal morphology and layer structure is unaltered in *ryr3*$^{-/-}$ mice. Fig. S2 shows photomicrographs of myotubes from EOM. Table S1 lists primers used for qPCR and for mouse genotyping. Table S2 lists kinetic properties of isolated EOM from WT and *ryr3*$^{-/-}$ mice. Video 1 shows a WT mouse swimming in a cued water maze. Video 2 shows a *ryr3*$^{-/-}$mouse swimming in a cued water maze.

Results

ryr3$^{-/-}$ mice have a defect in their visual acuity, and isolated muscles exhibit altered kinetic parameters

Mouse EOMs are similar to their human counterpart in that they express high levels of *RYR3* compared with limb muscles (Fig. 1 A); the ratio of RYR1 to RYR3 in WT mouse EOMs was assessed by qPCR and found to be 323 ± 65 to 1 (mean ± SEM, *n* = 4). We used *ryr3*$^{-/-}$ transgenic mice to evaluate the function of RYR3 in eye muscles. The total body *ryr3*$^{-/-}$ mouse line used in the present investigation was created by conventional gene targeting and was previously characterized by Takeshima et al. (1996). The presence of a cassette of ∼1,000 bp disrupting exon 1 of the genomic *RYR3* DNA was confirmed by PCR amplification (Fig. 1 B), and the absence of RYR3 protein was confirmed by mass spectrometry analysis (Fig. 1 C).

To assess visual function in WT and *ryr3*$^{-/-}$ mice, we used complementary noninvasive parameters, namely the cued water maze and the OKR test (Prusky et al., 2004; Thomas et al., 2004; Zulliger et al., 2011). The Morris water maze is a standard method used to assess spatial learning in rodents (Thomas et al., 2004; Zulliger et al., 2011). In one of its versions, animals need to locate a visible platform and are subsequently scored according to the total swimming distance and time required to identify the platform. Thereby, the animal relies on visual information to locate a platform. This test is often used to control for visual ability (Brown and Wong, 2007). As shown in Fig. 2 A and Videos 1 and 2, *ryr3*$^{-/-}$ mice performed significantly worse than age-matched WT mice. In particular, the mean swimming distance necessary to find the platform was increased by ∼50%, and the mean time taken to find the platform was increased by ∼30% (Fig. 2 A). Qualitatively similar results were obtained when visual acuity was assessed using the OptoMotry detection system, a simple and precise method for quantifying mouse vision (Prusky et al., 2004). It assesses the OKR, an involuntary fixation on objects that are moving in relationship to the head. The eyes have the tendency to track moving objects for a distance and then subsequently saccade in the opposite direction to reacquire a target. Saccades rely on EOMs to move the eyes the correct distance in the appropriate direction (Purves et al., 2001). In the OptoMotry detection system, unrestrained mice are placed on a central platform inside a virtual 3-D cylinder, and the reflective head movements in response to changes in the spatial frequency movement of a grid are scored (Thomas et al., 2004). The top panel of Fig. 2 B shows a schematic representation of the test setup (reproduced with permission from Prusky et al., 2004), and the bottom panel shows the results obtained in individual male and female mice. As shown in the figure, the visual acuity of *ryr3*$^{-/-}$ mice was decreased by ∼20% compared with WT mice. The

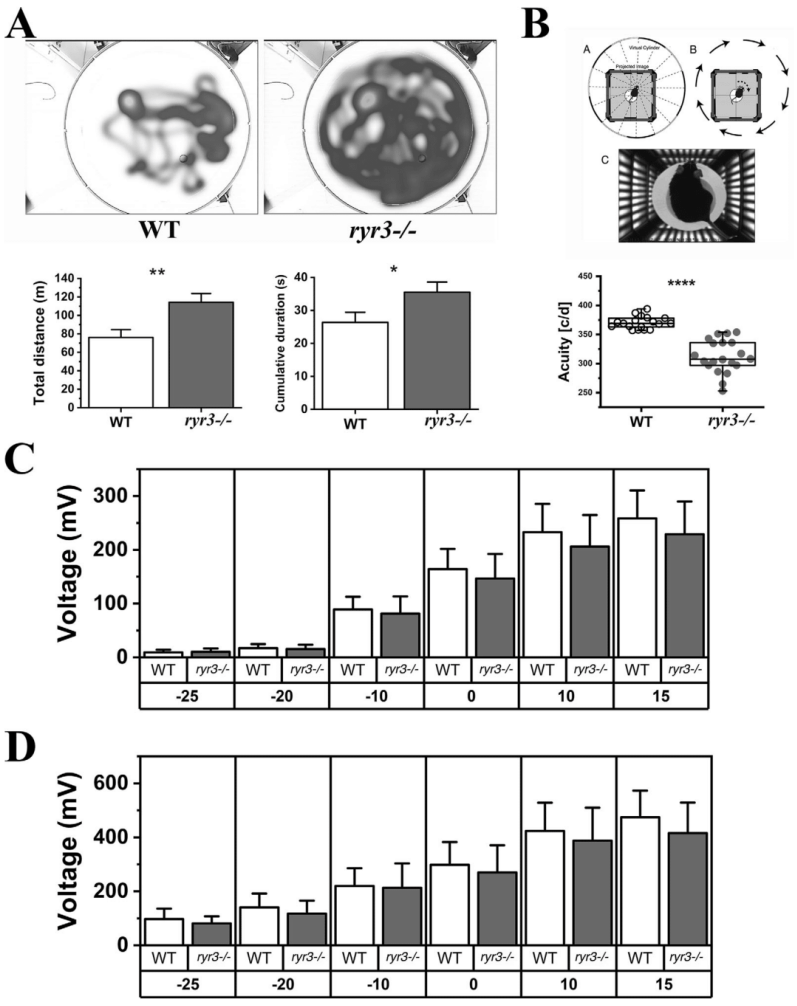

Figure 2. ***ryr3*$^{-/-}$ mice exhibit visual impairment. (A)** Cued water maze. Top: Representative heatmaps of the swimming path of WT (left) and *ryr3*$^{-/-}$ (right) mice. Bottom left: Total swimming distance (mean ± SEM) required to reach the platform. Bottom right: Time required to reach the platform. Experiments were performed on 10 mice per strain, and data from four different pool entry points were combined. **(B)** OKR. Top: OptoMotry setup. From Prusky et al. (2004), Fig. 2 B is reprinted with permission from *Investigative Ophthalmology & Visual Science*. Bottom: Visual acuity of two independent measurements performed under scotopic conditions on each mouse. Each symbol represents the visual acuity of a single mouse; empty circles, WT mice (n = 20); gray circles, *ryr3*$^{-/-}$ mice (n = 20). The unit of visual acuity is cycles/degree (c/d). **(C and D)** Scotopic ERG results of n = 9 WT (empty boxes) and n = 10 *ryr3*$^{-/-}$ (gray boxes). Amplitude (in millivolts) of A-waves (C) and B-waves (D); the x axes represent the intensity of the illuminating flash. *, P < 0.05; **, P < 0.005; ****, P < 0.0001, Student's *t* test.

results shown in Fig. 2 were obtained by pooling male and female mice, which were similar in their response. The decrease in visual capacity of *ryr3*$^{-/-}$ mice was not caused by alterations of the retinal function, since the electroretinogram under scotopic conditions was similar in WT and *ryr3*$^{-/-}$ mice (Fig. 2, C and D). The decrease in visual capacity was also not caused by alterations in the structure of the retina as a consequence of *RYR3* ablation, since no changes were observed in retinal thickness, spatial distribution, and appearance of the different layers constituting the retina (Fig. S1). Taken together, these results show that in vivo, *ryr3*$^{-/-}$ mice have an alteration of their visual capacity, but they do not discriminate whether the problem is of neuronal origin or relates to skeletal muscle function.

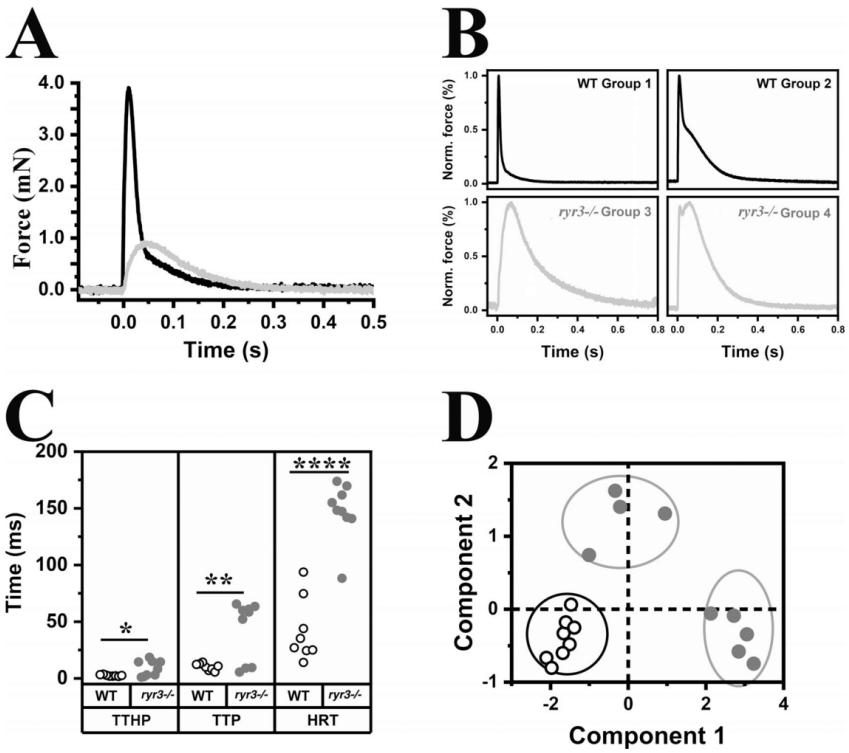

Figure 3. **Ex vivo isometric force measurements in mouse EOMs. (A)** Representative trace of the absolute twitch force obtained from isolated single extraocular rectus muscles from WT (black line; *n* = 8) and *ryr3*$^{-/-}$ (gray line, *n* = 9) muscles. Muscles were stimulated by electric field stimulation with a pulse of 24.6 V having a duration of 0.5 ms. **(B)** Objective classification of force measurements into four groups. The force was normalized to the maximum of each transient to illustrate the differences in the kinetics as well as the presence or absence of the fast and slow component of the twitch. **(C)** Kinetic twitch parameters (TTHP, TTP, and HRT). Each symbol represents the kinetic parameters of a single rectus EOM from a single mouse; empty circles, WT mice; gray circles, *ryr3*$^{-/-}$ mice. *, P < 0.05; **, P < 0.001; ****, P < 0.0001, Student's *t* test. Experiments were performed at room temperature. **(D)** Principal-component analyses of five twitch parameters (slow amplitude, fast amplitude, TTHP, TTP, and HRT). The axes represent the two principal components.

To answer this question directly, we investigated the mechanical properties of isolated EOM using a MyoStation-intact force transducer modified to measure twitch force in mounts of mouse EOMs as detailed in Materials and methods. In the experimental setup, we removed the oblique muscles and measured the force generated by electrical stimulation of medial rectal muscles. The force generated in response to a single pulse of 0.5 ms and of 24.6 V was significantly reduced and slower in EOMs from *ryr3*$^{-/-}$ mice (Fig. 3, A and B, light gray line; Table S2). The maximal peak force developed was ∼38% of that developed by EOMs from WT mice (WT: 0.328 ± 0.095 mN, *n* = 8; *ryr3*$^{-/-}$: 0.126 ± 0.017 mN, *n* = 9; Fig. 3, A and B, black line), and the kinetics was significantly slower. The kinetic properties of the muscles were not uniform and could be classified into four groups: twitches with a single rapid peak and rapid relaxation time (WT group 1), a rapid peak and a two-phased relaxation time of which one was rapid and the other slower (WT group 2), a slow peak and a slow relaxation time (*ryr3*$^{-/-}$ group 3), and rapid twitch with a double peak and slow relaxation time (*ryr3*$^{-/-}$ group 4). To facilitate their direct comparison, the individual peak maximal forces were each set to 100%. The results plotted in Fig. 3 C and detailed in Table S2 show that there were significant differences in the kinetic properties of WT and *ryr3*$^{-/-}$ EOMs. The mean TTHP was 2.5 ± 0.2 and 8.8 ± 2.3 ms, the mean TTP was 10.1 ± 1.1 and 42.8 ± 8.8 ms, and the mean HRT was 42.3 ± 9.8 and 147.4 ± 8.4 ms in WT (*n* = 8) and *ryr3*$^{-/-}$ mice (*n* = 9), respectively (values are the mean ± SEM). Fig. 3 D shows the kinetic data analyzed according to the principal-component analyses. This statistical procedure allows the simultaneous comparison of multiple variables or parameters that are reduced to a smaller set of data, facilitating the comparison of data by grouping similar datasets (Hwang et al., 2013). Analysis of the twitch parameters of muscles from WT mice (empty dots, Fig. 3 D) indicates that the values are similar to each other and can all be grouped into one cluster (bottom left, black bordered circle, Fig. 3 D); on the other hand, the data from the *ryr3*$^{-/-}$

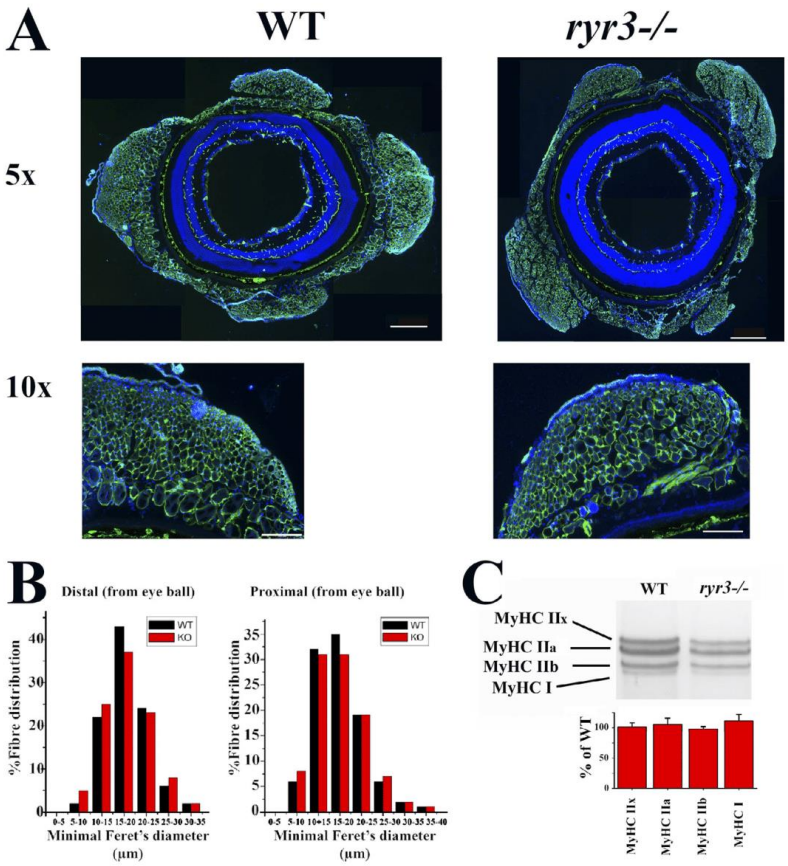

Figure 4. **Fiber type distribution and MyHC composition is similar in EOM muscles from WT and *ryr3*$^{-/-}$ mice. (A)** EOM from WT and *ryr3*$^{-/-}$ mice were sectioned, stained with anti-MyHC recognizing all isoforms and DAPI, and observed by fluorescent microscopy. Scale bars represent 500 µm (5× images) and 200 µm (10× images). **(B)** The fiber size distribution of EOMs was determined using the minimal Feret's diameter using MyHC immunohistochemistry (Delbono et al., 2007; black bars, WT; red bars *ryr3*$^{-/-}$). **(C)** High-resolution SDS-PAGE separation of MyHC isoforms in WT and *ryr3*$^{-/-}$ EOM muscles (Talmadge and Roy, 1993). The bottom bar graphs show the percent specific MyHC isoform vs. total MyHC content in *ryr3*$^{-/-}$ relative to WT (mean ± SEM, n = 5 WT and n = 5 *ryr3*$^{-/-}$), which was set to 100%.

muscles (gray dots, Fig. 3 D) fall not within the same cluster but within two completely separate clusters (gray bordered circles, Fig. 3 D). These changes in the mechanical properties were not caused by muscle atrophy, as the overall size distribution of fibers within the eye muscles (minimal Feret's diameter) was similar in WT and *ryr3*$^{-/-}$ mice (Fig. 4, A and B), nor were the changes caused by gross alterations in the overall MyHC isoform composition (Fig. 4 C).

The content and subcellular localization of proteins involved in ECC in EOM from WT and *ryr3*$^{-/-}$ mice are similar

The changes in visual acuity and mechanical properties of the EOM from *ryr3*$^{-/-}$ mice could be due to alterations in the content of proteins involved in ECC and/or in their subcellular localization. Analysis of the transcripts encoding the major proteins involved in calcium regulation revealed only small differences between WT and *ryr3*$^{-/-}$ mice, with the latter mice showing a reduction in *RYR1* and *CASQ1* transcripts (Fig. 5 A). The expression levels of the $Ca_v1.1$ (*CACNA1S*) and $Ca_v1.2$ isoforms (*CACNA1C*) of the α 1 subunit of the DHPR were not affected by *RYR3* ablation (Fig. 5 A). As to protein levels, quantitative Western blot analysis did not reveal significant changes in content of proteins involved in ECC, except for an increase in parvalbumin (Fig. 5, B and C). We tested all commercially available anti-RYR3 antibodies, but none appeared to be specific. The absence of the RYR3 protein was confirmed by mass spectrometry analysis (Fig. 1 C).

To verify whether the observed changes in the mechanical properties of isolated EOMs in *ryr3*$^{-/-}$ mice were due to

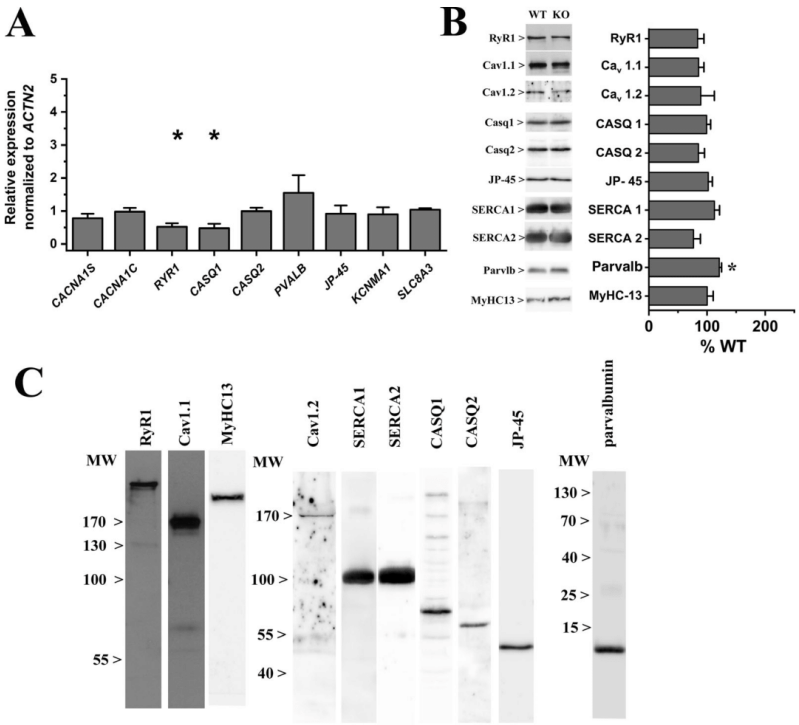

Figure 5. **Transcript expression and protein content of key players involved in skeletal muscle calcium homeostasis. (A)** Expression levels of transcripts encoding ECC proteins measured by qPCR. Values are plotted as mean (±SEM) fold change in *ryr3*$^{-/-}$ vs. WT levels (which were set as 1). *ACTN2* was used as housekeeping gene. The mean expression level of duplicate determinations obtained from pooled EOM from four to six mice is shown. Transcript levels of *RYR1* and *CASQ1* were reduced by ∼50%. *, $P < 0.05$, Student's *t* test. **(B)** Left: Representative immunopositive bands obtained from Western blots of EOM total homogenates probed with the indicated antibodies. Right: mean (±SEM) intensity values of the immunopositive bands normalized for desmin (except for MyHC13 that was normalized for total MyHC content). The mean intensity values were obtained from EOM muscles from four to eight mice. The intensity values of obtained from WT mice were set to 100%. *, $P < 0.05$, Student's *t* test. **(C)** The following commercial antibodies were used: rabbit anti-RyR1 (D4E1; 8153S; Cell Signaling), goat anti-$Ca_v1.1$ (sc-8160; Santa Cruz), rabbit anti-$Ca_v1.2$ (sc-25686; Santa Cruz), rabbit anti-calsequestrin-1 (CASQ1; C-0743; Sigma) and calsequestrin-2 (CASQ2; ab-3516; Abcam), goat anti-SERCA1 (sc-8093; Santa Cruz), goat anti-SERCA2 (sc-8095; Santa Cruz), mouse anti-MyHC (05–716; Millipore), mouse anti-MyHC13 (4A6; DSHB Iowa), and rabbit anti-parvalbumin (PV25; Swant). The rabbit anti-JP-45 polyclonal antibodies have been characterized previously (Zorzato et al., 2000). MW, molecular weight.

alterations in the subcellular localization of RYRs and/or of DHPRs, high-resolution confocal immunohistochemistry was performed on enzymatically dissociated EOM fibers stained with different antibody combinations. Fig. 6 shows a representative image of fibers from WT and *ryr3*$^{-/-}$ EOM stained for RYR1 (with rabbit anti-RYR1 mAb D4E1, whose epitope surrounds Arg830 of the human RYR1 protein; left panel, green color on the merged image) and of $Ca_v1.1$ (central panel, red color on merged images). The immunostaining of RYR1 and $Ca_v1.1$ was overall similar, as fibers from both mice showed the typical double row of overlapping fluorescence. More detailed analysis, however, revealed that the overlap of RYR1 and $Ca_v1.1$ fluorescence was reduced in fibers from *ryr3*$^{-/-}$ (Table 1), indicating that RYR3 ablation affects the subcellular distribution of the RYR1 and $Ca_v1.1$ calcium channels. Fig. 6 B shows that $Ca_v1.1$ (mouse mAb, left panel, red fluorescence on merged image) and $Ca_v1.2$ (rabbit polyclonal Ab, central panel, green fluorescence on merged image) do not share subcellular localization in EOMs. In fact, the fluorescent pattern of $Ca_v1.2$ showed a predominantly patchy appearance on the plasmalemma of the fibers, with low levels of fluorescence within the double rows that are positive for $Ca_v1.1$. The $Ca_v1.2$ antibodies are specific as they recognize a band of ∼170 kD on Western blot (Fig. 5 C) and do not recognize any structure when tested on extensor digitorum longus (EDL) muscle fibers that lack the $Ca_v1.2$ isoform (Fig. 6 B, bottom central panel). There was no apparent difference in the subcellular localization of $Ca_v1.2$ between WT and *ryr3*$^{-/-}$ mice (Table 1).

ECC in single EOM-muscle fibers and EOM-derived myotubes

Ca^{2+} homeostasis and the ECC characteristics of fibers isolated from WT and *ryr3*$^{-/-}$ mice were analyzed by fluorescence microscopy. Enzymatically dissociated fibers were loaded either

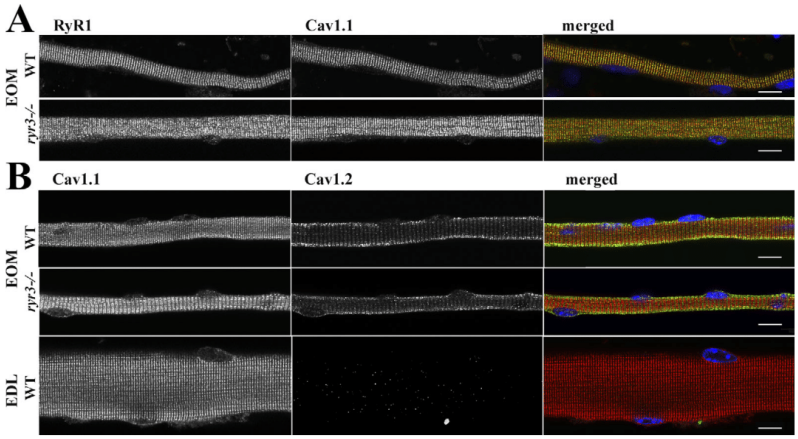

Figure 6. **Immunohistochemical analysis and subcellular localization of RYR1 and of the α 1 subunit of the DHPR in single muscle fibers from WT and *ryr3*$^{-/-}$ mice. (A)** Left and central panels show the staining obtained using rabbit anti-RYR1 mAb D4E1 (green in merged image) and mouse anti-$Ca_v1.1$ (red in merged image), respectively. The panel on the right shows the merged images as well as location of the myonuclei (DAPI, blue). **(B)** Left and central panels show the staining obtained using mouse anti-$Ca_v1.1$ (red in merged image) and rabbit anti-$Ca_v1.2$ (green in merged image), respectively. The panel on the right shows the merged images as well as location of the myonuclei (DAPI, blue). The bottom panels show staining of mouse EDL fibers, which are negative for $Ca_v1.2$ and were used as staining control. All images in B were acquired using the same settings for the laser intensities and acquisition parameters. Images were acquired using a Nikon A1 plus confocal microscope equipped with a Plan Apo 60× oil objective (numerical aperture, 1.4) and stained as described in Materials and methods. Orange pixels show areas of colocalization. Scale bars, 30 µm.

with the Ca^{2+} indicator Mag-Fluo-4 (Fig. 7, A, B, D, and E) for measurements of electrically evoked Ca^{2+} transients or fura-2 (Fig. 7 C) for measurements of the resting cytoplasmic $[Ca^{2+}]$. A representative trace of a Ca^{2+} transient elicited by field stimulation in EOM fibers from WT and *ryr3*$^{-/-}$ mice is shown in Fig. 7 B. Detailed quantitative analysis revealed that the peak ΔF/F was similar in WT and *ryr3*$^{-/-}$ EOM fibers (Fig. 7 D and Table 2), as was the TTP (Fig. 7 E and Table 2); however, the mean TTHP and HRTs were significantly slower in fibers from *ryr3*$^{-/-}$ mice (Table 2). We would like to point out that these experiments were performed at room temperature (23–25°C), and thus, the absolute kinetic values in vivo may be faster (at 37°C) than those reported here. Nevertheless, the impact of ambient temperature on the Ca^{2+} kinetics of fibers from WT and *ryr3*$^{-/-}$ should be the same. No significant difference was observed in the resting $[Ca^{2+}]$ (Fig. 7 C). Experiments were also performed to verify if EOM fibers exhibit sparks; 91 fibers from four WT mice were loaded with Fluo-4 (Lopez et al., 2016), but we failed to observe any spontaneous Ca^{2+} release events.

The results described so far indicate that RYR3 ablation causes specific alterations of intracellular calcium homeostasis and could be responsible for the reduced visual capacity of the *ryr3*$^{-/-}$ mice. However, the differences in calcium homeostasis observed between WT and *ryr3*$^{-/-}$ mice could potentially be caused by changes in muscle development brought about by the absence of RYR3 rather than to changes in calcium fluxes due to the specific absence of the Ca^{2+} channel. This point is especially relevant, since (a) the expression of the RYR3 isoform peaks during development and decreases in mature muscles (Conti et al., 2005) and (b) in EOMs, but not in other skeletal muscles, there is a continuous process of myonuclear addition into normal uninjured adult myofibrils. The myonuclei derive from activated satellite cells residing within uninjured EOMs (McLoon and Wirtschafter, 2002a,b; Stuelsatz et al., 2015).

To address the subject of abnormal calcium homeostasis directly and bypass issues linked to development or muscle adaptation due to the lack of RYR3 in innervating neurons, we isolated satellite cells from EOMs, cultured them, and analyzed Ca^{2+} homeostasis in the resulting multinucleated myotubes (Fig. S2). No gross change in the number of myotubes or in their fusing capacity was observed. Furthermore, no significant changes in the resting Ca^{2+} concentration

Table 1. **Colocalization analysis**

	RYR1 → $Ca_v1.1$ overlap	**$Ca_v1.1$ → RYR1 overlap**	**$Ca_v1.2$ → Ca_v 1.1 overlap**	**$Ca_v1.1$ → $Ca_v1.2$ overlap**
WT	0.801 ± 0.126 (n = 5)	0.747 ± 0.020 (n = 5)	0.479 ± 0.051 (n = 5)	0.278 ± 0.060 (n = 5)
ryr3$^{-/-}$	0.677 ± 0.068 (n = 4)*	0.647 ± 0.082 (n = 4)*	0.378 ± 0.127 (n = 4)	0.256 ± 0.100 (n = 4)

Values represent mean ± SD; n represents the number of fibers analyzed. n.s., not significant. *, P < 0.05, Student's t test.

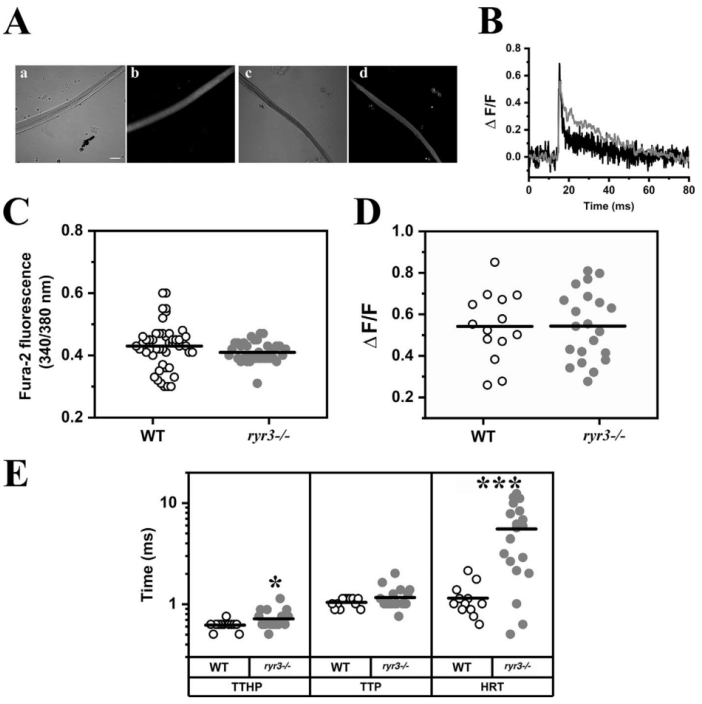

Figure 7. **Calcium homeostasis in isolated EOM fibers. (A)** Confocal images of WT (a and b) and *ryr3*$^{-/-}$ (c and d) fibers; a and c show the transmitted light channel, and b and d show Mag-Fluo4 fluorescence, excited at 488 nm and recorded at an emission between 500 and 550 nm. Scale bar, 30 µm. **(B)** Representative line scan traces of MagFluo4 calcium transients in EOM fibers from WT (black) and *ryr3*$^{-/-}$ (gray), recorded at 7,921 lines per second. **(C)** Measurements of resting Ca^{2+} expressed as ratio (340/380 nm) using the fluorescent indicator fura-2. Each symbol represents the ratio obtained from a single fiber. The horizontal black line shows the mean value. Fibers were isolated from a total of three mice per group, and a total of 49 fibers from WT and 40 fibers from *ryr3*$^{-/-}$ were analyzed. **(D)** Peak Ca^{2+} (ΔF/F) of the MagFluo4 fluorescence obtained by stimulating EOM fibers by electrical field stimulation with a 0.5-ms bipolar pulse. All experiments were performed at room temperature. Each symbol represents the value from a single fiber. The horizontal black line shows the mean value. A total of 14 fibers from four WT mice and 21 fibers from nine *ryr3*$^{-/-}$ mice were analyzed. **(E)** Analysis of the kinetics of the Ca^{2+} transients; TTHP, TTP, and HRT of the calcium transients are plotted. White dots, WT; gray dots, *ryr3*$^{-/-}$. A total of 12 fibers from four WT mice and 19 fibers from nine *ryr3*$^{-/-}$ mice were analyzed. *, P < 0.05; ***, P < 0.001, Student's *t* test.

(86.6 ± 3.2 nM vs. 95.3 ± 5.1 nM in WT and *ryr3*$^{-/-}$, respectively; *n* = 75 cells) or the size of the rapidly releasable intracellular stores (3,210.0 ± 539.6 vs. 2,548.5 ± 180.7 arbitrary units in WT and *ryr3*$^{-/-}$ respectively; *n* = 9) were observed. No Ca^{2+} sparks were detected in myotubes from WT or *ryr3*$^{-/-}$ as determined with the calcium indicator Fluo-4. Interestingly, however, EOM-derived myotubes exhibited extremely rapid, repetitive Ca^{2+} oscillations that were more frequent in cells from WT than *ryr3*$^{-/-}$ mice (Fig. 8, A–C). Additionally, the Ca^{2+} oscillations in *ryr3*$^{-/-}$ myotubes were significantly slower than those observed in myotubes from WT mice (Fig. 8 D and Table 2).

Discussion

In the present report, we investigated the role of RYR3 in skeletal muscle by studying the biochemical and physiological characteristics of EOMs from *ryr3*$^{-/-}$mice. Knockout mice exhibited reduced visual capacity that is caused by a change in the physiological properties of the muscles, since (a) the mechanical properties of isolated muscles assessed in vitro were significantly different and (b) calcium homeostasis in single fibers and cultured myotubes explanted from EOMs was altered.

EOMs are subspecialized and highly complex muscles showing single and multiple innervations, as well as the presence of fibers with mixed fast- and slow-twitch contractile

Table 2. **Analysis of the kinetics of the calcium transients in EOM fibers and myotubes from WT and *ryr3*$^{-/-}$mice**

Type of Ca^{2+} response	Genotype and cell type	Peak Ca^{2+} (ΔF)	TTHP (ms)	TTP (ms)	HRT (ms)
Electrically evoked transient parameters	WT EOM fibers	0.458 ± 0.036 (*n* = 14)	0.621 ± 0.019 (*n* = 12)	1.042 ± 0.032 (*n* = 12)	1.147 ± 0.125 (*n* = 12)
	ryr3$^{-/-}$ EOM fibers	0.424 ± 0.027 (*n* = 21)	0.718 ± 0.034* (*n* = 19)	1.310 ± 0.159 (*n* = 19)	5.531 ± 0.877*** (*n* = 19)
Spontaneous Ca^{2+} transient parameters	WT myotubes	0.506 ± 0.003 (*n* = 9,319)	20.598 ± 0.192 (*n* = 9,319)	29.885 ± 0.347 (*n* = 9319)	77.813 ± 0.8138 (*n* = 8,941)
	ryr3$^{-/-}$ myotubes	0.6111 ± 0.010***** (*n* = 1,368)	27.527 ± 0.570***** (*n* = 1,368)	46.878 ± 1.173***** (*n* = 1,368)	87.586 ± 1.931***** (*n* = 1,339)

Experiments were performed at room temperature. Values represent mean ± SEM. *, P < 0.05; ***, P < 0.001, Student's *t* test; *****, P < 0.00001, Welch's *t* test.

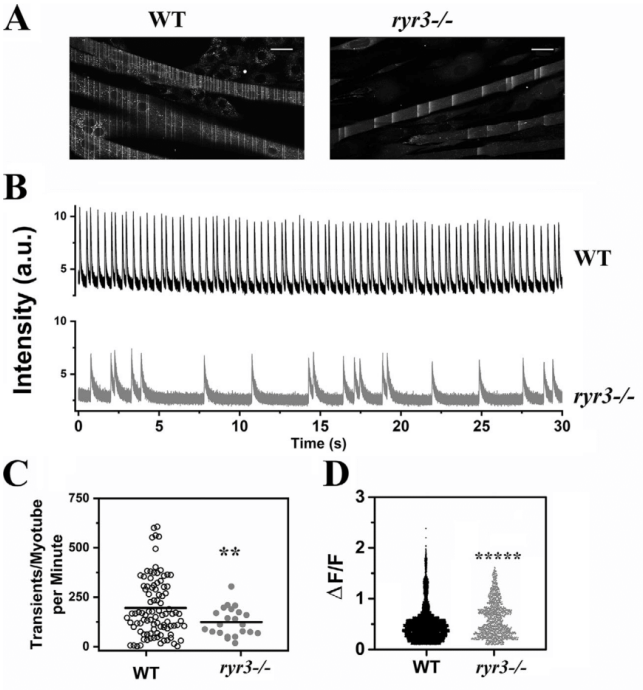

Figure 8. ***ryr3*$^{-/-}$ EOM-derived myotubes show fewer calcium waves than WT EOM-derived myotubes. (A)** WT (left) and *ryr3*$^{-/-}$ (right) confocal image of myotubes loaded with Fluo-4. Spontaneous calcium waves can be seen as lines during image acquisition. Scale bars, 30 µm. **(B)** Representative Fluo-4 line scan traces of WT (top, black line) and *ryr3*$^{-/-}$ (bottom, gray line) myotubes. a.u., arbitrary units. **(C)** Analysis of the frequency of the spontaneous Ca^{2+} transient. Each point represents the number of transients per minute recorded in a single myotube. Each myotube was recorded for 30 s, and the frequency output is given as frequency per minute. Experiments were performed at room temperature. The horizontal black line represents the mean value. Empty circles, WT (n = 95); gray circles, *ryr3*$^{-/-}$ (n = 22). **(D)** ΔF/F of the Fluo-4 transients. The number of transients analyzed was n = 9,319 and n = 1,368 for WT and *ryr3*$^{-/-}$, respectively. **, P < 0.005; *****, P < 0.0001, Welch's t test.

characteristics within a single contracting unit (Mayr, 1971; Ketterer et al., 2010). We found that the absolute maximum force developed by mouse EOMs is ∼10 times lower than that of other mouse limb muscles. In this study, because the size of mouse EOMs is very small (300–600 µm diameter) and a small error in the cross-sectional area measurements would have a large impact on the corrected developed force, we displayed the absolute and noncorrected force values. The mechanical properties of EOMs from adult (12–16-wk-old) *ryr3*$^{-/-}$ mice were different than those of WT mice. Indeed *ryr3*$^{-/-}$ EOM developed less force and had slower kinetics (but did not show changes in muscle cross-sectional area). Such data are consistent with a previous report (Bertocchini et al., 1997) showing that diaphragm strips from 15-d-old *ryr3*$^{-/-}$ mice stimulated at a frequency of 0.1 Hz developed less tension than their WT counterpart, though in muscles from adult mice, the differences disappeared.

The three- to fourfold slower half relaxation time observed in EOMs from *ryr3*$^{-/-}$ mice would significantly impact the speed of the eye movement necessary for the mice to perform the requested visual tasks, and we are confident that such dramatic changes in force account for the decreased visual acuity detected in vivo. It should be pointed out that neither the OKR nor the cued water maze directly assess ocular muscle function. The OKR represents an automatic compensatory eye movement without any conscious effort to stabilize the image and responds when animals move about in a visual scene. This reflex requires a visible retinal image and is particularly prominent in afoveate animals (i.e., animals lacking the fovea; Stahl, 2004). Performing the cued water maze task also requires intact eyesight and motor ability (swimming and eye movement) to focus the visible platform located at different locations in the respective trials (Vorhees and Williams, 2006). Therefore, although no direct conclusions can be drawn and we cannot totally exclude an effect caused by neuronal *RYR3* ablation, our results point toward an impact of *RYR3* ablation on eye muscle function, especially since (a) no morphological and electrophysiological retinal differences between WT and *ryr3*$^{-/-}$ animals were found, and (b) direct changes in the kinetics of the calcium signaling and velocity of contraction in isolated EOMs were found. We would also like to point out that *ryr3*$^{-/-}$ mice were reported to exhibit impaired spatial learning as assessed by the Morris water maze and increased spontaneous open-field activity (Balschun et al., 1999). In view of the present findings, it is also possible that the reported spatial memory defects observed in *ryr3*$^{-/-}$ mice were caused, at least in part, by altered ocular muscle function.

The reduced tension and speed of contraction observed in *ryr3*$^{-/-}$ EOMs are most likely not caused by differences in the expression levels of ECC proteins and/or contractile proteins, since the expressed MyHC isoforms were similar in WT and *ryr3*$^{-/-}$ EOMs and the ECC protein composition of total EOM extracts was similar in WT and transgenic mice. The small increase in the content of the calcium binding protein parvalbumin observed in *ryr3*$^{-/-}$ EOMs cannot account for the changes in

the kinetics of relaxation. Indeed, a higher content of parvalbumin would be expected to increase the speed of relaxation and not prolong it (Heizmann et al., 1982; Müntener et al., 1995), indicating that the changes in the kinetic properties must be due to a different mechanism. Of interest, we did observe a significant reduction in the expression of RYR1 and CASQ1 transcripts, but this did not result in an overall change in their level of protein content.

Although it is difficult to directly determine the cause of the slow relaxation times of *ryr3*$^{-/-}$ EOMs, they may relate to the location and physiological function of RYR3s. One possibility is that in murine EOMs, RYR3s are located parajunctionally, i.e., similar to their distribution in toadfish white swim muscle, frog sartorius, and 72 HPF zebrafish larvae (Felder and Franzini-Armstrong, 2002; Perni et al., 2015). This parajunctional subcellular localization could place the RYR3s adjacent to some SERCAs, whereby Ca^{2+} release via the parajunctional RYR3 would rapidly activate the Ca^{2+} pump, leading to a faster rate of relaxation. The lack of RYR3 would fail to rapidly activate the calcium ATPase, leading to a slower relaxation rate. Of note, close subcellular distribution of RYR3 and SERCA2a and of RYR2 and SERCA2b have also been reported in other tissues (Greene et al., 2000; Clark et al., 2010; Dally et al., 2010).

Since release of Ca^{2+} from intracellular stores is the driving force of skeletal muscle contraction, we hypothesized that the mechanism resulting in the changes in the mechanical properties of EOMs in the transgenic mice were due to alterations of Ca^{2+} release. In mammalian cells, RYR3s have been reported to reinforce CICR in developing murine skeletal muscles (Yang et al., 2001) and play a role in the duration and amplitude of osmotic shock–triggered Ca^{2+} sparks in adult skeletal muscle fibers (Weisleder et al., 2007). On the other hand, in non-mammalian skeletal muscles, RYR3s contribute both to the generation of sparks and to the Ca^{2+} transients (Zhou et al., 2003, 2004; Perni et al., 2015). Surprisingly, no sparks were observed in mouse EOM fibers, indicating that in the latter muscles spontaneous Ca^{2+} release events do not occur, possibly because of their particular expression of ECC protein machinery and dissimilar calcium homeostasis (Zeiger et al., 2010; Stuelsatz et al., 2015; Sekulic-Jablanovic et al., 2016). Interestingly, the kinetics of the Ca^{2+} transients (TTP and TTHP) in EOMs from WT mice were approximately four times faster than those reported using the same Ca^{2+} indicator in rat and mouse fast-twitch fibers. Indeed, in rat and mouse EDL fibers, the reported TTP of the Ca^{2+} transient was 4.6 ± 0.42 ms (Delbono and Stefani, 1993) and 4.4 ± 0.1 ms (Hollingworth et al., 2008), respectively, and the TTHP was 3.2 ± 0.1 ms, while in mouse EOMs, we calculated a TTP of 1.04 ± 0.03 ms and TTHP of 0.62 ± 0.02 ms. Thus, it is not only the presence of MyHC13, which is responsible for the superfast characteristics of EOM muscle contraction, but also their particular ECC machinery. Nevertheless, the observed changes of the Ca^{2+} transients between EOMs from WT and *ryr3*$^{-/-}$ mice are clearly insufficient to account for the large changes in force development. The reduction in force may be due in part to the different preparations used to measure force and Ca^{2+} or to changes occurring during development. Indeed, EOMs from *ryr3*$^{-/-}$ mice may have physiologically adapted to the lack of *RYR3* during muscle fiber maturation. To circumvent the possible alterations caused by modifications occurring during muscle fiber maturation, we studied Ca^{2+} homeostasis in myotubes obtained from satellite cells from adult EOMs and cultured and differentiated in vitro. Our results show that EOM-derived myotubes exhibit extremely rapid and repetitive Ca^{2+} oscillations, which occur in the absence of any exogenous stimulation and depend on extracellular Ca^{2+} (since they disappeared in Ca^{2+}-free medium). More importantly, the velocity of the Ca^{2+} transients was 1.6 times slower in *ryr3*$^{-/-}$ myotubes. The spontaneous oscillations were not completely abolished in myotubes from *ryr3*$^{-/-}$ mice, but their number was substantially reduced, corroborating the role of RYR3 as a calcium signal amplifier. Though presently we do not know the function played by these Ca^{2+} oscillations, the lack of signals generated by their diminished activity potentially alters the myotubes, resulting in impaired regeneration of EOM.

In conclusion, our studies show that the lack of RYR3 has a significant impact on visual acuity by affecting the function of ocular muscles. It also suggests that in the future, mutations in *RYR3* should be taken into consideration in patients with strabismus, ophthalmoplegia, and ptosis with or without involvement of the central nervous system.

Acknowledgments

The support of the Department of Anesthesia, Basel University Hospital and the technical support of Anne-Sylvie Monnet are gratefully acknowledged. We also thank Professors Stephan Frank and Jürgen Hench from the Institute for Medical Genetics and Pathology, Basel University Hospital for helpful discussions; Dr. Alexander Schmidt of the Proteomics Core Facility, Biozentrum Basel University, for performing the mass spectroscopy analysis; and Ms. Carolyn Trepp for help with the OKR experiments. We also acknowledge ARVO (copyright holder) for permission to reproduce Fig. 2 from Prusky et al., 2004.

This work was supported by the Swiss National Science Foundation (grant 31003A-169316), the OPO Stiftung (grant 2013/14-0038), and the Japan Society for the Promotion of Science (Core-to-core program).

The authors declare no competing financial interests.

Author contributions: J. Eckhardt designed and performed the experiments and analyzed the results with guidance from F. Zorzato and S. Treves; C. Bachmann performed the immunohistochemistry experiments on isolated fibers; M. Sekulic-Jablanovic performed the initial experiments on *RYR3* expression in mouse EOMs as well as some of the in vivo visual experiments. V. Enzmann supported J. Eckhardt and M. Sekulic-Jablanovic in the in vivo visual experiments. J. Ma, K. Ho Park, and H. Takeshima constructed and supplied the *ryr3*$^{-/-}$ mouse model. F. Zorzato and S. Treves designed the experiments on the mouse model, oversaw the project, and wrote the paper. All authors reviewed and helped elaborate the manuscript.

Eduardo Ríos served as editor.

Submitted: 24 January 2019
Accepted: 13 April 2019

References

Airey, J.A., C.F. Beck, K. Murakami, S.J. Tanksley, T.J. Deerinck, M.H. Ellisman, and J.L. Sutko. 1990. Identification and localization of two triad junctional foot protein isoforms in mature avian fast twitch skeletal muscle. *J. Biol. Chem.* 265:14187–14194.

Balschun, D., D.P. Wolfer, F. Bertocchini, V. Barone, A. Conti, W. Zuschratter, L. Missiaen, H.P.J. Lipp, J.U. Frey, and V. Sorrentino. 1999. Deletion of the ryanodine receptor type 3 (RyR3) impairs forms of synaptic plasticity and spatial learning. *EMBO J.* 18:5264–5273. https://doi.org/10.1093/emboj/18.19.5264

Bers, D.M. 2002. Cardiac excitation-contraction coupling. *Nature.* 415: 198–205. https://doi.org/10.1038/415198a

Bertocchini, F., C.E. Ovitt, A. Conti, V. Barone, H.R. Schöler, R. Bottinelli, C. Reggiani, and V. Sorrentino. 1997. Requirement for the ryanodine receptor type 3 for efficient contraction in neonatal skeletal muscles. *EMBO J.* 16:6956–6963. https://doi.org/10.1093/emboj/16.23.6956

Brown, R.E., and A.A. Wong. 2007. The influence of visual ability on learning and memory performance in 13 strains of mice. *Learn. Mem.* 14:134–144. https://doi.org/10.1101/lm.473907

Clark, J.H., N.P. Kinnear, S. Kalujnaia, G. Cramb, S. Fleischer, L.H. Jeyakumar, F. Wuytack, and A.M. Evans. 2010. Identification of functionally segregated sarcoplasmic reticulum calcium stores in pulmonary arterial smooth muscle. *J. Biol. Chem.* 285:13542–13549. https://doi.org/10.1074/jbc.M110.101485

Conti, A., C. Reggiani, and V. Sorrentino. 2005. Selective expression of the type 3 isoform of ryanodine receptor Ca2+ release channel (RyR3) in a subset of slow fibers in diaphragm and cephalic muscles of adult rabbits. *Biochem. Biophys. Res. Commun.* 337:195–200. https://doi.org/10.1016/j.bbrc.2005.09.027

Dally, S., E. Corvazier, R. Bredoux, R. Bobe, and J. Enouf. 2010. Multiple and diverse coexpression, location, and regulation of additional SERCA2 and SERCA3 isoforms in nonfailing and failing human heart. *J. Mol. Cell. Cardiol.* 48:633–644. https://doi.org/10.1016/j.yjmcc.2009.11.012

de Chaumont, F., S. Dallongeville, N. Chenouard, N. Hervé, S. Pop, T. Provoost, V. Meas-Yedid, P. Pankajakshan, T. Lecomte, Y. Le Montagner, et al. 2012. Icy: an open bioimage informatics platform for extended reproducible research. *Nat. Methods.* 9:690–696. https://doi.org/10.1038/nmeth.2075

Delbono, O., and E. Stefani. 1993. Calcium transients in single mammalian skeletal muscle fibres. *J. Physiol.* 463:689–707. https://doi.org/10.1113/jphysiol.1993.sp019617

Delbono, O., J. Xia, S. Treves, Z.M. Wang, R. Jimenez-Moreno, A.M. Payne, M.L. Messi, A. Briguet, F. Schaerer, M. Nishi, et al. 2007. Loss of skeletal muscle strength by ablation of the sarcoplasmic reticulum protein JP45. *Proc. Natl. Acad. Sci. USA.* 104:20108–20113. https://doi.org/10.1073/pnas.0707389104

Endo, M. 1977. Calcium release from the sarcoplasmic reticulum. *Physiol. Rev.* 57:71–108. https://doi.org/10.1152/physrev.1977.57.1.71

Enzmann, V., B.W. Row, Y. Yamauchi, L. Kheirandish, D. Gozal, H.J. Kaplan, and M.A. McCall. 2006. Behavioral and anatomical abnormalities in a sodium iodate-induced model of retinal pigment epithelium degeneration. *Exp. Eye Res.* 82:441–448. https://doi.org/10.1016/j.exer.2005.08.002

Felder, E., and C. Franzini-Armstrong. 2002. Type 3 ryanodine receptors of skeletal muscle are segregated in a parajunctional position. *Proc. Natl. Acad. Sci. USA.* 99:1695–1700. https://doi.org/10.1073/pnas.032657599

Franzini-Armstrong, C., and A.O. Jorgensen. 1994. Structure and development of E-C coupling units in skeletal muscle. *Annu. Rev. Physiol.* 56: 509–534. https://doi.org/10.1146/annurev.ph.56.030194.002453

Giannini, G., E. Clementi, R. Ceci, G. Marziali, and V. Sorrentino. 1992. Expression of a ryanodine receptor-Ca^{2+} channel that is regulated by TGF-β. *Science.* 257:91–94. https://doi.org/10.1126/science.1320290

Giannini, G., A. Conti, S. Mammarella, M. Scrobogna, and V. Sorrentino. 1995. The ryanodine receptor/calcium channel genes are widely and differentially expressed in murine brain and peripheral tissues. *J. Cell Biol.* 128:893–904. https://doi.org/10.1083/jcb.128.5.893

Greene, A.L., M.J. Lalli, Y. Ji, G.J. Babu, I. Grupp, M. Sussman, and M. Periasamy. 2000. Overexpression of SERCA2b in the heart leads to an increase in sarcoplasmic reticulum calcium transport function and increased cardiac contractility. *J. Biol. Chem.* 275:24722–24727. https://doi.org/10.1074/jbc.M001783200

Guiñón, J., E. Ortega, J. García-Antón, and V. Pérez-Herranz. 2007. Moving average and Savitzki-Golay smoothing filters using Mathcad. https://www.researchgate.net/publication/228407245_Moving_average_and_Savitzki-Golay_smoothing_filters_using_Mathcad

Heizmann, C.W., M.W. Berchtold, and A.M. Rowlerson. 1982. Correlation of parvalbumin concentration with relaxation speed in mammalian muscles. *Proc. Natl. Acad. Sci. USA.* 79:7243–7247. https://doi.org/10.1073/pnas.79.23.7243

Hoh, J.F.Y., S. Hughes, G. Hugh, and I. Pozgaj. 1989. Three hierarchies in skeletal muscle fibre classification: allotype, isotype and phenotype. *In UCLA Symposia on Molecular and Cellular Biology.* F. Stockdale, and L. Kedes, editors. Alan R. Liss, New York. 15–26.

Hollingworth, S., U. Zeiger, and S.M. Baylor. 2008. Comparison of the myoplasmic calcium transient elicited by an action potential in intact fibres of mdx and normal mice. *J. Physiol.* 586:5063–5075. https://doi.org/10.1113/jphysiol.2008.160507

Hollingworth, S., K.R. Gee, and S.M. Baylor. 2009. Low-affinity Ca^{2+} indicators compared in measurements of skeletal muscle Ca^{2+} transients. *Biophys. J.* 97:1864–1872. https://doi.org/10.1016/j.bpj.2009.07.021

Hwang, H., K. Jung, Y. Takane, and T.S. Woodward. 2013. A unified approach to multiple-set canonical correlation analysis and principal components analysis. *Br. J. Math. Stat. Psychol.* 66:308–321. https://doi.org/10.1111/j.2044-8317.2012.02052.x

Kaminski, H.J., and R.L. Ruff. 1997. Ocular muscle involvement by myasthenia gravis. *Ann. Neurol.* 41:419–420. https://doi.org/10.1002/ana.410410402

Ketterer, C., U. Zeiger, M.T. Budak, N.A. Rubinstein, and T.S. Khurana. 2010. Identification of the neuromuscular junction transcriptome of extraocular muscle by laser capture microdissection. *Invest. Ophthalmol. Vis. Sci.* 51:4589–4599. https://doi.org/10.1167/iovs.09-4893

Lopez, R.J., S. Byrne, M. Vukcevic, M. Sekulic-Jablanovic, L. Xu, M. Brink, J. Alamelu, N. Voermans, M. Snoeck, E. Clement, et al. 2016. An RYR1 mutation associated with malignant hyperthermia is also associated with bleeding abnormalities. *Sci. Signal.* 9:ra68. https://doi.org/10.1126/scisignal.aad9813

Mayr, R. 1971. Structure and distribution of fibre types in the external eye muscles of the rat. *Tissue Cell.* 3:433–462. https://doi.org/10.1016/S0040-8166(71)80045-9

McLoon, L.K., and J. Wirtschafter. 2002a. Activated satellite cells are present in uninjured extraocular muscles of mature mice. *Trans. Am. Ophthalmol. Soc.* 100:119–123, discussion:123–124.

McLoon, L.K., and J.D. Wirtschafter. 2002b. Continuous myonuclear addition to single extraocular myofibers in uninjured adult rabbits. *Muscle Nerve.* 25:348–358. https://doi.org/10.1002/mus.10056

Meissner, G. 2017. The structural basis of ryanodine receptor ion channel function. *J. Gen. Physiol.* 149:1065–1089. https://doi.org/10.1085/jgp.201711878

Müntener, M., L. Käser, J. Weber, and M.W. Berchtold. 1995. Increase of skeletal muscle relaxation speed by direct injection of parvalbumin cDNA. *Proc. Natl. Acad. Sci. USA.* 92:6504–6508. https://doi.org/10.1073/pnas.92.14.6504

Ogawa, Y., N. Kurebayashi, and T. Murayama. 2000. Putative roles of type 3 ryanodine receptor isoforms (RyR3). *Trends Cardiovasc. Med.* 10:65–70. https://doi.org/10.1016/S1050-1738(00)00050-5

Ostertagova, E., and O. Ostertag. 2016. Methodology and Application of Savitzky-Golay Moving Average Polynomial Smoother. *Global J. Pure Appl. Math.* 12:3201–3210.

Percival, A.L., A.J. Williams, J.L. Kenyon, M.M. Grinsell, J.A. Airey, and J.L. Sutko. 1994. Chicken skeletal muscle ryanodine receptor isoforms: ion channel properties. *Biophys. J.* 67:1834–1850. https://doi.org/10.1016/S0006-3495(94)80665-4

Perni, S., K.C. Marsden, M. Escobar, S. Hollingworth, S.M. Baylor, and C. Franzini-Armstrong. 2015. Structural and functional properties of ryanodine receptor type 3 in zebrafish tail muscle. *J. Gen. Physiol.* 145: 173–184. https://doi.org/10.1085/jgp.201411303

Porter, J.D., S. Khanna, H.J. Kaminski, J.S. Rao, A.P. Merriam, C.R. Richmonds, P. Leahy, J. Li, and F.H. Andrade. 2001. Extraocular muscle is defined by a fundamentally distinct gene expression profile. *Proc. Natl. Acad. Sci. USA.* 98:12062–12067. https://doi.org/10.1073/pnas.211257298

Protasi, F., H. Takekura, Y. Wang, S.R. Chen, G. Meissner, P.D. Allen, and C. Franzini-Armstrong. 2000. RYR1 and RYR3 have different roles in the assembly of calcium release units of skeletal muscle. *Biophys. J.* 79: 2494–2508. https://doi.org/10.1016/S0006-3495(00)76491-5

Prusky, G.T., N.M. Alam, S. Beekman, and R.M. Douglas. 2004. Rapid quantification of adult and developing mouse spatial vision using a virtual optomotor system. *Invest. Ophthalmol. Vis. Sci.* 45:4611–4616. https://doi.org/10.1167/iovs.04-0541

Purves, D., G.J. Augustine, D. Fitspatrick. L.C. Katz, A.S. LaMantia, J.O. McNamara, and S.M. Williams, editors. 2001. *Neuroscience.* Second

edition. Sinauer Associates, Sunderland, MA. Available at: https://www.ncbi.nlm.nih.gov/books/NBK10799/.
Ríos, E., and G. Pizarro. 1991. Voltage sensor of excitation-contraction coupling in skeletal muscle. *Physiol. Rev.* 71:849–908. https://doi.org/10.1152/physrev.1991.71.3.849
Schägger, H., and G. von Jagow. 1987. Tricine-sodium dodecyl sulfate-polyacrylamide gel electrophoresis for the separation of proteins in the range from 1 to 100 kDa. *Anal. Biochem.* 166:368–379. https://doi.org/10.1016/0003-2697(87)90587-2
Schindelin, J., I. Arganda-Carreras, E. Frise, V. Kaynig, M. Longair, T. Pietzsch, S. Preibisch, C. Rueden, S. Saalfeld, B. Schmid, et al. 2012. Fiji: an open-source platform for biological-image analysis. *Nat. Methods.* 9:676–682. https://doi.org/10.1038/nmeth.2019
Sekulic-Jablanovic, M., A. Palmowski-Wolfe, F. Zorzato, and S. Treves. 2015. Characterization of excitation-contraction coupling components in human extraocular muscles. *Biochem. J.* 466:29–36. https://doi.org/10.1042/BJ20140970
Sekulic-Jablanovic, M., N.D. Ullrich, D. Goldblum, A. Palmowski-Wolfe, F. Zorzato, and S. Treves. 2016. Functional characterization of orbicularis oculi and extraocular muscles. *J. Gen. Physiol.* 147:395–406. https://doi.org/10.1085/jgp.201511542
Spencer, R.F., and J.D. Porter. 1988. Structural organization of the extraocular muscles. *Rev. Oculomot. Res.* 2:33–79.
Stahl, J.S. 2004. Using eye movements to assess brain function in mice. *Vision Res.* 44:3401–3410. https://doi.org/10.1016/j.visres.2004.09.011
Stuelsatz, P., A. Shearer, Y. Li, L.A. Muir, N. Ieronimakis, Q.W. Shen, I. Kirillova, and Z. Yablonka-Reuveni. 2015. Extraocular muscle satellite cells are high performance myo-engines retaining efficient regenerative capacity in dystrophin deficiency. *Dev. Biol.* 397:31–44. https://doi.org/10.1016/j.ydbio.2014.08.035
Takeshima, H., S. Nishimura, T. Matsumoto, H. Ishida, K. Kangawa, N. Minamino, H. Matsuo, M. Ueda, M. Hanaoka, T. Hirose, and S. Numa. 1989. Primary structure and expression from complementary DNA of skeletal muscle ryanodine receptor. *Nature.* 339:439–445. https://doi.org/10.1038/339439a0
Takeshima, H., T. Ikemoto, M. Nishi, N. Nishiyama, M. Shimuta, Y. Sugitani, J. Kuno, I. Saito, H. Saito, M. Endo, et al. 1996. Generation and characterization of mutant mice lacking ryanodine receptor type 3. *J. Biol. Chem.* 271:19649–19652. https://doi.org/10.1074/jbc.271.33.19649
Talmadge, R.J., and R.R. Roy. 1993. Electrophoretic separation of rat skeletal muscle myosin heavy-chain isoforms. *J. Appl. Physiol.* 75:2337–2340. https://doi.org/10.1152/jappl.1993.75.5.2337
Thomas, B.B., M.J. Seiler, S.R. Sadda, P.J. Coffey, and R.B. Aramant. 2004. Optokinetic test to evaluate visual acuity of each eye independently. *J. Neurosci. Methods.* 138:7–13. https://doi.org/10.1016/j.jneumeth.2004.03.007
Treves, S., M. Vukcevic, P.Y. Jeannet, S. Levano, T. Girard, A. Urwyler, D. Fischer, T. Voit, H. Jungbluth, S. Lillis, et al. 2011. Enhanced excitation-coupled $Ca^{(2+)}$ entry induces nuclear translocation of NFAT and contributes to IL-6 release from myotubes from patients with central core disease. *Hum. Mol. Genet.* 20:589–600. https://doi.org/10.1093/hmg/ddq506
Vaithianathan, T., D. Narayanan, M.T. Asuncion-Chin, L.H. Jeyakumar, J. Liu, S. Fleischer, J.H. Jaggar, and A.M. Dopico. 2010. Subtype identification and functional characterization of ryanodine receptors in rat cerebral artery myocytes. *Am. J. Physiol. Cell Physiol.* 299:C264–C278. https://doi.org/10.1152/ajpcell.00318.2009
Vorhees, C.V., and M.T. Williams. 2006. Morris water maze: procedures for assessing spatial and related forms of learning and memory. *Nat. Protoc.* 1:848–858. https://doi.org/10.1038/nprot.2006.116
Weisleder, N., C. Ferrante, Y. Hirata, C. Collet, Y. Chu, H. Cheng, H. Takeshima, and J. Ma. 2007. Systemic ablation of RyR3 alters Ca^{2+} spark signaling in adult skeletal muscle. *Cell Calcium.* 42:548–555. https://doi.org/10.1016/j.ceca.2007.01.009
Yang, D., Z. Pan, H. Takeshima, C. Wu, R.Y. Nagaraj, J. Ma, and H. Cheng. 2001. RyR3 amplifies RyR1-mediated $Ca^{(2+)}$-induced $Ca_{(2+)}$ release in neonatal mammalian skeletal muscle. *J. Biol. Chem.* 276:40210–40214. https://doi.org/10.1074/jbc.M106944200
Zeiger, U., C.H. Mitchell, and T.S. Khurana. 2010. Superior calcium homeostasis of extraocular muscles. *Exp. Eye Res.* 91:613–622. https://doi.org/10.1016/j.exer.2010.07.019
Zhou, J., G. Brum, A. Gonzalez, B.S. Launikonis, M.D. Stern, and E. Rios. 2003. Ca2+ sparks and embers of mammalian muscle. Properties of the sources. *J. Gen. Physiol.* 122:95–114. https://doi.org/10.1085/jgp.200308796
Zhou, J., B.S. Launikonis, E. Ríos, and G. Brum. 2004. Regulation of Ca2+ sparks by Ca2+ and Mg2+ in mammalian and amphibian muscle. An RyR isoform-specific role in excitation-contraction coupling? *J. Gen. Physiol.* 124:409–428. https://doi.org/10.1085/jgp.200409105
Zhou, Y., D. Liu, and H.J. Kaminski. 2010. Myosin heavy chain expression in mouse extraocular muscle: more complex than expected. *Invest. Ophthalmol. Vis. Sci.* 51:6355–6363. https://doi.org/10.1167/iovs.10-5937
Zorzato, F., J. Fujii, K. Otsu, M. Phillips, N.M. Green, F.A. Lai, G. Meissner, and D.H. MacLennan. 1990. Molecular cloning of cDNA encoding human and rabbit forms of the Ca^{2+} release channel (ryanodine receptor) of skeletal muscle sarcoplasmic reticulum. *J. Biol. Chem.* 265:2244–2256.
Zorzato, F., A.A. Anderson, K. Ohlendieck, G. Froemming, R. Guerrini, and S. Treves. 2000. Identification of a novel 45 kDa protein (JP-45) from rabbit sarcoplasmic-reticulum junctional-face membrane. *Biochem. J.* 351:537–543.
Zulliger, R., S. Lecaudé, S. Eigeldinger-Berthou, U.E. Wolf-Schnurrbusch, and V. Enzmann. 2011. Caspase-3-independent photoreceptor degeneration by N-methyl-N-nitrosourea (MNU) induces morphological and functional changes in the mouse retina. *Graefes Arch. Clin. Exp. Ophthalmol.* 249:859–869. https://doi.org/10.1007/s00417-010-1584-6

JGP

Supplemental material

Eckhardt et al., https://doi.org/10.1085/jgp.201912333

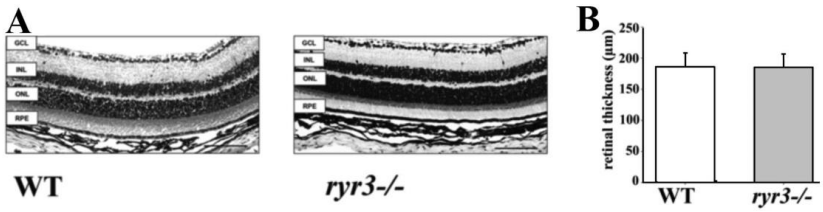

Figure S1. **Retinal morphology and layer structure is unaltered in *ryr3*$^{-/-}$ mice. (A)** Overview staining of 5-µm paraffin sections using hematoxylin and eosin revealed no changes in the retinal structure of *ryr3*$^{-/-}$ mice compared with their WT controls. GCL, ganglion cell layer; INL, inner nuclear layer; ONL, outer nuclear layer; RPE, retinal pigment epithelium. Scale bars, 100 µm. **(B)** Furthermore, no significant difference in mean (±SEM) retinal thickness was detectable.

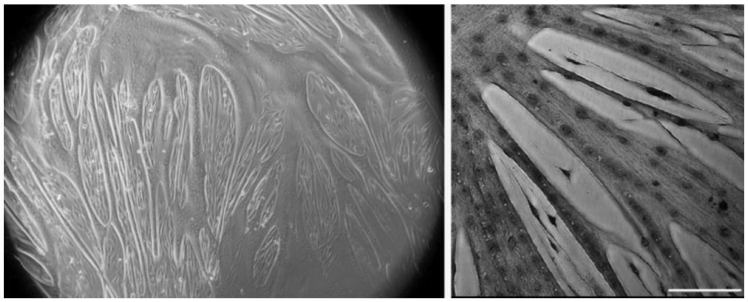

Figure S2. **Photomicrographs of myotubes from EOM**. Left: Low-magnification view of myotubes after 1–2 d in differentiation medium. Right: Cells were fixed with 3% paraformaldehyde 5 d after differentiation medium and stained with hematoxylin and eosin. Scale bar, 50 µm.

Table S1. **Primers used for qPCR and mouse genotyping**

Gene	Forward	Reverse
ACTN2	5′-CATCGAGGAGGATTTCAGGAAC-3′	5′-CAATCTTGTGGAACCGCATTTT-3′
CACNA1C	5′-TCCCGAGCACATCCCTACTC-3′	5′-ACTGACGGTAGAGATGGTTGC-3′
CACNA1S	5′-TCAGCATCGTGGAATGGAAAC-3′	5′-GTTCAGAGTGTTGTTGTCATCCT-3′
CASQ1	5′-ATGAGAGCTACCGACAGGATG-3′	5′-CACCGTCGTACTCAGGGAAG-3′
CASQ2	5′-TGCTCATGGTGGGGGTTTATC-3′	5′-AGGTTCGTGGTAATAGAGACAGA-3′
JP-45	5′-CGGGCTCAAGAAGATGGAAA-3′	5′-CTTGTTGAGCGTCAGATCTCC-3′
KCNMA1	5′-GCCAACAGAGAGAGCCGAAT-3′	5′-TCTTCAAAATAGATCAGCCGCC-3′
PVALB	5′-ATCAAGAAGGCGATAGGAGCC-3′	5′-GGCCAGAAGCGTCTTTGTT-3′
RYR1	5′-GCCTTTGACGTGGGATTACAG-3′	5′-CCCCAACTCGAACCTTCTCTC-3′
RYR3	5′-ACCAGCAGG AGCAAG TAC G-3′	5′-GGGGTCGTGTCAAAGTAGTCA-3′
RYR3 genotyping	5′-ATGAAGTTGTACTCCAGTGCATTGC-3′	5′-TCCAGGAATCTCTGGTATACTAGG-3′
SLC8A3	5′-GCATATGGGGAGCTGGAGTT-3′	5′-GCTTCCTGTCTGTCACTTCTGAT-3′

Table S2. **Kinetic properties of isolated EOM from WT and *ryr3*$^{-/-}$ mice**

	EOM	Peak force (ms)	TTHP (ms)	TTP (ms)	HRT (ms)
Twitch force kinetic parameters	WT EOM	0.328 ± 0.095	2.53 ± 0.24	10.09 ± 1.06	42.28 ± 9.82
		(*n* = 8)	(*n* = 8)	(*n* = 8)	(*n* = 8)
	ryr3$^{-/-}$ EOM	0.126 ± 0.017*	8.81 ± 2.29*	42.75 ± 8.78**	147.44 ± 8.36****
		(*n* = 9)	(*n* = 9)	(*n* = 9)	(*n* = 9)

Experiments were performed at 30°C. Values represent mean ± SEM. *, P < 0.05; **, P < 0.01; ****, P < 0.0001, Student's *t* test.

Video 1. **WT mouse swimming in cued water maze.** Experiments were performed as described in the Materials and methods section.

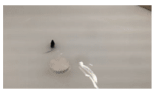

Video 2. ***ryr3*$^{-/-}$ mouse swimming in cued water maze.** Experiments were performed as described in the Materials and methods section.

2.3 Paper 2

Molecular basis of impaired extraocular muscle function in a mouse model of congenital myopathy due to compound heterozygous RYR1

Jan Eckhardt[a], Christoph Bachmann[a], Sofia Benucci[a], Moran Elbaz[a], Alexis Ruiz[a], Francesco Zorzato[a,b] and Susan Treves*[1a,b].

[a]Departments of Biomedicine and Anaesthesia, Basel University Hospital, Hebelstrasse 20, 4031 Basel, Switzerland.

[b]Department of Life Science and Biotechnology, University of Ferrara, Via Borsari 46, 44100, Ferrara, Italy.

*To whom correspondence should be sent: Prof Susan Treves, LAB 408 ZLF, Hebelstrasse 20, 4031 Basel, Switzerland. E-mail: susan.treves@unibas.ch Tel. +41612652373; FAX +41612653704

Classification: Biological sciences: physiology, medical sciences, genetics

Key words: ryanodine receptor, mutations, congenital myopathies, extra ocular muscles, MYH13, mouse model

Abstract

Mutations in the *RYR1* gene are the most common cause of human congenital myopathies and patients with recessive mutations are severely affected and characteristically display ptosis and/or ophthalmoplegia. In order to gain insight into the mechanism leading to extraocular muscle involvement, we investigated the biochemical, structural and physiological properties of eye muscles from mouse models we created knocked-in for *RYR1* mutations. *Ex vivo* force production in extraocular muscles from compound heterozygous RyR1p.Q1970fsX16+p.A4329D mutant mice was significantly reduced compared to that observed in WT, single heterozygous mutant carriers or homozygous RyR1p.A4329D. The decrease in muscle force was also accompanied by approximately a 40% reduction in RyR1 protein content, a decrease in electrically evoked calcium transients, disorganization of the muscle ultrastructure and a decrease in the number of calcium release units. Unexpectedly, the superfast and ocular-muscle specific myosin heavy chain-EO isoform was almost undetectable in RyR1p.Q1970fsX16+p.A4329D mutant mice.

The results of this study show for the first time that the extraocular muscle phenotype caused by the RyR1p.Q1970fsX16+p.A4329D compound heterozygous *RYR1* mutations is complex and due to a combination of modifications including a direct effect on the macromolecular complex involved in calcium release and indirect effects on the expression of myosin heavy chain isoforms.

Introduction

In skeletal muscle, calcium is a key second messenger regulating contraction and the sarcoplasmic reticulum (SR) is the intracellular organelle involved in its regulation (1, 2). The ryanodine receptor Ca^{2+} channel (RyR1) present on the terminal cisternae of the SR, is closely apposed to and is directly activated by, the dihydropyridine receptor (DHPR) an L-type Ca^{2+} channel which functions as voltage sensor (3). Upon depolarization, the voltage sensor undergoes a conformational change which causes the opening of the RyR1, leading to the release of Ca^{2+} from the lumen of the SR; this elevation of the myoplasmic [Ca^{2+}] is necessary for, and leads to, muscle contraction and this process is called excitation-contraction coupling (ECC) (1-4).

Mutations in *RYR1*, the gene encoding the RyR1, are the most common cause of neuromuscular diseases having a calculated incidence of approximately 1:3000 (5-7). Patients can present a variety of symptoms and phenotypes ranging from Malignant Hyperthermia Susceptibility (MHS; MIM#145600), exertional rhabdomyolysis, central core disease (CCD; MIM#11700), King-Denborough Syndrome, some forms of Multi-minicore Disease (MmD, MIM #255320), Centronuclear myopathy (CNM, MIM #255320) and Congenital Fiber Type Disproportion (CFTD). The disease phenotype resulting from *RYR1* mutations largely depends on their location within the *RYR1* coding sequence and whether the mutations are dominant or recessive (5, 6). Dominant mutations are more commonly associated with the MHS/exertional rhabdomyolysis and CCD phenotypes, while most cases of MmD, CNM and CFTD are associated with recessive mutations. Importantly, the phenotypic characteristics of patients carrying dominant and recessive *RYR1* mutations are quite distinct. Patients carrying dominant mutations display involvement of proximal and axial muscles (5, 8) whereas patients with recessive mutations are typically more severely affected, often requiring nocturnal ventilation and characteristically displaying involvement of extraocular muscles (EOM), leading to ophthalmoplegia and or ptosis (5, 7, 9). From a biochemical point of view patients with recessive (but not dominant) mutations show a significant reduction of RyR1 protein content in their muscles (10, 11) leading us to hypothesize that the pathomechanism of dominant and recessive *RYR1* mutations is different.

In order to gain deeper insight into the mechanism leading to severe muscle involvement in patients with recessive ryanodinopathies, we recently created the RyR1p.Q1970fsX16+p.A4329D double knock in (referable as DKI mice) mutant mouse model, knocked in for *RYR1* mutations identified in a severely affected patient (12). Extensive biochemical and physiological characterization of EDL and soleus muscles from the DKI mice revealed that their muscles contained reduced amounts of RyR1 protein, had cores and areas of myofibrillar disorganization and exhibited decreased electrically evoked Ca^{2+} transients. The DKI mice also ran significantly less and showed a decrease in body weight (13). Thus, the skeletal muscle phenotype of the mouse model recapitulates the clinical picture of patients. The result of this first study, however, shed little light into the molecular mechanism through which EOMs are selectively affected in patients with recessive *RYR1* mutations.

EOMs constitute a separate muscle allotype compared to limb or respiratory muscles: they have a different embryonic origin, are innervated from the cranial nerves, are highly vascularized, have almost no glycogen stores and contain a large number of mitochondria (14-17). Additionally, they are super-fast, fatigue resistant and express a specific myosin heavy chain isoform called MyHC-EO encoded by the *MYH13* gene (18, 19). EOMs are specifically spared in patients with Duchenne muscular dystrophy but affected in patients with myasthenia gravis and mitochondrial myopathies (20-22). Mutations in several genes important for the maintenance of mitochondrial DNA (mtDNA) have been identified in patients with progressive ophthalmoplegia (22). Additionally, mutations in *MYF5*, *MYH2* and *RYR1* have been identified in patients with myopathies and ophthalmoplegia (7, 23, 24) but little is known about the molecular basis of EOM involvement. We therefore used the mouse models we created (13, 25) to investigate the physiological and biochemical properties of EOMs from mice carrying recessive *RYR1* mutations. Our results show that the eye muscle phenotype is the result of a combination of changes, including defects in ECC, changes in the ultrastructural organization of the EOM and decreased mitochondria and the almost complete absence of MyHC-EO.

Results

EOM force is significantly diminished in RyR1p.Q1970fsX16+p.A4329D mutant mice.

Patients with recessive *RYR1* mutations frequently, show involvement of EOMs (5, 7, 9). We therefore investigated whether such muscles are also affected in a *RYR1* mutant mouse models. In order to answer this question directly we investigated the mechanical properties of isolated EOMs from single heterozygous *RYR1* mutant carriers (heterozygous RyR1p.Q1970fsX16, referable as Ex36; heterozygous RyR1p.A4329D, referable as Ex91), homozygous RyR1p.A4329D (referable as HO91) and DKI mice (RyR1p.Q1970fsX16+p.A4329D) compared to WT. Using a force transducer, we measured the force generated by electrical stimulation of medial rectal muscles from which oblique muscles had been removed, as previously reported (26). The mean force generated in response to a single pulse of 1.0 msec and of 24.6 V was not significantly different between WT compared to single heterozygous *RYR1* and HO91 mutant mice; however, EOMs from the DKI mice developed almost no force (Fig. 1 and Supplementary Table 1). The mean absolute force ($\pm$SEM) developed by WT, Ex36, Ex91 and HO91 EOMs was 656$\pm$140 (n=10), 529$\pm$63 (n=8), 633$\pm$53 (n=4) and 817$\pm$239 (n=4) μNewtons, respectively while that developed by the DKI mice was 50$\pm$21 (n=6) or more than 10 times lower resulting in a significant decrease in the specific force (Supplementary Table 1). Additionally, the presence of the Ex36 and DKI *RYR1* mutations significantly decreased the overall length, weight and cross section of EOMs, whereas the presence of the HO91 mutation increased the weight and cross section of the EOMs. (Supplementary Table 1). Kinetic analysis of the twitches showed that the half time to peak and half relaxation times were significantly increased in EOMs from the DKI mice while the time to peak was only affected in the HO91 EOMs (Supplementary Table 2).

These results demonstrate that the presence of compound heterozygous *RYR1* mutations, but not of single *RYR1* mutations nor of the homozygous Ex91 *RYR1* mutation, significantly affect force generated in response to electrical stimulation. This effect was independent of neuronal RyR1 expression since isolated muscles were directly investigated by inducing action potentials via supramaximal field stimulation.

The presence of the RyR1p.Q1970fsX16+p.A4329D compound heterozygous mutation affects ECC.

The changes in the mechanical properties of EOMs from the DKI mice could be due to alterations in the content of proteins involved in ECC. Indeed, the RyR1 protein content in *extensor digitorum longus* (EDL) and soleus muscles from the same transgenic DKI mouse line was significantly decreased (13). We thus investigated by western blot analysis the relative expression of the major protein components of the ECC machinery. RyR1 protein content was approximately 40% lower compared to that in EOMs from WT littermates (Fig. 2A and B) as was the content of $Ca_v1.1$ and ß1. The content of the other SR proteins investigated was similar in WT and DKI mice (Fig. 2A and B). Similar results were obtained when ECC protein content was analyzed by Mass Spectrometry analysis (Supplementary Fig. 1), though in the latter case, calsequestrin 1 and 2, SERCA2 and calreticulin content was significantly increased whereas sarcalumenin content was decreased. We also investigated the expression levels of the transcripts encoding RYR1 and RYR3 (Fig. 2C); qPCR results confirm that the transcript encoding RYR1 was significantly decreased (from 1.0±0.13 to 0.60±0.06 in WT vs DKI mice, respectively; $P<0.05$ Student's *t* test) while that encoding RYR3 was increased from 1.0±0.2 to 1.90±0.24 (in WT vs DKI mice, respectively; $P<0.01$ Student's *t* test). Interestingly, in EOMs from single heterozygous and HO91 *RYR1* mutant mice the relative expression of the RYR1 transcript was either increased (Ex36 and Ex91) or unchanged (HO91) while the RyR1 protein content did not change, as assessed by quantitative western blot analysis. RYR3 transcript levels were similar in EOMs from WT, single heterozygous and HO91 *RYR1* mutant mice (Supplementary Fig.2A and B).

Since enzymes involved in epigenetic modifications are altered in limb muscles from patients with recessive *RYR1* myopathies (27, 28), we also investigated their expression levels in DKI EOMs. No changes in the expression levels of the DNA methylating enzymes DNMT1 and TRDMT1 were apparent, however transcripts encoding class II histone de-acetylases HDAC4 and HDAC9 were increased and there was a small but significant increase in HDAC1 in EOMs from the DKI mice (Figure 2C). As far as the HDAC1, -4 and -9 expression in HO91 EOMs, their levels were similar to those of EOMs from WT mice (values were 1.0± 0.11 and 0.867±0.05 for HDAC1;

1.0±0.12 and 0.93±0.15 for HDAC4 and 1.0±0.23 and 0.91±0.18 for HDAC9 in WT and HO91, respectively. N= 5).

The presence of the compound heterozygous *RYR1* mutations affects the content of the two main macromolecular complexes involved in ECC, namely the RyR1 and the DHPR. The decrease in these two calcium channels is likely to impact Ca^{2+} release, leading to a decrease in force development. In order to verify this directly, we studied the properties of electrically evoked Ca^{2+} transients in single isolated EOM fibers. Fibers were loaded with the calcium indicator Mag-Fluo-4 (Fig. 3A) and stimulated with a 0.5 msec bipolar pulse by means of a computer-controlled stimulator. The electrically evoked peak Ca^{2+} transient ($\Delta F/F$) was reduced by approximately 50% from 0.4±0.1 to 0.21± 0.1 in fibers from WT and the DKI mice, respectively (Fig. 3B and C), whereas the kinetics including half time to peak (HTTP), time to peak (TTP) and half relaxation times (HRT) were similar in WT and DKI EOM fibers (Fig. 3D).

EM analysis reveals myofibrillar disorganization and a decrease in the number of CRU in EOMs from RyR1p.Q1970fsX16+p.A4329D mutant mice.

Muscles of patients with *RYR1* mutations exhibit areas of myofibrillar disorganization and the presence of cores, a finding that was also made while examining EDL muscles from the DKI mouse (13). EM analysis of EOMs from DKI mice confirmed that the latter muscles exhibit alterations of the muscle architecture, myofibrillar disorganization and a decrease in the number of calcium release units (CRU) (Fig.4). Quantitative analysis showed that mis-alignment of the Z-discs occurred in 80% of the fibers from the DKI mice versus 0% in WT littermates (Supplementary Table 3). Quantitative analysis of CRU in 12 fibers from 3 WT and 15 fibers from 3 DKI mice, confirmed the visual observations, namely that EOMs from the DKI mice contain significantly fewer CRU/100 μm^2 (70.7±6.0 vs 40.8±3.7 in WT and DKI, respectively; P<0.001). Muscles from the DKI mice also showed a significant reduction in the number of mitochondria adjacent to CRU (30.0 ±3.3 vs 16.3 ±1.5 in WT and DKI, respectively; P<0.001, Student's *t* test) and an increase in the percentage of dyads (1.3±0.8 vs 6.1±2.7 in WT and DKI, respectively)(Supplementary Table 3).

DKI EOMs have reduced levels of MyHC-EO and altered content of many other skeletal muscle proteins.

EOMs are complex muscles, made up of different fiber types and expressing a mixture of MyHC isoforms including the EOM-specific isoform MyHC-EO (17, 18, 29). Quantitative PCR revealed differences between WT and DKI mice, namely a small increase in the MYH2 transcripts encoding the MyHC2A as well as the embryonic/fetal isoform MYH8 (MyHC-neo), MyHC6 (α-cardiac isoform) and of the slow MYH7 isoform. Surprisingly this was accompanied by a dramatic reduction in the EOM-specific MYH13 (Fig. 5A). High resolution gel electrophoresis, western blot and Mass Spectrometry analysis confirmed that changes were occurring at the protein level as well (Fig. 5B, C and D, respectively). Importantly, the immunoreactive band corresponding to MyHC-EO was almost completely absent in EOMs form the DKI mice (Fig. 5C). Analysis of MYH transcript expression in the single heterozygous and HO91 *RYR1* mutant mice showed that there was an increase in MYH7 expression in EOMs from heterozygous RyR1p.Q1970fsX16 mice (Supplementary Fig. 2C); no changes in the MyHC-EO protein content in the EOMs from single *RYR1* mutant mice (Supplementary Fig. 2D). The transcript encoding MYH13 as well as MyHC-EO protein were decreased in HO91 EOMs, however not to the same extent as in the DKI mice (transcript values were 0.80 ± 0.03 $p<0.0001$ and % MyHC-EO protein content was $46.07 \pm 12.13\%$ $p<0.01$ N=5 in HO91 vs WT, respectively) (Supplementary Figure 2C and 2D).

To assess in-depth changes occurring as a consequence of the compound heterozygous *RYR1* mutations we performed extensive Mass Spectrometry analysis. Significant ($q<0.05$) changes in the content of >1200 protein occurred between WT and DKI EOMs (Fig. 6A and B). The proteins showing the greatest decrease in content being MyHC-EO (MYH13), phosducin-like protein, myosin binding protein H-like (MYBPHL), RyR1, protein FAM171A2 and protein PBDC1 (Fig. 6 and Supplementary Table 4). On the other hand, the skeletal muscle carbonic anhydrase 3 isoform was the most up-regulated protein, showing an increase of approximately 17 times, followed by Myosin regulatory light chain 2 ventricular/ cardiac muscle isoform, Homeodomain-only protein, Secretory carrier-associated membrane protein 2, MyHC7, Major urinary protein 1 and TnnC1 (Fig. 6B and Supplementary Table 5). Cellular component pathway analysis indicated

that most mitochondrial proteins (including those of the mitochondrial envelope, inner membrane, matrix, respiratory chain and cytochrome complexes) are down-regulated, confirming the EM observations that EOMs from the DKI contain fewer mitochondria. Additionally, myosin content was severely altered. KEGG pathway enrichment analysis revealed that the most affected pathways are those involved in oxidative phosphorylation and the TCA cycle, as well as muscle contraction (Fig. 6C).

Discussion

In the present study we investigated EOMs from a compound heterozygous mouse model carrying two *RYR1* mutations identified in a child severely affected by MmD. Our results provide mechanistic insight into the molecular basis of impaired extraocular muscle function and indicate that the phenotype of our mouse model faithfully recapitulates the clinical picture of MmD patients with compound heterozygous *RYR1* mutations.

The striated muscle phenotype of congenital myopathies linked to recessive *RYR1* mutations is influenced by the genetic status of the patients, that is whether they carry dominant or recessive mutations. In particular, in the presence of dominant mutations EOMs are usually spared whereas they are often compromised in the presence of recessive mutations which present either as homozygous mutations or as two distinct mutations at the heterozygous state (5-9). Since *RYR1* encodes the RyR1 SR Ca^{2+} release channel playing a fundamental role in ECC, our first aim was to assess the impact of mutations on the mechanical, biochemical and physiological properties of isolated EOMs. Upon *ex vivo* electrical stimulation the force developed by EOMs from the DKI mice was close to zero. Such a result was not completely unexpected since the mechanical properties of isolated EDL and soleus muscles from the same transgenic DKI mouse line were also severely reduced, albeit to a lower extent compared to EOMs (13). The presence of single heterozygous (RyR1p.Q1970fsX16 or RyR1p.A4329D) or homozygous (RyR1p.A4329D) mutations cause different phenotypes depending on muscle type and mutation. Indeed, the missense RyR1p.A4329D mutation at the heterozygous and homozygous state does not significantly impact force production in EOMs (this manuscript), nor in EDL muscles (manuscript in preparation) whereas the expression of the RyR1p.Q1970fsX16 frame shift mutation (leading to a premature stop codon), affects limb muscles (25), but spares EOMs (this manuscript). In fact, both the proband and mouse model carrying the Ex36 frameshift mutation at the heterozygous state had a skeletal muscle phenotype characterized by generalized muscle weakness and fatigability. This was accompanied by fibre size variability, a predominance of slow twitch fibres, fewer calcium release units, a decrease in the electrically evoked peak calcium transient as well as a decrease of RyR1 protein in their skeletal muscles (25). Thus the presence of Ex36 frameshift mutation at the heterozygous state is not associated with central core disease,

though it is associated with a myopathic phenotype sparing EOMs. Although we have no clear explanation for why EOMs are spared in the presence of the single heterozygous (dominant Ex36 or Ex91) and homozygous HO91 *RYR1* mutations, but not in the presence of the compound heterozygous (Ex36+Ex91 DKI) *RYR1* mutations, we cannot exclude the possibility that this is also linked to the content of RyR1 in EOMs. In fact, contrary to our findings in EDL and soleus muscles from the Ex36 heterozygous *RYR1* mutant mice (25), the presence of the WT allele plus the RyR1p.Q1970fsX16 frameshift mutation does not affect RyR1 content in EOMs (present study). Similarly, the presence of the HO91 mutation does not impact RyR1 content. Quantitative mass spectrometry analysis shows that the default RyR1 protein content in WT EOMs is approximately 50% lower than that of WT EDL (the unadjusted RyR1 protein ratio content in mouse EDL vs EOM is 0.596, q value=2.91×10^{-7}). Thus, we hypothesize that the reduction of the default RyR1 protein content in EOMs from WT mice may be due to differences in transcriptional regulation between EOMs and limb muscles (16, 17, 30, 31). We speculate that the difference of transcriptional regulation may blunt the effect of the monallelic expression of the WT RYR1 allele in EOMs from the heterozygous RyR1p.Q1970fsX16 mice. In the presence of the compound heterozygous p.Q1970fsX16+p.A4329D RyR1 mutations however, EOMs express 50% less RyR1 protein leading to fewer CRU resulting in a decrease of calcium release and poor muscle contraction.

Striated skeletal muscles are highly dependent upon their finely defined architecture as the Ca^{2+} released from the SR by structures referred to as CRU binds to the neighboring contractile proteins to initiate muscle contraction. Mitochondria are often associated with or appear in close proximity to the CRU (32, 33). In EOMs from the DKI mice there is a 43% reduction in the number of CRU, myofibrillar disorganization and sarcomeric disruption. The effect was so severe that Z-disc mis-alignment was evident in 80% of the examined electron micrographs of EOMs from the DKI mice but none from WT littermates; muscles from the mutant mice also contained dyads and importantly, showed a reduced number of mitochondria associated with the CRU. The decrease in the number of mitochondria observed in EM micrographs was supported by the Mass Spectrometry/proteomic analysis data which confirmed that mitochondrial proteins as well as metabolic pathways are significantly downregulated in EOMs from DKI mice. Involvement of EOM leading to progressive external ophthalmoplegia and ptosis are common in patients with

mitochondrial diseases caused by mutations in mtDNA (reviewed in 22). This is linked to the functional demands of EOMs which are different from those of other muscles, since they must remain active for extended periods of time, even during sleep. To cope with their constant activity, EOMs contain a large number of mitochondria, express higher levels of mitochondrial enzymes and rely on blood glucose oxidized via the Krebs cycle as a constant energy source (16, 17). Thus, a decrease in the number of mitochondria would compromise EOM activity leading to ophthalmoplegia, as seen in patients with recessive *RYR1* mutations. Nevertheless, it should be pointed out that the pathomechanism of EOM involvement in patients with recessive *RYR1* mutation and chronic progressive ophthalmoplegia is different. Mouse models created to study mitochondrial myopathies as well as affected patients show (i) a progressive course, which is not the case in recessive *RYR1*-myopathies, (ii) muscles show an increase (not a decrease) in the number of mitochondria and (iii) the contractile properties (force generated) of muscles from mice mutated in mitochondrial genes are only slightly decreased (33, 35).

The results of the present study demonstrate that additional factors contribute to the weak eye muscle phenotype in the DKI mice (and patients). An important finding relates to the altered expression of MyHC isoforms in the RyRp.Q1970fsX16+p.A4329D, but not in the single heterozygous mutant mice. In the former mouse line, there is an almost total absence of the MYH13 transcript and barely detectable levels of MyHC-EO, the isoform responsible for the superfast characteristic of EOM (18, 19, 29). Concomitantly, there is an increase of cardiac atrial α-myosin (MYH6) and of slow muscle myosin MYH7. The absence of MyHC-EO is puzzling but parallels the decrease in RyR1 protein content and does not occur in single heterozygous *RYR1* mutant mice (though its level is decreased in the HO91 RYR1 mutant mouse but not to the same extent). Under normal conditions MyHC-EO expression in mice has a late onset, occurring at the end of the first postnatal week (18, 36) and, importantly, muscle activity is important for initiating and maintaining its expression (37). Thus, its very low expression levels may be caused by the decrease of ECC, calcium release and muscle activity during eye muscle development. Decreased EOM activity also leads to additional changes as confirmed by the altered expression of many enzymes identified by Mass Spectrometry, including carbonic anhydrase 3, CaM kinase and creatine kinase.

In conclusion the results of this study show for the first time the molecular basis of EOM dysfunction linked to compound heterozygous *RYR1* mutations causing a congenital myopathy. The altered calcium homeostasis and reduced calcium released by muscle fibres during ECC, leads to reduced activity of the eye muscles during development causing mis-expression of MyHC isoforms, lack of MyHC-EO, myofibrillar disorganization, displacement and decreased number of mitochondria.

Materials and Methods

Animal Model and ethical permits: The RyR1p.Q1970fsX16+p.A4329D mouse model was generated in our laboratory using CRISPR/Cas9 as previously described (13, 25). Experiments were carried out on 8-12 weeks old mice. All experimental procedures were approved by the Cantonal Veterinary Authorities (BS Kantonales Veterinäramt Permit numbers 1728 and 2115). All experiments were performed in accordance with relevant guidelines and regulations.

Isometric force measurements: Electrically evoked force was measured in isolated EOMs as previously described (26). Briefly, EOMs were mounted intact on a MyoStation-intact (Myotronic, Heidelberg, Germany). The force transducer was equipped with small hooks. The medial rectus muscle was tied with a prolene suture (Ethicon, EP8703H) by stitching through the eyeball close to the entry point of the muscle. The other side was ligated with a surgical suture on the leftover orbital socket bone (Look, SP102). After ligation, the remaining EOMs, the optic nerve and the retractor bulbi muscle were surgically removed. For force measurements, EOMs were stimulated with a single pulse of 1 msec and of 24.6 V. Experiments were performed at 30° C. Muscle force was digitized at 4 kHz using an AD Instrument (Powerlab 2/25) or MyoDat (Myotronic, Heidelberg, Germany) including its interface and computer-controlled stimulator.

Quantitative Real-time PCR: Total RNA was extracted from the EOMs using Trizol (Invitrogen, 15596-018) following the manufacturer's protocol. 1000 ng were reverse transcribed using the high capacity cDNA Reverse Transcription Kit (Applied Biosystems, 4368814). cDNA was amplified by quantitative real-time PCR (qPCR) using Power-Up™ Sybr™ Green Master Mix (Applied Biosystems, A25742) as previously described (26, 28). The sequence of the primers used for qPCR is given in Supplementary Table 6. Quantitative PCR (qPCR) was performed on a 7500 Fast Real-Time PCR machine from Applied Biosystems using the 7500 software v2.3. Gene expression was normalized to *ACTN2* expression as a muscle-specific gene, using the ΔΔCt method. Results are expressed as fold change of gene expression in DKI mice compared to expression in WT mice.

Electrophoresis and Immunoblotting: Total muscle homogenates were prepared form flash frozen EOM samples in 10 mM HEPES pH 7.4, 150 mM NaCl, 1 mM EDTA and anti-protease (Roche, 11873580001) as previously described (25). Protein concentration was determined using a Protein Assay Kit II (Bio-Rad Laboratories, 500-0002) and BSA was used as a standard. SDS-PAGE, protein transfer on to nitrocellulose membranes and immunostaining were performed as previously

described (25), except for parvalbumin and MyHC. For parvalbumin, proteins were separated on a 10% Tris-Tricine gel (38) and subsequently transferred onto nitrocellulose. For separation of MyHC isoforms, high resolution gel electrophoresis was performed (39). The following primary antibodies were used for Western Blotting: anti-RyR1 (Cell Signaling, 8153S), anti-$Ca_v1.1$ (Santa Cruz sc-8160), anti-$Ca_v1.2$ (Santa Cruz, sc-25686), anti- DHPR β1a (Santa Cruz, sc-32079), anti-calreticulin (Abcam, ab-92516), anti-sarcalumenin (Thermo Fischer Scientific, MA3–932), anti-calsequestrin-1 (Sigma, C-0743) and calsequestrin-2 (Abcam, ab-3516), anti-SERCA1 (Santa Cruz, sc-8093), anti-SERCA2 (Santa Cruz, sc-8095), anti-JP-45 (40), anti-parvalbumin (Swant, PV25), anti-MyHC (Millipore, 05-716) and anti-MyHC13 (DSHB Iowa, 4A6). Secondary peroxidase conjugates were Protein G-peroxidase (Life Technologies, P21041) and peroxidase-conjugated goat anti-mouse IgG (Sigma, A2304). The immunopositive bands were visualized by chemiluminescence using the WesternBright ECL-HRP Substrate (Advansta, K-12045-D50) or the Chemiluminescence kit from Roche (Roche, 11500694001). Representative immunoblots are shown in Supplementary Figure 3. Analysis of the intensity of the immunopositive bands was performed using ImageJ/FIJI as previously described (13, 25, 26)(Schindelin et al., 2012)(Schindelin et al., 2012)(Schindelin et al., 2012)(Schindelin et al., 2012). The intensity values were normalized to the intensity of MyHC all (Millipore) antibody.

***Proteomics analysis using tandem mass tags*.**

Peptide samples were prepared, including TMT labeling, HpH-fractionation and LC-MS and data analysis from mouse muscle tissues as recently described (41). In brief, 1µg of TMT labeled peptides were LC-MS/MS analyzed on Q-Exactive HF mass spectrometer coupled to an EASY nano-LC 1000 system (both Thermo Fisher Scientific) using a linear 90 minute LC gradient and a top10 MS approach at a MS2 resolution of 30k (FWHM at 200 m/z). The data were analyzed by searching against a protein database containing sequences of the predicted SwissProt entries of *mus musculus* (www.ebi.ac.uk, release date 2019/03/27), Myh2 and Myh13 from Trembl, the six calibration mix proteins and commonly observed contaminants (in total 17,414 sequences) using the SpectroMine software (Biognosys, version 1.0.20235.13.16424). Protein quantification and statically analysis was carried out using our in-house developed SafeQuant R script as recently described (v2.3) (42). P-values were calculated using empirical Bayes moderated t-statistics and were corrected for multiple testing using the Benjamini–Hochberg method into q-values. The

errors were calculated according to the propagation of uncertainty.

EM analysis: Data were collected from EOMs isolated from three months-old WT (n=3 mice) and RyR1p.Q1970fsX16+p.A4329D (n=3 mice). In each sample, 12-15 fibers were analyzed. In each fiber 2-3 micrographs (all at the same magnification, 14K, and of non-overlapping regions) were randomly collected from longitudinal sections. CRUs and mitochondria were marked and counted in each micrograph. The number of CRUs/area, mitochondria/area and mitochondria-CRUs pairs/area is reported as an average number/100 μm^2 (13, 25). For mitochondrial quantification 14 fibers from 3 WT mice and 15 fibers from 3 DKI mice were analyzed. In each EM image we also determined the number of dyads i.e. incomplete triads expressed as percentages over the total number of CRUs.

Single fiber calcium measurements: Ca^{2+} measurements were performed on single EOM fibers, isolated as previously described (26). Briefly, isolated EOM fibers were plated on a chamber with a glass coverslip bottom, previously coated with 2 µl of laminin 1 mg/ml (Sigma, Darmstadt, Germany) and incubated for 20 min at 20 °C in Ringer solution containing 10 µM of the low affinity calcium indicator Mag-Fluo-4 AM (Invitrogen, M14206). Fibers were stimulated by means of a 0.5 msec bipolar pulse using a computer-controlled stimulator (Myotronic, Heidelberg, Germany, MyoDat + Stimulator Amplifier). A Nikon A1R laser-scanning confocal microscope (Nikon Instruments Inc.) with a 60× oil immersion Plan Apo VC Nikon objective (numerical aperture, 1.4) in resonant mode at super high temporal resolution (7918 lines per second) was used to record the linescans. These were saved as stacked images using the microscope software (NIS-Elements, version 4.60). All measurements were performed at room temperature.

Analysis of calcium transient: A detailed description of the method was recently published (26). Briefly, for analysis of the Ca^{2+} transient, the baseline was calculated as the average of the first 5 msec of the profile. Once the maximum height of the transient was reached, the $\Delta F/F$ was calculated. The beginning of the peak was defined as the time where the transient increased by 5% of the maximum height, with respect to the baseline, for the first time. Time To Peak (TTP) is the time from the beginning of the peak to the maximum height. Half Time To Peak (HTTP) is the time from the beginning of the peak to the time where the transient increases by 50% of the maximum height with respect to the baseline, for the first time. Half Relaxation Time (HRT) is the

time from the maximum height until the time where the transient is higher than 50% of the maximum height, for the last time.

Statistical analysis and graphical software: Statistical analysis was performed using the unpaired two-tailed Student's *t* test or the ANOVA test followed by the Bonferroni post hoc test for multiple group comparisons. Means were considered statistically significant when the P value was <0.05. Data was processed, analyzed and plotted using the software OriginPro 2019 (OriginLab Corporation, Northampton, MA, USA) or GraphPad Prism 4.00 (GraphPad Software Inc., San Diego, CA, USA). Images were assembled using Adobe Photoshop CS (version 8.0).

Acknowledgements

This work was supported by a grant from the Swiss National Science Foundation (SNF N° 31003A-169316), a grant from the Swiss muscle foundation (FSRMM), a grant from NeRAB, a grant from the OPO Stiftung (N°2013/14-0038), Botnar Stiftung (N° OOG-19-001) and PRIN 2015 to FZ. The support of the Department of Anesthesia Basel University Hospital and the technical support of Anne-Sylvie Monnet and of Cinzia Tiberi Schmidt of the BioEM C-CINA are gratefully acknowledged. We also thank Dr. Alexander Schmidt and the group of the proteomics core facility, Biozentrum, Basel University, for performing and analysing the mass spectrometry experiments.

Conflict of interests: The authors declare that no conflict of interests exists.

References

1. Rios, E., and Pizarro, G. (1991) Voltage sensor of excitation-contraction coupling in skeletal muscle. *Physiol. Rev.,* 71**,** 849-908.
2. Endo, M. (1977) Calcium release from the sarcoplasmic reticulum. *Physiol. R*ev., 57, 71-108.
3. Fleischer, S., and Inui, M. (1989) Biochemistry and biophysics of excitation-contraction coupling. *Annu. Rev. Biophys. Biophys. Chem.,* 18, 333-364.
4. Franzini-Armstrong, C., and Jorgensen, A. (1994) Structure and development of E-C coupling units in skeletal muscle *Annu. Rev. Physiol.* 56, 509-534.
5. Jungbluth, H., Treves, S., Zorzato, F., Sarkozy, A., Ochala, J., Sewry, C., Phadke, R., Gautel, M., and Muntoni, F. (2018) Congenital myopathies: disorders of excitation-contraction coupling and muscle contraction. *Nat. Rev. Neurol.,* 14, 151-167.
6. Treves, S., Jungbluth, H., Muntoni, F., and Zorzato, F. (2008) Congenital muscle disorders with cores: the ryanodine receptor calcium channel paradigm. *Curr. Opin. Pharmacol.,* 8, 319-326.
7. Treves, S., Jungbluth, H., Voermans, N., Muntoni, F., and Zorzato, F. (2017) Ca^{2+} handling abnormalities in early onset muscle diseases: novel concepts and perspectives. *Stem. Cell Develop. Biol.,* 64, 201-212.
8. Jungbluth, H. (2007) Central core disease. *Orphanet. J. Rare Dis.,* 2, 25 DOI: 10.1186/1750-1172-2-2-25.
9. Jungbluth, H. (2007) Multi-minicore disease. *Orphanet. J. Rare Dis.*, 2, 31 DOI: 10.1186/1750-1172-2-31.
10. Monnier, N., Marty, I., Faure, J., Castiglioni, C., Desnuelle, C., Sacconi, S., Estournet, B., Ferreiro, A., Romero, N., Laquerriere, A., Lazaro, L., Martin, J. J., Morava, E., Rossi, A., Van der Kooi, A., de Visser, M., Verschuuren, C., and Lunardi, J. (2008). Null mutations causing depletion of the type 1 ryanodine receptor (RYR1) are commonly associated with recessive structural congenital myopathies. *Hum. Mutat.,* 29, 670-678.
11. Zhou, H., Jungbluth, H., Sewry, C. A., Feng, L., Bertini, E., Bushby, K., Straub, V., Roper, H., Rose, M.R., Brockington, M., Kinali, M., Manzur, A., Robb, S., Appleton, R., Messina, S., D'Amico, A., Quinlivan, R., Swash, M., Müller, C. R., Brown, S., Treves, S., and

Muntoni, F. (2007) Molecular mechanisms and phenotypic variation in RYR1-related congenital myopathies. *Brain*, 130, 2024-2036.

12. Klein, A., Lillis, S., Munteanu, I., Scoto, M., Zhou, H., Quinlivan, R., Straub, V., Manzur, A.Y., Roper, H., Jeannet, P.Y., Rakowicz, W., Jones, D.H., Jensen, U.B., Wraige, E., Trump, N., Schara, U., Lochmuller, H., Sarkozy, A., Kingston, H., Norwood, F., Damian, M., Kirschner, J., Longman, C., Roberts, M., Auer-Grumbach, M., Hughes, I., Bushby, K., Sewry, C., Robb, S., Abbs, S., Jungbluth, H., and Muntoni. F (2012) Clinical and genetic findings in a large cohort of patients with ryanodine receptor 1 gene-associated myopathies. *Hum. Mutat.*, 33, 981-988.
13. Elbaz, M., Ruiz, A., Bachmann, C., Eckhardt, J., Pelczar, P., Venturi, E., Lindsay, C., Wilson, A. D., Alhussni, A., Humberstone, T., Pietrangelo, L., Boncompagni, S., Sitsapesan, R., Treves, S., and Zorzato, F. (2019) Quantitative RyR1 reduction and loss of calcium sensitivity of RyR1Q1970fsX16+A4329D cause cores and loss of muscle strength. *Hum. Mol. Genet.*, 28, 2987-2999.
14. Hoh, J. F. Y., Hughes, S., Hugh, G., and Pozgaj, I. (1989) Three hierarchies in skeletal muscle fibre classification: allotype, isotype and phenotype. In UCLA Symposia on Molecular and Cellular Biology (Stockdale, F. and Kedes, L., eds), pp. 15–26, Alan R. Liss, New York.
15. Hauschka, S. D. (1994) The embryonic origin of muscle. In Myology (Engel, A.G. and Franzini-Armstrong, C., eds), pp. 3–73, McGraw Hill, New York.
16. Porter, J. D., Khanna, S., Kaminski, H. J., Rao, J. S., Merriam, A. P., Richmonds, C. R., Leahy, P., Li, J., and Andrade, F. H. (2001) Extraocular muscle is defined by a fundamentally distinct gene expression profile. *Proc. Natl. Acad. Sci. U.S.A.*, 98, 12062-12067.
17. Fischer, M. D., Gorospe, J. R., Felder, E., Bogdanovich, S., Pedrosa-Domellöf, F., Ahima, N. A., Rubinstein, N. A., Hoffman, E. P., and Khurana, T. S. (2002) Expression profiling reveals metabolic and structural components of extraocular muscles. *Physiol. Genomics*, 9, 71-84.
18. Wieczorek, D. F., Periasamy, M., Butler-Browne, G. S., Whalen, R. G, and Nadal- Ginard, B. (1985) Co-expression of multiple myosin heavy chain genes, in addition to a tissue-specific one, in extraocular musculature. *J. Cell Biol.*, 101, 618–629.

19. Schiaffino, S., Rossi, A. C., Smerdu, V., Leinwand, L. A., and Reggiani, C. (2015) Developmental myosins: expression patterns and functional significance. *Skeletal Muscle*, 5, 22 DOI 10.1186/s13395-015-0046-6.
20. Porter, J. D., Merriam, A. P., Khanna, S., Andrade, F. H., Richmonds, C. R., Leahy, P., Cheng, G., Karathanasis, P., Zhou, X., Kusner, L. L., Adams, M. E., Willem, M., Mayer, U., and Kaminski, H. J. (2003) Constitutive properties, not molecular adaptations, mediate extraocular muscle sparing in dystrophic mdx mice. *FASEB. J.*, 17, 893-895.
21. Kaminski, H. J., and Ruff, R. L. (1997) Ocular muscle involvement by myasthenia gravis. *Ann. Neurol.*, 41, 419–420.
22. Schrier, S. A., and Falk, M. J. (2011) Mitochondrial disorders and the eye. *Curr. Opin. Ophthalmol.*, 22, 325-331.
23. Lossos, A., Oldfors, A., Fellig, Y., Meiner,V., Argov, Z., and Tajsharghi, H. (2013) MYH2 mutation in recessive myopathy with external ophthalmoplegia linked to chromosome 17p13.1-p12. *Brain*, 136:, e238 doi. 1093/brain/aw365.
24. Di Gioia, S.A., Shaaban, S., Tüysüz, B., Elcioglu, N.H., Chan, W.M., Robson, C.D., Ecklund, K., Gilette, N.M., Hamzaoglu, A., Tayfun, G.A., Traboulsi, E.I., and Engle, E.C. (2018) Recessive MYF5 Mutations Cause External Ophthalmoplegia, Rib, and Vertebral Anomalies. *Am. J. Hum. Genet.*, 103, 115-124.
25. Elbaz, M., Ruiz, A., Eckhardt, J., Pelczar, P., Muntoni, F., Boncompagni, S., Treves, S., and Zorzato, F. (2019) Quantitative reduction of RyR1 protein caused by a single-allele frameshift mutation in RYR1 ex36 impairs the strength of adult skeletal muscle fibres. *Hum. Mol. Genet*., 28, 1872-1884.
26. Eckhardt, J., Bachmann, C., Sekulic-Jablanovic, M., Enzmann, V., Park, K.H., Ma, J., Takeshima, H., Zorzato, F., and Treves, S. (2019) Extraocular muscle function is impaired in *ryr3-/-* mice. *J. Gen. Physiol.*, 151, 929-943.
27. Rokach, O., Sekulic-Jablanovic, M., Voermans, N., Wilmshurst, J., Pillay, K., Heytens, L., Zhou, H., Muntoni, F., Gautel, M., Nevo, Y., Mitrani-Rosenbaum, S., Attali, R., Finotti, A., Gambari, R., Mosca, B., Jungbluth, H., Zorzato, F. and Treves, S. (2015) Epigenetic changes as a common trigger of muscle weakness in congenital myopathies. *Hum. Mol. Genet.*, 24, 4636-4647.
28. Bachmann, C., Noreen, F., Voermans, N.C., Schär, P.L., Vissing, J., Fock, J.M., Bulk, S., Kusters, B., Moore, S.A., Beggs, A.H., Mathews, K.D., Meye,r M., Genetti, C.A., Meola,

G., Cardani, R., Mathews, E., Jungbluth, H., Muntoni, F., Zorzato, F., and Treves, S. (2019) Aberrant regulation of epigenetic modifiers contributes to the pathogenesis in patients with selenoprotein N-related myopathies. *Hum. Mutat.* 40: 962-974.

29. Briggs, M. M., and Schachat, F. (2002) The superfast extraocular myosin (MYH13) is localized in the innervation zone in both the global and orbital layers of rabbit extraocular muscles. *J. Exp. Biol*., 205, 3133-3142.
30. Kish, P. E., Bohnsack, B. L., Gallina, D., Kasprick, D. S., and Kahana, D (2011) The eye as an organizer of craniofacial development. *Genesis*, 49, 222-230.
31. Verma, M., Fitzpatrick, K., and McLoon, L. K. (2017) Extraocular muscle repair and regeneration. *Curr. Ophthalmol. Rep.*, 5, 207-215 DOI 10.1007/s40135-017-0141-4.
32. Boncompagni, S., Rossi, A.E., Micaroni, M., Beznoussenko, G.V., Polishchuk, R.S., Dirksen, R.T., and Protasi, F. (2009) Mitochondria are linked to calcium stores in striated muscle by developmentally regulated tethering structures. *Mol. Biol. Cell.*, 20, 1058-1067.
33. Franzini-Armstrong, C., and Boncompagni, S. (2011) The evolution of the mitochondria - to-calcium release units relationship in vertebrate skeletal muscles. *J. Biomed. Biotechnol*., 2011, 830573 DOI 10.1155/2011/830573.
34. Wredenberg, A., Wibom, R., Wilhelmsson, H., Graff, C., Wiener, H. H., Burden, S. J., Oldfors, A., Westerblad, H., and Larsson, N. G. (2002) Increased mitochondrial mass in mitochondrial myopathy mice. *Proc. Natl. Acad. Sci. U.S.A.*, 99, 15066-15071.
35. Yin, H., Stahl, J. S., Andrade, F. H., McMullen, C. A., Webb-Wood, S., Newman, N. J., Biousse, V., Wallace, D. C., and Pardue, M. T. (2005) Eliminating the Ant1 isoform produces a mouse with CPEO pathology but normal ocular motility. *Invest. Ophthalmol. Vis. Sci*., 46, 4555-4562.
36. Brueckner,J. K., Itkis, O., and Porter, J. D. (1996) Spatial and temporal patterns of myosin heavy chain expression in developing rat extraocular muscle. *J. Muscle Res. Cell Motil.*, 17, 297-312.
37. Brueckner, J. K., Ashby, L. P., Prichard, J. R., and Porter, J. D. (1999) Vestibulo-ocular pathways modulate extraocular muscle myosin expression patterns. *Cell Tissue Res.*, 295, 477-484.
38. Schägger, H., and von Jagow, G. (1987) Tricine-sodium dodecyl sulfatepolyacrylamide gel electrophoresis for the separation of proteins in the range from1 to 100 kDa. *Anal. Biochem*.,166, 368–379.

39. Talmadge, R. J., and Roy, R. R. (1985) Electrophoretic separation of rat skeletal muscle myosin heavy chain isoforms. *J. Appl. Physiol*., 75, 2337-2340.
40. Zorzato, F., Anderson, A. A., Ohlendieck, K., Froemming, G., Guerrini, R., and Treves, S. (2000) Identification of a novel 45 kDa protein (JP-45) from rabbit sarcoplasmic-reticulum junctional-face membrane. *Biochem. J.,* 351, 537–543.
41. Obradovic, M. M. S., Hamelin, B., Manevsk, N., Couto, J. P., Sethi, A., Coissieux, M. M., Münst, S., Okamoto, R., Kohler, H., Schmidt, A., and Bentires-Alj, M. (2019) Glucocorticoids promote breast cancer metastasis. *Nature,* 567, 540-544.
42. Ahrné, E., Glatter, T., Viganò, C., von Schubert, C., Nigg, E. A., and Schmidt, A. (2016) Evaluation and improvement of quantification accuracy in isobaric Mass Tag-based protein quantification experiments. *J. Proteome Res.,* 15, 2537-2547.

Figure Legends

Figure 1: *Ex vivo* isometric force measurements in mouse EOM. A. Representative traces of the absolute twitch force obtained from isolated single extra ocular rectus muscles from WT, heterozygous Ex36, heterozygous Ex91 and DKI mice. **B**. Bar plot analysis of absolute twitch force. The bars represent the mean (±SEM). N= 10 WT, N=8 Ex36, N=4 Ex91, N= 5 HO91, N=6 DKI. Muscles were stimulated by electric field stimulation (EFS; 24.6V; 1 msec pulse). *P< 0.05

Figure 2: ECC proteins are diminished in EOMs from DKI mice. A. Representative immunoblots of total homogenates of EOMs from WT and DKI mice probed with the indicated antibodies. **B.** Immunoblot quantification panels show relative content of the indicated proteins as a % of the content of the same protein in EOMs from WT mice normalized to total MyHC content. Bar graphs represent the mean (± SEM) values from 2-4 separate pools of EOMs, each pool obtained from 3-4 mice. The intensity values obtained from WT mice were considered 100%. **C.** Quantitative real-time PCR (RT-qPCR) of the indicated transcripts in EOMs from DKI (filled triangles) mice relative to WT mice (empty circles). The latter were set as 1. Transcript levels were normalized to *ACTN2* as a muscle specific gene using the ΔΔCt method. Each symbol represents the duplicate value obtained in a single mouse *p<0.05; **p<0.01; (Student's *t* test).

Figure 3: Electrically evoked Ca^{2+} transients are diminished in EOM fibers from DKI mice. A. Confocal images of a single isolated fiber under transmitted light (bottom), and fluorescence (Mag-Fluo-4 fluorescence, 488nm excitation and 500-550 nm emission). Scale bars=30 μm. **B.** Representative traces of Ca^{2+} transients in EOM fibers from WT (black) and DKI (red) mice, evoked by EFS with a 0.5 ms bipolar pulse. **C.** Peak Ca^{2+} (ΔF/F) of the Mag-Fluo-4 fluorescence obtained by stimulating EOM fibers. A total of 33 fibers from 3 WT mice and 35 fibers from 2 DKI mice were analyzed. Box plots represents the upper and lower ΔF/F values. The central dot shows the mean value. **D.** Analysis of the kinetics of the Ca^{2+} transients: Half Time To Peak (HTTP), Time To Peak (TTP) and Half Relaxation Time (HRT) of the calcium transients are plotted White dots WT; grey dots DKI. A total of 33 fibers from 3 WT mice and 35 fibers from 2 DKI mice were analyzed. There were no significant differences in the properties of the kinetics. ****p<0.0001; Student's *t* test).

Figure 4: Ultrastructural disruption in EOMs from DKI mice. In WT EOM (left panels) sarcomeres, defined by the space between two Z lines, are highly organized and ordered. The I bands (black arrowheads) contain the CRU which are mainly made up by triads, that are composed by two SR vesicles and a central t-tubule (bottom left image, white arrows). Mitochondria are abundant and not placed in an orderly fashion next to CRU as in EDL muscles. In fibers from the DKI mice (right panels) there are fewer mitochondria; additionally, muscles contain many areas characterized by total disruption of the myofibrillar organization (black arrowheads). Many CRUs are either missing or damaged (bottom right image, white arrows). Scale bars, top 1 μm; bottom 0.4 μm.

Figure 5: EOMs from DKI mice show altered expression and content of myosin heavy chain isoforms. A. Quantitative real-time PCR (RT-qPCR) of the indicated transcripts in EOMs from DKI (filled triangles) mice relative to WT mice (empty circles). The latter were set as 1. Transcript levels were normalized to *ACTN2* as a muscle specific gene using the ΔΔCt method. The expression levels of MYH2 (encoding MyHC2A), MYH6, (encoding the α cardiac isoform), MYH7 (encoding MyHC slow) and MYH8 (encoding MyHC-neo) were significantly increased; transcript levels of MYH13 (encoding MyHC-EO) were significantly decreased. Each symbol represents the duplicate value obtained in EOMs from a single mouse *p<0.05; **p<0.01; ***p<0.001. **B.** Representative Coomassie Blue stained high resolution 7.5% acrylamide gel of myosin heavy chain isoforms present in WT and DKI EOMs. **C.** Western blot of a high resolution 7.5% acrylamide gel. **Top panel**, membrane stained with Ponceau Red; **central panel**, blots stained with a monoclonal Ab specific for MyHC-EOM (top lanes) and a monoclonal Ab specific for MyHC1 (bottom lanes); **bottom panel**, blot stained with a monoclonal Ab recognizing all MyHC. **D.** Relative expression of MyHC in EOMs as determined by Mass Spectrometry analysis. Results show the mean (±SEM) of 5 experiments and asterisks indicate a significant change based on q values *q<0.05.

Figure 6: Proteomic analysis of EOMs from DKI reveals significant differences in proteins involved in metabolic pathways as well as in the content of contractile proteins. A. Hierarchically clustered heatmaps of the relative abundance of proteins in DKI mice (green group) versus age and sex-matched wild type littermates (red group). Blue blocks represent proteins which are over-expressed, yellow blocks proteins which are decreased in DKI versus WT. Upper left inset, colors indicating relative protein content. Right shows overall number of increased

(blue) and decreased (yellow) proteins. Areas are relative to their numbers. **B.** Volcano plot of a total of 1253 quantified proteins which showed significant increased (blue) and decreased (yellow) content. The horizontal coordinate is the difference multiple (logarithmic transformation at the base of 2), and the vertical coordinate is the significant difference p value (logarithmic transformation at the base of 10). The proteins showing major change in content are abbreviated. **C.** Enriched GO terms analysis using Functional Enrichment Analysis from String v11.0 showing major pathways affected in the DKI EOMs. A q-value of equal or less than 0.05 was used to filter significant changes prior to the pathway analyses. Blue bars, Uniport key words; red bars, KEGG pathway; yellow bars, molecular function pathway; green bars, cellular component pathway.

Abbreviations: CCD, Central core disease; CNM, centronuclear myopathy; CFTD, congenital fiber type disproportion; CRU, calcium release units; DHPR, dihydropyridine receptor; DKI, double knock in mouse model; ECC, excitation contraction coupling; EDL, *extensor digitorum longus***;** EOM, extra ocular muscles; HO91, mouse model carrying the RyR1p.A4329D mutation at the homozygous state; HRT, half relaxation time; HTTP, half time to peak; MmD, Multi-minicore disease; mtDNA, mitochondrial DNA; MyHC, myosin heavy chain; RyR1, ryanodine receptor 1; SR, sarcoplasmic reticulum; TTP, time to peak; WT, wild type.

Figure 1

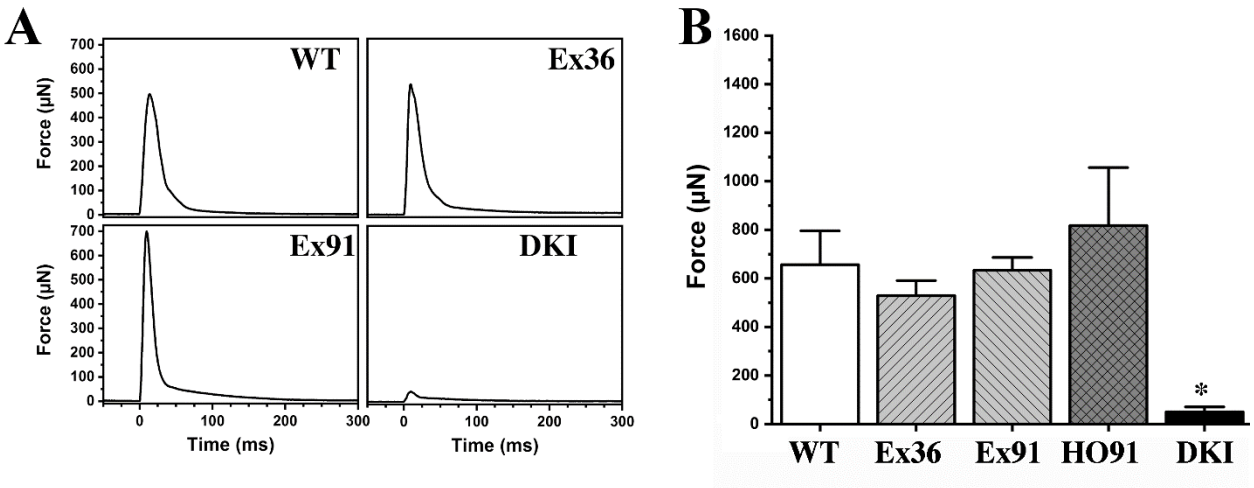
A
WT
Ex36
Ex91
DKI
Force (μN)
Time (ms)
B
Force (μN)
WT
Ex36
Ex91
HO91
DKI
*

Figure 2

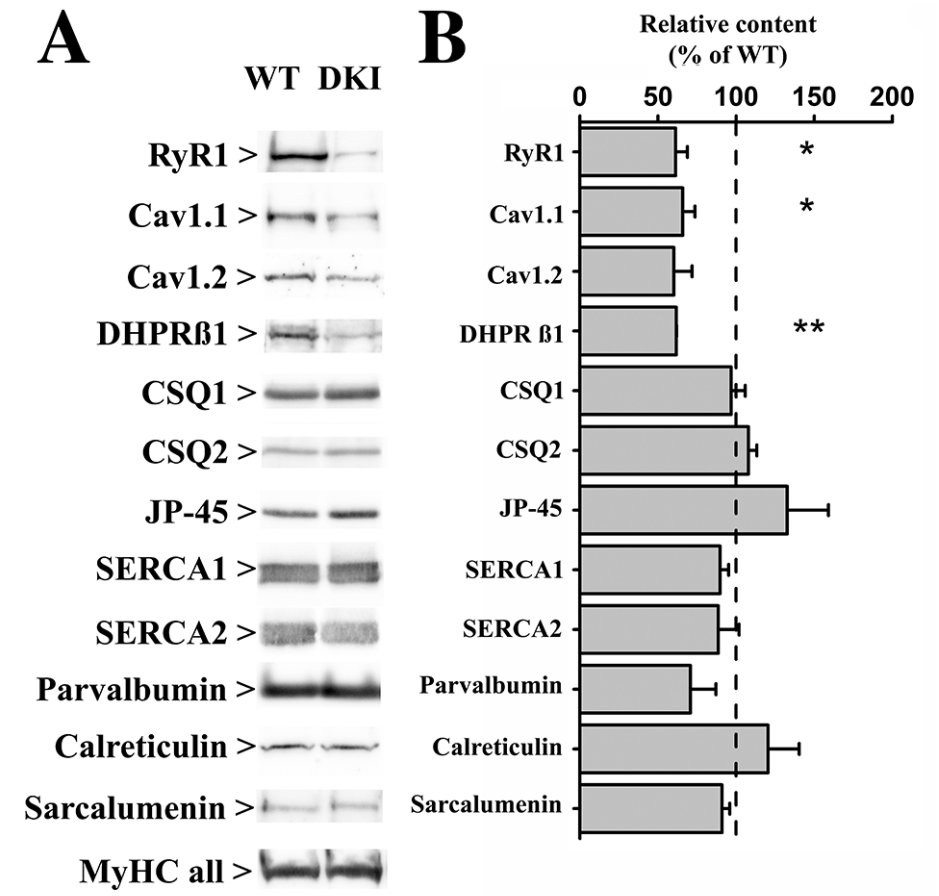
A
WT DKI
RyR1 >
Cav1.1 >
Cav1.2 >
DHPRß1 >
CSQ1 >
CSQ2 >
JP-45 >
SERCA1 >
SERCA2 >
Parvalbumin >
Calreticulin >
Sarcalumenin >
MyHC all >
B
Relative content
(% of WT)
0 50 100 150 200
RyR1 *
Cav1.1 *
Cav1.2
DHPR ß1 **
CSQ1
CSQ2
JP-45
SERCA1
SERCA2
Parvalbumin
Calreticulin
Sarcalumenin

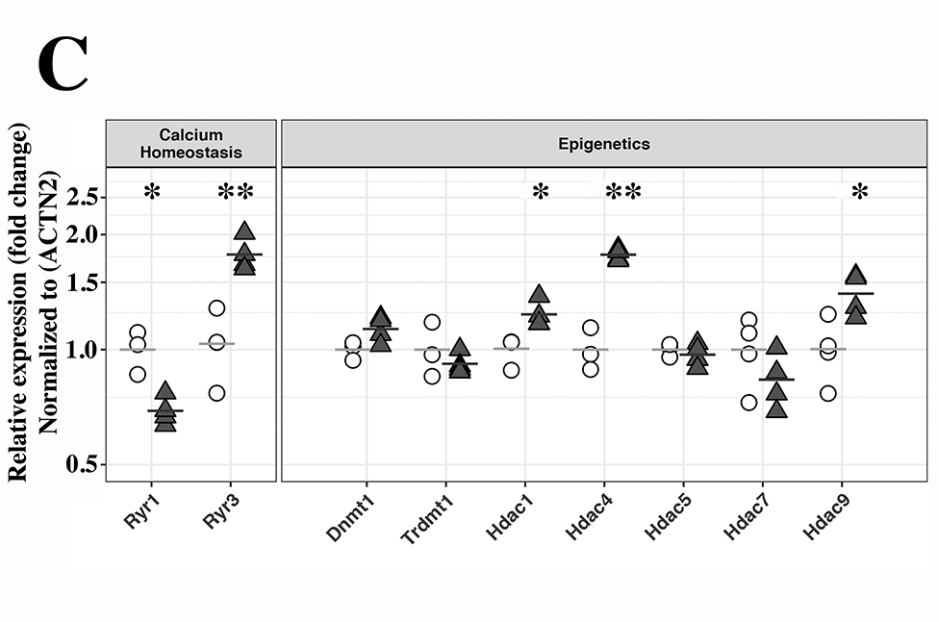
C
Calcium Homeostasis
Epigenetics
Relative expression (fold change) Normalized to (ACTN2)
2.5
2.0
1.5
1.0
0.5
Ryr1
Ryr3
Dnmt1
Trdmt1
Hdac1
Hdac4
Hdac5
Hdac7
Hdac9

Figure 3

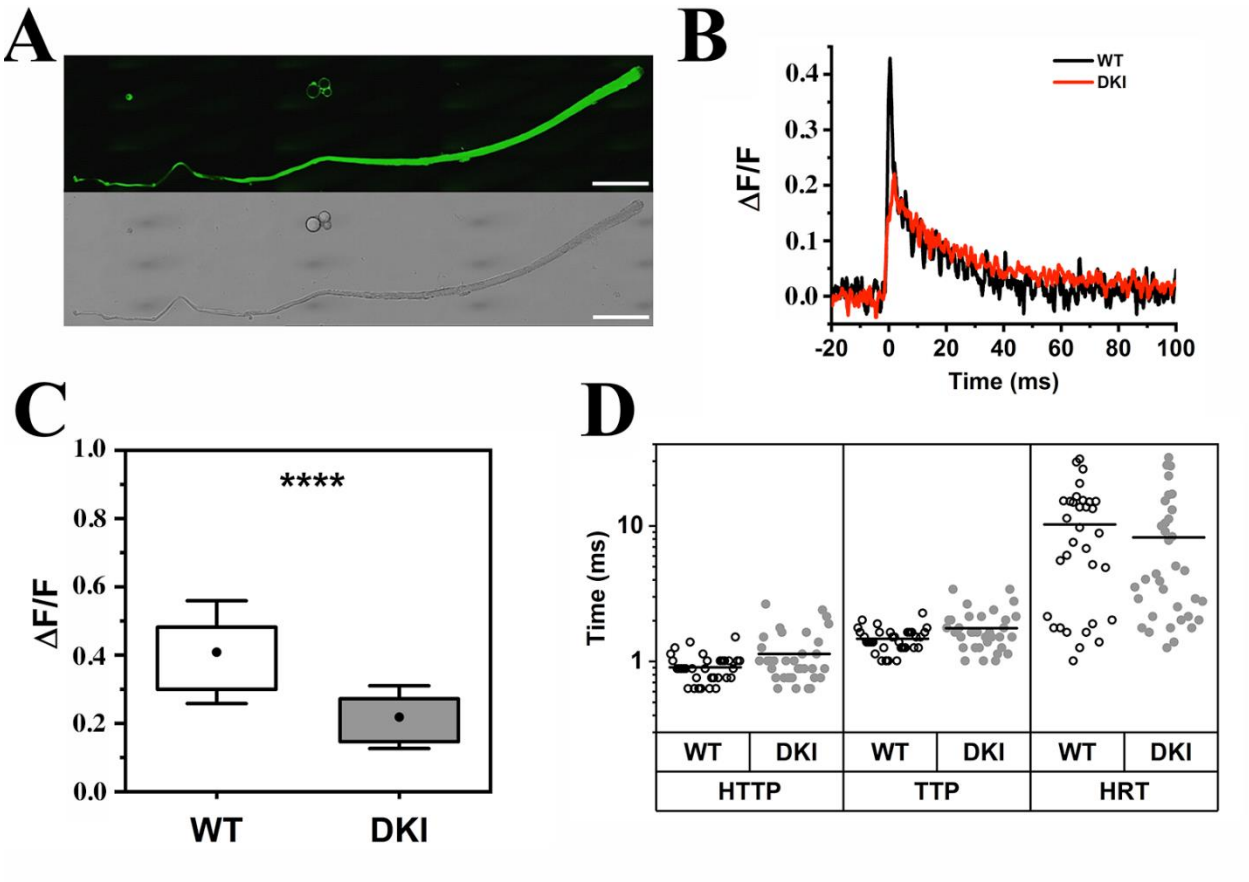
A
B
WT
DKI
ΔF/F
0.4
0.3
0.2
0.1
0.0
-20
0
20
40
60
80
100
Time (ms)
C
****
ΔF/F
1.0
0.8
0.6
0.4
0.2
0.0
WT
DKI
D
Time (ms)
10
1
WT
DKI
WT
DKI
WT
DKI
HTTP
TTP
HRT

Figure 4

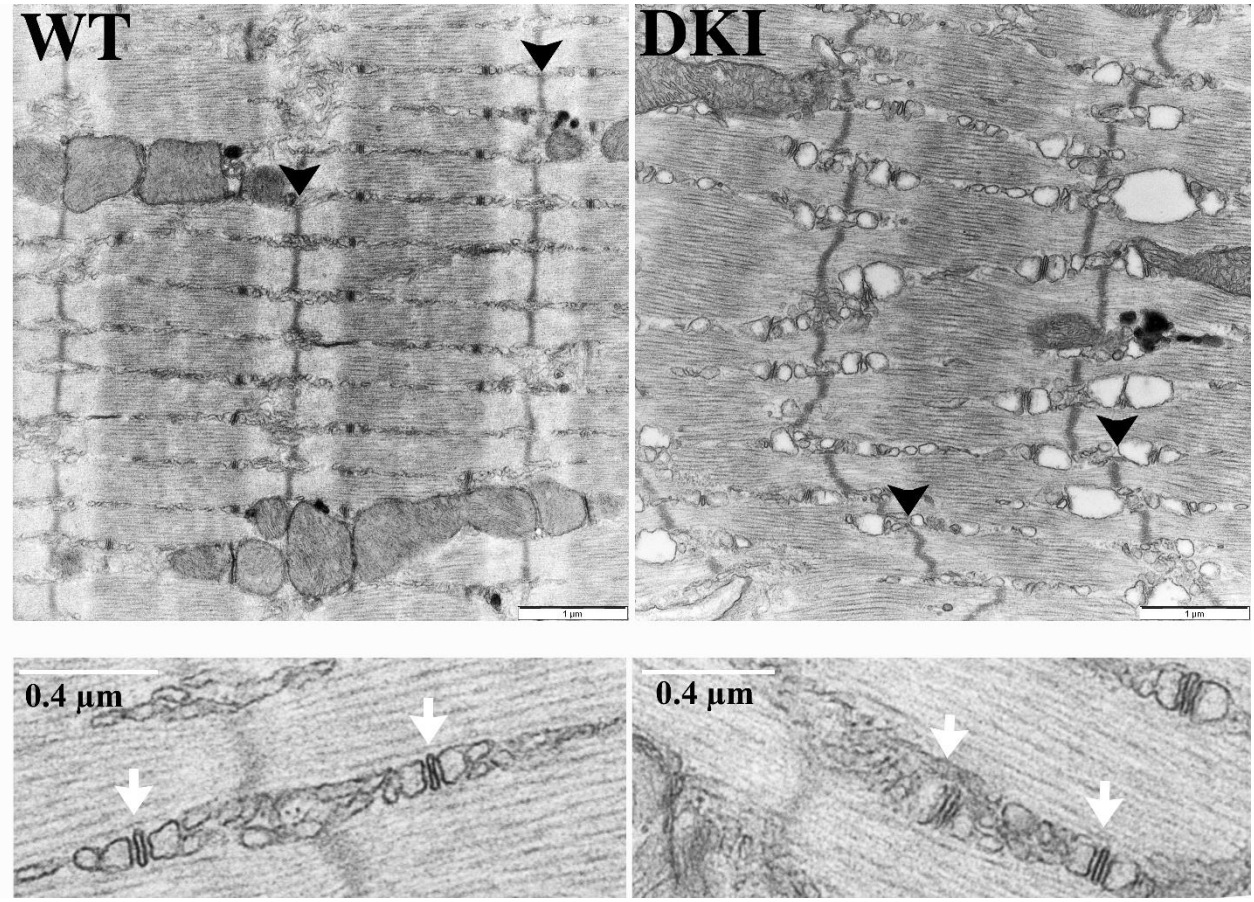

Figure 5

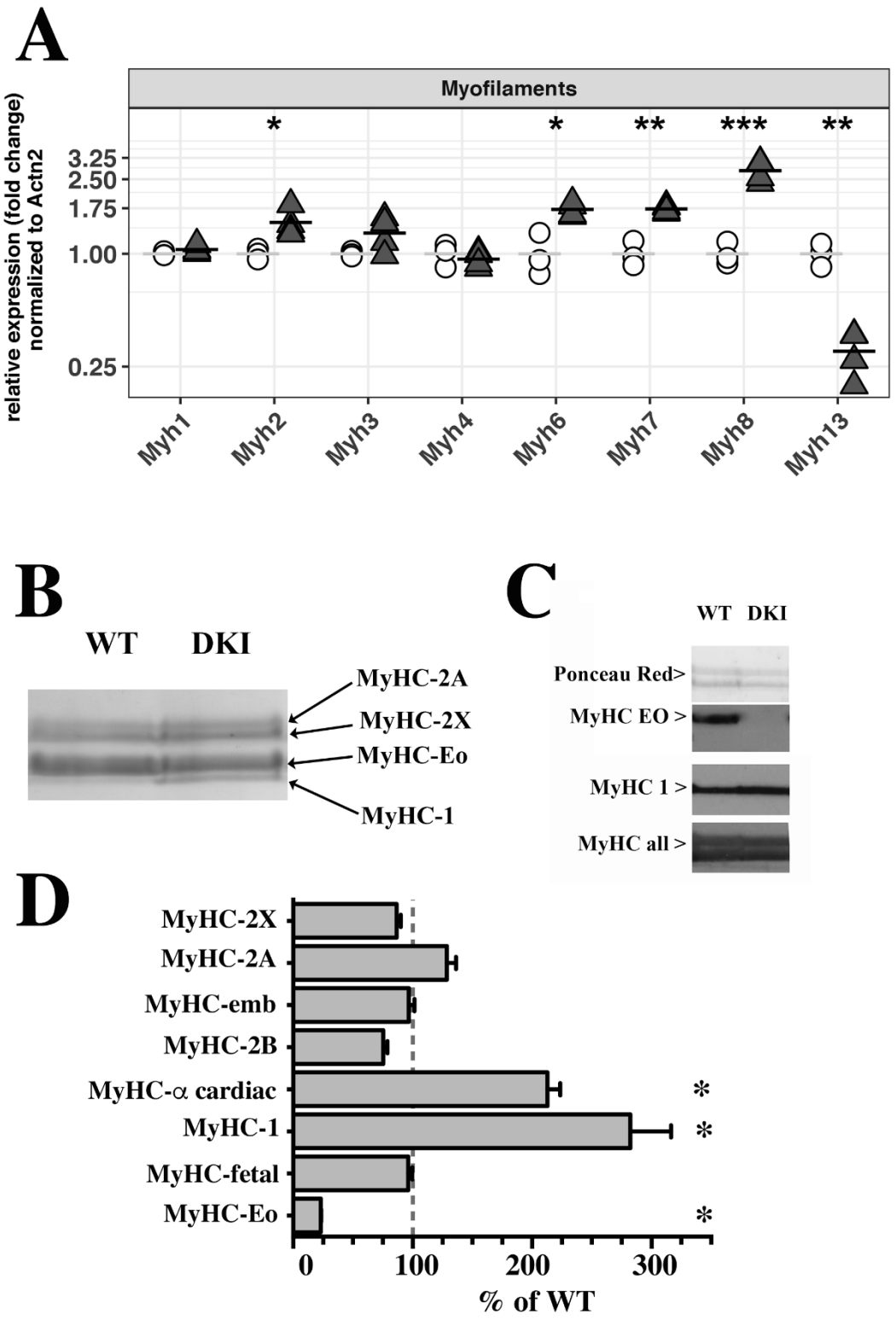
A
Myofilaments
relative expression (fold change) normalized to Actn2
3.25
2.50
1.75
1.00
0.25
*
*
**
***
**
Myh1
Myh2
Myh3
Myh4
Myh6
Myh7
Myh8
Myh13
B
WT
DKI
MyHC-2A
MyHC-2X
MyHC-Eo
MyHC-1
C
WT
DKI
Ponceau Red>
MyHC EO >
MyHC 1 >
MyHC all >
D
MyHC-2X
MyHC-2A
MyHC-emb
MyHC-2B
MyHC-α cardiac
MyHC-1
MyHC-fetal
MyHC-Eo
*
*
*
0
100
200
300
% of WT

Figure 6

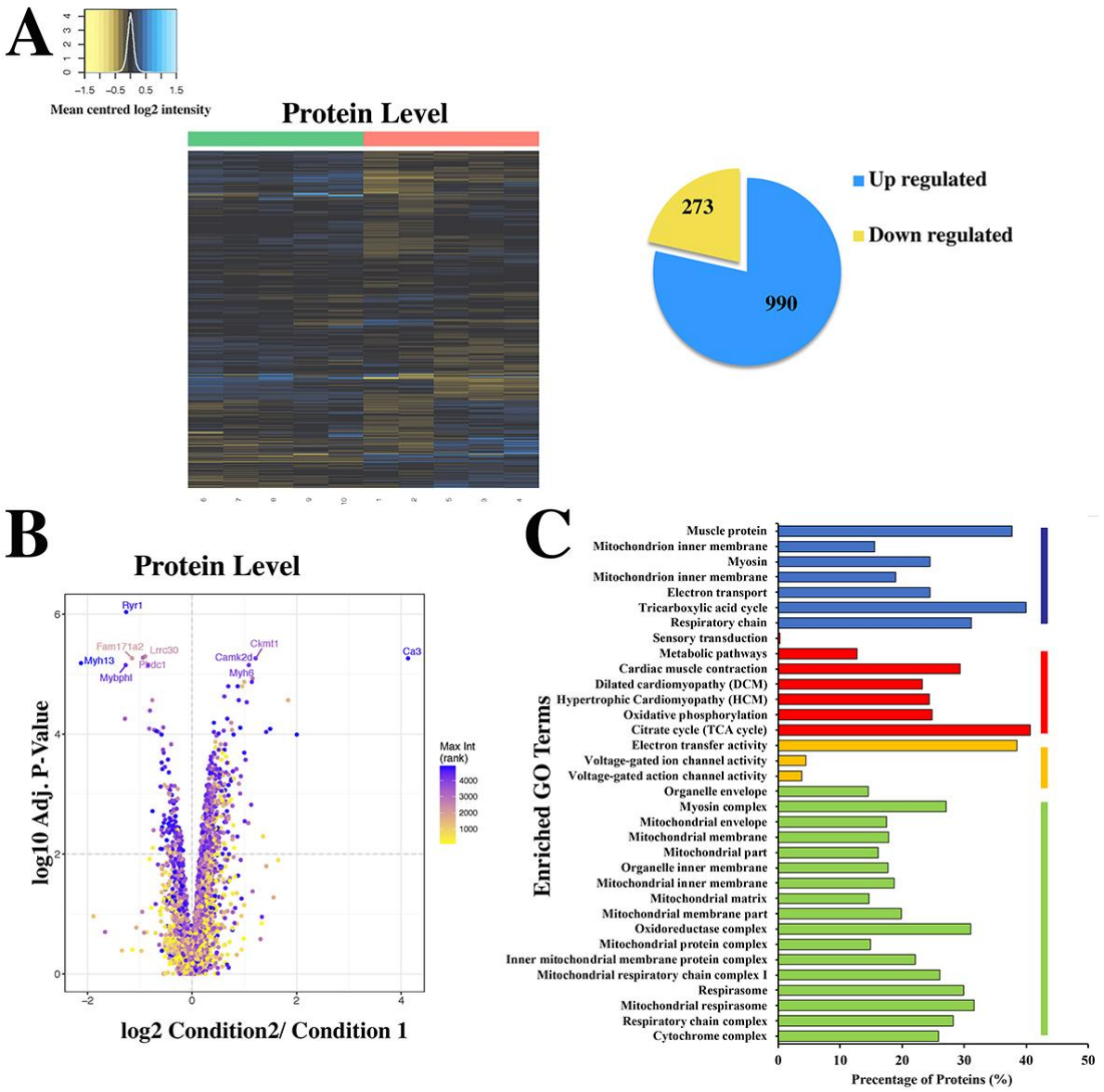
A
Mean centred log2 intensity
Protein Level
273
990
Up regulated
Down regulated
B
Protein Level
log10 Adj. P-Value
log2 Condition2/ Condition 1
Max Int (rank)
Ryr1
Fam171a2
Lrrc30
Myh13
Pkdc1
Mybphl
Camk2d
Ckmt1
Myh6
Ca3
C
Enriched GO Terms
Muscle protein
Mitochondrion inner membrane
Myosin
Mitochondrion inner membrane
Electron transport
Tricarboxylic acid cycle
Respiratory chain
Sensory transduction
Metabolic pathways
Cardiac muscle contraction
Dilated cardiomyopathy (DCM)
Hypertrophic Cardiomyopathy (HCM)
Oxidative phosphorylation
Citrate cycle (TCA cycle)
Electron transfer activity
Voltage-gated ion channel activity
Voltage-gated action channel activity
Organelle envelope
Myosin complex
Mitochondrial envelope
Mitochondrial membrane
Mitochondrial part
Organelle inner membrane
Mitochondrial inner membrane
Mitochondrial matrix
Mitochondrial membrane part
Oxidoreductase complex
Mitochondrial protein complex
Inner mitochondrial membrane protein complex
Mitochondrial respiratory chain complex I
Respirasome
Mitochondrial respirasome
Respiratory chain complex
Cytochrome complex
Precentage of Proteins (%)

Supplementary Material

Molecular basis of impaired extraocular muscle function in a mouse model of congenital myopathy due to compound heterozygous *RYR1* mutations

Jan Eckhardt[1], Christoph Bachmann[1], Sofia Benucci[1], Moran Elbaz[1], Alexis Ruiz[1], Francesco Zorzato[1,2] and Susan Treves*[1,2].

[1]Departments of Biomedicine and Anaesthesia, Basel University Hospital, Hebelstrasse 20, 4031 Basel, Switzerland.

[2]Department of Life Science and Biotechnology, University of Ferrara, Via Borsari 46, 44100, Ferrara, Italy.

Corresponding Author: Susan Treves

E-mail: susan.treves@unibas.ch

This document includes:

Supplementary Tables 1 to 6

Supplementary Figures 1-3

<u>Supplementary Table 1:</u> Average weight and length of EOMs from WT, single and DKI mutant mice.

	Length (mm)	Wet weight (mg)	Cross section (mm^2)	Specific force (mN/mm^2)
WT EOM	4.58 ± 0.21 n=11	0.95 ± 0.12 n=11	0.222±0.03 n=11	3.09±0.68 n=10
Ex36 EOM	4.23± 0.19** n=9	0.71 ± 0.09** n=8	0.179±0.022** n=8	2.95±0.30 n=6
Ex91 EOM	4.73± 0.08 n=4	0.90 ± 0.17 n=4	0.201±0.036 n=4	3.50±0.69 n=4
HO91 EOM	4.56 ± 0.22 n=5	1.22 ± 0.16** n=5	0.281±0.031** n=5	3.23±1.02 n=5
DKI EOM	4.03 ± 0.28*** n=7	0.72 ± 0.11** n=6	0.180±0.023* n=6	0.33±0.17* n=5

Data show mean ± SEM. N represents the number of individual muscles that were measured. Length was measured using a stereomicroscope (Zeiss, Stemi 508) with a micrometer scale incorporated into the eyepiece (Nikon CFI 10x/22). Wet weight was obtained using a Mettler Toledo balance (AG204 DeltaRange) after removal of the eyeballs and bones. *P<0.05; **P<0.01; ***P<0.001 ANOVA followed by the Bonferroni post hoc test (WT as control).

<u>Supplementary Table 2</u>: Kinetic analysis of the twitch force generated in EOMs from WT, single mutant and DKI mutant mice.

	HTTP (ms)	TTP (ms)	HRT (ms)
WT EOM	4.36± 0.27 n=9	10.29 ± 0.63 n=10	11.54± 0.86 n=10
Ex36 EOM	4.12 ± 0.26 n=4	9.53 ± 0.31 n=8	11.19 ± 1.07 n=8
Ex91 EOM	4.25 ± 0.14 n=3	9.12 ± 0.68 n=4	10.06 ± 1.10 n=4
HO91 EOM	5.72±0.39*** n=5	11.64±0.74* n=5	10.04±1.44 n=5
DKI EOM	3.43 ± 0.91** n=5	11.06 ± 1.54 n=6	39.93 ± 13.12*** n=6

Three parameters were analysed: Half Time to peak (HTTP); Time to peak (TTP) and half relaxation time (HRT). Data are shown as mean ± SEM. N represent individual muscles that were measured. *P<0.05; **P<0.01; ***P<0.001 ANOVA followed by the Bonferroni post hoc test (WT as control).

<u>Supplementary Table 3</u>: Analysis of Z-disc alignment and of CRU in EOMs from WT and DKI mice

	% Z-disc aligned	% Z-disc not aligned	N° of CRU/ 100 µm^2	% of Dyads	No. of Mitochondria adjacent to CRU /100 µm^2
WT	100%	0%	70.7 ± 6.0	1.3± 0.8	30.0± 3.3
DKI	20%	80%	40.8± 3.7***	6.1± 2.7	16.3 ± 1.5***

Z-disk were grouped into two groups: aligned and not aligned. Data are shown as percentage of all analysed Z-discs. The mean (±SEM) number of Z-discs per micrograph was 2.23±0.47 for WT and 2.33±0.53 for DKI. 13 micrographs of fibres from 3 WT mice, 15 micrographs of fibres from 3 DKI mice were analysed. For analysis of CRU: 15 fibres from 3 WT and 3 DKI mice were analysed. For analysis of N° of mitochondria: 14 fibres from 3 WT and 15 fibres from 3 DKI mice were analysed. A total of 284 and 196 CRU were analysed in WT and DKI EOMs, respectively. Results are expressed as mean ± SEM (***P< 0.001, Student's *t* test).

<u>Supplementary Table 4:</u> List of expressed proteins with more than 0.67-fold decreased content in EOM from DKI mice.

UniProtKB protein ID	Gene symbol	Protein description (MOUSE)	Fold change	Log_2 ratio	q Value
B1AR69	Myh13	Myosin, heavy polypeptide 13	0.230	-2.121	6.54E-06
Q9DBX2	Pdcl	Phosducin-like protein	0.412	-1.280	5.54E-05
Q5FW53	Mybphl	Myosin-binding protein H-like	0.416	-1.266	7.07E-06
E9PZQ0	Ryr1	Ryanodine receptor 1	0.418	-1.257	9.18E-07
A2A699	Fam171a2	Protein FAM171A2	0.452	-1.144	5.44E-06
Q9D0B6	Pbdc1	Protein PBDC1	0.522	-0.937	5.31E-06
Q3UV48	Lrrc30	Leucine-rich repeat-containing protein 30	0.539	-0.892	5.04E-06
Q9Z0J4	Nos1	Nitric oxide synthase, brain	0.560	-0.837	7.07E-06
Q9D164	Fxyd6	FXYD domain-containing ion transport regulator 6	0.568	-0.815	8.11E-05
Q80UP3	Dgkz	Diacylglycerol kinase zeta	0.571	-0.808	1.22E-02
Q08460	Kcnma1	Calcium-activated potassium channel subunit alpha	0.574	-0.801	4.05E-05
P70663	Sparcl1	SPARC-like protein 1	0.592	-0.757	2.71E-05
P02088	Hbb-b1	Hemoglobin subunit beta-1	0.594	-0.752	1.93E-03

P05366	Saa1	Serum amyloid A-1 protein	0.596	-0.746	7.89E-03
Q9QY80	Hacd1	Very-long-chain (3R)-3-hydroxyacyl-CoA dehydratase 1	0.602	-0.733	4.01E-03
O09110	Map2k3	Dual specificity mitogen-activated protein kinase kinase 3	0.607	-0.721	8.54E-05
P16125	Ldhb	L-lactate dehydrogenase B chain	0.625	-0.677	8.90E-05
Q8BK30	Ndufv3	NADH dehydrogenase [ubiquinone] flavoprotein 3	0.638	-0.649	1.50E-02
A2VDH3	Lrrc38	Leucine-rich repeat-containing protein 38	0.643	-0.637	9.25E-05
Q9CRB6	Tppp3	Tubulin polymerization-promoting protein family member 3	0.660	-0.598	7.52E-04
Q9D855	Uqcrb	Cytochrome b-c1 complex subunit 7	0.660	-0.598	8.21E-03

<u>Supplementary Table 5:</u> List of preferentially expressed proteins with more than 2.0-fold increase in content in EOM from DKI mice.

UniProtKB protein ID	Gene symbol	Protein description (MOUSE)	Fold change	Log_2 ratio	q Value
P16015	Ca3	Carbonic anhydrase 3	17.577	4.136	5.44E-06
P51667	Myl2	Myosin regulatory light chain 2 ventricular/ cardiac muscle isoform	4.018	2.006	1.02E-04
Q8R1H0	Hopx	Homeodomain-only protein	3.584	1.842	2.71E-05
Q9ERN0	Scamp2	Secretory carrier-associated membrane protein 2	3.139	1.650	1.27E-02
Q91Z83	Myh7	Myosin-7	2.822	1.497	8.19E-05
P11588	Mup1	Major urinary protein 1	2.681	1.423	1.60E-02
P19123	Tnnc1	Troponin C, slow skeletal and cardiac muscles	2.679	1.422	9.21E-05
Q5NCE8	Mrs2	Magnesium transporter MRS2 homolog, mitochondrial	2.569	1.361	5.08E-03
Q6PHZ2	Camk2d	Calcium/calmodulin-dependent protein kinase type II subunit delta	2.332	1.221	5.44E-06
P30275	Ckmt1	Creatine kinase U-type, mitochondrial	2.327	1.219	5.44E-06
P63044	Vamp2	Vesicle-associated membrane protein 2	2.237	1.162	4.20E-02
Q80UG2	Plxna4	Plexin-A4	2.235	1.160	1.18E-05
Q8R4E4	Myoz3	Myozenin-3	2.215	1.147	1.35E-05
Q7TQF7	Amph	Amphiphysin	2.195	1.134	1.51E-03
Q02566	Myh6	Myosin-6	2.127	1.089	7.07E-06
P33267	Cyp2f2	Cytochrome P450 2F2	2.113	1.079	3.05E-03

P97355	Sms	Spermine synthase	2.067	1.048	2.94E-05
Q8VCT4	Ces1d	Carboxylesterase 1D	2.038	1.027	2.68E-04
Q8BFZ9	Erlin2	Erlin-2	2.014	1.010	2.84E-03
P59108	Cpne2	Copine-2	2.004	1.003	1.35E-05
Q9WUZ5	Tnni1	Troponin I, slow skeletal muscle	2.002	1.001	2.05E-04

<u>Supplementary Table 6:</u> Sequence of primers used and target gene

Primer Details		Primer sequence	
		Forward	**Reverse**
Ex36 Ryr1	Genotyping	GGG TGG TGC TGG CTT CAG AGT GAT	CGA GGG AAG TTG AGG TTG GGG
Ex91 Ryr1	Genotyping	GAGATGTTCGTGAGTTTCTGCGAGG	TGAGGGTTGTTCTTGGTGTATTTGG
Actn2	qPCR	CAT CGA GGA GGA TTT CAG GAA C	CAA TCT TGT GGA ACC GCA TTT T
Myh1	qPCR	GAC CGA AGG CGG AAC TAC TG	TGA CAG TGA CGC AGA ACA GG
Myh2	qPCR	ACA ACA TCA CTG GCT GGC TG	CAC CAC TAC TTG CCT CTG CTT
Myh3	qPCR	TAC AAC AGA TGC GGA CGG TG	CCT GGG GTC TTG GTT TCG TT
Myh4	qPCR	AAG ACC AAG GAG GAG GAG CA	TCG GGA AAA CTC GCC TGA C
Myh6	qPCR	GCC AAT GAG TACCGC GTG AA	CCT AGC CAA CTC CCC GTT CT
Myh7	qPCR	CGG ACA AAG GCA AAG GCA AG	TCC ATC ACC CCT GGA GAC TTT
Myh8	qPCR	GCG GTC TGT AGG GGA TAC CTA A	GGT TTT TCA CCT TGT TCT CCG TG
Myh13	qPCR	CTG AAT GAG ACC GTG GTG GG	GAG TCA CCT GCT TCT GCT CC
Ryr1	qPCR	GCC TTT GAC GTG GGA TTA CAG	CCC CAA CTC GAA CCT TCT CTC
Ryr3	qPCR	TAG AAA CCG AGG GGG AGG AG	AGA GCA ACT GAA AGA GGC CC
Dnmt1	qPCR	AGG ACA AAG CAC CCA CGA AA	GAC AGA CCT CAC AGA CAC CAC
Trdmt1	qPCR	TGT GGT GGC TGC TAT TGA TGT	CCC CTG TAG GCC AAT TCT TGT
Hdac1	qPCR	AAC GCA TCT CCA TCT GCT CC	GAC CAC CTT CTC CCT CCT CA
Hdac4	qPCR	CAC TGC ATT TCC AGC GAT CC	AAG ACG GGG TGG TTG TAG GA
Hdac5	qPCR	GAC TTT CCC CTC CGT AAA ACG	TGC CAT CCT TTC GAC GCA G
Hdac7	qPCR	GGC AGG CTT ACA CCA GCA A	TGG GCA GGC TGT AGG GAA TA
Hdac9	qPCR	GCG GTC CAG GTT AAA ACA GAA	GCC ACC TCA AAC ACT CGC TT

<u>Supplementary Figure 1</u>: Average change in content of main proteins involved in skeletal muscle ECC, as determined by mass spectrometry analysis. The relative protein content in EOMs from WT mice (n=5) was set to 100%. Results show the mean (±SEM) fold change expressed as % of the indicated protein in EOMs from 5 DKI mice. Errors are calculated according the propagation of uncertainty. *q value <0.05.

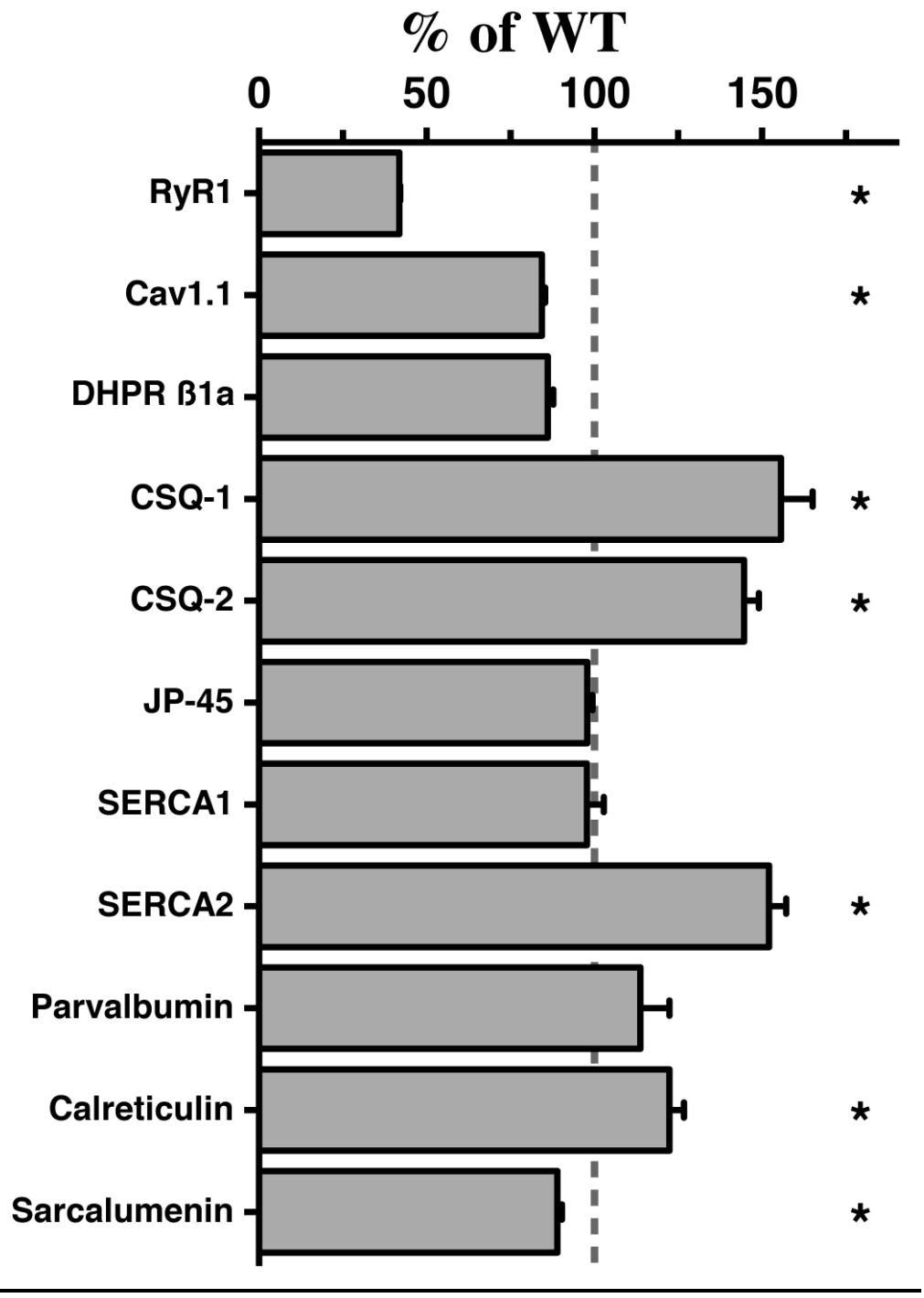

<u>Supplementary Figure 2</u>: RYR and MyHC expression in WT, heterozygous RyR1p.Q1970fsX16, heterozygous RyR1p.A4329D, homozygous RyR1p.A4329D and compound heterozygous RyR1p.Q1970fsX16+p.A4329D EOMs. A. Quantitative real-time PCR (RT-qPCR) of RYR1and RYR3 transcripts in EOMs from the different mouse lines relative to WT mice. The latter were set as 1. Transcript levels were normalized to *ACTN2* as a muscle specific gene using the ΔΔCt method. Each symbol represents the duplicate value obtained in a single mouse. **B.** Quantification of RyR1 protein content mean (±SEM) in EOMs. Values were normalized for MyHC content, which was obtained using an antibody recognizing all MyHC isoforms. WT, n=6; Ex36, n=3; Ex91, n=3; HO91, n=4; DKI, n=5. where n represents the number of pooled muscles from the indicated number of mice. **C.** Quantitative real-time PCR (RT-qPCR) of the transcripts encoding the indicated myosin heavy chain (MYH) isoforms in EOMs from the different mouse lines relative to WT mice. The latter were set as 1. Transcript levels were normalized to *ACTN2* as a muscle specific gene using the ΔΔCt method. Each symbol represents the duplicate value obtained in a single mouse. **D.** Western blot of high-resolution gel 7.5% acrylamide gel. Top blot probed with anti-MyHC-EO showing its presence in WT, Ex36, Ex91and HO91EOMs, and its very low content in EOMs from DKI mice. Bottom, the same blot was probed with anti-MyHC recognizing all isoforms. *p<0.05; **p<0.01; ***p<0.001.

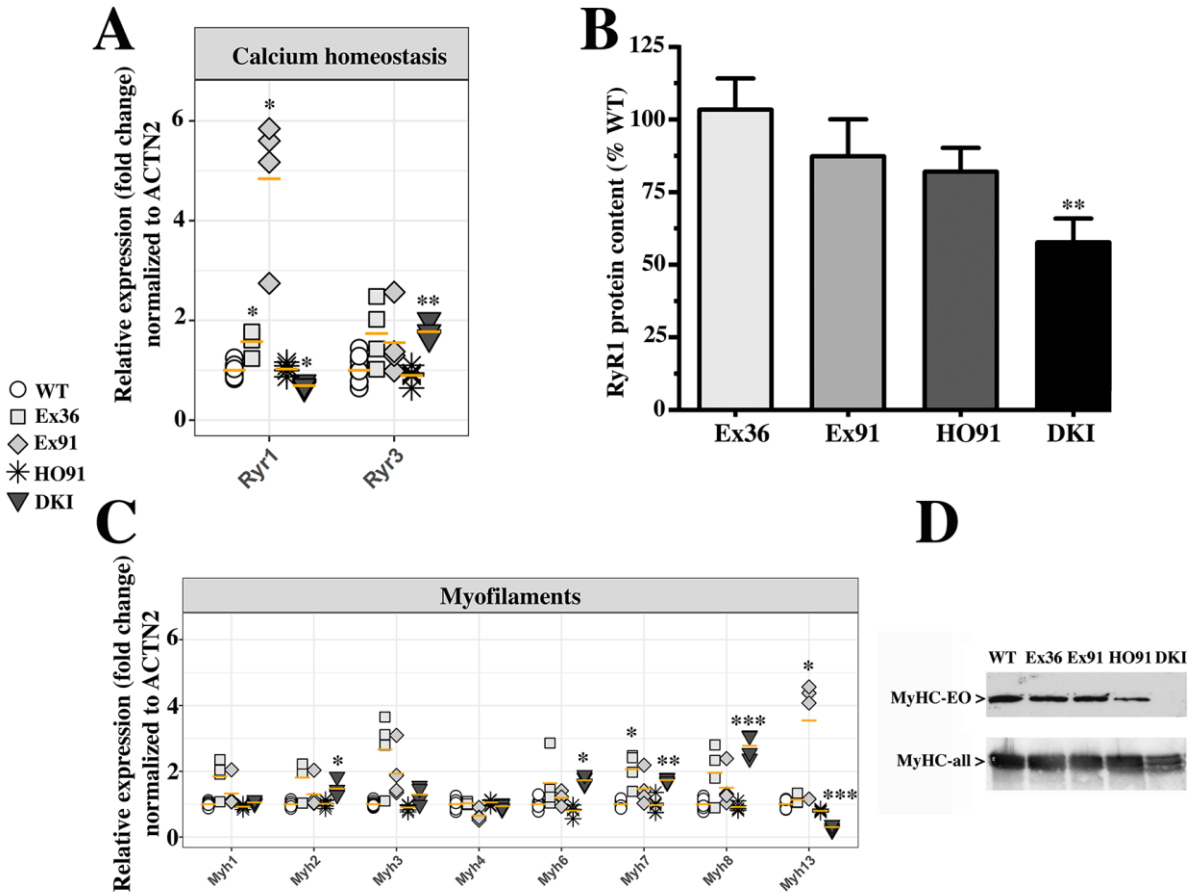

<u>Supplementary Figure 3</u>: Immunoreactivity of the antibodies used in the present study. Total muscle homogenates were prepared from WT EOMs; proteins were separated on 6% (left blot), 7.5 % (second from left blots), 10% SDS PAGE (third from left blots) and tris-tricine gel (right blot), blotted onto nitrocellulose and probed with the indicated primary antibodies. Blots were then incubated with peroxidase conjugated anti-mouse IgG or peroxidase conjugated protein-G and the bands were visualized by chemiluminescence.

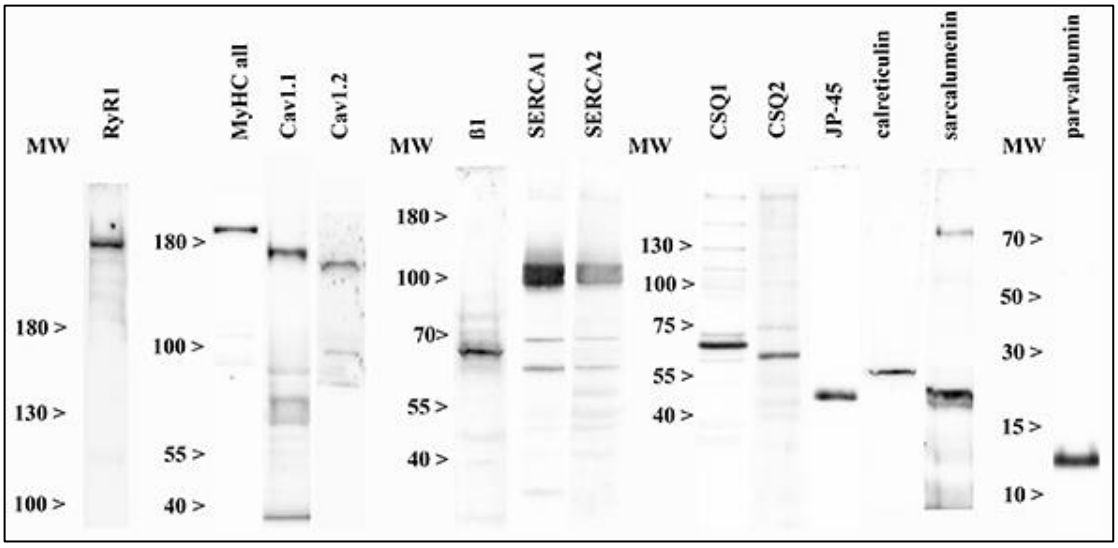

2.4 Additional Results

2.4.1 Contribution to other Papers

At the beginning of my thesis I was investigating the JP45-Calsequestrin complex in EDL and soleus muscle. For this I measured the force from three different mouse lines (JP45-CASQ1 double KO, JP45-CASQ2 double KO and JP45-CASQ1-CASQ2 triple KO) in different conditions: first in normal Krebs-Ringer solution with 1,8 mM Ca^{2+} then in a solution where the calcium is substituted with 100µM La^{3+} and finally again in normal Krebs-Ringer solution. Our results demonstrate that the triple KO rely on calcium entry via La^{3+}- and nifedipine-sensitive calcium channels. (Mosca et al., 2016)

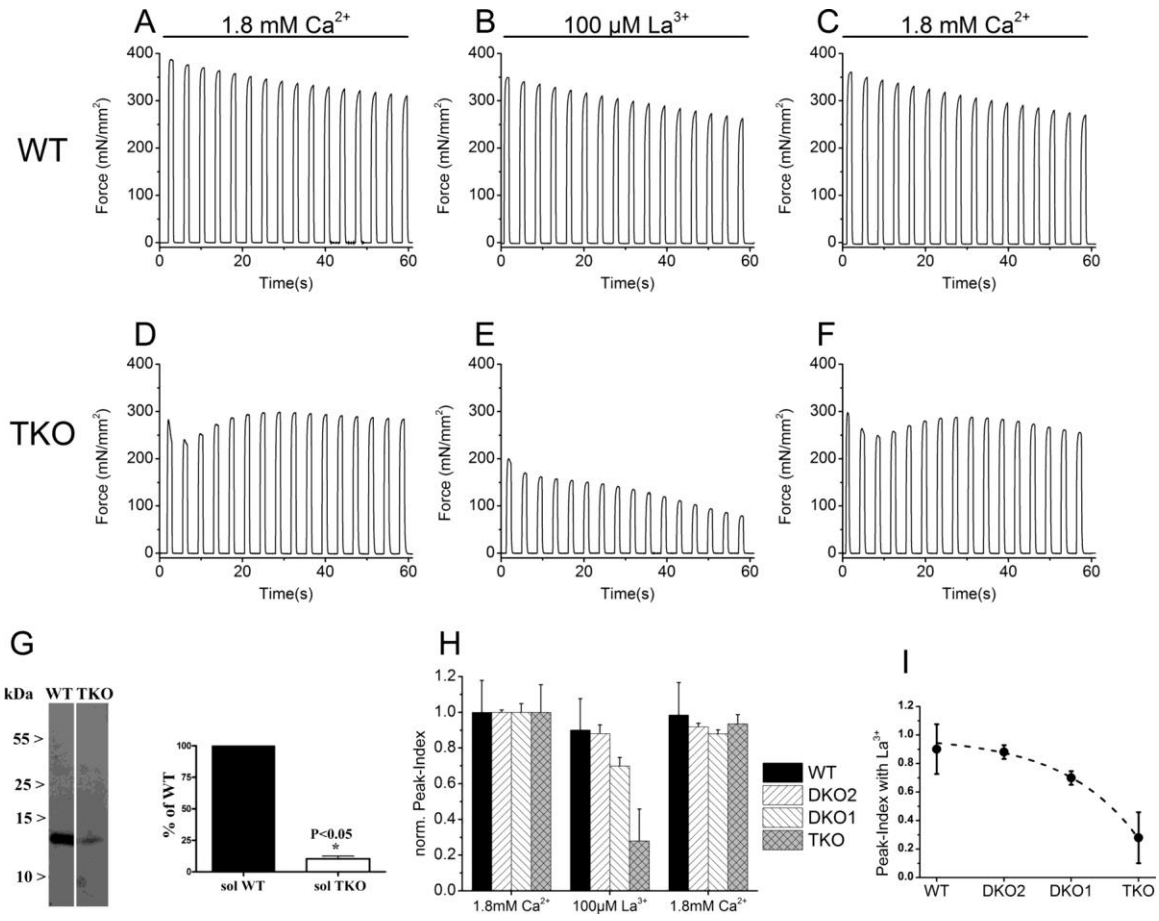

Figure 2.1: Tetanic contraction of soleus from WT/DKO1/DKO2 and TKO mice.

(A–F) Traces of a train of tetanic contractures in wild-type and TKO carried out according the protocol described under "Experimental Procedures" in (Mosca et al., 2016). Shown is a representative response of 9 muscles from 10 mice. **(G)** Western blot of 37.5 µg of total homogenate of soleus from WT and TKO stained with anti-parvalbumin Ab. Histograms report values (mean ± S.D.) from four to six determinations from three different total homogenate preparations. Values are the mean ± S.D. *, p value of unpaired Student's t test. **(H)** Normalized peak indexes of four strains. Values are the mean ± S.D. of 4–6 muscles from 2 or 3 mice; in the presence of 100 µm La3+ the overall ANOVA p values are <0.0001; multicomparison Dunnett's ANOVA post test: WT versus DKO2, $p > 0.05$; WT versus DKO1, $p < 0.05$; WT versus TKO, $p < 0.05$. **(I)** Exponential curve fitting of the values of the peak indexes in the presence of La3+ values, which are reported in panel H. (Mosca et al., 2016)

Beside this I also contributed to two additional papers: (Elbaz et al., 2019b; a).

2.4.2 Unpublished Data

Similar to the RyR3 KO paper (Chapter 2.2: Paper 1) (Eckhardt et al., 2019) I also analysed the spontaneous calcium transient of myotubes from the DKI mouse (featured in Chapter 2.3: Paper 2). Similar to our findings in myotubes from RyR3 KO mice we found a significant reduction in the number of myotubes spontaneously exhibiting calcium waves. Additionally, the frequency of the calcium waves was also reduced in DKI EOM-derived myotubes (Figure 2.2: Spontaneous calcium waves in DKI EOM-derived myotubes). This data was not added in the paper because it was out of the scope of the paper and it would not give any new insight in the ECC machinery.

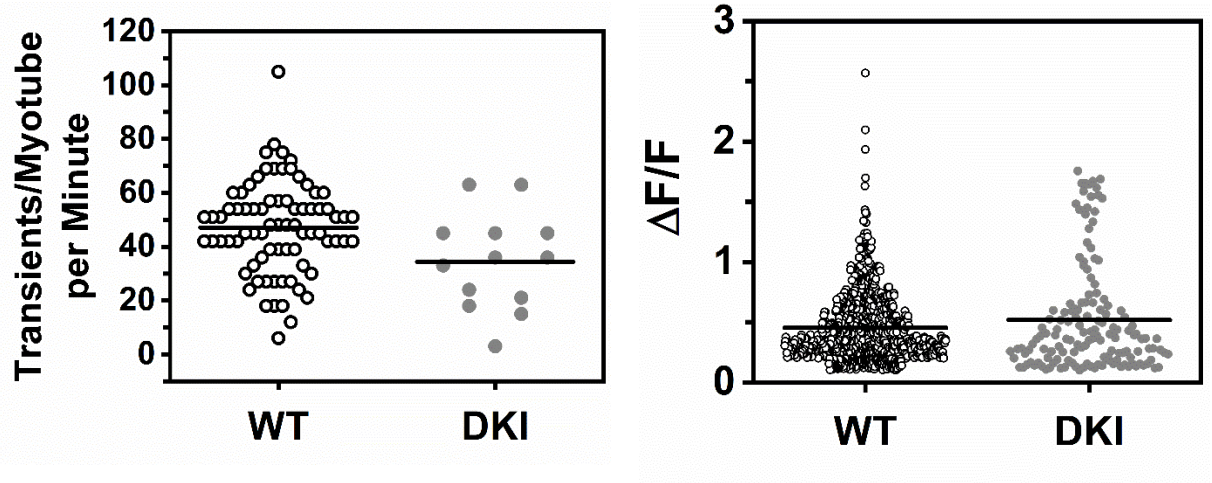

Figure 2.2: Spontaneous calcium waves in DKI EOM-derived myotubes

(Left) Analysis of the frequency of the spontaneous Ca^{2+} transient. Each point represents the number of transients per minute recorded in a single myotube. Each myotube was recorded for 30 s, and the frequency output is given as frequency per minute. Experiments were performed at room temperature. Empty circles, WT ; gray circles, DKI. (**Right)** $\Delta F/F$ of the Fluo-4 transients. The horizontal black line represents the mean value.

In collaboration with Dr. Corina Kohler (FG Neutzner / Scholl; DBM Basel) we also performed the OKR experiments on the DKI mouse, here stated as dHT (Figure 2.3: OKR of DKI). Interestingly, we could not see any differences between DKI and WT. In the RyR3 KO paper we interpreted the

significant difference in the accuracy as the result of impaired EOMs. And indeed, we proved the impairment of the EOMs in this paper by measuring the force and calcium release in isolated EOMs but nevertheless the interpretation of the OKR might have been wrong. Nevertheless, in order to really show that impaired EOMs does not affect the OKR, deeper investigation need to be performed. Thus, these controversial results were not included in the DKI paper.

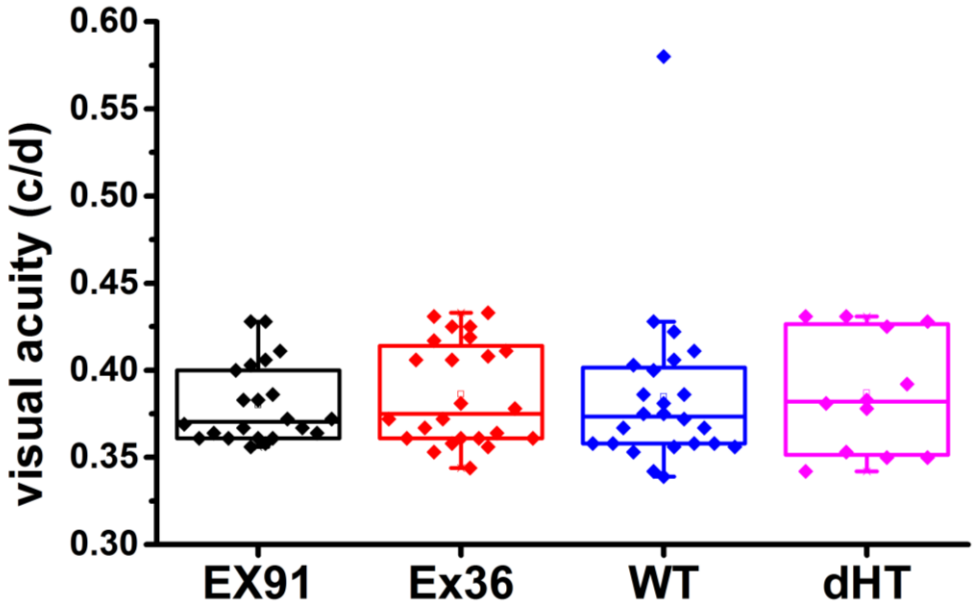

Figure 2.3: OKR of DKI

Visual acuity of single heterozygous mouse lines (Ex36 & Ex91), double hetero mouse line (dHT) and wild type mouse line (WT). Each eye is represented as a single point. The units of visual acuity are cycles/degree (c/d

2.4.3 Peak Analyses Program

To analyses the calcium transients from isolated singe EOM fibers and EOM-derived myotubes I developed a small Vb.Net based program. The main goal was it to get a repeatable analysis which can also be used to analyse multiple transients in one run (batch analyses). In the following pages I outline the main function "PeakCalculationFiber" which analyses the individual peakparameter. The rest of the code is omitted in order to keep it a manageable amount of code.

```
Public Function PeakCalculationFiber(ByVal FileName As String, ByVal
OriginalFileName As String, ByRef DataArray() As DataPoint, ByVal CenterTime
As Double, Optional OriginalData() As DataPoint = Nothing) As Boolean
        Try
```

```
            Dim NewFinalPeak As FinalPeakFiber = New FinalPeakFiber
            NewFinalPeak.FileName = FileName
            NewFinalPeak.OriginalFileName = OriginalFileName
            ''Dim Center As Double = Center

            Dim CenterIndex As Integer = Array.FindIndex(DataArray, Function(x
As DataPoint) Math.Abs(x.Time - CenterTime) <= 0.0000000001)


            ''calculate Baseline
            Dim i As Integer = 0
            Dim BaseLine As Double = 0
            Dim EndBaseLine As Double = 0
            For i = 0 To BaseLineWindowCount - 1
                BaseLine = DataArray(i).Value + BaseLine
                EndBaseLine = EndBaseLine + DataArray(DataArray.Count - 1 -
i).Value
            Next
            BaseLine = BaseLine / BaseLineWindowCount
            EndBaseLine = EndBaseLine / BaseLineWindowCount

            Dim PeakHeightOriginal As Double = Double.NaN
            If IsNothing(OriginalData) Then
            Else
                PeakHeightOriginal = OriginalData.Max(Function(p) p.Value) -
BaseLine
            End If
            Dim PeakHeight As Double = DataArray(CenterIndex).Value - BaseLine
            Dim Peakfirst5Percent As Double = 0.05 * PeakHeight + BaseLine
            Dim Peak5firstPercentIndex As Integer = 0
            Dim Peaklast10Percent As Double = 0.1 * PeakHeight + BaseLine
            Dim Peaklast10PercentIndex As Integer = 0
            Dim Peaklast90Percent As Double = 0.9 * PeakHeight + BaseLine
            Dim Peaklast90PercentIndex As Integer = 0
            Dim PeakHalfMax As Double = 0.5 * PeakHeight + BaseLine
            Dim HTTPIndex As Integer = 0
            Dim HRTIndex As Integer = 0

            ''HAP
            Dim HeightAfterPeak As Double = DataArray(CenterIndex).Value -
EndBaseLine
            Dim Peakfirst5PercentHAP As Double = 0.05 * HeightAfterPeak +
EndBaseLine
            Dim Peakfirst5PercentHAPIndex As Integer = 0
            Dim Peaklast10PercentHAP As Double = 0.1 * HeightAfterPeak +
EndBaseLine
            Dim Peaklast10PercentHAPIndex As Integer = 0
            Dim Peaklast90PercentHAP As Double = 0.9 * HeightAfterPeak +
EndBaseLine
            Dim Peaklast90PercentHAPIndex As Integer = 0
            Dim PeakHalfMaxHAP As Double = 0.5 * HeightAfterPeak + EndBaseLine
            Dim HRTIndexHAP As Integer = 0
            Dim HTTPIndexHAP As Integer = 0



            If IsNothing(OriginalData) Then
```

```
            Else
                NewFinalPeak.HeightOriginal = PeakHeightOriginal
                NewFinalPeak.DFdivideFOriginal = PeakHeightOriginal / BaseLine
            End If
            NewFinalPeak.Baseline = BaseLine
            NewFinalPeak.Height = PeakHeight
            NewFinalPeak.DFdivideF = PeakHeight / BaseLine
            NewFinalPeak.EndBaselineValue = EndBaseLine
            NewFinalPeak.Height_AP = HeightAfterPeak
            NewFinalPeak.DFdivideF_AP = HeightAfterPeak / EndBaseLine

            PreCenterArray = New DataPoint(CenterIndex) {}
            Array.Copy(DataArray, PreCenterArray, CenterIndex + 1)
            Peak5firstPercentIndex = Array.FindLastIndex(PreCenterArray,
Function(x As DataPoint) x.Value <= Peakfirst5Percent)
            HTTPIndex = Array.FindLastIndex(PreCenterArray, Function(x As
DataPoint) x.Value <= PeakHalfMax)
            HTTPIndexHAP = Array.FindLastIndex(PreCenterArray, Function(x As
DataPoint) x.Value <= PeakHalfMaxHAP)

            NewFinalPeak.HTTP = DataArray(CenterIndex).Time -
DataArray(HTTPIndex).Time
            NewFinalPeak.TTP = DataArray(CenterIndex).Time -
DataArray(Peak5firstPercentIndex).Time

            ''Klassifikation
            Select Case Math.Abs(NewFinalPeak.Baseline -
NewFinalPeak.EndBaselineValue)
                Case < PeakHeight * 0.1
                    NewFinalPeak.PeakClass = PeakClassification.Equal



                    PostCenterArray = New DataPoint(DataArray.Count -
CenterIndex - 1) {}
                    Array.Copy(DataArray, CenterIndex, PostCenterArray, 0,
DataArray.Count - CenterIndex)
                    Peaklast10PercentIndex =
Array.FindLastIndex(PostCenterArray, Function(x As DataPoint) x.Value >=
Peaklast10Percent)
                    Peaklast90PercentIndex =
Array.FindLastIndex(PostCenterArray, Function(x As DataPoint) x.Value >=
Peaklast90Percent)
                    HRTIndex = Array.FindLastIndex(PostCenterArray, Function(x
As DataPoint) x.Value >= PeakHalfMax)

                    NewFinalPeak.NinetyToTen =
PostCenterArray(Peaklast10PercentIndex).Time -
PostCenterArray(Peaklast90PercentIndex).Time
                    NewFinalPeak.HRT = PostCenterArray(HRTIndex).Time -
DataArray(CenterIndex).Time
                    NewFinalPeak.FWHM = PostCenterArray(HRTIndex).Time -
DataArray(HTTPIndex).Time


                Case Else
```

```
                    If (NewFinalPeak.Baseline - NewFinalPeak.EndBaselineValue)
> 0 Then
                        NewFinalPeak.PeakClass =
PeakClassification.FirstHigher

                        PostCenterArray = New DataPoint(DataArray.Count -
CenterIndex - 1) {}
                        Array.Copy(DataArray, CenterIndex, PostCenterArray, 0,
DataArray.Count - CenterIndex)
                        Peaklast10PercentIndex =
Array.FindLastIndex(PostCenterArray, Function(x As DataPoint) x.Value >=
Peaklast10Percent)
                        Peaklast90PercentIndex =
Array.FindLastIndex(PostCenterArray, Function(x As DataPoint) x.Value >=
Peaklast90Percent)
                        HRTIndex = Array.FindLastIndex(PostCenterArray,
Function(x As DataPoint) x.Value >= PeakHalfMax)

                        NewFinalPeak.NinetyToTen =
PostCenterArray(Peaklast10PercentIndex).Time -
PostCenterArray(Peaklast90PercentIndex).Time
                        NewFinalPeak.HRT = PostCenterArray(HRTIndex).Time -
DataArray(CenterIndex).Time
                        NewFinalPeak.FWHM = PostCenterArray(HRTIndex).Time -
DataArray(HTTPIndex).Time

                    Else
                        NewFinalPeak.PeakClass = PeakClassification.LastHigher
                        PostCenterArray = New DataPoint(DataArray.Count -
CenterIndex - 1) {}
                        Array.Copy(DataArray, CenterIndex, PostCenterArray, 0,
DataArray.Count - CenterIndex)
                        If Math.Abs(NewFinalPeak.Baseline -
NewFinalPeak.EndBaselineValue) < PeakHeight * 0.5 Then

                            HRTIndex = Array.FindLastIndex(PostCenterArray,
Function(x As DataPoint) x.Value >= PeakHalfMax)
                            NewFinalPeak.HRT = PostCenterArray(HRTIndex).Time
- DataArray(CenterIndex).Time
                            NewFinalPeak.FWHM = PostCenterArray(HRTIndex).Time
- DataArray(HTTPIndex).Time
                        End If

                    End If
            End Select


            ''Berechnung mit Bezug auf Höhe des decay(HAP)

            Peaklast10PercentHAPIndex = Array.FindLastIndex(PostCenterArray,
Function(x As DataPoint) x.Value >= Peaklast10PercentHAP)
            Peaklast90PercentHAPIndex = Array.FindLastIndex(PostCenterArray,
Function(x As DataPoint) x.Value >= Peaklast90PercentHAP)
            HRTIndexHAP = Array.FindLastIndex(PostCenterArray, Function(x As
DataPoint) x.Value >= PeakHalfMaxHAP)
```

```
            NewFinalPeak.NinetyToTen_AP =
PostCenterArray(Peaklast10PercentHAPIndex).Time -
PostCenterArray(Peaklast90PercentHAPIndex).Time
            NewFinalPeak.HRT_AP = PostCenterArray(HRTIndexHAP).Time -
DataArray(CenterIndex).Time
            NewFinalPeak.FWHM_AP = PostCenterArray(HRTIndexHAP).Time -
DataArray(HTTPIndexHAP).Time



            FinalPeakFiberList.Add(NewFinalPeak)

        Catch e As Exception

            MessageBox.Show(e.Message)
            Return False
        End Try
        Return True

    End Function
```

3 CONCLUSION AND PERSPECTIVES

A major goal of this PhD thesis was to establish and optimize methods to make EOMs available for functional measurements, specifically force measurements on individual EOMs and Ca^{2+} dynamic and homeostasis at the single fiber level as well as static measurements such as immunohistochemistry and structural EM imaging on whole EOMs.

Extraocular muscles are a unique type of skeletal muscle. This is already reflected by a different developmental origin than the other skeletal muscles. They are known to be among the fastest and fatigue resistant muscles. Our previous studies showed that EOMs express a unique panel of transcripts and proteins. Unlike other skeletal muscle they express the cardiac DHP receptor, the ryanodine receptor type 3 as well as MyHC13.

The RyR3 transcript expression in EOM's drew our interest. The reason was that RyR3 is expressed widely in different tissues but no real functional role in skeletal muscles was found; there were reports associating RyR3 ablation with minor cognitive impairments, but its true functional role was still not clear. We used the new methods I established to investigate the role of RyR3 in EOMs by using a mouse model lacking RyR3, the $RyR3^{-/-}$ mouse. Our results reveal for the first time an important role for RyR3 in extraocular muscle function. After the first observation that $RyR3^{-/-}$ mice have an impaired visual apparatus determined by a reduced acuity (OKR and water maze) we decided to study the properties of isolated EOMs to reduce the complexity of the visual apparatus from three possible impairments, the brain, the eye and the EOM, to one. We were able show significant reduction of force and kinetic twitch parameter. Since proteins involved in ECC, as well as the MyHC composition were similar to the WT we concluded that the altered twitch causes the phenotype. After digging deeper in the ECC machinery and analyzing the Ca^{2+} transients we found changes in some of the kinetic parameters but not in the peak Ca^{2+} release. Interestingly the half relaxation time (during force measurements and in the Ca^{2+} transients) was consistently increased. This might sound contradictory at first view because the lack of RyR3, a Ca^{2+} releasing channel should not alter the uptake of Ca^{2+} into the SR. But we hypothesized that the different location of the RyR3 might be the reason. There are a couple of papers showing that the RyR3 is located parajunctional in the SR (Felder and Franzini-Armstrong, 2002; Perni et al.,

2015) and other papers showing that RyR3 is in close proximity to the SERCA (Clark et al., 2010). Therefore, it is reasonable to say that the release of Ca^{2+} by RyR3 in WT activates the SERCA and speeds up the half relaxation time. This novel mechanism is unique to EOMs and may reflect their physiological function because EOMs require super-fast Ca^{2+} uptake due to their physiological characteristics of being both the fastest muscles and of being fatigue resistant. One fact which may point into the direction of a role of RyR3-SERCA and fatigue resistance is that another skeletal muscle, namely the diaphragm also expresses RyR3. The diaphragm is not known to be fast twitch muscle, but it is a muscle which needs to constantly work since it is involved in breathing.

Even though our kinetic of force and Ca^{2+} release results were consistent we were unable to show that the reduction in force is due to the reduced Ca^{2+} release. There might be two reasons for this. The first is just the different preparation between that used for force measurements (whole muscle mount) and that used for Ca2+ measurements (isolated single fibers). Thus, the reduction in force can be due to a systematic effect which only appears at whole muscle level while we could only isolate functional subpopulations of fibers. Indeed, during enzymatic isolation of fibers it is possible that we lost exactly the fibers which have reduced Ca^{2+} release because they are damaged and are not able to survive the procedure. Another possibility of the reduced force is that the development of the EOM is altered because it is well known that the RyR3 is expressed during maturation. Compatibly, we were able to show alterations at the developmental level in $RyR3^{-/-}$ myotubes by measuring spontaneous Ca^{2+} oscillations.

In conclusion, in our first paper we were able to find an EOM phenotype in the $RyR3^{-/-}$ mouse. This phenotype is caused by a reduced force and altered force kinetic which is a result of alterations at the developmental level as well as altered Ca^{2+} release kinetics. From a clinical perspective our study shows a new possible pathomechanism for ophthalmoplegia, strabismus, and ptosis with a new possible screening target, the *RYR3*.

In our second paper we focused on the *RYR1*, since there are hundreds of mutations in this gene shown to cause disease, specifically myopathies. We investigated the molecular basis of the EOM impairment in compound heterozygous *RYR1* mutant carriers. Our group created and characterized a compound heterozygous mouse model (DKI). The mouse model was created to carry *RYR1* mutations identified in a patient with congenital myopathy (Klein et al., 2012; Elbaz et

al., 2019b; a). We performed experiments similar to those performed in the RyR3$^{-/-}$ mouse. We compared WT mice, single heterozygous *RYR1* mutants as well as the DKI mice and could show that only the EOMs from the DKI mouse has a decreased force; the change in force was very large, i.e. a factor of 8-10 times compared to single heterozygous, homozygous mutant carriers or WT mice. Because of these results we performed the next series of experiments only on EOMs from DKI mice. Unlike the RyR3$^{-/-}$ mouse, the DKI showed significant reduction in the Ca^{2+} release by 50%, which is consistent with the finding that the EOMs of the DKI only express 60% RyR1 content compared to WT, as determined by western blotting and mass spectrometry. Additionally, similar to the RyR1 DHPR content is also reduced, suggesting an overall reduction of CRU. And indeed, we were able to show, via EM, that the number of CRU decrease by 57% compared to WT. The reduced Ca^{2+} release clearly plays a significant part of the reduced force production. But we also found a tremendous reduction and almost complete absence of the EOM specific MyHC, MyHC13 in the DKI. This was an unexpected but very interesting finding. MyHCs are directly involved in the force production so this reduction also plays an important role in the reduced force phenotype. Importantly EOMs needs to be active during development to express MyHC13 and its presence cannot be restored in grown-ups (Brueckner et al., 1999). In summary we showed that the DKI representing a congenital myopathy with compound heterozygous *RYR1* mutations have EOM impairment. This is the first time that the molecular basis of EOM impairment linked to congenital myopathies has been investigated. Remarkably this dysfunction is only present in the DKI and not in the single heterozygous or homozygous mice. Now that the mouse model and the methods are available it is possible to screen which kind of treatment can increase the recovery of EOM force in the mouse model and this might be a potentially useful drug for patients. One should also keep in mind however that our results showing reduced MyHC13 content also suggest that the damage to the EOM is already present very early in life or during development. So, whether EOM function can be recovered remains an open question and must be determined experimentally in future studies.

In conclusion in this work we uncovered that RyR3 plays in important role in ECC of EOMs, a fact that was unknow previously and might be useful for potential mutation-screening targets in the future. In the second part we demonstrated that our congenital mouse model has an EOM

dysfunction and can serve as mouse model for congenital myopathies with EOM involvement. In this mouse model we also showed a possible connection between EOM dysfunction and the lack of MyHC13. Our established methods, findings and mouse models basically open the field for in ex-vivo ECC studies in EOM.

4 REFERENCES

Anderson, A.A., S. Treves, D. Biral, R. Betto, D. Sandonà, M. Ronjat, and F. Zorzato. 2003. The novel skeletal muscle sarcoplasmic reticulum JP-45 protein. Molecular cloning, tissue distribution, developmental expression, and interaction with alpha 1.1 subunit of the voltage-gated calcium channel. *J. Biol. Chem.* 278:39987–92. doi:10.1074/jbc.M305016200.

Anderson, D.M., K.M. Anderson, C.-L. Chang, C.A. Makarewich, B.R. Nelson, J.R. McAnally, P. Kasaragod, J.M. Shelton, J. Liou, R. Bassel-Duby, and E.N. Olson. 2015. A micropeptide encoded by a putative long noncoding RNA regulates muscle performance. *Cell*. 160:595–606. doi:10.1016/j.cell.2015.01.009.

Andrade, F.H., J.D. Porter, and H.J. Kaminski. 2000. Eye muscle sparing by the muscular dystrophies: Lessons to be learned? *Microsc. Res. Tech.* 48:192–203. doi:10.1002/(SICI)1097-0029(20000201/15)48:3/4<192::AID-JEMT7>3.0.CO;2-J.

Au, Y. 2004. The muscle ultrastructure: a structural perspective of the sarcomere. *Cell. Mol. Life Sci.* 61:3016–3033. doi:10.1007/s00018-004-4282-x.

Barone, V., F. Bertocchini, R. Bottinelli, F. Protasi, P.D. Allen, C. Franzini Armstrong, C. Reggiani, and V. Sorrentino. 1998. Contractile impairment and structural alterations of skeletal muscles from knockout mice lacking type 1 and type 3 ryanodine receptors. *FEBS Lett.* 422:160–4. doi:10.1016/s0014-5793(98)00003-9.

Barone, V., D. Randazzo, V. Del Re, V. Sorrentino, and D. Rossi. 2015. Organization of junctional sarcoplasmic reticulum proteins in skeletal muscle fibers. *J. Muscle Res. Cell Motil.* 36:501–515. doi:10.1007/s10974-015-9421-5.

Baylor, S.M., and S. Hollingworth. 2003. Sarcoplasmic reticulum calcium release compared in slow-twitch and fast-twitch fibres of mouse muscle. *J. Physiol.* 551:125–38. doi:10.1113/jphysiol.2003.041608.

Bellinger, A.M., S. Reiken, M. Dura, P.W. Murphy, S.-X. Deng, D.W. Landry, D. Nieman, S.E. Lehnart, M. Samaru, A. LaCampagne, and A.R. Marks. 2008. Remodeling of ryanodine

receptor complex causes “leaky” channels: a molecular mechanism for decreased exercise capacity. *Proc. Natl. Acad. Sci. U. S. A.* 105:2198–2202. doi:10.1073/pnas.0711074105.

Berridge, M.J. 2008. Smooth muscle cell calcium activation mechanisms. *J. Physiol.* 586:5047–61. doi:10.1113/jphysiol.2008.160440.

Bers, D.M. 2002. Cardiac excitation–contraction coupling. *Nature*. 415:198–205. doi:10.1038/415198a.

Bicer, S., and P.J. Reiser. 2009. Myosin Isoform Expression in Dog Rectus Muscles: Patterns in Global and Orbital Layers and among Single Fibers. *Investig. Opthalmology Vis. Sci.* 50:157. doi:10.1167/iovs.08-2416.

Blausen.com staff. 2014. Medical gallery of Blausen Medical 2014. *WikiJournal Med.* 1. doi:10.15347/wjm/2014.010.

Brillantes, A.-M.B., K. Ondrias, A. Scott, E. Kobrinsky, E. Ondriašová, M.C. Moschella, T. Jayaraman, M. Landers, B.E. Ehrlich, and A.R. Marks. 1994. Stabilization of calcium release channel (ryanodine receptor) function by FK506-binding protein. *Cell*. 77:513–523. doi:10.1016/0092-8674(94)90214-3.

Brini, M., and E. Carafoli. 2009. Calcium Pumps in Health and Disease. *Physiol. Rev.* 89:1341–1378. doi:10.1152/physrev.00032.2008.

Brueckner, J.K., L.P. Ashby, J.R. Prichard, and J.D. Porter. 1999. Vestibulo-ocular pathways modulate extraocular muscle myosin expression patterns. *Cell Tissue Res.* 295:477–84. doi:10.1007/s004410051253.

Buratti, R., G. Prestipino, P. Menegazzi, S. Treves, and F. Zorzato. 1995. Calcium-Dependent Activation of Skeletal-Muscle Ca2+ Release Channel (Ryanodine Receptor) by Calmodulin. *Biochem. Biophys. Res. Commun.* 213:1082–1090. doi:10.1006/BBRC.1995.2238.

Büttner-Ennever, J. 2007. Anatomy of the oculomotor system. *Dev. Ophthalmol.* 40:1–14. doi:10.1159/000100345.

Caiozzo, V.J., F. Haddad, M. Baker, S. McCue, and K.M. Baldwin. 2000. MHC polymorphism in

rodent plantaris muscle: effects of mechanical overload and hypothyroidism. *Am. J. Physiol. Physiol.* 278:C709–C717. doi:10.1152/ajpcell.2000.278.4.C709.

Calderón, J.C., P. Bolaños, and C. Caputo. 2014. The excitation-contraction coupling mechanism in skeletal muscle. *Biophys. Rev.* 6:133–160. doi:10.1007/s12551-013-0135-x.

Catterall, W.A. 1995. Structure and Function of Voltage-Gated Ion Channels. *Annu. Rev. Biochem.* 64:493–531. doi:10.1146/annurev.bi.64.070195.002425.

Catterall, W.A., J. Striessnig, T.P. Snutch, and E. Perez-Reyes. 2003. International Union of Pharmacology. XL. Compendium of voltage-gated ion channels: calcium channels. *Pharmacol. Rev.* 55:579–581. doi:10.1124/pr.55.4.8.and.

Chang, C.-N., and C. Kioussi. 2018. Location, Location, Location: Signals in Muscle Specification. *J. Dev. Biol.* 6. doi:10.3390/jdb6020011.

Chen, W., R. Wang, B. Chen, X. Zhong, H. Kong, Y. Bai, Q. Zhou, C. Xie, J. Zhang, A. Guo, X. Tian, P.P. Jones, M.L. O'Mara, Y. Liu, T. Mi, L. Zhang, J. Bolstad, L. Semeniuk, H. Cheng, J. Zhang, J. Chen, D.P. Tieleman, A.M. Gillis, H.J. Duff, M. Fill, L.-S. Song, and S.R.W. Chen. 2014. The ryanodine receptor store-sensing gate controls Ca2+ waves and Ca2+-triggered arrhythmias. *Nat. Med.* 20:184–192. doi:10.1038/nm.3440.

Clancy, J.S., H. Takeshima, S.L. Hamilton, and M.B. Reid. 1999. Contractile function is unaltered in diaphragm from mice lacking calcium release channel isoform 3. *Am. J. Physiol.* 277:R1205-9.

Clark, J.H., N.P. Kinnear, S. Kalujnaia, G. Cramb, S. Fleischer, L.H. Jeyakumar, F. Wuytack, and a M. Evans. 2010. Identification of functionally segregated sarcoplasmic reticulum calcium stores in pulmonary arterial smooth muscle. *J. Biol. Chem.* 285:13542–13549. doi:10.1074/jbc.M110.101485.

Clarke, O.B., and W.A. Hendrickson. 2016. Structures of the colossal RyR1 calcium release channel. *Curr. Opin. Struct. Biol.* 39:144–152. doi:10.1016/j.sbi.2016.09.002.

Close, R.I., and A.R. Luff. 1974. Dynamic properties of inferior rectus muscle of the rat. *J. Physiol.*

236:259–70. doi:10.1113/jphysiol.1974.sp010434.

Costello, B., C. Chadwick, A. Saito, A. Chu, A. Maurer, and S. Fleischer. 1986. Characterization of the junctional face membrane from terminal cisternae of sarcoplasmic reticulum. *J. Cell Biol.* 103:741–53. doi:10.1083/jcb.103.3.741.

Craig, R. 2017. Molecular structure of muscle filaments determined by electron microscopy. *Appl. Microsc.* 47:226–232. doi:10.9729/am.2017.47.4.226.

Craig, R., and J.L. Woodhead. 2006. Structure and function of myosin filaments. *Curr. Opin. Struct. Biol.* 16:204–212. doi:10.1016/j.sbi.2006.03.006.

Demer, J.L., S.Y. Oh, and V. Poukens. 2000. Evidence for active control of rectus extraocular muscle pulleys. *Investig. Ophthalmol. Vis. Sci.* 41:1280–1290.

Díaz-Vegas, A., V. Eisner, and E. Jaimovich. 2019. Skeletal muscle excitation-metabolism coupling. *Arch. Biochem. Biophys.* 664:89–94. doi:10.1016/j.abb.2019.01.037.

Dorr, M., M. Kwon, L.A. Lesmes, A. Miller, M. Kazlas, K. Chan, D.G. Hunter, Z.-L. Lu, and P.J. Bex. 2019. Binocular Summation and Suppression of Contrast Sensitivity in Strabismus, Fusion and Amblyopia. *Front. Hum. Neurosci.* 13:234. doi:10.3389/fnhum.2019.00234.

Drum, S.N., R. Weatherwax, and J.B. Dixon. 2016. Physiology of skeletal muscle. *Muscular Inj. Posterior Leg Assess. Treat.* 13–26. doi:10.1007/978-1-4899-7651-2_2.

Durston, J.H. 1974. Histochemistry of primate extraocular muscles and the changes of denervation. *Br. J. Ophthalmol.* 58:193–216. doi:10.1136/bjo.58.3.193.

Eckhardt, J., C. Bachmann, M. Sekulic-Jablanovic, V. Enzmann, K.H. Park, J. Ma, H. Takeshima, F. Zorzato, and S. Treves. 2019. Extraocular muscle function is impaired in ryr3-/- mice. *J. Gen. Physiol.* 151:929–943. doi:10.1085/jgp.201912333.

Efremov, R.G., A. Leitner, R. Aebersold, and S. Raunser. 2015. Architecture and conformational switch mechanism of the ryanodine receptor. *Nature*. 517:39–43. doi:10.1038/nature13916.

Eisner, D.A., J.L. Caldwell, K. Kistamás, and A.W. Trafford. 2017. Calcium and Excitation-Contraction Coupling in the Heart. *Circ. Res.* 121:181–195.

doi:10.1161/CIRCRESAHA.117.310230.

Elbaz, M., A. Ruiz, C. Bachmann, J. Eckhardt, P. Pelczar, E. Venturi, C. Lindsay, A.D. Wilson, A. Alhussni, T. Humberstone, L. Pietrangelo, S. Boncompagni, R. Sitsapesan, S. Treves, and F. Zorzato. 2019a. Quantitative RyR1 reduction and loss of calcium sensitivity of RyR1Q1970fsX16+A4329D cause cores and loss of muscle strength. *Hum. Mol. Genet.* 28:2987–2999. doi:10.1093/hmg/ddz092.

Elbaz, M., A. Ruiz, J. Eckhardt, P. Pelczar, F. Muntoni, S. Boncompagni, S. Treves, and F. Zorzato. 2019b. Quantitative reduction of RyR1 protein caused by a single-allele frameshift mutation in RYR1 ex36 impairs the strength of adult skeletal muscle fibres. *Hum. Mol. Genet.* 28:1872–1884. doi:10.1093/hmg/ddz025.

Elíes, J., M. Yáñez, T.M.C. Pereira, J. Gil-Longo, D.A. MacDougall, and M. Campos-Toimil. 2020. An Update to Calcium Binding Proteins. Springer, Cham. 183–213.

Felder, E., and C. Franzini-Armstrong. 2002. Type 3 ryanodine receptors of skeletal muscle are segregated in a parajunctional position. *Proc. Natl. Acad. Sci. U. S. A.* 99:1695–1700. doi:10.1073/pnas.032657599.

Fessenden, J.D., Y. Wang, R.A. Moore, S.R.W. Chen, P.D. Allen, and I.N. Pessah. 2000. Divergent Functional Properties of Ryanodine Receptor Types 1 and 3 Expressed in a Myogenic Cell Line. *Biophys. J.* 79:2509–2525. doi:10.1016/S0006-3495(00)76492-7.

Fischer, M.D., J.R. Gorospe, E. Felder, S. Bogdanovich, F. Pedrosa-Domellöf, R.S. Ahima, N.A. Rubinstein, E.P. Hoffman, and T.S. Khurana. 2002. Expression profiling reveals metabolic and structural components of extraocular muscles. *https://doi.org/10.1152/physiolgenomics.00115.2001*. doi:10.1152/PHYSIOLGENOMICS.00115.2001.

Fleischer, S., E.M. Ogunbunmi, M.C. Dixon, and E.A. Fleer. 1985. Localization of Ca2+ release channels with ryanodine in junctional terminal cisternae of sarcoplasmic reticulum of fast skeletal muscle. *Proc. Natl. Acad. Sci.* 82:7256–7259. doi:10.1073/pnas.82.21.7256.

Franzini-Armstrong, C. 1987. The structure of calsequestrin in triads of vertebrate skeletal muscle:

a deep-etch study. *J. Cell Biol.* 105:49–56. doi:10.1083/jcb.105.1.49.

Franzini-Armstrong, C. 2018. The relationship between form and function throughout the history of excitation–contraction coupling. *J. Gen. Physiol.* 150:189–210. doi:10.1085/jgp.201711889.

Franzini-Armstrong, C., and G. Nunzi. 1983. Junctional feet and particles in the triads of a fast-twitch muscle fibre. *J. Muscle Res. Cell Motil.* 4:233–252. doi:10.1007/BF00712033.

Franzini-Armstrong, C., and L.D. Peachey. 1981. Striated muscle-contractile and control mechanisms. *J. Cell Biol.* 91:166s-186s. doi:10.1083/jcb.91.3.166s.

Frontera, W.R., and J. Ochala. 2015. Skeletal Muscle: A Brief Review of Structure and Function. *Calcif. Tissue Int.* 96:183–195. doi:10.1007/s00223-014-9915-y.

Fuentes, O., C. Valdivia, D. Vaughan, R. Coronado, and H.H. Valdivia. 1994. Calcium-dependent block of ryanodine receptor channel of swine skeletal muscle by direct binding of calmodulin. *Cell Calcium*. 15:305–316. doi:10.1016/0143-4160(94)90070-1.

Furuichi, T., D. Furutama, Y. Hakamata, J. Nakai, H. Takeshima, and K. Mikoshiba. 1994. Multiple types of ryanodine receptor/Ca2+ release channels are differentially expressed in rabbit brain. *J. Neurosci.* 14:4794–805.

Galfré, E., S.J. Pitt, E. Venturi, M. Sitsapesan, N.R. Zaccai, K. Tsaneva-Atanasova, S. O'Neill, and R. Sitsapesan. 2012. FKBP12 Activates the Cardiac Ryanodine Receptor Ca2+-Release Channel and Is Antagonised by FKBP12.6. *PLoS One*. 7:e31956. doi:10.1371/journal.pone.0031956.

Gambardella, J., B. Trimarco, G. Iaccarino, and G. Santulli. 2017. New Insights in Cardiac Calcium Handling and Excitation-Contraction Coupling. *In* Advances in experimental medicine and biology. 373–385.

des Georges, A., O.B. Clarke, R. Zalk, Q. Yuan, K.J. Condon, R.A. Grassucci, W.A. Hendrickson, A.R. Marks, and J. Frank. 2016. Structural Basis for Gating and Activation of RyR1. *Cell*. 167:145-157.e17. doi:10.1016/j.cell.2016.08.075.

Giannini, G., E. Clementi, R. Ceci, G. Marziali, and V. Sorrentino. 1992. Expression of a ryanodine

receptor-Ca2+ channel that is regulated by TGF-beta. *Science*. 257:91–4. doi:10.1126/SCIENCE.1320290.

Giannini, G., A. Conti, S. Mammarella, M. Scrobogna, and V. Sorrentino. 1995. The ryanodine receptor/calcium channel genes are widely and differentially expressed in murine brain and peripheral tissues. *J. Cell Biol.* 128:893–904. doi:10.1083/JCB.128.5.893.

Greenstein, J.L., and R.L. Winslow. 2011. Integrative systems models of cardiac excitation-contraction coupling. *Circ. Res.* 108:70–84. doi:10.1161/CIRCRESAHA.110.223578.

Guerrini, R., P. Menegazzi, R. Anacardio, M. Marastoni, R. Tomatis, F. Zorzato, and S. Treves. 1995. Calmodulin Binding Sites of the Skeletal, Cardiac, and Brain Ryanodine Receptor Ca2+ Channels: Modulation by the Catalytic Subunit of cAMP-Dependent Protein Kinase? *Biochemistry*. 34:5120–5129. doi:10.1021/bi00015a024.

Hakamata, Y., J. Nakai, H. Takeshima, and K. Imoto. 1992. Primary structure and distribution of a novel ryanodine receptor/calcium release channel from rabbit brain. *FEBS Lett.* 312:229–235. doi:10.1016/0014-5793(92)80941-9.

Hall, J.E. (John E. 2016. Guyton and Hall textbook of medical physiology. Saunders. 1168 pp.

Hamilton, S., and D. Terentyev. 2019. Altered Intracellular Calcium Homeostasis and Arrhythmogenesis in the Aged Heart. *Int. J. Mol. Sci.* 20:2386. doi:10.3390/ijms20102386.

Harrison, A.R., B.C. Anderson, L. V Thompson, and L.K. McLoon. 2007. Myofiber length and three-dimensional localization of NMJs in normal and botulinum toxin treated adult extraocular muscles. *Invest. Ophthalmol. Vis. Sci.* 48:3594–601. doi:10.1167/iovs.06-1239.

Helveston, E.M. 2010. Understanding, detecting, and managing strabismus. *Community eye Heal.* 23:12–4.

Hernández-Ochoa, E.O., and M.F. Schneider. 2018. Voltage sensing mechanism in skeletal muscle excitation-contraction coupling: coming of age or midlife crisis? *Skelet. Muscle*. 8:22. doi:10.1186/s13395-018-0167-9.

Hill, J.A., E.N. Olson, and K.K. Griendling. 2012. Muscle : fundamental biology and mechanisms of

disease. Academic Press.

Horstick, E.J., J.W. Linsley, J.J. Dowling, M.A. Hauser, K.K. McDonald, A. Ashley-Koch, L. Saint-Amant, A. Satish, W.W. Cui, W. Zhou, S.M. Sprague, D.S. Stamm, C.M. Powell, M.C. Speer, C. Franzini-Armstrong, H. Hirata, and J.Y. Kuwada. 2013. Stac3 is a component of the excitation–contraction coupling machinery and mutated in Native American myopathy. *Nat. Commun.* 4:1952. doi:10.1038/ncomms2952.

Huang, X., B. Fruen, D.T. Farrington, T. Wagenknecht, and Z. Liu. 2012. Calmodulin-binding Locations on the Skeletal and Cardiac Ryanodine Receptors. *J. Biol. Chem.* 287:30328–30335. doi:10.1074/jbc.M112.383109.

Hwang, J.H., F. Zorzato, N.F. Clarke, and S. Treves. 2012. Mapping domains and mutations on the skeletal muscle ryanodine receptor channel. *Trends Mol. Med.* 18:644–657. doi:10.1016/j.molmed.2012.09.006.

Ikemoto, T., M. Iino, and M. Endo. 1995. Enhancing effect of calmodulin on Ca(2+)-induced Ca2+ release in the sarcoplasmic reticulum of rabbit skeletal muscle fibres. *J. Physiol.* 487:573–582. doi:10.1113/jphysiol.1995.sp020901.

Jayaraman, T., A.M. Brillantes, A.P. Timerman, S. Fleischer, H. Erdjument-Bromage, P. Tempst, and A.R. Marks. 1992. FK506 binding protein associated with the calcium release channel (ryanodine receptor). *J. Biol. Chem.* 267:9474–7.

Jungbluth, H. 2007a. Multi-minicore Disease. *Orphanet J. Rare Dis.* 2:31. doi:10.1186/1750-1172-2-31.

Jungbluth, H. 2007b. Central core disease. *Orphanet J. Rare Dis.* 2:25. doi:10.1186/1750-1172-2-25.

Jungbluth, H., C.A. Sewry, and F. Muntoni. 2011. Core myopathies. *Semin. Pediatr. Neurol.* 18:239–249. doi:10.1016/j.spen.2011.10.005.

Jungbluth, H., S. Treves, F. Zorzato, A. Sarkozy, J. Ochala, C. Sewry, R. Phadke, M. Gautel, and F. Muntoni. 2018. Congenital myopathies: disorders of excitation–contraction coupling and

muscle contraction. *Nat. Rev. Neurol.* 14:151–167. doi:10.1038/nrneurol.2017.191.

Al Kahtani, E.S., R. Khandekar, K. Al-Rubeaan, A.M. Youssef, H.M. Ibrahim, and A.H. Al-Sharqawi. 2016. Assessment of the prevalence and risk factors of ophthalmoplegia among diabetic patients in a large national diabetes registry cohort. *BMC Ophthalmol.* 16:118. doi:10.1186/s12886-016-0272-7.

Kallestad, K.M., S.L. Hebert, A.A. McDonald, M.L. Daniel, S.R. Cu, and L.K. McLoon. 2011. Sparing of extraocular muscle in aging and muscular dystrophies: A myogenic precursor cell hypothesis. *Exp. Cell Res.* 317:873–885. doi:10.1016/j.yexcr.2011.01.018.

Khanna, S., C.R. Richmonds, H.J. Kaminski, and J.D. Porter. 2003. Molecular Organization of the Extraocular Muscle Neuromuscular Junction: Partial Conservation of and Divergence from the Skeletal Muscle Prototype. *Investig. Opthalmology Vis. Sci.* 44:1918. doi:10.1167/iovs.02-0890.

Khurana, T.S., R.A. Prendergast, H.S. Alameddine, F.M. Tomé, M. Fardeau, K. Arahata, H. Sugita, and L.M. Kunkel. 1995. Absence of extraocular muscle pathology in Duchenne's muscular dystrophy: role for calcium homeostasis in extraocular muscle sparing. *J. Exp. Med.* 182:467–75. doi:10.1084/jem.182.2.467.

Kimlicka, L., and F. Van Petegem. 2011. The structural biology of ryanodine receptors. *Sci. China Life Sci.* 54:712–724. doi:10.1007/s11427-011-4198-2.

King, W.M. 2011. Binocular coordination of eye movements--Hering's Law of equal innervation or uniocular control? *Eur. J. Neurosci.* 33:2139–46. doi:10.1111/j.1460-9568.2011.07695.x.

Kjellgren, D., L.-E. Thornell, J. Andersen, and F. Pedrosa-Domello¨f. 2003. Myosin Heavy Chain Isoforms in Human Extraocular Muscles. *Investig. Opthalmology Vis. Sci.* 44:1419. doi:10.1167/iovs.02-0638.

Klein, A., S. Lillis, I. Munteanu, M. Scoto, H. Zhou, R. Quinlivan, V. Straub, A.Y. Manzur, H. Roper, P.-Y. Jeannet, W. Rakowicz, D.H. Jones, U.B. Jensen, E. Wraige, N. Trump, U. Schara, H. Lochmuller, A. Sarkozy, H. Kingston, F. Norwood, M. Damian, J. Kirschner, C. Longman, M. Roberts, M. Auer-Grumbach, I. Hughes, K. Bushby, C. Sewry, S. Robb, S. Abbs, H. Jungbluth,

and F. Muntoni. 2012. Clinical and genetic findings in a large cohort of patients with ryanodine receptor 1 gene-associated myopathies. *Hum. Mutat.* 33:981–8. doi:10.1002/humu.22056.

Kranjc, B.S., J. Sketelj, A. D'Albis, M. Ambrož, and I. Eržen. 2000. Fibre types and Myosin heavy chain expression in the Ocular Medial Rectus Muscle of the Adult Rat. *J. Muscle Res. Cell Motil.* 21:753–761. doi:10.1023/A:1010362926221.

Kushnir, A., and A.R. Marks. 2010. The ryanodine receptor in cardiac physiology and disease. *Adv. Pharmacol.* 59:1–30. doi:10.1016/S1054-3589(10)59001-X.

Kuwajima, G., A. Futatsugi, M. Niinobe, S. Nakanishi, and K. Mikoshiba. 1992. Two types of ryanodine receptors in mouse brain: skeletal muscle type exclusively in Purkinje cells and cardiac muscle type in various neurons. *Neuron*. 9:1133–42. doi:10.1016/0896-6273(92)90071-k.

Lai, F.A., M. Dent, C. Wickenden, L. Xu, G. Kumari, M. Misra, H.B. Lee, M. Sar, and G. Meissner. 1992. Expression of a cardiac Ca(2+)-release channel isoform in mammalian brain. *Biochem. J.* 288 (Pt 2):553–64. doi:10.1042/bj2880553.

Laitinen, P.J., K.M. Brown, K. Piippo, H. Swan, J.M. Devaney, B. Brahmbhatt, E.A. Donarum, M. Marino, N. Tiso, M. Viitasalo, L. Toivonen, D.A. Stephan, and K. Kontula. 2001. Mutations of the Cardiac Ryanodine Receptor (RyR2) Gene in Familial Polymorphic Ventricular Tachycardia. *Circulation*. 103:485–490. doi:10.1161/01.CIR.103.4.485.

Laitinen, P.J., H. Swan, and K. Kontula. 2003. Molecular genetics of exercise-induced polymorphic ventricular tachycardia: identification of three novel cardiac ryanodine receptor mutations and two common calsequestrin 2 amino-acid polymorphisms. *Eur. J. Hum. Genet.* 11:888–91. doi:10.1038/sj.ejhg.5201061.

Lamb, G. 2000. Excitation-Contraction Coupling In Skeletal Muscle: Comparisons With Cardiac Muscle. *Clin. Exp. Pharmacol. Physiol.* 27:216–224. doi:10.1046/j.1440-1681.2000.03224.x.

Lanner, J.T., D.K. Georgiou, A.D. Joshi, and S.L. Hamilton. 2010. Ryanodine Receptors: Structure, Expression, Molecular Details, and Function in Calcium Release. *Cold Spring Harb. Perspect.*

Biol. 2:a003996. doi:10.1101/CSHPERSPECT.A003996.

Lasa-Elgarresta, J., L. Mosqueira-Martín, N. Naldaiz-Gastesi, A. Sáenz, A. López de Munain, and A. Vallejo-Illarramendi. 2019. Calcium Mechanisms in Limb-Girdle Muscular Dystrophy with CAPN3 Mutations. *Int. J. Mol. Sci.* 20:4548. doi:10.3390/ijms20184548.

Lattanzio, F.A., R.G. Schlatterer, M. Nicar, K.P. Campbell, and J.L. Sutko. 1987. The effects of ryanodine on passive calcium fluxes across sarcoplasmic reticulum membranes. *J. Biol. Chem.* 262:2711–8.

Lee, L.A., A. Karabina, L.J. Broadwell, and L.A. Leinwand. 2019. The ancient sarcomeric myosins found in specialized muscles. *Skelet. Muscle*. 9:7. doi:10.1186/s13395-019-0192-3.

Liao, M., E. Cao, D. Julius, and Y. Cheng. 2013. Structure of the TRPV1 ion channel determined by electron cryo-microscopy. *Nature*. 504:107–112. doi:10.1038/nature12822.

Liu, X., M.J. Betzenhauser, S. Reiken, A.C. Meli, W. Xie, B.-X. Chen, O. Arancio, and A.R. Marks. 2012. Role of Leaky Neuronal Ryanodine Receptors in Stress- Induced Cognitive Dysfunction. *Cell*. 150:1055–1067. doi:10.1016/j.cell.2012.06.052.

Liu, Z., J. Zhang, M.R. Sharma, P. Li, S.R.W. Chen, and T. Wagenknecht. 2001. Three-dimensional reconstruction of the recombinant type 3 ryanodine receptor and localization of its amino terminus. *Proc. Natl. Acad. Sci.* 98:6104–6109. doi:10.1073/pnas.111382798.

Lopez, R.J., S. Byrne, M. Vukcevic, M. Sekulic-Jablanovic, L. Xu, M. Brink, J. Alamelu, N. Voermans, M. Snoeck, E. Clement, F. Muntoni, H. Zhou, A. Radunovic, S. Mohammed, E. Wraige, F. Zorzato, S. Treves, and H. Jungbluth. 2016. An RYR1 mutation associated with malignant hyperthermia is also associated with bleeding abnormalities. *Sci. Signal.* 9:ra68. doi:10.1126/scisignal.aad9813.

MacIntosh, B.R., P.F. Gardiner, and A.J. McComas. 2006. Skeletal muscle : form and function. Human Kinetics. 423 pp.

MacLennan, D.H., and E.G. Kranias. 2003. Phospholamban: a crucial regulator of cardiac contractility. *Nat. Rev. Mol. Cell Biol.* 4:566–577. doi:10.1038/nrm1151.

Marieb, E.N., P.B. Wilhelm, and J. Mallatt. Human anatomy. 895 pp.

Marks, A.R., P. Tempst, K.S. Hwang, M.B. Taubman, M. Inui, C. Chadwick, S. Fleischer, and B. Nadal-Ginard. 1989. Molecular cloning and characterization of the ryanodine receptor/junctional channel complex cDNA from skeletal muscle sarcoplasmic reticulum. *Proc. Natl. Acad. Sci. U. S. A.* 86:8683–7. doi:10.1073/pnas.86.22.8683.

Matsuo, N., K. Tanda, K. Nakanishi, N. Yamasaki, K. Toyama, K. Takao, H. Takeshima, and T. Miyakawa. 2009. Comprehensive behavioral phenotyping of ryanodine receptor type 3 (RyR3) knockout mice: decreased social contact duration in two social interaction tests. *Front. Behav. Neurosci.* 3:3. doi:10.3389/neuro.08.003.2009.

Mayr, R. 1971. Structure and distribution of fibre types in the external eye muscles of the rat. *Tissue Cell*. 3:433–462. doi:10.1016/S0040-8166(71)80045-9.

McLoon, L.K., and F. Andrade. 2012. Craniofacial Muscles: A New Framework for Understanding the Effector Side of Craniofacial Muscle Control. L.K. McLoon and F. Andrade, editors. Springer New York, New York, NY.

McLoon, L.K., V.M. Harandi, T. Brännström, P.M. Andersen, and J.-X. Liu. 2014. Wnt and extraocular muscle sparing in amyotrophic lateral sclerosis. *Invest. Ophthalmol. Vis. Sci.* 55:5482–96. doi:10.1167/iovs.14-14886.

McLoon, L.K., H. n. Park, J.-H. Kim, F. Pedrosa-Domellof, and L. V. Thompson. 2011. A continuum of myofibers in adult rabbit extraocular muscle: force, shortening velocity, and patterns of myosin heavy chain colocalization. *J. Appl. Physiol.* 111:1178–1189. doi:10.1152/japplphysiol.00368.2011.

Meissner, G. 1975. Isolation and characterization of two types of sarcoplasmic reticulum vesicles. *Biochim. Biophys. Acta - Biomembr.* 389:51–68. doi:10.1016/0005-2736(75)90385-5.

Meissner, G. 1986. Ryanodine activation and inhibition of the Ca2+ release channel of sarcoplasmic reticulum. *J. Biol. Chem.* 261:6300–6.

Meissner, G. 2002. Regulation of mammalian ryanodine receptors. *Front. Biosci.* 7:d2072-80.

Meissner, G., E. Darling, and J. Eveleth. 1986. Kinetics of rapid calcium release by sarcoplasmic reticulum. Effects of calcium, magnesium, and adenine nucleotides. *Biochemistry*. 25:236–244. doi:10.1021/bi00349a033.

Meissner, G., E. Rios, A. Tripathy, and D.A. Pasek. 1997. Regulation of Skeletal Muscle Ca $^{2+}$ Release Channel (Ryanodine Receptor) by Ca $^{2+}$ and Monovalent Cations and Anions. *J. Biol. Chem.* 272:1628–1638. doi:10.1074/jbc.272.3.1628.

Menegazzi, P., F. Larini, S. Treves, R. Guerrini, M. Quadroni, and F. Zorzato. 1994. Identification and Characterization of Three Calmodulin Binding Sites of the Skeletal Muscle Ryanodine Receptor. *Biochemistry*. 33:9078–9084. doi:10.1021/bi00197a008.

Michailovici, I., T. Eigler, and E. Tzahor. 2015. Craniofacial Muscle Development. *Curr. Top. Dev. Biol.* 115:3–30. doi:10.1016/BS.CTDB.2015.07.022.

Miller, J.M. 2007. Understanding and misunderstanding extraocular muscle pulleys. *J. Vis.* 7:10. doi:10.1167/7.11.10.

MOLLER, J., P. NISSEN, T. SORENSEN, and M. MAIRE. 2005. Transport mechanism of the sarcoplasmic reticulum Ca-ATPase pump. *Curr. Opin. Struct. Biol.* 15:387–393. doi:10.1016/j.sbi.2005.06.005.

Moncman, C.L., and F.H. Andrade. 2010. Nonmuscle myosin IIB, a sarcomeric component in the extraocular muscles. *Exp. Cell Res.* 316:1958–65. doi:10.1016/j.yexcr.2010.03.018.

Morgan, D.L., and U. Proske. 1984. Vertebrate slow muscle: its structure, pattern of innervation, and mechanical properties. *Physiol. Rev.* 64:103–169. doi:10.1152/physrev.1984.64.1.103.

Mosca, B., O. Delbono, M. Laura Messi, L. Bergamelli, Z.-M. Wang, M. Vukcevic, R. Lopez, S. Treves, M. Nishi, H. Takeshima, C. Paolini, M. Martini, G. Rispoli, F. Protasi, and F. Zorzato. 2013. Enhanced dihydropyridine receptor calcium channel activity restores muscle strength in JP45/CASQ1 double knockout mice. *Nat. Commun.* 4:1541. doi:10.1038/ncomms2496.

Mosca, B., J. Eckhardt, L. Bergamelli, S. Treves, R. Bongianino, M. De Negri, S.G. Priori, F. Protasi, and F. Zorzato. 2016. Role of the JP45-calsequestrin complex on calcium entry in slow twitch

skeletal muscles. *J. Biol. Chem.* 291:14555–14565. doi:10.1074/jbc.M115.709071.

Mühlendyck, H. 1978. Die Größe der motorischen Einheiten der unterschiedlich innervierten Augenmuskelfasern. J.F. Bergmann-Verlag. 17–26.

Nakai, J., T. Imagawa, Y. Hakamata, M. Shigekawa, H. Takeshima, and S. Numa. 1990a. Primary structure and functional expression from cDN A of the cardiac ryanodine receptor/calcium release channel. *FEBS Lett.* 271:169–177. doi:10.1016/0014-5793(90)80399-4.

Nakai, J., T. Imagawa, Y. Hakamata, M. Shigekawa, H. Takeshima, and S. Numa. 1990b. Primary structure and functional expression from cDN A of the cardiac ryanodine receptor/calcium release channel. *FEBS Lett.* 271:169–177. doi:10.1016/0014-5793(90)80399-4.

Nakashima, Y., S. Nishimura, A. Maeda, E.L. Barsoumian, Y. Hakamata, J. Nakai, P.D. Allen, K. Imoto, and T. Kita. 1997. Molecular cloning and characterization of a human brain ryanodine receptor. *FEBS Lett.* 417:157–62. doi:10.1016/s0014-5793(97)01275-1.

Nathan, E., A. Monovich, L. Tirosh-Finkel, Z. Harrelson, T. Rousso, A. Rinon, I. Harel, S.M. Evans, and E. Tzahor. 2008. The contribution of Islet1-expressing splanchnic mesoderm cells to distinct branchiomeric muscles reveals significant heterogeneity in head muscle development. *Development*. 135:647–57. doi:10.1242/dev.007989.

Nelson, B.R., F. Wu, Y. Liu, D.M. Anderson, J. McAnally, W. Lin, S.C. Cannon, R. Bassel-Duby, and E.N. Olson. 2013. Skeletal muscle-specific T-tubule protein STAC3 mediates voltage-induced Ca2+ release and contractility. *Proc. Natl. Acad. Sci.* 110:11881–11886. doi:10.1073/pnas.1310571110.

Neylon, C.B., S.M. Richards, M.A. Larsen, A. Agrotis, and A. Bobik. 1995. Multiple types of ryanodine receptor/Ca2+ release channels are expressed in vascular smooth muscle. *Biochem. Biophys. Res. Commun.* 215:814–21. doi:10.1006/bbrc.1995.2536.

Noden, D.M., and P. Francis-West. 2006. The differentiation and morphogenesis of craniofacial muscles. *Dev. Dyn.* 235:1194–1218. doi:10.1002/dvdy.20697.

Von Noorden, G.K., and E.C. (Emilio C.. Campos. 2002. Binocular vision and ocular motility : theory

and management of strabismus. Mosby. 653 pp.

Odermatt, A., S. Becker, V.K. Khanna, K. Kurzydlowski, E. Leisner, D. Pette, and D.H. MacLennan. 1998. Sarcolipin regulates the activity of SERCA1, the fast-twitch skeletal muscle sarcoplasmic reticulum Ca2+-ATPase. *J. Biol. Chem.* 273:12360–9. doi:10.1074/jbc.273.20.12360.

Ogawa, Y., N. Kurebayashi, and T. Murayama. 2000. Putative Roles of Type 3 Ryanodine Receptor Isoforms (RyR3). *Trends Cardiovasc. Med.* 10:65–70. doi:10.1016/S1050-1738(00)00050-5.

Otsu, K., H.F. Willard, V.K. Khanna, F. Zorzato, N.M. Green, and D.H. MacLennan. 1990. Molecular cloning of cDNA encoding the Ca2+ release channel (ryanodine receptor) of rabbit cardiac muscle sarcoplasmic reticulum. *J. Biol. Chem.* 265:13472–83.

OTTINI, L., G. MARZIALI, A. CONTI, A. CHARLESWORTH, and V. SORRENTINO. 1996. α and β isoforms of ryanodine receptor from chicken skeletal muscle are the homologues of mammalian RyR1 and RyR3. *Biochem. J.* 315:207–216. doi:10.1042/bj3150207.

Pachter, B.R., J. Davidowitz, and G.M. Breinin. 1976. Light and electron microscopic serial analysis of mouse extraocular muscle: morphology, innervation and topographical organization of component fiber populations. *Tissue Cell*. 8:547–60.

Park, K.A., J. Lim, S. Sohn, and S.Y. Oh. 2012. Myosin heavy chain isoform expression in human extraocular muscles: Longitudinal variation and patterns of expression in global and orbital layers. *Muscle and Nerve*. 45:713–720. doi:10.1002/mus.23240.

Peng, W., H. Shen, J. Wu, W. Guo, X. Pan, R. Wang, S.R.W. Chen, and N. Yan. 2016. Structural basis for the gating mechanism of the type 2 ryanodine receptor RyR2. *Science*. 354. doi:10.1126/science.aah5324.

Periasamy, M., and A. Kalyanasundaram. 2007. SERCA pump isoforms: Their role in calcium transport and disease. *Muscle Nerve*. 35:430–442. doi:10.1002/mus.20745.

Perni, S., K.C. Marsden, M. Escobar, S. Hollingworth, S.M. Baylor, and C. Franzini-Armstrong. 2015. Structural and functional properties of ryanodine receptor type 3 in zebrafish tail muscle. *J.*

Gen. Physiol. 145:253. doi:10.1085/jgp.20141130302112015c.

Van Petegem, F. 2015. Ryanodine Receptors: Allosteric Ion Channel Giants. *J. Mol. Biol.* 427:31–53. doi:10.1016/J.JMB.2014.08.004.

Pineles, S.L., M.Y. Chang, E.L. Oltra, M.S. Pihlblad, J.P. Davila-Gonzalez, T.C. Sauer, and F.G. Velez. 2018. Anterior segment ischemia: etiology, assessment, and management. *Eye*. 32:173–178. doi:10.1038/eye.2017.248.

Polster, A., S. Perni, H. Bichraoui, and K.G. Beam. 2015. Stac adaptor proteins regulate trafficking and function of muscle and neuronal L-type Ca2+channels. *Proc. Natl. Acad. Sci. U. S. A.* 112:602–606. doi:10.1073/pnas.1423113112.

Porter, J.D., S. Khanna, H.J. Kaminski, J.S. Rao, A.P. Merriam, C.R. Richmonds, P. Leahy, J. Li, and F.H. Andrade. 2001. Extraocular muscle is defined by a fundamentally distinct gene expression profile. *Proc. Natl. Acad. Sci. U. S. A.* 98:12062–7. doi:10.1073/pnas.211257298.

Pouvreau, S., L. Royer, J. Yi, G. Brum, G. Meissner, E. Ríos, and J. Zhou. 2007. Ca(2+) sparks operated by membrane depolarization require isoform 3 ryanodine receptor channels in skeletal muscle. *Proc. Natl. Acad. Sci. U. S. A.* 104:5235–5240. doi:10.1073/pnas.0700748104.

Powers, S.K. (Scott K., and E.T. Howley. 2018. Exercise physiology : theory and application to fitness and performance. 10th ed. McGraw-Hill Education. 594 pp.

Priori, S.G., C. Napolitano, N. Tiso, M. Memmi, G. Vignati, R. Bloise, V. Sorrentino, and G.A. Danieli. 2001. Mutations in the Cardiac Ryanodine Receptor Gene (*hRyR2*) Underlie Catecholaminergic Polymorphic Ventricular Tachycardia. *Circulation*. 103:196–200. doi:10.1161/01.CIR.103.2.196.

Protasi, F., H. Takekura, Y. Wang, S.R.W. Chen, G. Meissner, P.D. Allen, and C. Franzini-Armstrong. 2000. RYR1 and RYR3 Have Different Roles in the Assembly of Calcium Release Units of Skeletal Muscle. *Biophys. J.* 79:2494–2508. doi:10.1016/S0006-3495(00)76491-5.

Rashed, R.M., and S.H. El-Alfy. 2012. Ultrastructural organization of muscle fiber types and their

distribution in the rat superior rectus extraocular muscle. *Acta Histochem.* 114:217–225. doi:10.1016/J.ACTHIS.2011.04.007.

Rashed, R.M., S.H. El-Alfy, and I.K. Mohamed. 2010. Histochemical analysis of muscle fiber types of rat superior rectus extraocular muscle. *Acta Histochem.* 112:536–545. doi:10.1016/j.acthis.2009.05.009.

Rebbeck, R.T., Y. Karunasekara, P.G. Board, N.A. Beard, M.G. Casarotto, and A.F. Dulhunty. 2014. Skeletal muscle excitation-contraction coupling: Who are the dancing partners? *Int. J. Biochem. Cell Biol.* 48:28–38. doi:10.1016/j.biocel.2013.12.001.

Ríos, E. 2018. Calcium-induced release of calcium in muscle: 50 years of work and the emerging consensus. *J. Gen. Physiol.* 150:521–537. doi:10.1085/jgp.201711959.

Ríos, E., D. Gillespie, and C. Franzini-Armstrong. 2019. The binding interactions that maintain excitation–contraction coupling junctions in skeletal muscle. *J. Gen. Physiol.* 151:593–605. doi:10.1085/jgp.201812268.

Rosenberg, H., N. Pollock, A. Schiemann, T. Bulger, and K. Stowell. 2015. Malignant hyperthermia: a review. *Orphanet J. Rare Dis.* 10:93. doi:10.1186/s13023-015-0310-1.

Rossi, A.C., C. Mammucari, C. Argentini, C. Reggiani, and S. Schiaffino. 2010. Two novel/ancient myosins in mammalian skeletal muscles: MYH14/7b and MYH15 are expressed in extraocular muscles and muscle spindles. *J. Physiol.* 588:353–364. doi:10.1113/jphysiol.2009.181008.

Rubinstein, N.A., and J.F. Hoh. 2000. The distribution of myosin heavy chain isoforms among rat extraocular muscle fiber types. *Invest. Ophthalmol. Vis. Sci.* 41:3391–3398.

Rushbrook, J.I., C. Weiss, K. Ko, M.H. Feuerman, S. Carleton, A. Ing, and J. Jacoby. 1994. Identification of alpha-cardiac myosin heavy chain mRNA and protein in extraocular muscle of the adult rabbit. *J. Muscle Res. Cell Motil.* 15:505–15.

Ruskell, G.L., I.-B. Kjellevold Haugen, J.R. Bruenech, and F. van der Werf. 2005. Double insertions of extraocular rectus muscles in humans and the pulley theory. *J. Anat.* 206:295–306. doi:10.1111/j.1469-7580.2005.00383.x.

Saito, A., S. Seiler, A. Chu, and S. Fleischer. 1984. Preparation and morphology of sarcoplasmic reticulum terminal cisternae from rabbit skeletal muscle. *J. Cell Biol.* 99:875–885. doi:10.1083/jcb.99.3.875.

Sambasivan, R., S. Kuratani, and S. Tajbakhsh. 2011. An eye on the head: the development and evolution of craniofacial muscles. *Development*. 138:2401–15. doi:10.1242/dev.040972.

Samsó, M., and T. Wagenknecht. 2002. Apocalmodulin and Ca2+-calmodulin bind to neighboring locations on the ryanodine receptor. *J. Biol. Chem.* 277:1349–1353. doi:10.1074/jbc.M109196200.

Samsó, M., T. Wagenknecht, and P.D. Allen. 2005. Internal structure and visualization of transmembrane domains of the RyR1 calcium release channel by cryo-EM. *Nat. Struct. Mol. Biol.* 12:539–544. doi:10.1038/nsmb938.

Santulli, G., D. Lewis, A. des Georges, A.R. Marks, and J. Frank. 2018. Ryanodine Receptor Structure and Function in Health and Disease. *In* Sub-cellular biochemistry. 329–352.

Santulli, G., D.R. Lewis, and A.R. Marks. 2017a. Physiology and pathophysiology of excitation-contraction coupling: the functional role of ryanodine receptor. *J. Muscle Res. Cell Motil.* 38:37–45. doi:10.1007/s10974-017-9470-z.

Santulli, G., R. Nakashima, Q. Yuan, and A.R. Marks. 2017b. Intracellular calcium release channels: an update. *J. Physiol.* 595:3041–3051. doi:10.1113/JP272781.

Santulli, G., G. Pagano, C. Sardu, W. Xie, S. Reiken, S.L. D'Ascia, M. Cannone, N. Marziliano, B. Trimarco, T.A. Guise, A. Lacampagne, and A.R. Marks. 2015. Calcium release channel RyR2 regulates insulin release and glucose homeostasis. *J. Clin. Invest.* 125:1968–1978. doi:10.1172/JCI79273.

Schiaffino, S., and C. Reggiani. 2011. Fiber types in mammalian skeletal muscles. *Physiol. Rev.* 91:1447–531. doi:10.1152/physrev.00031.2010.

Schindelin, J., I. Arganda-Carreras, E. Frise, V. Kaynig, M. Longair, T. Pietzsch, S. Preibisch, C. Rueden, S. Saalfeld, B. Schmid, J.-Y. Tinevez, D.J. White, V. Hartenstein, K. Eliceiri, P.

Tomancak, and A. Cardona. 2012. Fiji: an open-source platform for biological-image analysis. *Nat. Methods*. 9:676–682. doi:10.1038/nmeth.2019.

Sekulic-Jablanovic, M., A. Palmowski-Wolfe, F. Zorzato, and S. Treves. 2015. Characterization of excitation–contraction coupling components in human extraocular muscles. *Biochem. J.* 466:29–36. doi:10.1042/BJ20140970.

Sekulic-Jablanovic, M., N.D. Ullrich, D. Goldblum, A. Palmowski-Wolfe, F. Zorzato, and S. Treves. 2016a. Functional characterization of orbicularis oculi and extraocular muscles. *J. Gen. Physiol.* 147:395–406. doi:10.1085/jgp.201511542.

Sekulic-Jablanovic, M., N.D. Ullrich, D. Goldblum, A. Palmowski-Wolfe, F. Zorzato, and S. Treves. 2016b. Functional characterization of orbicularis oculi and extraocular muscles. *J. Gen. Physiol.* 147:395–406. doi:10.1085/jgp.201511542.

Sharma, M.R., L.H. Jeyakumar, S. Fleischer, and T. Wagenknecht. 2000. Three-dimensional Structure of Ryanodine Receptor Isoform Three in Two Conformational States as Visualized by Cryo-electron Microscopy. *J. Biol. Chem.* 275:9485–9491. doi:10.1074/jbc.275.13.9485.

Shy, G.M., and K.R. Magee. 1956. A NEW CONGENITAL NON-PROGRESSIVE MYOPATHY. *Brain*. 79:610–621. doi:10.1093/brain/79.4.610.

Siebeck, R., and P. Kruger. 1955. Die histologische Struktur der äuβeren Augenmuskeln als Ausdruck ihrer Funktion. *Albrecht Von Graefes. Arch. Ophthalmol.* 156:636–52.

Skalicky, S.E. 2015. Ocular and Visual Physiology: Clinical Application. 28. 366 pp.

Spencer, R.F., and J.D. Porter. 2005. Biological organization of the extraocular muscles. *Prog. Brain Res.* 151:43–80. doi:10.1016/S0079-6123(05)51002-1.

Stirn Kranjc, B., V. Smerdu, and I. Eržen. 2009. Histochemical and immunohistochemical profile of human and rat ocular medial rectus muscles. *Graefe's Arch. Clin. Exp. Ophthalmol.* 247:1505–1515. doi:10.1007/s00417-009-1128-0.

Supnet, C., C. Noonan, K. Richard, J. Bradley, and M. Mayne. 2010. Up-regulation of the type 3 ryanodine receptor is neuroprotective in the TgCRND8 mouse model of Alzheimerâ€™s

disease. *J. Neurochem.* 112:356–365. doi:10.1111/j.1471-4159.2009.06487.x.

Susan Treves, *,‡, ‡ Erica Scutari, § Mylène Robert, § Séverine Groh, ‖ Michela Ottolia, ‖ Gianfranco Prestipino, § and Michel Ronjat, and F. Zorzato‡. 1997. Interaction of S100A1 with the Ca2+ Release Channel (Ryanodine Receptor) of Skeletal Muscle†. doi:10.1021/BI970160W.

Takeshima, H., T. Ikemoto, M. Nishi, N. Nishiyama, M. Shimuta, Y. Sugitani, J. Kuno, I. Saito, H. Saito, M. Endo, M. Iino, and T. Noda. 1996. Generation and characterization of mutant mice lacking ryanodine receptor type 3. *J. Biol. Chem.* 271:19649–52. doi:10.1074/JBC.271.33.19649.

Takeshima, H., S. Komazaki, K. Hirose, M. Nishi, T. Noda, and M. Iino. 1998. Embryonic lethality and abnormal cardiac myocytes in mice lacking ryanodine receptor type 2. *EMBO J.* 17:3309–3316. doi:10.1093/emboj/17.12.3309.

Takeshima, H., S. Nishimura, T. Matsumoto, H. Ishida, K. Kangawa, N. Minamino, H. Matsuo, M. Ueda, M. Hanaoka, T. Hirose, and S. Numa. 1989. Primary structure and expression from complementary DNA of skeletal muscle ryanodine receptor. *Nature*. 339:439–445. doi:10.1038/339439a0.

Takeshima, H., T. Yamazawa, T. Ikemoto, H. Takekura, M. Nishi, T. Noda, and M. Iino. 1995. Ca(2+)-induced Ca2+ release in myocytes from dyspedic mice lacking the type-1 ryanodine receptor. *EMBO J.* 14:2999–3006.

Talbot, J., and L. Maves. 2016. Skeletal muscle fiber type: using insights from muscle developmental biology to dissect targets for susceptibility and resistance to muscle disease. *Wiley Interdiscip. Rev. Dev. Biol.* 5:518–34. doi:10.1002/wdev.230.

Tarroni, P., D. Rossi, A. Conti, and V. Sorrentino. 1997. Expression of the Ryanodine Receptor Type 3 Calcium Release Channel during Development and Differentiation of Mammalian Skeletal Muscle Cells. *J. Biol. Chem.* 272:19808–19813. doi:10.1074/jbc.272.32.19808.

Theis, S., K. Patel, P. Valasek, A. Otto, Q. Pu, I. Harel, E. Tzahor, S. Tajbakhsh, B. Christ, and R. Huang. 2010. The occipital lateral plate mesoderm is a novel source for vertebrate neck

musculature. *Development*. 137:2961–71. doi:10.1242/dev.049726.

Tibrewal, S., and R. Kekunnaya. 2018. Risk of Anterior Segment Ischemia Following Simultaneous Three Rectus Muscle Surgery: Results from a Single Tertiary Care Centre. *Strabismus*. 26:77–83. doi:10.1080/09273972.2018.1450429.

Tiso, N., D.A. Stephan, A. Nava, A. Bagattin, J.M. Devaney, F. Stanchi, G. Larderet, B. Brahmbhatt, K. Brown, B. Bauce, M. Muriago, C. Basso, G. Thiene, G.A. Danieli, and A. Rampazzo. 2001. Identification of mutations in the cardiac ryanodine receptor gene in families affected with arrhythmogenic right ventricular cardiomyopathy type 2 (ARVD2). *Hum. Mol. Genet.* 10:189–194. doi:10.1093/hmg/10.3.189.

Toyoshima, C. 2009. How Ca2+-ATPase pumps ions across the sarcoplasmic reticulum membrane. *Biochim. Biophys. Acta - Mol. Cell Res.* 1793:941–946. doi:10.1016/j.bbamcr.2008.10.008.

Treves, S., H. Jungbluth, F. Muntoni, and F. Zorzato. 2008a. Congenital muscle disorders with cores: the ryanodine receptor calcium channel paradigm. *Curr. Opin. Pharmacol.* 8:319–326. doi:10.1016/j.coph.2008.01.005.

Treves, S., H. Jungbluth, F. Muntoni, and F. Zorzato. 2008b. Congenital muscle disorders with cores: the ryanodine receptor calcium channel paradigm. *Curr. Opin. Pharmacol.* 8:319–326. doi:10.1016/j.coph.2008.01.005.

Treves, S., M. Vukcevic, M. Maj, R. Thurnheer, B. Mosca, and F. Zorzato. 2009. Minor sarcoplasmic reticulum membrane components that modulate excitation-contraction coupling in striated muscles. *J. Physiol.* 587:3071–9. doi:10.1113/jphysiol.2009.171876.

Tripathy, A., L. Xu, G. Mann, and G. Meissner. 1995. Calmodulin activation and inhibition of skeletal muscle Ca2+ release channel (ryanodine receptor). *Biophys. J.* 69:106–119. doi:10.1016/S0006-3495(95)79880-0.

Tzahor, E. 2009. Heart and craniofacial muscle development: A new developmental theme of distinct myogenic fields. *Dev. Biol.* 327:273–279. doi:10.1016/j.ydbio.2008.12.035.

Venturi, E., E. Galfré, F. O'Brien, S.J. Pitt, S. Bellamy, R.B. Sessions, and R. Sitsapesan. 2014.

FKBP12.6 Activates RyR1: Investigating the Amino Acid Residues Critical for Channel Modulation. *Biophys. J.* 106:824–833. doi:10.1016/j.bpj.2013.12.041.

Vukcevic, M., M. Broman, G. Islander, M. Bodelsson, E. Ranklev-Twetman, C.R. M??ller, and S. Treves. 2010. Functional properties of RYR1 mutations identified in Swedish patients with malignant hyperthermia and central core disease. *Anesth. Analg.* 111:185–190. doi:10.1213/ANE.0b013e3181cbd815.

Vukcevic, M., G.C. Spagnoli, G. Iezzi, F. Zorzato, and S. Treves. 2008. Ryanodine receptor activation by Ca v 1.2 is involved in dendritic cell major histocompatibility complex class II surface expression. *J. Biol. Chem.* 283:34913–22. doi:10.1074/jbc.M804472200.

Wagenknecht, T., R. Grassucci, J. Berkowitz, G.J. Wiederrecht, H.B. Xin, and S. Fleischer. 1996. Cryoelectron microscopy resolves FK506-binding protein sites on the skeletal muscle ryanodine receptor. *Biophys. J.* 70:1709–15. doi:10.1016/S0006-3495(96)79733-3.

Wagenknecht, T., C.-E. Hsieh, B.K. Rath, S. Fleischer, and M. Marko. 2002. Electron Tomography of Frozen-Hydrated Isolated Triad Junctions. *Biophys. J.* 83:2491–2501. doi:10.1016/S0006-3495(02)75260-0.

Wasicky, R., F. Ziya-Ghazvini, R. Blumer, J.R. Lukas, and R. Mayr. 2000. Muscle fiber types of human extraocular muscles: a histochemical and immunohistochemical study. *Invest. Ophthalmol. Vis. Sci.* 41:980–90.

Xiong, J., X. Liu, Y. Gong, P. Zhang, S. Qiang, Q. Zhao, R. Guo, Y. Qian, L. Wang, L. Zhu, R. Wang, Z. Hao, H. Wen, J. Zhang, K. Tang, W.-F. Zang, Z. Yuchi, H. Chen, S.R.W. Chen, W. Zheng, S.-Q. Wang, Y.-W. Xu, and Z. Liu. 2018. Pathogenic mechanism of a catecholaminergic polymorphic ventricular tachycardia causing-mutation in cardiac calcium release channel RyR2. *J. Mol. Cell. Cardiol.* 117:26–35. doi:10.1016/j.yjmcc.2018.02.014.

Yan, Z., X. Bai, C. Yan, J. Wu, Z. Li, T. Xie, W. Peng, C. Yin, X. Li, S.H.W. Scheres, Y. Shi, and N. Yan. 2015. Structure of the rabbit ryanodine receptor RyR1 at near-atomic resolution. *Nature*. 517:50–55. doi:10.1038/nature14063.

Yáñez, M., J. Gil-Longo, and M. Campos-Toimil. 2012. Calcium Binding Proteins. Springer,

Dordrecht. 461–482.

Yanoff, M., and J.S. Duker. 2018. Ophthalmology. 1440 pp.

Yuchi, Z., K. Lau, and F. Van Petegem. 2012. Disease Mutations in the Ryanodine Receptor Central Region: Crystal Structures of a Phosphorylation Hot Spot Domain. *Structure*. 20:1201–1211. doi:10.1016/j.str.2012.04.015.

Zaharieva, I.T., A. Sarkozy, P. Munot, A. Manzur, G. O'Grady, J. Rendu, E. Malfatti, H. Amthor, L. Servais, J.A. Urtizberea, O.A. Neto, E. Zanoteli, S. Donkervoort, J. Taylor, J. Dixon, G. Poke, A.R. Foley, C. Holmes, G. Williams, M. Holder, S. Yum, L. Medne, S. Quijano-Roy, N.B. Romero, J. Fauré, L. Feng, L. Bastaki, M.R. Davis, R. Phadke, C.A. Sewry, C.G. Bönnemann, H. Jungbluth, C. Bachmann, S. Treves, and F. Muntoni. 2018. STAC3 variants cause a congenital myopathy with distinctive dysmorphic features and malignant hyperthermia susceptibility. *Hum. Mutat.* 39:1980–1994. doi:10.1002/humu.23635.

Zalk, R., O.B. Clarke, A. des Georges, R.A. Grassucci, S. Reiken, F. Mancia, W.A. Hendrickson, J. Frank, and A.R. Marks. 2015. Structure of a mammalian ryanodine receptor. *Nature*. 517:44–49. doi:10.1038/nature13950.

Zeiger, U., C.H. Mitchell, and T.S. Khurana. 2010. Superior calcium homeostasis of extraocular muscles. *Exp. Eye Res.* 91:613–622. doi:10.1016/J.EXER.2010.07.019.

Zhang, L., Y. Liu, F. Song, H. Zheng, L. Hu, H. Lu, P. Liu, X. Hao, W. Zhang, and K. Chen. 2011. Functional SNP in the microRNA-367 binding site in the 3'UTR of the calcium channel ryanodine receptor gene 3 (RYR3) affects breast cancer risk and calcification. *Proc. Natl. Acad. Sci.* 108:13653–13658. doi:10.1073/pnas.1103360108.

Zhou, Y., D. Liu, and H.J. Kaminski. 2010. Myosin heavy chain expression in mouse extraocular muscle: more complex than expected. *Invest. Ophthalmol. Vis. Sci.* 51:6355–63. doi:10.1167/iovs.10-5937.

Ziermann, J.M., R. Diogo, and D.M. Noden. 2018. Neural crest and the patterning of vertebrate craniofacial muscles. *genesis*. 56:e23097. doi:10.1002/dvg.23097.

Zipes, D.P., J. Jalife, W.G. Stevenson, A. Kushnir, and S.O. Marx. 2018. Voltage-Gated Calcium Channels. *Card. Electrophysiol. From Cell to Bedside*. 12–24. doi:10.1016/B978-0-323-44733-1.00002-X.

Zoladz, J.A. 2018. Muscle and exercise physiology. Academic Press. 618 pp.

Zorzato, F., A.A. Anderson, K. Ohlendieck, G. Froemming, R. Guerrini, and S. Treves. 2000. Identification of a novel 45 kDa protein (JP-45) from rabbit sarcoplasmic-reticulum junctional-face membrane. *Biochem. J.* 351 Pt 2:537–43. doi:10.1042/BJ3510537.

Zorzato, F., J. Fujii, K. Otsu, M. Phillips, N.M. Green, F.A. Lai, G. Meissner, and D.H. MacLennan. 1990a. Molecular cloning of cDNA encoding human and rabbit forms of the Ca2+ release channel (ryanodine receptor) of skeletal muscle sarcoplasmic reticulum. *J. Biol. Chem.* 265:2244–56.

Zorzato, F., J. Fujii, K. Otsu, M. Phillips, N.M. Green, F.A. Lai, G. Meissner, and D.H. MacLennan. 1990b. Molecular cloning of cDNA encoding human and rabbit forms of the Ca2+ release channel (ryanodine receptor) of skeletal muscle sarcoplasmic reticulum. *J. Biol. Chem.* 265:2244–56.

Zorzato, F., A. Margreth, and P. Volpe. 1986. Direct photoaffinity labeling of junctional sarcoplasmic reticulum with [14C]doxorubicin. *J. Biol. Chem.* 261:13252–13257.